



Universitat Autònoma de Barcelona

ADVERTIMENT. L'accés als continguts d'aquesta tesi queda condicionat a l'acceptació de les condicions d'ús establertes per la següent llicència Creative Commons:  http://cat.creativecommons.org/?page_id=184

ADVERTENCIA. El acceso a los contenidos de esta tesis queda condicionado a la aceptación de las condiciones de uso establecidas por la siguiente licencia Creative Commons:  <http://es.creativecommons.org/blog/licencias/>

WARNING. The access to the contents of this doctoral thesis it is limited to the acceptance of the use conditions set by the following Creative Commons license:  <https://creativecommons.org/licenses/?lang=en>



**Universitat Autònoma
de Barcelona**

Hydroxypropyl Cellulose as Enabling Material for the Nanofabrication of Photonic Architectures

Camilla Dore

Tesi Doctoral

Programa de Doctorat en Ciència de Materials

Agustin Mihi (Director)

Jordi Hernando (Tutor)

Institut de Ciència de Materials de Barcelona

(ICMAB-CSIC)

2020



**Universitat Autònoma
de Barcelona**

Memòria presentada per aspirar al Grau de Doctor per
Camilla Dore

Vist i plau

Dr. Agustin Mihi
(Director)

Dr. Jordi Hernando
(Tutor)

Bellaterra, 17/11/2020

*Nella vita non c'è nulla da temere,
solo da capire*

Margherita Hack

A Barcelona

Abstract

The increasing concerns about environmental impact and sustainability of human activities have led to a renewed interest in naturally derived materials. In this frame, cellulose, the most abundant polymer on earth, has attracted increasing attention, since it is extracted from cheap and renewable sources, it is extremely versatile and already widely employed in different technological sectors. In this thesis, I optimized industrially scalable nanofabrication processes based on soft-lithographic techniques, for the realization of tailored photonic architectures in hydroxypropyl cellulose (HPC), a water soluble and biocompatible cellulose derivative. I illustrate different strategies to fabricate photonic and plasmonic crystal into HPC using nanoimprint lithography (NIL), one of the most promising techniques for large-scale manufacturing. Cellulose membranes can be easily patterned into submicrometric periodic lattices that exhibit tunable structural colors, can host an organic dye and boost its photoluminescence. Metal coating these cellulose photonic architectures results in flexible plasmonic crystals with excellent optical properties that can be used as disposable surface-enhanced Raman spectroscopy substrates. An alternative route to integrate functional materials into HPC is by transfer printing technique, a nanofabrication strategy that provides a straightforward way for the assembly of independently processed materials into spatially tailored architectures. I explore the high versatility of this approach embedding metal nanoparticles arrays and carbon nanotube networks into HPC adhesive films, obtaining respectively Moiré multilayer superstructures and semitransparent conducting electrodes. Interestingly, the HPC adhesives can also work as transient tapes for transferring material from a donor substrate to a receiver one, in an ecofriendly fashion. HPC tapes adhere perfectly to uneven substrates and can be simply washed away using water. Specifically, I demonstrate improved performance of this method compared to standard transfer based on elastomers, showing crack free stripping, transfer and piling up of both patterned and continuous thin metallic films. Following the line of reducing chemical pollution in nanofabrication processes, I employed HPC as non-toxic and water processable sacrificial material for advanced and ecofriendly nanofabrication aided by NIL. HPC showed excellent performance when employed as resist under standard electronic manufacturing processes, such as reactive ion etching and metal lift off. Silicon nanostructures with feature

sizes down to 100 nm and metal nanoparticle arrays are straightforwardly fabricated employing just HPC and water as solvent.

Resumen

La creciente preocupación por el impacto medioambiental y la sostenibilidad de las actividades humanas ha llevado a un renovado interés para los materiales de origen natural. En este marco, la celulosa, el polímero natural más abundante del mundo, ha recibido una gran atención. La celulosa se extrae de fuentes baratas y renovables y es un material extremadamente versátil y ya ampliamente empleado en diferentes sectores tecnológicos. En esta tesis, se han optimizado procesos de nanofabricación escalables y compatibles con la industria empleando la técnica de litografía suave, para la fabricación de arquitecturas fotónicas en hidroxipropilcelulosa (HPC). La HPC es un derivado de celulosa que es soluble en agua y biocompatible. En la tesis se ilustrarán las diferentes estrategias adoptadas para fabricar cristales fotónicos y plasmónicos en HPC utilizando la litografía por nanoimpresión (NIL), una de las técnicas más prometedoras para la fabricación a gran escala de nanoestructuras. Las membranas de celulosa se pueden imprimir fácilmente con motivos periódicos de tamaño submicrométrico, dando como resultado colores estructurales, además la celulosa puede hospedar colorantes orgánicos y mediante la corrugación aumentar su fotoluminiscencia. El recubrimiento metálico de estas arquitecturas fotónicas de celulosa da como resultado cristales plasmónicos flexibles con excelentes propiedades ópticas que se pueden utilizar como sustratos desechables para espectroscopía Raman amplificada en superficie. En esta tesis también se incluye el estudio de una ruta alternativa para integrar materiales funcionales en la HPC mediante la técnica de impresión por transferencia. Esta estrategia de nanofabricación proporciona una manera sencilla para ensamblar materiales que han sido procesados independientemente combinándolos en arquitecturas más complejas. Además, se demuestra la gran versatilidad de esta técnica fabricando redes ordenadas de nanopartículas metálicas y matrices de nanotubos de carbono soportadas en películas adhesivas de HPC, obteniendo respectivamente superestructuras tipo Moiré y electrodos conductores semitransparentes. Las membranas de HPC también pueden funcionar como cintas adhesivas solubles en agua empleadas para transferir material de un sustrato donante a uno receptor de manera respetuosa con el medio ambiente. Las cintas de HPC se adhieren perfectamente a sustratos irregulares y se pueden eliminar con agua. Específicamente, se demuestra una mejora en la transferencia de membranas de metal utilizando este método respecto al procedimiento estándar que emplea siliconas. La transferencia con HPC previene la aparición de grietas durante el proceso de transferencia y permite el apilamiento de películas metálicas

finas, tanto con patrón como continuas. Por último y siguiendo la idea de reducir la contaminación derivada de los procesos de nanofabricación, se emplea la HPC como resina transitoria no tóxica y procesable con agua para su empleo en técnicas de nanofabricación avanzada y ecológica como la técnica NIL. La HPC ha demostrado una resistencia y compatibilidad excelente al emplearse en procesos de nanofabricación estándar, como el grabado con iones reactivos o la deposición de máscaras de metal. Empleando HPC como resina, se han producido nanoestructuras de silicio con tamaños mínimos de hasta 100 nm, también se han conseguido fabricar redes de nanopartículas metálicas de manera sencilla empleando solo HPC y agua como disolvente.

List of abbreviations

AAO	Anodic aluminum oxide	LSR	Surface lattice resonance
ARC	Antireflection coating	μ CP	Microcontact printing
CD	Circular dichroism	NIL	Nanoimprint lithography
CMOS	Complementary metal-oxide semiconductor	NP	Nanoparticle
CNC	Cellulose nanocrystals	nTP	Nano-transfer printing
CNF	Cellulose nanofibers	PhC	Photonic crystal
CNT	Carbon nanotubes	PDMS	Polydimethylsiloxane
DBR	Diffuse Brag reflector	PLA	Polylactic acid
DNA	Deoxyribonucleic acid	PMMA	Polymethyl methacrylate
EBL	Electron beam lithography	PU	Polyurethane
EOT	Extraordinary optical transmission	PVA	Polyvinyl alcohol
FCC	Face centered cubic	RT	Room temperature
HPC	Hydroxypropyl cellulose	SEM	Scanning electron microscope
IBL	Ion beam lithography	SERS	Surface enhanced Raman spectroscopy
IC	Integrated circuit	SIO	Silk inverse opal
IoT	Internet of Things	SPP	Surface plasmon polariton
LiDAR	Light detection and ranging	tNIL	temperature assisted NIL
LSPR	Localized surface plasmon resonance	UV	Ultraviolet

Table of Contents

Motivation.....	1
Scope of this thesis	3
Chapter 1 Photonic architectures	4
1.1 Photonic crystals.....	5
1.2 Surface plasmon resonances.....	9
1.2.1 Plasmonic crystals	13
1.3 Biomaterials for photonics and plasmonics.....	16
1.4 Commercial applications	19
1.5 References	20
Chapter 2 Cellulosic biomaterials	25
2.1 Cellulose structure and properties	27
2.2 Cellulose derivatives.....	28
2.3 Hydroxypropyl cellulose.....	30
2.4 References	33
Chapter 3 Lithographic techniques	37
3.1 Radiation based lithography	38
3.1.1 Photolithography	39
3.1.2 Interference lithography	41
3.1.3 Electron beam lithography (EBL).....	42
3.1.4 Ion beam lithography (IBL)	44
3.2 Nanoimprint lithography.....	45
3.2.1 Thermal nanoimprint lithography (tNIL).....	45

Table of contents

3.2.2	UV nanoimprint lithography (UV-NIL)	47
3.3	Soft lithography.....	49
3.3.1	Soft nanoimprinting lithography	49
3.3.2	Micro-contact printing (μ -CP)	50
3.3.3	Transfer printing	52
3.3.4	Template induced assembly.....	53
3.4	Environmental and economic impact of lithography.....	54
3.5	References	57
Chapter 4 Soft nanoimprinting optimization.....		64
4.1	Replica molding process.....	64
4.2	Molds fabrication.....	65
4.2.1	Pattern resolution.....	66
4.2.2	Pattern mechanical instabilities	68
4.2.3	Materials for stamp fabrication.....	74
4.3	Hot embossing process	77
4.3.1	Nanoimprinting tool (NILT CNI).....	79
4.4	References	80
Chapter 5 Compilation of articles		83
5.1	Hydroxypropyl cellulose photonic architectures by soft nanoimprinting lithography	83
5.2	Adhesives for Transfer Printing of Carbon Nanotubes and Metallic Nanostructures.....	104
5.3	A water-processable cellulose-based resist for advanced nanofabrication	124
Summary of results.....		144
Conclusions and Outlook		148
Appendix A Optimization of metal films deposition.....		150

Appendix B Cellupack: Hydroxypropyl cellulose packaging..... 154

Scientific contributions..... 156

Motivation

Nowadays, optoelectronics devices play a key role in our daily life, being fundamental components of high-technological products, such as computers, smartphones and televisions and empowering essential sectors like telecommunications, data storage and medical diagnostics. The advent of the internet of things (IoT) era has resulted in a dramatic change in the way optoelectronic devices finds application around us. An increasing number of cheap and relatively simple physical objects are rapidly getting embedded with sensors, software, and communication systems. Our society is becoming extremely connected with everyday products and even human being themselves continuously exchanging data with each other, and this is only the early stage of IoT. Given their capability to improve the rapid flux of information through the IoT, implantable, wearable and product-integrated optoelectronic technologies are attracting increasing attention in a wide range of emerging field, such as real-time healthcare monitoring and treatment, ambient control, soft robotics, prosthetics, smart clothing and smart packaging, among others.

While connectivity is expanding in our world, sustainability, the greatest concern of modern times, is deeply modifying our approach to product development in different fields, some of which will inevitably overlap and influence the design of IoT technologies. Among the various challenges that our society is facing, the reduction of toxic and oil-based product use, is one of the pivotal themes of discussions. The development of cleaner and more efficient manufacturing processes and the substitution of nonrenewable raw materials with more ecofriendly alternatives, have already become a government enforced constrain in many industrial sectors, exponentially powering the biomaterials research. A good example of these new policies is the recent ban to single-use plastic products in most European countries (EU directive 2019/904). The restriction in plastic use has brought the industry focus to naturally derived polymers, and biodegradable products like starch plastic bags or polylactic acid cups that almost perfectly resemble plastic are currently commercialized. However, how will IoT and the sustainability challenge affect the next generation of optoelectronic devices? Which new requirements should they satisfy to be marketable? Here are few considerations we can infer from the above discussion.

- **Materials.**

Definitively, naturally derived materials will be protagonists, thanks to their sustainable nature: they are typically non-toxic, biodegradable, and their primary sources of extraction are renewable. Electronic waste is an already well-known issue, but if we consider that optoelectronic devices will be embedded into mass produced goods, having them fabricated with low environmental impact materials will be extremely beneficial for their end-of-life disposal and for their easier integration into new generation ecofriendly products. Furthermore, biomaterials and specifically biopolymers are excellent candidate for the realization of flexible and biocompatible devices, which makes them an extremely promising platform for application in the fast-growing field of biotechnology.

- **Fabrication processes.**

Sustainability is not only about the material of which a product is made, but also about its production process. It is definitively necessary to find low environmental impact fabrication processes with lesser toxic residues and CO₂ generation. From a more economical point of view, if optoelectronic devices are supposed to become component also in relatively cheap and widespread mass-produced goods, their fabrication should be low cost and have high throughput.

Scope of this thesis

Nanotechnology has definitively marked a turning point in material science, allowing a deeper understanding of the nanoscale phenomena and enabling novel applications for unconventional materials, among which biopolymers. In this frame, cellulose and its derivatives have raised a renewed interest both in industry and in the scientific community. The huge availability and the indisputable low cost and renewability of its sources of extraction together with the already high maturity of cellulose related technologies, makes cellulose an excellent candidate for the large-scale production of different ecofriendly and biocompatible materials. Today a huge number of cellulose derivatives are implemented as functional and sustainable materials in a wide range of high-end technologies such as biomimetic, bioengineering, flexible electronic, biofuels production and composite materials. Among the commercially available cellulose derivatives, Hydroxypropyl cellulose (HPC) is a particularly interesting material with a unique combination of characteristics: It is water soluble, thermoformable, biocompatible, edible and biodegradable. HPC can form transparent films with excellent mechanical properties, insoluble hydrogels, and it assembles in liquid chiral crystals that presents iridescent structural colors when sediments in water. Many efforts have been done to provide additional functionality to this multifunctional material, particularly in order to make it responsive to external stimuli. Despite the interesting properties of HPC, there is still missing a fabrication technique to pattern with high resolution this multifunctional material. In particular, patterning of other water-soluble biopolymers such as silk or other cellulose derivatives have been recently demonstrated, showing promising results and enabling novel applications of those type biomaterials in different branches of photonics. The development of a set of nano structuring technologies that are scalable and allow controlled patterning of HPC films would be extremely beneficial to provide further functionalities to this widely available and low cost material, opening new paths for its implementation in the large-scale fabrication of next generation ecofriendly and biocompatible optoelectronic devices.

CHAPTER 1

Photonic architectures

Properties and applications

The way an object appears to our eyes depends on how it interacts with visible light, the region of the electromagnetic radiation with wavelength comprised between 400 and 700 nm. A medium that strongly absorbs all wavelengths appears black, while one that does not absorb will look transparent. However, the surface or contour of an object will also play a role on the final object appearance, inducing reflection, refraction, scattering or diffraction effects. This is for instance the reason why clouds look white (Figure 1.1a) or the opal gemstones look so beautifully colored (Figure 1.1b), even if the materials from which they are made (water and glass respectively) are transparent.



Figure 1.1. Light matter interaction in nature. a) Light scattering from water droplets gives rise to the white appearance of clouds. b) The colorful appearance of opals is due to light diffraction from ordered arrays of silica nanospheres inside the gemstones.

The fraction of light that human beings can perceive represents only a small portion of the electromagnetic radiation spectrum, that ranges from tens of picometer of γ -rays to the kilometer of radio waves, comprising, X-rays, infrared, UV and microwaves. The interaction between the oscillating electromagnetic waves and the charged particles that constitute matter gives rise to a wide variety of interesting phenomena, that since centuries it has stimulated the curiosity of scientists, leading to today's modern photonics. Specifically the recent advances in nanotechnology have enabled light manipulation throughout the development of new materials with enhanced functionalities and engineered optical properties. The

exploration of light coupling to nanostructured materials has rapidly expanded, finding applications in countless fields, such as energy harvesting, lightning, imaging, sensing and biomimetics. Among the wide range of photonic systems that are being currently investigated, periodic patterns have attracted great attention for their capability to confine light, improve the performance of optoelectronic devices or access extraordinary optical phenomena.

In this chapter, I will introduce some of the unique properties of photonic and plasmonic crystals, which are periodic nanostructured architectures that I widely exploit in this thesis. I will also illustrate some of their most advanced applications both in industry and in research, particularly focusing on biomaterial-based ones.

1.1 Photonic crystals

Photonic crystals (PhCs) are natural or artificial structures that presents a periodic modulation of the refractive index. PhCs present a clear a similarity with the periodically arrangement of atoms in crystal lattice structures. Specifically, the behavior of photons in a PhC is comparable to the one of electrons in a crystal lattice. PhCs are indeed capable to provide a photonic band gap (PBG), that is a range of energies (frequencies) at which photons cannot propagate inside the structure and that is responsible for most of the practical properties of the PhCs. PhCs can be divided in three main groups,¹ depending on structure geometry, as illustrated in Figure 1.2.

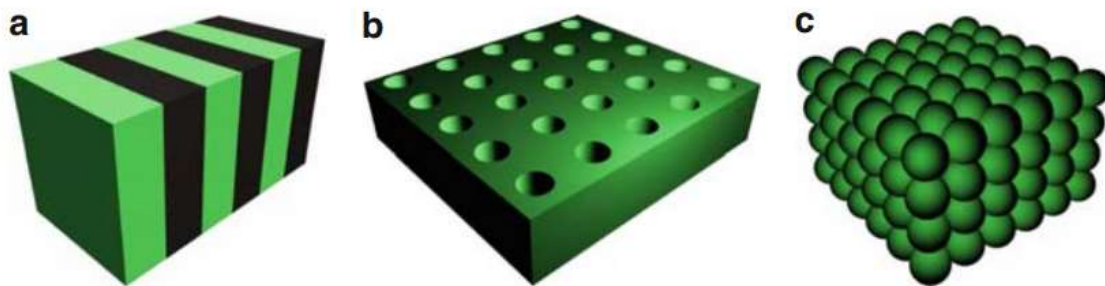


Figure 1.2 Photonic crystal types. a) One-dimensional (1-D PhC). b) Two-dimensional (2-D PhC). c) Three dimensional (3-D PhC).²

- **One-dimensional (1-D PhC or Bragg stacks):** the periodicity occurs in one direction, while in two other directions structure is uniform. This class of structures consists in stacks of alternate layers of

media with different refractive index, and they are typically employed dielectric mirrors, exploiting the forbidden interval for light propagation (photonic bandgap) perpendicular to the periodicity.²

- **Two-dimensional (2-D PhC):** the periodicity occurs in two directions. This class of structures typically presents surface patterns with square or hexagonal lattice consisting in periodically arranged pores or protrusions (assuming that one of the two media is air). They are employed as antireflection coating, index matching interfaces, photonic crystal fibers, resonant antennas, and for structural color generation. These structures show photonic bands and bandgaps in-plane and act as diffraction gratings under normal incidence ²
- **Three dimensional (3-D PhC):** The modulation of permittivity occurs along all three directions. This class of structures presents the largest variety of configurations, being opals the most well-known example of 3D PhCs found in nature (Figure 1.1b). They consist in silica microspheres assembled in a face-centered cubic lattice (FCC) that reflect light with a strong dependence of the incident angle. These structures showed have the potential to sustain a full photonic band gap, a forbidden interval for light propagation for all directions which great interest for light manipulation ²

Structures and functionalities of PhC

The optical properties of the PhCs can be tailored to specific functionalities by the properly designing the materials that compose them, their crystal lattice structure, the shape of the features and by combining two or more of these approaches. It is possible for instance to obtain specific and selective responses to light polarization, wavelength and direction, among others.

Figure 1.3 shows some example of PhC architectures and their resulting optical properties. Diffraction gratings can be designed to achieve maximum efficiency in one given diffraction order like in the case of the Blazed grating structure illustrated in Figure 1.3a. Using this type of PhC the maximum optical power for a specific wavelength is concentrated in a desired diffraction order, minimizing residual power in the other orders, particularly the zeroth. Depending on the grating geometry different wavelengths and diffraction directions can be selected. Further functionalities can be obtained employing patterns of anisotropic or chiral features. For instance, using the gammadion shape illustrated in Figure 1.3b, it is possible to obtain circular dichroism, a selective response to right and left circularly polarized light.³

Another example that is particularly easy to find in nature, is the structural color generation. If a radiation whose frequency falls inside the PBG impinges on the PhC, it will be completely reflected, giving rise to a colorful appearance that is not originated by dyes or pigments. Typically PhC colors are iridescent, that is they depend on the angle of incidence or observation. However, the morpho butterfly illustrated in Figure 1.3c has developed a lamellar hierarchical structure that allows its wings to look blue from almost any point of view. PhCs are efficient systems for reflecting light with specific wavelength or polarity, yet they can be also designed to broadly suppress interface reflection, acting as antireflection coatings (ARC),⁴ as illustrated in Figure 1.3d.⁵ Interestingly, by introducing defects in the crystal structure of a PhC, it is possible to obtain strong spatial light confinement, a strategy that is widely employed in photonic crystal waveguides (Figure 1.3e) and that is also the basic principle of operation of distributed Bragg reflector laser (DBR) with vertical cavity. Different light emitting devices often employ photonic crystals to enhance both the intensity and directionality of radiation.⁶⁻⁸ Finally by engineering the subwavelength units of the PhC it is possible to fabricate metamaterials, unique artificial structures that exhibit properties not attainable with ordinary media. Figure 1.3f shows an all dielectric metamaterial that presents an epsilon-near-zero response to infrared light that has been fabricated using silicon and silicon dioxide alternate periodic stacks.⁹

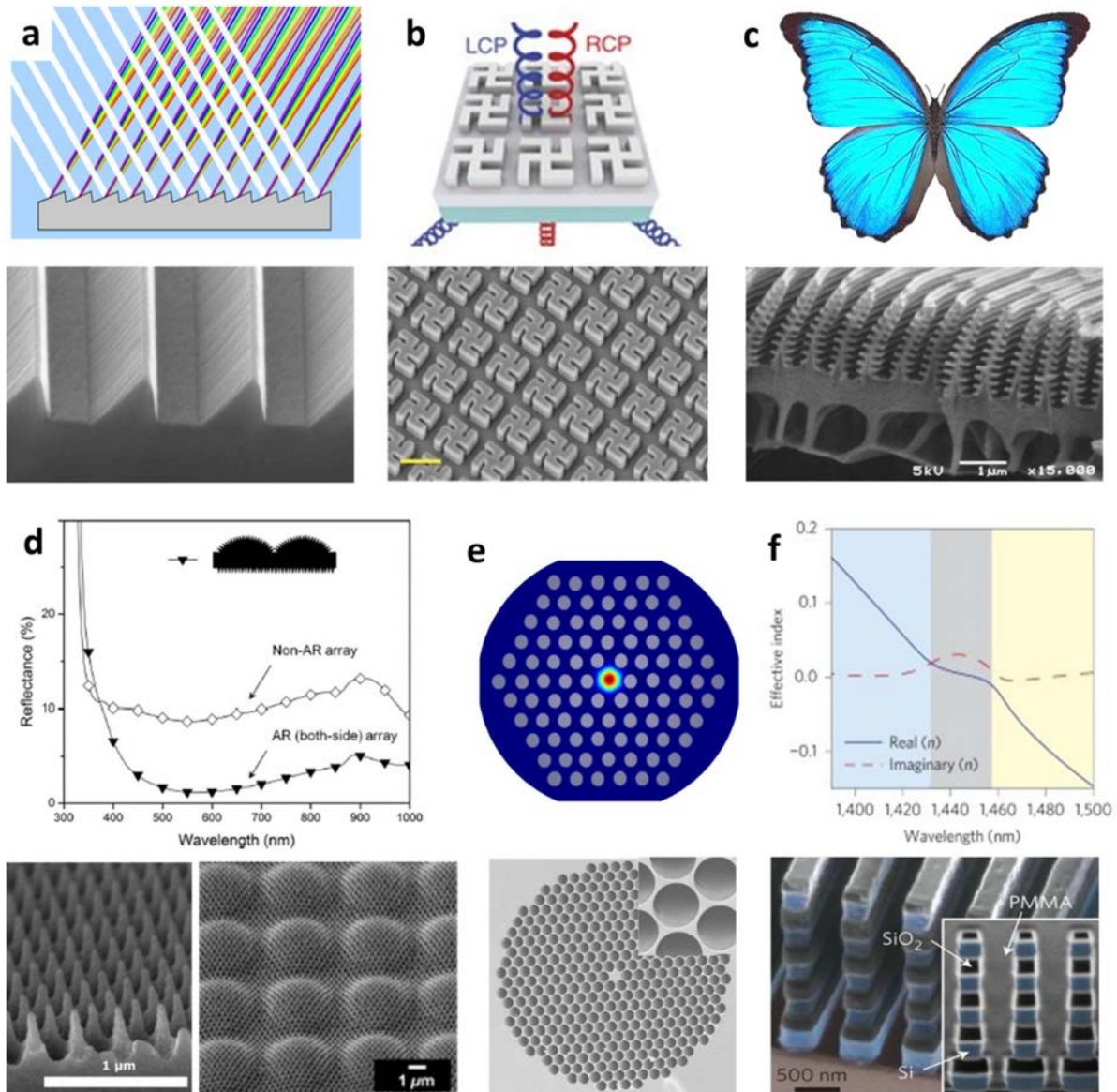


Figure 1.3 Example of photonic crystal structures and their corresponding functionalities. a) Blazed diffraction grating structure fabricated by NILT technology company. b) Pattern of TiO₂ gammadions showing intrinsic chirality response. RCP light (red helix) is transmitted in the zero-order while LCP light (blue helix) is transmitted the first order.³ c) lamellar microstructures of the morpho butterfly that originates its characteristic blue color. d) Microlenses array whose surface has been patterned with an antireflection coating (ARC).⁵ e) Section of a photonic crystal fiber and corresponding simulation of electric field intensity distribution in point defect cavity (Lumerical Inc.).⁹ f) Epsilon-near-zero all dielectric metamaterial.⁹

In this thesis, I fabricated 2-D and 1-D photonic crystals in hydroxypropyl cellulose, employing different lattice geometries and characterizing their correspondent optical properties of (see Chapter 5)

1.2 Surface plasmon resonances

The optical properties of metals are extremely different from the ones of dielectric materials. In metals light electromagnetic waves can promote resonant oscillations of the free electron cloud (plasma). These electron excitations, called surface plasmons, are tightly bounded to the metal surface where they originate intense electromagnetic fields with a strong spatial confinement. These characteristics allow precise tuning of their associated electromagnetic field distribution by simply designing the metal surface structure, and to obtain extremely intense field enhancement in small volumes using very low excitation powers. Surface plasmons are also extremely susceptible to physical and chemical changes in their surrounding environment, a characteristic that enabled plasmonic-based sensors to reach detections sensitivities down to single molecules.

There are two main types of surface plasmons, named propagating surface plasmon polaritons (simply abbreviated SPPs) and localized surface plasmon polaritons (LSPRs).

- **Propagating surface plasmon polaritons (SPPs)**

SPPs are hybrid photon-electron excitations that travels at the interface between a dielectric and a metallic medium. They emerge due to coupling of the light EM wave with a longitudinal oscillation of the metal charge density (Figure 1.4a). SPPs can propagate in plane at the interface, but they are evanescent in the perpendicular directions, penetration depths of the order of tens of nanometers (Figure 1.4b).¹⁰

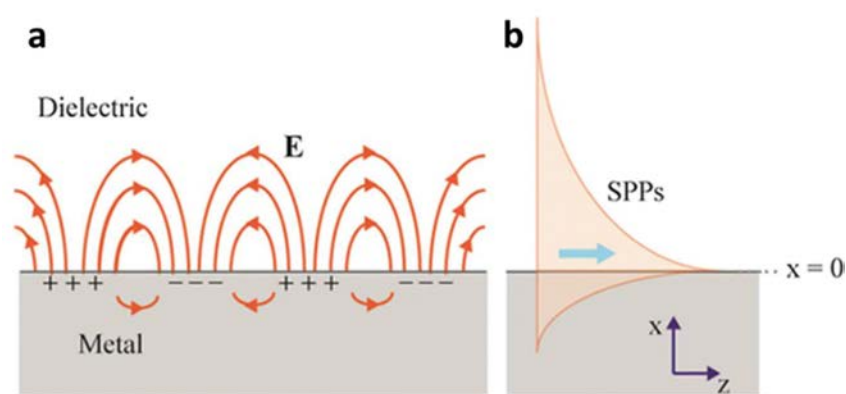


Figure 1.4 Propagating surface plasmon polaritons. a) Electric charge density waves of surface plasmon polaritons propagating at the metal-dielectric interface. b) Decay of the perpendicular electric field intensity inside the dielectric and the metal.

SPPs only exist for the transverse magnetic (TM) polarization, that is, with the magnetic field perpendicular to the propagation plane. Solving Maxwell's equations with this boundary condition leads to the dispersion relation of SPP:

$$k_{||} = k_0 \sqrt{\frac{\epsilon_m \epsilon_d}{\epsilon_m + \epsilon_d}} \quad (1.1)$$

$$k_0 = \frac{\omega}{c} \quad (1.2)$$

where $k_{||}$ is the wavevector parallel to the surface, ω the wave frequency and c the speed of light in vacuum while ϵ_m and ϵ_d are the metal and dielectric permittivities. However, considering that in the dielectric media, light follows the linear dispersion relation:

$$k_{||} = \frac{\omega}{c} \sqrt{\epsilon_d} \quad (1.3)$$

the SPP wavevector results always higher than in the dielectric or air. This means that light impinging at a dielectric-metal interface will require an extra in-plane momentum to be able to excite the SPPs. There are several strategies to provide this extra momentum to the incoming light, including illumination through a prism by total internal reflection, or benefitting from the diffraction of a grating (Figure 1.5), being the latter the more practical way for integration in real devices, since it allows for direct incorporation of the coupling mechanism into the structure.

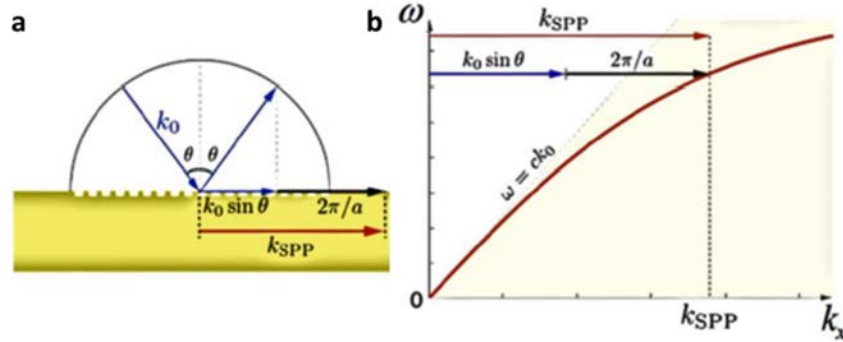


Figure 1.5 Excitation of SPPs on a metal-dielectric grating at an incidence ϑ . **b** Dispersion relation of SPP (red). The blue vector represents the momentum provided by impinging light, while the black vector is the momentum provided by the grating.

For a square grating of period a , the coupling condition can be expressed as follow:

$$k_{||} = k_{||}^{in} + m|G| \quad (1.4)$$

where $k_{||}^{in}$ is the parallel component of the incident wavevector, G is the reciprocal lattice vector of the grating in the same direction of $k_{||}^{in}$ and is connected to the lattice parameter of the grating as follow:

$$|G|=2\pi/a \quad (1.5)$$

- **Localized surface plasmon polaritons (LSPRs).**

Localized surface plasmon resonance arises when a light wave impinges on a conductive nanoparticle whose size is smaller than the wavelength of light. This interaction produces coherent plasmon oscillations (Figure 1.6a) localized in the nanoparticle, whose resonances occur at specific frequencies determined by the particle material, shape, size, and by the surrounding environment. LSPR do not have a specific propagation direction, but they are strongly coupled to the incident electromagnetic radiation and yield to a dramatic increase of the electronic field at the metal-dielectric interface.

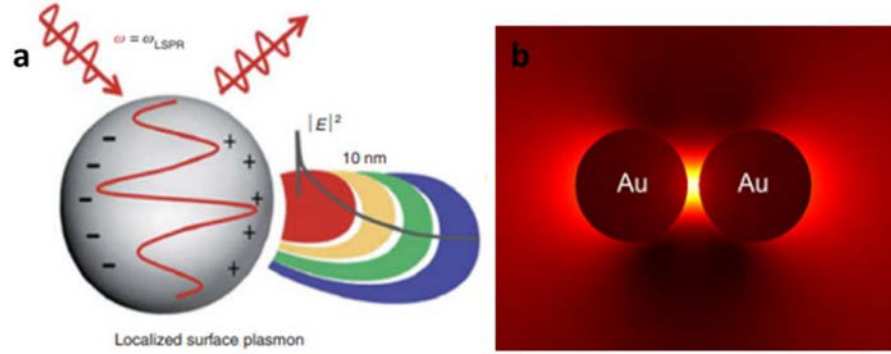


Figure 1.6 Localized surface plasmon polaritons (LSPR). **a)** Electric charge density of a metallic sphere immersed in an oscillating electromagnetic field and decay of the generated electric field intensity outside the particle. **b)** Electric field intensity enhancement between to close plasmonic particles (hot-spot).

In order to explain how the electromagnetic field enhancement works, we consider a metallic sphere subject to an external oscillating electromagnetic field E_0 (Figure 1.6a). If the diameter of the particle is smaller than the radiation wavelength, the electric field can be assumed to be constant on the particle surface (electrostatic approximation). The behavior of the metallic particle can be thus associated with a fluctuating electric dipole, and the resulting electric field at the surface E_s will consist of two different contributions.

$$E_s = E_0 + E_{sp} \quad (1.6)$$

Where E_{sp} is the contribution of the surface plasmon. The value of the induced dipole can be expressed (for spherical particles) as:

$$\mu = \varepsilon_2 \alpha(\omega) E_0 \quad (1.7)$$

in which ε_2 is the dielectric constants of the dielectric material. The polarizability $\alpha(\omega)$ depends on the shape, dimension and distribution of the metallic nanoparticles through the function $f(r,d)$ and can be expressed as following

$$\alpha(\omega) = f(r,d) \frac{\varepsilon_1(\omega) - \varepsilon_2}{\varepsilon_1(\omega) - 2\varepsilon_2} \quad (1.8)$$

Where the numerical factor 2 is representative of the spherical shape and $\epsilon_1(\omega)$ is the complex dielectric constant of the metal. Maximum values of E_{sp} can be thus obtained for the resonance condition $Re(\epsilon_1) = -2\epsilon_2$ and for minimum values of energy dissipation that is low value of $Im(\epsilon_1)$ (Fröhlich condition). For wavelengths belonging to the visible range metals like gold and silver are capable to satisfy the conditions above.

Another interesting feature or localized plasmon resonances are the near-field coupling effects between particles lying close to each other, like in the case of nanosphere aggregates. As can be seen in Figure 1.6b the region between the two particles, so called Hot-Spot, experiences a higher enhancement of the local field as compared to that of a single particle.¹¹

1.2.1 Plasmonic crystals

Spatially periodic metallic structures are appealing architectures thanks to their capability to excite and manipulate the plasmonic resonances, modifying the optical properties of metallic surfaces. The excitation of an SPP on a metallic grating for instance, manifests itself as dip in the reflection spectra (Wood's anomalies). When the periodicity of the surface structure is comparable with the wavelength of the SPP it will cooperatively influence the in-plane propagation of SPPs accessing unusual optical phenomena.^{12,13} A well-known example is the extraordinary optical transmission (EOT) that can be observed in metal film perforated with a periodic hole array. In such systems, EOT is originated by resonant light tunnelling involving SPP states.¹⁴ In the case of a periodic array of discrete plasmonic nanoparticles, the coherent interaction that arises from the multiple scattering of ordered elements and the incoming wave can induce a spatial redistribution of the LSPR electromagnetic field. The hybrid modes that arise from diffractive coupling of light induced by ordered arrays of plasmonic elements are called surface lattice resonances (SLR). SLRs, typically give rise to far-field coupling phenomena that are characterized by lower losses compared to LSPR and an ultra-narrow absorption peak.¹⁵⁻¹⁷

Similarly to PhCs, different configurations of lattices and scattering elements will originate different plasmonic responses. Figure 1.7 shows selected examples of the countless possibilities that can be explored using plasmonic crystal architectures. As for PhC, plasmonic system can also have a polarization dependent response. For instance, chiral reflectors can be fabricated employing achiral structures like the holes arrays illustrated in Figure 1.7a, where selectivity to circularly polarized light has been achieved exploiting Moiré

super-structures fabricate by stacking twisted layers of holes arrays.¹⁸ An analogous design has been implemented by Zheng et al. who obtained a linear polarization rotator piling up multiple layer of plasmonic gold lines arrays (Figure 1.7c).¹⁹ The coherent nature of surface lattice resonances (SLR) and their large spatial extension (that only arise when multiples plasmonic scatterers are placed in a periodically ordered fashion) can be instead employed to boost the photoluminescence emission of a dye, simultaneously obtaining a much higher directional emission compared to standard LSPR modes (Figure 1.7b).²⁰ The strong localized fields that characterise LSPR typically underpin the enhancement of Raman signal, named surface enhanced Raman spectroscopy (SERS). By placing gold nanosphere clusters in a periodic array (superlattice), Matricardi et al. demonstrated first, that an enhancement of the localized field compared to isolate clusters. Second, by changing the superlattice parameter, they achieved broad tunability of the LSPR-SLR hybrid mode wavelength along the visible and near infrared region (Figure 1.7d).¹¹

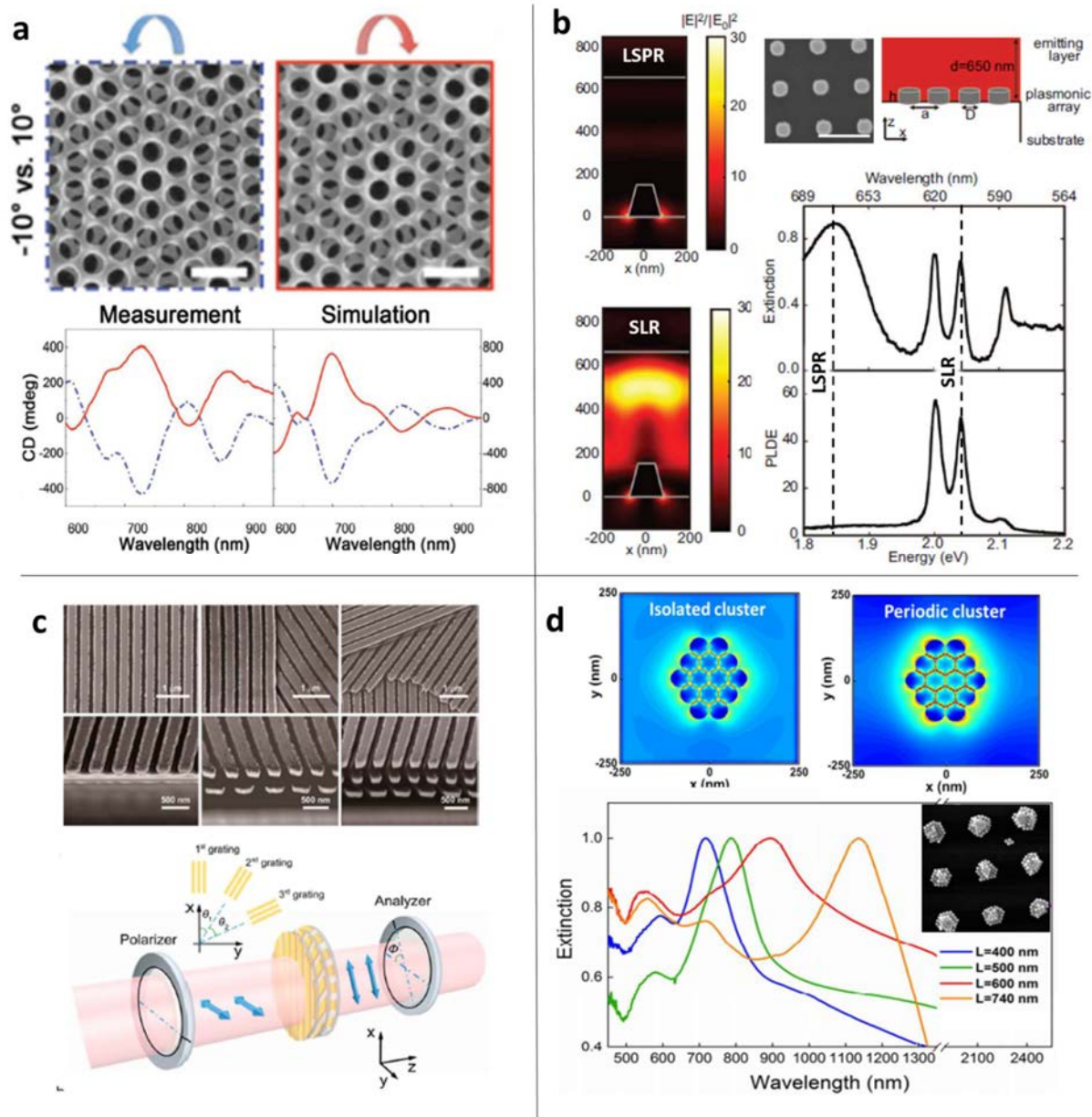


Figure 1.7 Example of plasmonic crystal structures and their corresponding functionalities. a) Moiré chiral metamaterials fabricated by twisted overlapping of holes arrays in gold films.¹⁸ b) Surface lattice resonance (SLR) enhancement of photoluminescent signal compared to localized surface plasmon resonance. Sample consists in a thick layer of glass (substrate), a periodic array of aluminum particles (plasmonic array) and a layer of dye molecules embedded in polystyrene (emitting layer).²⁰ c) Linear polarization rotator fabricated via stacking twisted lines arrays.¹⁹ d) Simulation of near-field enhancement in a cluster of nanoparticles due to periodic array configuration. Extinction spectra, normalized to the maximum, of gold cluster arrays with different lattice parameters.¹¹

1.3 Biomaterials for photonics and plasmonics

Despite the widespread use of inorganic materials for the fabrication of optical and electronic devices, their intrinsic mechanical rigidity, fragility, and potential toxicity make it challenging to use them in emerging applications like flexible electronics and biotechnology. In this frame, naturally derived polymers already demonstrated excellent flexibility, combined with unique physical properties, among which biocompatibility and environmental sustainability. This field of research has rapidly grown in the last two decades,²¹ particularly pushed by the urge to substitute plastic materials with ecofriendly alternatives and by the huge advances in human-machine interfaces and implantable medical devices.

Transient and ecofriendly applications

With the advent of the new era of internet of things (IoT) and wireless networks, mechanical flexible and electronically functional devices, have blossomed. In particular, optoelectronic devices are expected to be wirelessly interconnected, sharing relevant information in an ultra-fast way and providing real-time communication. For this reasons wearable and product-integrated optoelectronic devices are catching on in various aspects of our daily life, among which, healthcare monitoring and treatment, ambient control, soft robotics, prosthetics, flexible optoelectronic devices, textile, packaging, among others.²²

In this context the recent environmental concerns regarding material sustainability are pushing almost any technological sector towards the preferential substitution of highly contaminating materials by others with lower environmental impact, and easy disposability properties. Photonics is not an exception.²¹ Figure 1.8 shows some example of the employment of biodegradable materials for the realization of transient photonic and electronic devices. Among these materials, cellulose is widely investigated thanks to its low cost, availability and versatility (see Chapter 2 for further details about this material and its derivatives). Many pioneering work have been published regarding the fabrication of electronics on paper,²³⁻²⁵ and this material as recently attracted interest also for application as low cost transient substrate for plasmonic sensing²⁶⁻²⁸. One example is reported in Figure 1.8e, where a burnable colorimetric sensor for biomolecules detection has been developed functionalizing paper with plasmonic NPs.²⁶

Besides paper, other cellulosic materials have been implemented for the realization of biodegradable electronic and photonic architectures. For instance, Figure 1.8a shows biodegradable and flexible electronic circuits fabricated using a transparent cellulose nanofibril substrate²⁹ and Figure 1.8c shows a

biodegradable photonic crystals made of pure cellulose fibers, fabricated using replica molding technique.³⁰ Silk is another widely investigated material for the realization of biodegradable optoelectronic devices, as show in Figure 1.8b, where an array of antennas (operating in ThZ) have been fabricated on edible silk substrates and conformally transferred onto food surfaces.³¹ Silk is another widely investigated material for the realization of biodegradable optoelectronic devices, as show in Figure 1.8b, where an array of antennas (operating in ThZ) have been fabricated on edible silk substrates and conformally transferred onto food surfaces.³¹ Finally, transient substrates could be combined with transient metals or other non-toxic materials. Figure 1.8d shows a sweat and humidity sensor fabricate using a plasmonic crystal made of water soluble metallic magnesium on a polyurethane (NOA) substrate.³²

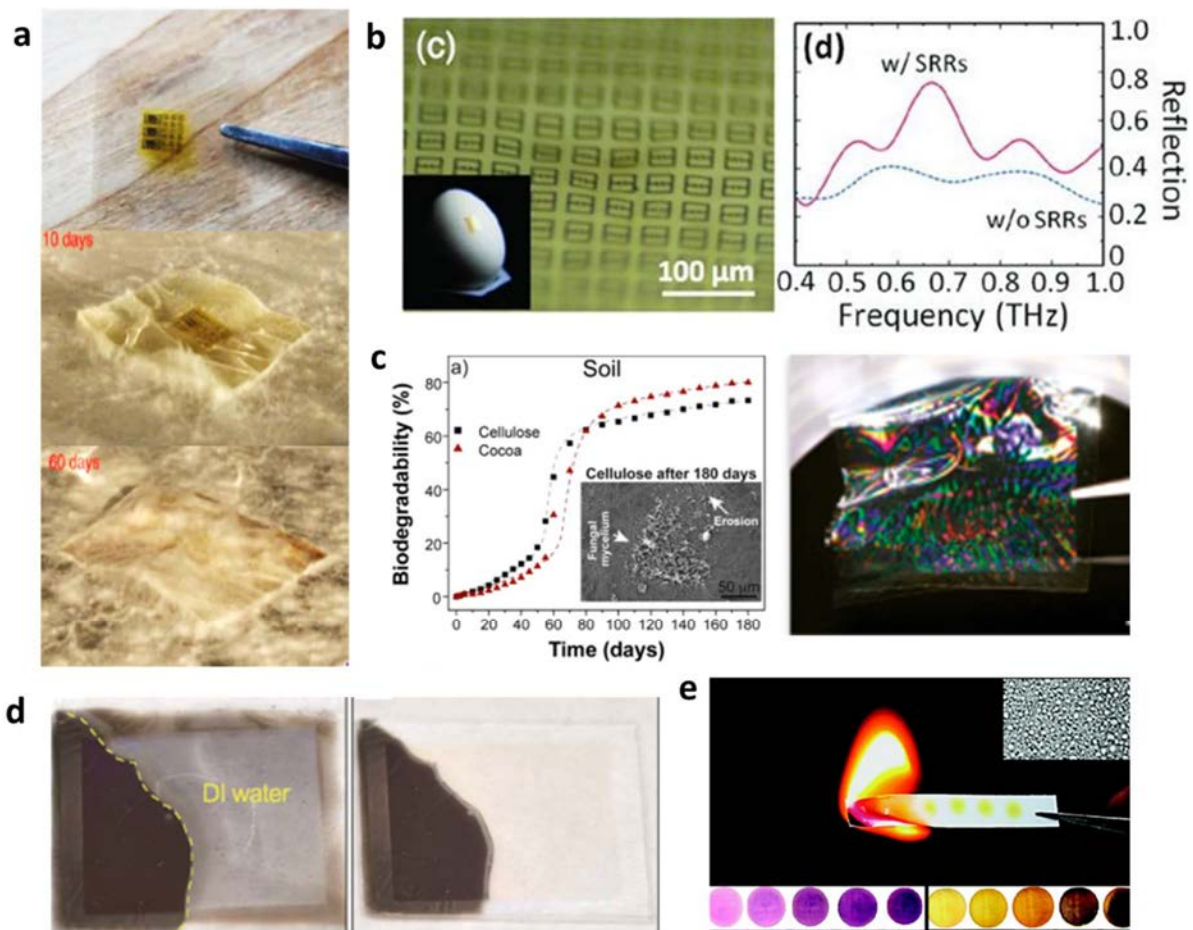


Figure 1.8 Examples of ecofriendly photonics and electronics devices. a) Electronic circuit printed on cellulose nanofibril paper and its biodegradation (10 and 60 days).²⁹ b) Edible silk adhesive with a ThZ split ring resonators (SRRs) conformally adhered onto an egg.³¹ c) Biodegradable pure cellulose photonic crystal.³⁰ d) Sweat and humidity plasmonic crystal sensor fabricated depositing water soluble magnesium on top of a polyurethane

substrate.³² e) burnable colorimetric sensor for biomolecules detection based on paper substrate functionalized with plasmonic nanoparticles.²⁶

Biotechnology applications

One of the general trends in biotechnology and medicine is to have intracorporeal or epidermally applicable biocompatible devices for continuous monitoring and treatment.³³ Many applications of photonics and plasmonics are in bio-related fields.²¹ Light indeed can penetrate living tissue up to few centimeters, allowing for nondestructive imaging and sensing techniques, activating chemical reactions or inducing temperature changes.

Implantable waveguides are one of the mostly investigated systems, since they enable light to reach deeper tissues for in-vivo monitoring and treatment. Biocompatible and resorbable hydrogel patches for instance that both guide light and accommodate functional elements (cells, therapeutic agents, fluorescent proteins etc.)³⁴ are promising platforms as implantable devices. Hydrogels can create a low resistance path for light inside the body³⁴ as illustrated in Figure 1.9b, and eventually, they can be biologically resorbed by the host body after a certain extent (Figure 1.9a).³⁵ Another example is the realization of colorimetric sensors that takes advantage of the environmental sensitivity of the optical properties of PhC.³⁶ Following this approach, Omentetto et al. fabricated biocompatible silk inverse opals (SIO) for colorimetric sensing of glucose contents in liquid media (Figure 1.9c).³⁷ Furthermore, they demonstrated improvement of the heating efficiency of gold nanoparticles when integrated in the SIO structure relative to those embedded in an unstructured fibroin film.³⁸ The efficient production of heat under optical illumination from plasmonic nanoparticles, (plasmon resonance-induced heating)³⁹ is of particular interest for biomedical application since it can be used to systematically target and destroy malign tissues, as in anticancer therapies. Finally, biocompatible plasmonic arrays can be implemented as SERS substrates for in vivo measurements. Figure 1.9d illustrated a cell culture on a Ag/Au nanoantennas array demonstrating good cell adhesion combined high plasmonic enhancement of the Raman signal coming from the cell membranes.⁴⁰

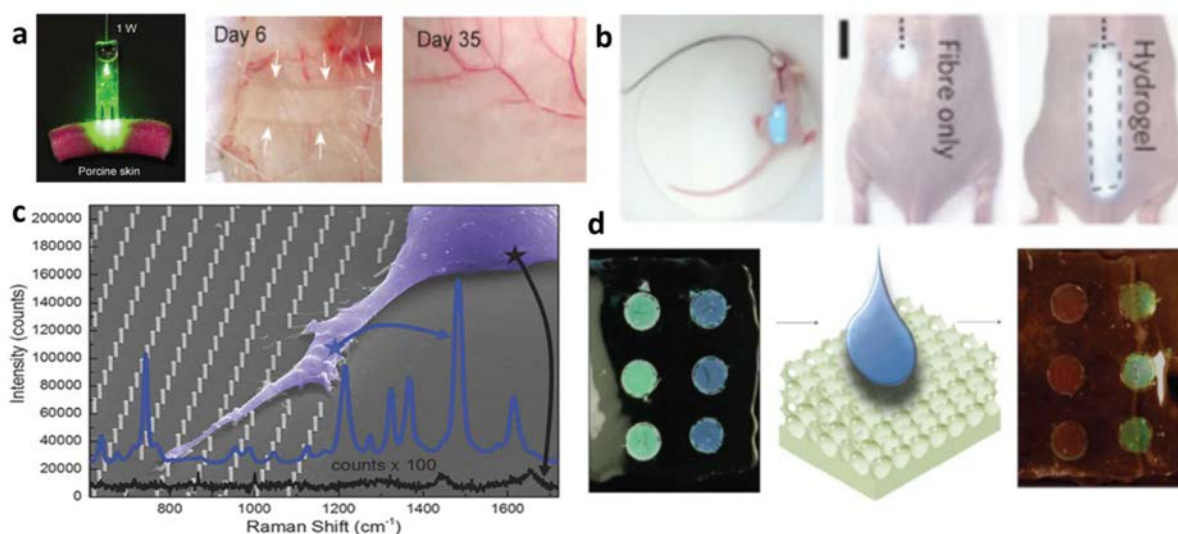


Figure 1.9 Application of biocompatible photonics in biotechnology. a-b) Polylactic acid (PLA) hydrogels as resorbable waveguides in living tissues.³⁴⁻³⁵ c) biocompatible SERS substrate for cell growth and in vivo membrane biosensing.⁴⁰ d) Colorimetric glucose sensor fabricated with silk inverse opal structure.³⁷

1.4 Commercial applications

The photonic technology market is already huge and has great growing potential, with forecasts saying it will reach \$800 billion in 2023.⁴¹ Light-based technologies indeed play a critical role in a broad range of technological sectors, among which telecommunications, data storage, medical diagnostics, autonomous driving, green energy and more. In this frame, dielectric photonic architectures can be found as fundamental components in devices like lasers, detectors, sensors, imaging set-ups and optical fibers. Those technologies are already widespread in industry thanks to their relatively easy integration in semiconductor manufacturing technology and CMOS compatibility⁴² (they mostly employ same materials as electronic industry). Specifically, nanostructured photonic crystals that allows for enhanced light manipulation are also approaching commercialization. For example, diffractive optics elements like the ones developed by NILT technology company (Figure 1.10c) can be used as beam shaping, beam splitting, diffusers, pattern projections, diffractive focusing lenses and gratings and can be found in long range distance sensors like LiDAR (Light Detection And Ranging), short range distance sensors, position sensors, motion detection and projection systems. In addition, surface-emitting semiconductor lasers with an integrated photonic crystal structure featuring a narrow spot beam pattern with narrow spectral linewidth are currently commercialized by HAMAMATSU (Figure 1.10a).

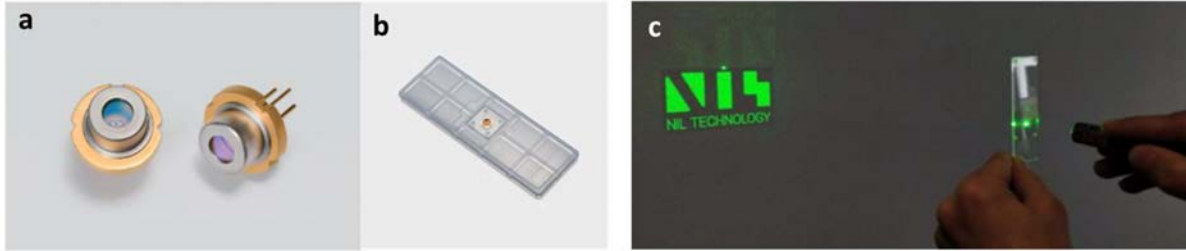


Figure 1.10 Commercial application of photonic and plasmonic crystals. a) surface-emitting semiconductor laser with a photonic crystal structure integrated (HAMAMATSU). A chip of metallic nano/sub-micro structure used as SERS substrate (HAMAMATSU). A diffractive optics element made of plastic developed by NILT technology.

One of the main driving forces towards the large-scale commercialization of those technologies is the development of smart manufacturing techniques that has reduced remarkably their still high cost of fabrication. One example of company that bets on large-scale manufacturing strategies is NILT technology, who specialized in high-end design and fabrication of photonic nanostructures and in their low cost and high throughput replication using nanoimprinting based techniques.

Despite their great potential Plasmonic-based technologies are much further from industrialization, and their commercial employments are mostly limited to few companied developing SERS substrates for sensing applications (Figure 1.10b).^{42,43} The inability to scale up to large-scale nanofabrication of plasmonic devices plays a key role in their slow commercialization process. Apart from being expensive, common plasmonic materials like silver and gold are not compatible with industrial fabrication workflows.⁴³ For instance, dry etching of noble metals is difficult due to the lack of volatile compound formation.⁴⁴ In sum, new fabrication techniques and new enabling application for plasmonic materials has to be developed in order to see this technology on the market.

1.5 References

- (1) Sukhoivanov, I. A.; Guryev, I. V. *Photonic crystals. Physics and practical modeling* / Igor A. Sukhoivanov, Igor V. Guryev, Springer series in optical sciences, 0342-4111, Vol. 152; Springer, 2009.
- (2) Joannopoulos, J. D. *Photonic crystals. Molding the flow of light* / John D. Joannopoulos ... [et al.], 2nd ed.; Princeton University Press, 2008.

- (3) Zhu, A. Y.; Chen, W. T.; Zaidi, A.; Huang, Y.-W.; Khorasaninejad, M.; Sanjeev, V.; Qiu, C.-W.; Capasso, F. Giant intrinsic chiro-optical activity in planar dielectric nanostructures. *Light, science & applications* **2018**, *7*, 17158. DOI: 10.1038/lsa.2017.158.
- (4) Hung, Y.-J.; Lee, S.-L.; Coldren, L. A. Deep and tapered silicon photonic crystals for achieving anti-reflection and enhanced absorption. *Optics express* **2010**, *18* (7), 6841–6852. DOI: 10.1364/OE.18.006841.
- (5) Raut, H. K.; Dinachali, S. S.; Loke, Y. C.; Ganesan, R.; Ansah-Antwi, K. K.; Góra, A.; Khoo, E. H.; Ganesh, V. A.; Saifullah, M. S. M.; Ramakrishna, S. Multiscale ommatidial arrays with broadband and omnidirectional antireflection and antifogging properties by sacrificial layer mediated nanoimprinting. *ACS Nano* **2015**, *9* (2), 1305–1314. DOI: 10.1021/nn5051272.
- (6) Wu, S.; Xia, H.; Xu, J.; Sun, X.; Liu, X. Manipulating Luminescence of Light Emitters by Photonic Crystals. *Advanced materials (Deerfield Beach, Fla.)* **2018**, *30* (47), e1803362. DOI: 10.1002/adma.201803362.
- (7) Wu, Q.; Liu, B.; Zhu, Z.; Gu, M.; Chen, H.; Xue, C.; Zhao, J.; Wu, Y.; Tai, R.; Ouyang, X. Directional emission of plastic luminescent films using photonic crystals fabricated by soft-X-ray interference lithography and reactive ion etching. *Scientific reports* **2018**, *8* (1), 9254. DOI: 10.1038/s41598-018-27593-w.
- (8) Wierer, J. J.; David, A.; Megens, M. M. III-nitride photonic-crystal light-emitting diodes with high extraction efficiency. *Nature Photon* **2009**, *3* (3), 163–169. DOI: 10.1038/nphoton.2009.21.
- (9) Moitra, P.; Yang, Y.; Anderson, Z.; Kravchenko, I. I.; Briggs, D. P.; Valentine, J. Realization of an all-dielectric zero-index optical metamaterial. *Nature Photon* **2013**, *7* (10), 791–795. DOI: 10.1038/nphoton.2013.214.
- (10) William L Barnes. Surface plasmon\textendashpolariton length scales: a route to sub-wavelength optics. *Journal of Optics A: Pure and Applied Optics* **2006**, *8* (4), S87 - S93.
- (11) Matricardi, C.; Hanske, C.; Garcia-Pomar, J. L.; Langer, J.; Mihi, A.; Liz-Marzán, L. M. Gold Nanoparticle Plasmonic Superlattices as Surface-Enhanced Raman Spectroscopy Substrates. *ACS Nano* **2018**, *12* (8), 8531–8539. DOI: 10.1021/acsnano.8b04073.
- (12) Kasani, S.; Curtin, K.; Wu, N. A review of 2D and 3D plasmonic nanostructure array patterns: fabrication, light management and sensing applications. *Nanophotonics* **2019**, *8* (12), 2065–2089. DOI: 10.1515/nanoph-2019-0158.

- (13) Dickson, W.; Wurtz, G. A.; Zayats, A. V. Plasmonic Crystals: Controlling Light With Periodically Structured Metal Films. In *Photonics technology and instrumentation*, Andrews, D. L., Ed.; Photonics, volume III; John Wiley & Sons, Inc, 2015; pp 107–167. DOI: 10.1002/9781119011781.ch3.
- (14) Lee, S. H.; Johnson, T. W.; Lindquist, N. C.; Im, H.; Norris, D. J.; Oh, S.-H. Linewidth-Optimized Extraordinary Optical Transmission in Water with Template-Stripped Metallic Nanohole Arrays. *Adv. Funct. Mater.* **2012**, *22* (21), 4439–4446. DOI: 10.1002/adfm.201200955.
- (15) Conde-Rubio, A.; Fraile Rodríguez, A.; Espinha, A.; Mihi, A.; Pérez-Murano, F.; Batlle, X.; Labarta, A. Geometric frustration in ordered lattices of plasmonic nanoelements. *Scientific reports* **2019**, *9* (1), 3529. DOI: 10.1038/s41598-019-40117-4.
- (16) Kravets, V. G.; Kabashin, A. V.; Barnes, W. L.; Grigorenko, A. N. Plasmonic Surface Lattice Resonances: A Review of Properties and Applications. *Chemical reviews* **2018**, *118* (12), 5912–5951. DOI: 10.1021/acs.chemrev.8b00243.
- (17) Cherqui, C.; Bourgeois, M. R.; Wang, D.; Schatz, G. C. Plasmonic Surface Lattice Resonances: Theory and Computation. *Accounts of chemical research* **2019**, *52* (9), 2548–2558. DOI: 10.1021/acs.accounts.9b00312.
- (18) Wu, Z.; Zheng, Y. Moiré Chiral Metamaterials. *Advanced Optical Materials* **2017**, *5* (16), 1700034. DOI: 10.1002/adom.201700034.
- (19) Zheng, C.; Shen, Y.; Liu, M.; Liu, W.; Wu, S.; Jin, C. Layer-by-Layer Assembly of Three-Dimensional Optical Functional Nanostructures. *ACS Nano* **2019**, *13* (5), 5583–5590. DOI: 10.1021/acsnano.9b00549.
- (20) Lozano, G.; Rodriguez, S. R.; Verschuuren, M. A.; Gómez Rivas, J. Metallic nanostructures for efficient LED lighting. *Light, science & applications* **2016**, *5* (6), e16080. DOI: 10.1038/lsa.2016.80.
- (21) Xiong, R.; Luan, J.; Kang, S.; Ye, C.; Singamaneni, S.; Tsukruk, V. V. Biopolymeric photonic structures: design, fabrication, and emerging applications. *Chemical Society reviews* **2020**, *49* (3), 983–1031. DOI: 10.1039/c8cs01007b.
- (22) Shi, Q.; Dong, B.; He, T.; Sun, Z.; Zhu, J.; Zhang, Z.; Lee, C. Progress in wearable electronics/photronics—Moving toward the era of artificial intelligence and internet of things. *InfoMat* **2020**, *2* (6), 1131–1162. DOI: 10.1002/inf2.12122.
- (23) Tobjörk, D.; Österbacka, R. Paper electronics. *Advanced materials (Deerfield Beach, Fla.)* **2011**, *23* (17), 1935–1961. DOI: 10.1002/adma.201004692.

- (24) Martins, R.; Ferreira, I.; Fortunato, E. Electronics with and on paper. *Phys. Status Solidi RRL* **2011**, *5* (9), 332–335. DOI: 10.1002/pssr.201105247.
- (25) Zhang, Y.; Zhang, L.; Cui, K.; Ge, S.; Cheng, X.; Yan, M.; Yu, J.; Liu, H. Flexible Electronics Based on Micro/Nanostructured Paper. *Advanced materials (Deerfield Beach, Fla.)* **2018**, *30* (51), e1801588. DOI: 10.1002/adma.201801588.
- (26) Tseng, S.-C.; Yu, C.-C.; Wan, D.; Chen, H.-L.; Wang, L. A.; Wu, M.-C.; Su, W.-F.; Han, H.-C.; Chen, L.-C. Eco-friendly plasmonic sensors: using the photothermal effect to prepare metal nanoparticle-containing test papers for highly sensitive colorimetric detection. *Analytical chemistry* **2012**, *84* (11), 5140–5145. DOI: 10.1021/ac300397h.
- (27) Susu, L.; Campu, A.; Craciun, A. M.; Vulpoi, A.; Astilean, S.; Focsan, M. Designing Efficient Low-Cost Paper-Based Sensing Plasmonic Nanoplatforms. *Sensors (Basel, Switzerland)* **2018**, *18* (9). DOI: 10.3390/s18093035.
- (28) Purwidyantri, A.; Karina, M.; Hsu, C.-H.; Srikandace, Y.; Prabowo, B. A.; Lai, C.-S. Facile Bacterial Cellulose Nanofibrillation for the Development of a Plasmonic Paper Sensor. *ACS Biomater. Sci. Eng.* **2020**, *6* (5), 3122–3131. DOI: 10.1021/acsbomaterials.9b01890.
- (29) Jung, Y. H.; Chang, T.-H.; Zhang, H.; Yao, C.; Zheng, Q.; Yang, V. W.; Mi, H.; Kim, M.; Cho, S. J.; Park, D.-W.; Jiang, H.; Lee, J.; Qiu, Y.; Zhou, W.; Cai, Z.; Gong, S.; Ma, Z. High-performance green flexible electronics based on biodegradable cellulose nanofibril paper. *Nature communications* **2015**, *6*, 7170. DOI: 10.1038/ncomms8170.
- (30) Caligiuri, V.; Tedeschi, G.; Palei, M.; Miscuglio, M.; Martin-Garcia, B.; Guzman-Puyol, S.; Hedayati, M. K.; Kristensen, A.; Athanassiou, A.; Cingolani, R.; Sorger, V. J.; Salerno, M.; Bonaccorso, F.; Krahne, R.; Heredia-Guerrero, J. A. Biodegradable and Insoluble Cellulose Photonic Crystals and Metasurfaces. *ACS Nano* **2020**, *14* (8), 9502–9511. DOI: 10.1021/acsnano.0c03224.
- (31) Tao, H.; Brenckle, M. A.; Yang, M.; Zhang, J.; Liu, M.; Siebert, S. M.; Averitt, R. D.; Mannoor, M. S.; McAlpine, M. C.; Rogers, J. A.; Kaplan, D. L.; Omenetto, F. G. Silk-based conformal, adhesive, edible food sensors. *Advanced materials (Deerfield Beach, Fla.)* **2012**, *24* (8), 1067–1072. DOI: 10.1002/adma.201103814.
- (32) Li, R.; Xie, S.; Zhang, L.; Li, L.; Kong, D.; Wang, Q.; Xin, R.; Sheng, X.; Yin, L.; Yu, C.; Yu, Z.; Wang, X.; Gao, L. Soft and transient magnesium plasmonics for environmental and biomedical sensing. *Nano Res.* **2018**, *11* (8), 4390–4400. DOI: 10.1007/s12274-018-2028-6.

- (33) Humar, M.; Kwok, S. J. J.; Choi, M.; Yetisen, A. K.; Cho, S.; Yun, S.-H. Toward biomaterial-based implantable photonic devices. *Nanophotonics* **2017**, *6* (2), 414–434. DOI: 10.1515/nanoph-2016-0003.
- (34) Choi, M.; Choi, J. W.; Kim, S.; Nizamoglu, S.; Hahn, S. K.; Yun, S. H. Light-guiding hydrogels for cell-based sensing and optogenetic synthesis in vivo. *Nature Photon* **2013**, *7*, 987–994. DOI: 10.1038/nphoton.2013.278.
- (35) Nizamoglu, S.; Gather, M. C.; Humar, M.; Choi, M.; Kim, S.; Kim, K. S.; Hahn, S. K.; Scarcelli, G.; Randolph, M.; Redmond, R. W.; Yun, S. H. Bioabsorbable polymer optical waveguides for deep-tissue photomedicine. *Nature communications* **2016**, *7*, 10374. DOI: 10.1038/ncomms10374.
- (36) Gao, L.; Zhang, Y.; Malyarchuk, V.; Jia, L.; Jang, K.-I.; Webb, R. C.; Fu, H.; Shi, Y.; Zhou, G.; Shi, L.; Shah, D.; Huang, X.; Xu, B.; Yu, C.; Huang, Y.; Rogers, J. A. Epidermal photonic devices for quantitative imaging of temperature and thermal transport characteristics of the skin. *Nature communications* **2014**, *5*, 4938. DOI: 10.1038/ncomms5938.
- (37) Kim, S.; Mitropoulos, A. N.; Spitzberg, J. D.; Tao, H.; Kaplan, D. L.; Omenetto, F. G. Silk inverse opals. *Nature Photon* **2012**, *6* (12), 818–823. DOI: 10.1038/nphoton.2012.264.
- (38) MacLeod, J.; Rosei, F. Photonic crystals: Sustainable sensors from silk. *Nature materials* **2013**, *12* (2), 98–100. DOI: 10.1038/nmat3552.
- (39) Jain, P. K.; Huang, X.; El-Sayed, I. H.; El-Sayed, M. A. Review of Some Interesting Surface Plasmon Resonance-enhanced Properties of Noble Metal Nanoparticles and Their Applications to Biosystems. *Plasmonics* **2007**, *2* (3), 107–118. DOI: 10.1007/s11468-007-9031-1.
- (40) La Rocca, R.; Messina, G. C.; Dipalo, M.; Shalabaeva, V.; Angelis, F. de. Out-of-Plane Plasmonic Antennas for Raman Analysis in Living Cells. *Small (Weinheim an der Bergstrasse, Germany)* **2015**, *11* (36), 4632–4637. DOI: 10.1002/smll.201500891.
- (41) Anne Fischer. *Six Strong Business Segments in the Light Technologies Industry*. **2019**. https://www.novuslight.com/six-strong-business-segments-in-the-light-technologies-industry_N9545.html.
- (42) Graydon, O. A colourful future? *Nature Photon* **2015**, *9* (8), 487–488. DOI: 10.1038/nphoton.2015.136.
- (43) Commercializing plasmonics. *Nature Photon* **2015**, *9* (8), 477. DOI: 10.1038/nphoton.2015.149.
- (44) Chen, J. K.-C.; Altieri, N. D.; Kim, T.; Chen, E.; Lill, T.; Shen, M.; Chang, J. P. Directional etch of magnetic and noble metals. II. Organic chemical vapor etch. *Journal of Vacuum Science & Technology A: Vacuum, Surfaces, and Films* **2017**, *35* (5), 05C305. DOI: 10.1116/1.4983830.

CHAPTER 2

Cellulosic biomaterials

Unique features and applications

If we think about the world “cellulose” today, probably the first thing that comes to mind is paper. The main and definitely the most well-known usage of cellulose is actually the production of paper and paperboard, but we should bear in mind that, along the course of history, cellulose based materials shaped a considerable part of our culture, playing a key role in countless applications: textile, knowledge storage, pharmaceuticals, food industry, packaging, fuels, electronics, transportation and construction among others. It is not surprising that such a widespread material is the second most widely used in the world, after concrete. The secret beyond the success of cellulose, lies in more than one essential feature that characterized this material and that, from past to present, have raised the interests of human beings toward the development of cellulose-based technologies.

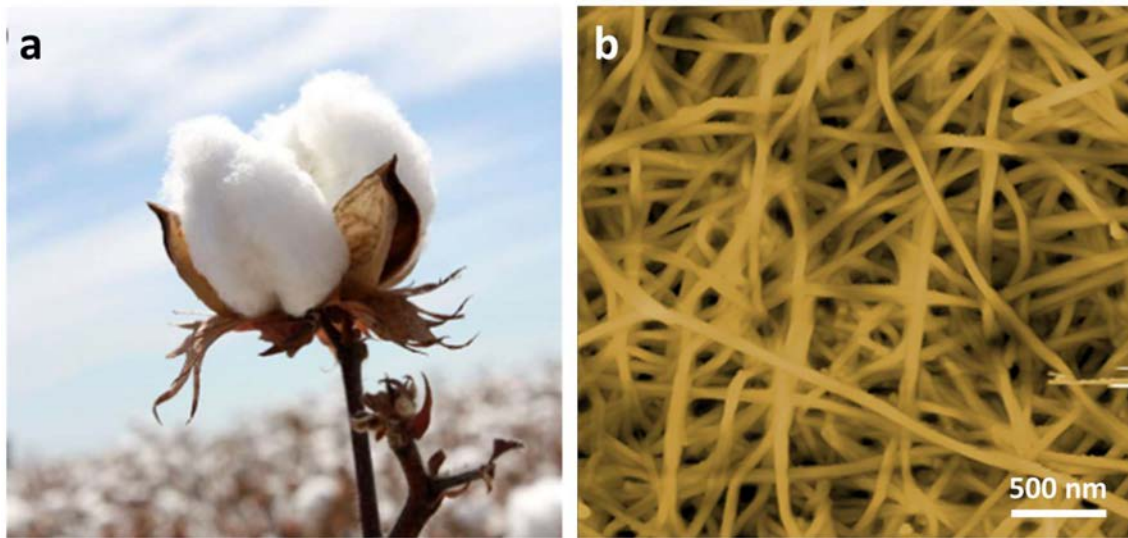


Figure 2.1 Sources of almost pure cellulose in nature a) Photo of a cotton flower. b) AFM image of bacterial cellulose fibrils.

- Abundancy

Cellulose is the most abundant organic polymer on earth, and it is derived from broadly available resources. Wood, the oldest material utilized by human beings along with stone, contains 40-50% of cellulose. Cotton (Figure 2.1a), probably the most popular textile fiber, is almost pure cellulose, accounting with a 90% in content. Also, some species of bacteria produce it as secretion to form protective biofilms, as illustrated in Figure 2.1b. These sources of extractions are also renewable: during the photosynthesis plants uses water and solar energy to produce cellulose uptaking carbon dioxide from the atmosphere.

- **Versatility**

The range of modification of cellulose based materials is broad and many books and reviews on this subject have been published.¹⁻⁴ Many different derivates with tailored optical, mechanical and chemical characteristic can be obtained by chemical or physical modification of cellulose, giving to this material the multifunctionality that is the basis of its widespread industrial applications.

- **Biodegradability**

Biodegradation is defined as the brake down of matter into simpler substances through the action of living microorganisms. This important feature has recently bought cellulose the focus of attention. Cellulose based products could indeed are fully biodegradable and could reduce environmental footprint, allowing easy disposability and recyclability of the products made from this material and from most of its derivatives.⁵

- **Biocompatibility**

A material can be defined biocompatible if it does not produce a toxic or immunological response when exposed to the body or bodily fluids. Also biocompatibility is an attractive feature that have interested the scientific community interest toward the development of cellulose based materials for application in pharmaceutical industry and in biotechnology.⁶

In this chapter the main characteristics of cellulose and its derivatives are presented, and a specific section is devoted to illustrating more in detail the properties and applications of hydroxypropyl cellulose, the cellulose derivative implemented in this thesis.

2.1 Cellulose structure and properties

What gives cellulose all these interesting properties is its chemical structure, which is represented in Figure 2.2. It consists in a polysaccharide chain (chemical formula $(C_6H_{10}O_5)_n$) in which several hundred to thousands of β -glucose units are repeated. The polysaccharide chains interact with each other via hydrogen bonding, forming alternate crystalline and amorphous phases and creating nanofibrillar structures. Nanofibrils hierarchically assemble into microfibrils and in turn into the actual cellulose fibers, that together with lignin and hemicellulose constitute the plant cell wall.

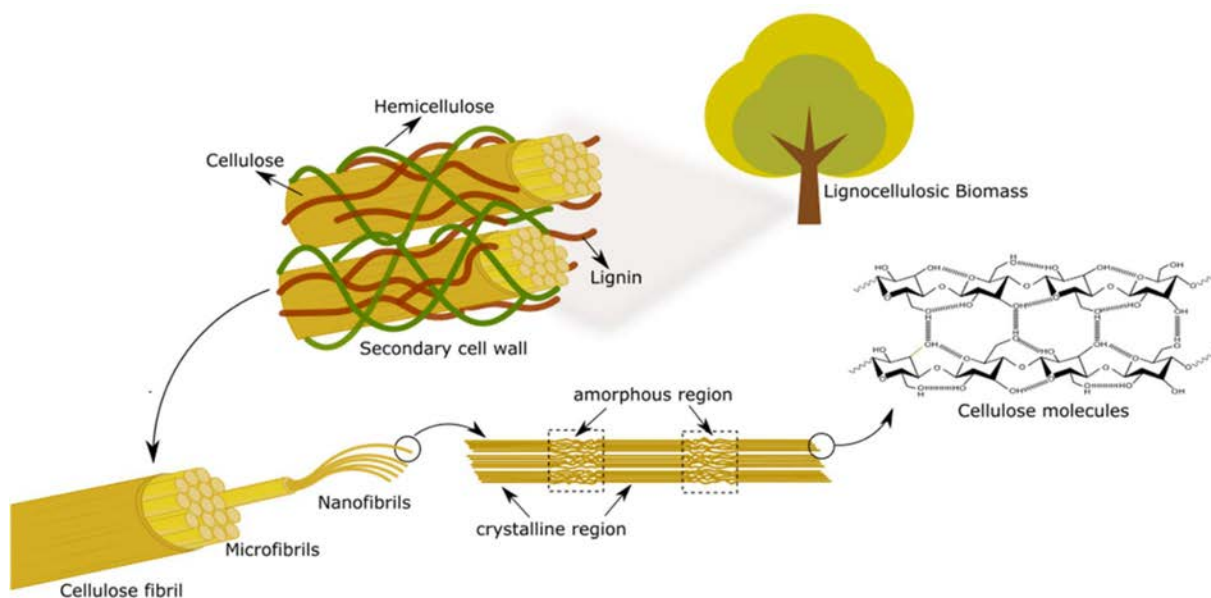


Figure 2.2 Schematic representation of cellulose chemical structure and of its supramolecular hierarchical organization found in plants cell walls.

This particular supramolecular arrangement and the presence of multiple hydroxyl groups is what imparts cellulose its unique properties, among which toughness, variable optical appearance, hydrophilicity and a broad chemical variability, which is fostered by the high reactivity of the OH groups.

A huge number of cellulose derivatives are nowadays produced and commercialized,^{1,3,5,7} finding application in a broad range of multidisciplinary fields.⁸⁻¹⁰ Some of the tailored chemical and physical properties that can be imparted to this multifunctional material are discussed in the next section.

2.2 Cellulose derivatives

Cellulose derivatives can be divided in two main groups:

- **Cellulose nanomaterials**

Cellulose possesses a semi crystalline structure in which amorphous and densely packed crystalline regions coexist. Like many other biopolymers, cellulose is susceptible to hydrolysis, being the amorphous regions more inclined than the crystalline ones. This allows to isolate the so-called cellulose nanocrystals (CNC, Figure 2.3a) a colloidal form of cellulose which can be dispersed in water. Also, cellulose nanofibers (CNF) are another type of cellulose nanomaterial consisting in long fibrils that partially retain the amorphous regions, with lateral size comparable to the one of CNC (c.a. 10 nm).⁹

- **Cellulosic polymers**

A wide range of cellulose based biopolymers can be obtained by chemically substituting the hydroxyl group with functional moieties. The properties and the solubility of this group of materials strongly depend on the degree of substitution (DS) and the distribution of the functional groups along the polymer chain. The most commercially well-known class of chemically modified cellulose derivatives are the cellulose esters,² first and foremost cellulose acetate, one of the earliest synthetic fibers synthesized, and cellophane. Another important class of cellulose derivatives are the cellulose ethers, which includes carboxymethyl cellulose (CMC), methyl cellulose (MC), ethyl cellulose (EC), hydroxyethyl cellulose (HEC), hydroxypropyl cellulose (HPC). These materials are particularly interesting, since they are nontoxic, biocompatible and most often water-soluble.¹¹

The main motivations to modify the cellulose is to modify its low solvent solubility and to provide it better formability properties (e.g. thermoformability) allowing for easier processing and film formation,⁵ as can be seen in Figure 3.1 Figure 2.3b. The above-mentioned modifications of cellulose also allow to tune and better exploit some unique characteristic of this material, among which its structural and optical properties.

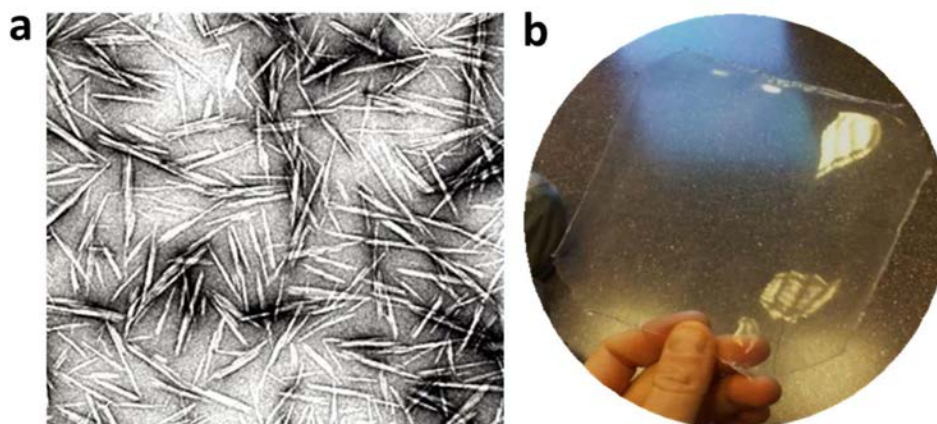


Figure 2.3 a) SEM image of cellulose nanocrystals (CNC). b) thin film of hydroxypropyl cellulose (HPC) fabricated by the author spincasting HPC from water solution.

Structural properties

Cellulose is a very strong material. It is used as structural component by plants and algae. Considering the density difference, cellulose is stronger than steel, as it has been recently demonstrated by Song et. Al, who densified natural wood obtaining a light weight ultraresistant material with better performances than aluminum alloys.⁴ The tensile strength of cellulose crystalline phase (7.5-7.7 GPa)¹² is comparable to that of carbon nanotubes (CNT), and for this reason, cellulose nanomaterials are widely investigated as mechanical reinforcement in composite blends. Also cellulose derivatives are well-known for the capability to create hydrogels and aerogels, a particular class of materials consisting in a network of crosslinked polymer chains that creates a highly porous frame, that can be filled by a solvent (hydrogel)^{10,13} or a gas (aerogel).¹⁴ Aerogel and hydrogel are very interesting materials for different application fields, thanks to their high surface, low density, and low thermal conductivity.

Optical properties

The typical arrangement of cellulose into microfibrils scatters light diffusively, providing the well-known white color of paper. However, when it is properly densified, it is optically in the visible range. Most of cellulosic polymer can form transparent and flexible films, but also CNF and CNF have been recently used to produce transparent nanopaper.⁹ Finally, both plants and animals can create peculiar cellulose structures with a diffractive color appearance. Many studies tried to mimic the complex architectures found

nature,^{15,16} providing different strategies to fabricate both liquid and solid cellulose based photonic crystals.¹⁷

Among cellulose derivatives, the properties and application of hydroxypropyl cellulose, a particularly versatile and commercially available cellulose ether, that has been widely implemented in this thesis, are reviewed in the following paragraph.

2.3 Hydroxypropyl cellulose

Hydroxypropyl cellulose (HPC), commercially known as 'Klucel®' is a cellulose derivative in which some of the OH group -typically 2.5 to 4¹⁸- of a linear cellulose backbone has been substituted with an ether group (Figure 2.4b). It is industrially produced by alkalization and esterification processes using propylene oxide. The resulting polymer presents a remarkable combination of properties, which are summarized in Table 1. HPC is readily soluble in many organic solvents and in water, below its critical solution temperature, which is approximately 42° C. Above this temperature HPC precipitates, giving rise to a cloudy dispersion. This process is reversible and HPC can be rehydrated by cooling back down the water temperature. HPC maintains the non-toxicity and biocompatibility properties of pristine cellulose, furthermore it is also the only cellulose ether which is at the same time edible and thermoformable.⁵ It can form tasteless and colorless transparent films which can be sealed molded and extruded at relatively low temperatures (100-150° C).¹⁸ The mechanical properties of HPC are also remarkable, with stiffens modulus ranging from 20 to 110 MPa and a high flexibility without requiring plasticizer.^{19,20}

The current industrial application of HPC are manifold, but the most widespread are in pharmaceutical and food industry. In pharmaceutical industry, HPC is used as artificial tears for eyes lubrication (Lacrisert, manufactured by Aton Pharma, Figure 2.4a) and as a binder, coating, and passive excipient for controlled released of active ingredients in pharmaceutical tablets (Klucel "F"). In food industry, HPC is used as a thickener and as an emulsion stabilizer (European Food Safety Authority number E463). Another food-related application of HPC is as edible coatings for food products, and it can be applied by extrusion or from liquid solution.¹ More generally, HPC protective coating are also employed in paper and paper packaging as oil barrier.^{2,5}

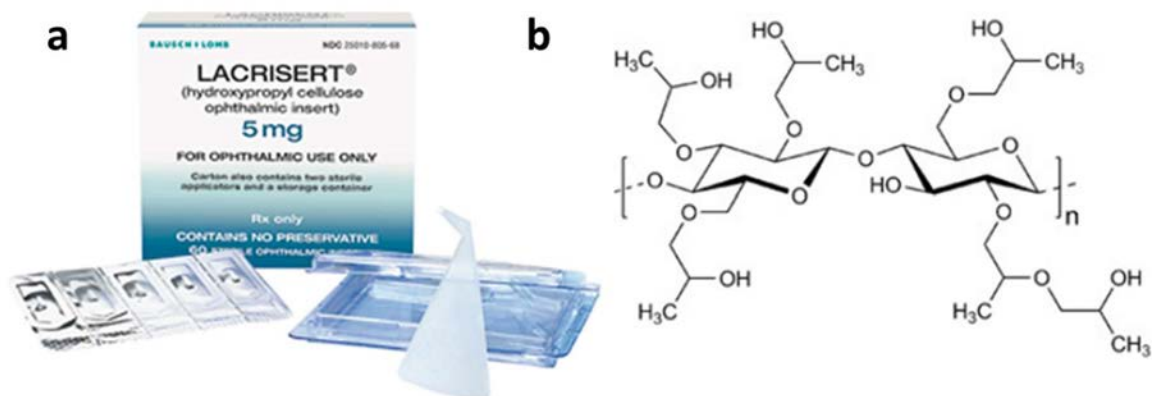


Figure 2.4 a) Artificial tears for eyes lubrication based on HPC water solution. b) Chemical structure of HPC.

Unconventional applications of HPC

Besides the common industrial applications, many efforts are being done to provide innovative functionalities to HPC for exploit its application in fast-growing fields such as biotechnology and nanophotonic. Like many other cellulose derivatives, films and coatings of HPC can be also made water insoluble by crosslinking of the freely available hydroxyl groups. This can be done adding curing agents or by radiation induced crosslinking technique (see section 3.1). The final degree of crosslinking, that will determine the solubility and porosity of the film, can be tuned in order to obtain hydrogel structures, like the one illustrated in Figure 3.1b,²¹. This class materials are made of highly porous polymeric networks that can swollen absorbing large quantities of solvents, and they are widely investigated for water purification²² and for biomedical applications such as in drug delivery and release systems,¹⁸ as well as wound dressings²³ and as tissue engineering.²⁴ Finally, Qi et al. recently demonstrated the photolithographic patterning of HPC hydrogel by grafting HPC with methacrylic anhydride, but the minimum features resolution is limited to mm range (Figure 3.1a).²⁵

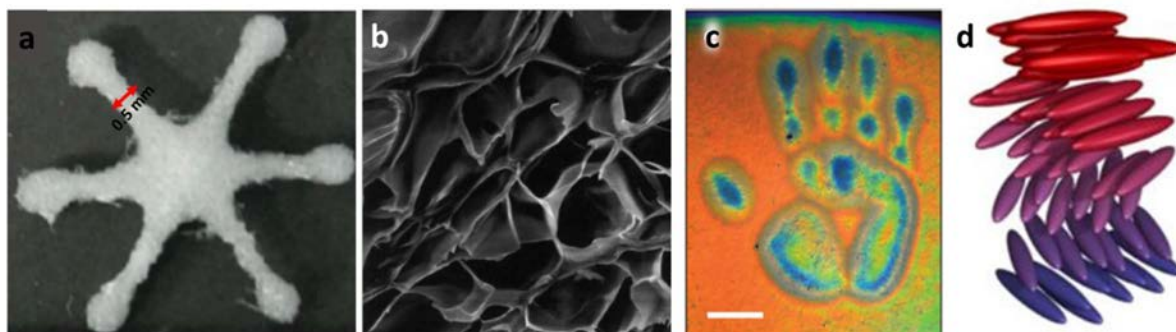


Figure 2.5 Emerging applications of HPC a) Hydroxypropyl cellulose methacrylate photo-patternable hydrogel. Patterning resolution is in the mm range.²⁵ b) HPC hydrogel obtained by electron irradiation of water solutions.²¹ c) Handprint recorded on a strain-responsive sensor fabricated using HPC cholesteric liquid crystals. d) Representation of a cholesteric arrangement.²⁶

HPC is also well known for its optical properties, in particular for the capability to form nematic liquid crystalline phase in concentrated aqueous solutions (above 50% in weight). This mesophase presents a cholesteric structure, in which the linear molecular chains arrange a helicoidal structure, giving rise to iridescent colors and chiral response that depend on the pitch between helices. This behavior of HPC is very attractive for the development of optically responsive systems, since the reflected color of HPC cholesteric crystal can change when subjected to various external stimuli such as a concentration or medium refractive index variation, mechanical stress, temperature. Figure 2.5c shows a colorimetric strain sensor based on HPC liquid crystal, fabricated with roll-to-roll process by the group of Vignolini.^{26,27} Besides the interesting properties of HPC (summarized in Table 1), there is still missing a fabrication technique that allows to pattern with high resolution this multifunctional material. In particular, patterning of other water soluble biopolymer like silk²⁸ or other cellulose derivatives have been recently demonstrated,²⁹ showing promising results and enabling novel applications of those type biomaterials in different branches of photonics. The development of a set of nano structuring technologies that are scalable and that allows controlled patterning of HPC film would be extremely beneficial to provide further functionalities to this available and low cost material, opening the path for its implementation in the large-scale fabrication of new generation ecofriendly optoelectronic devices.

Table 1. HPC properties and applications

Mechanical properties	Stiffness modulus: 20 - 150 Mpa (depending on molecular weight). Extremely flexible without plasticizer. Good film adhesion to substrates
Plasticity	Real glass transition 150° C, plus a beta transition at 0° C. Thermoformable, extrudable, heat sealable, excellent film formation properties.
Solubility	Soluble in cold water (cloud point 42°C). Soluble in most organic solvent. Non soluble in toluene, slightly soluble in acetone
Crosslinking	Chemical or irradiation (electron, ions, gamma-ray) Can form Hydrogels
Hazard	Non-toxic, nonreactive, nonexplosive.
Biocompatibility	Edible and biocompatible Food and pharma certified. (E463)
Biodegradability	Inherently biodegradable (biodegradability rate depends on the degree of substitution). Susceptible to both chemical and biological degradation in water solution.
Optical properties	Refractive index: 1.47 In water: transparent below 42°C, milky above 42°C, iridescent above 50% wt. concentration Solid: transparent films. Powder transparent to whitish or yellowish.
Molecular weight	Commercially available from 40.000 to 2.500.000 kDa Moles of substitutions (DS): 2 - 4
Industrial application	Adhesive, Printing (binder for ink based on water), Pharmaceuticals (tablets coating and filler, controlled release), Paper (protective coating, oil barrier), Food (stabilizer, edible coating, encapsulation), Plastic foams, extruded films and sheets, Cosmetic.
Emerging applications	Biocompatible colorimetric strains sensors Tissue engineering (wound dressing) Responsive hydrogels

2.4 References

- (1) Wüstenberg, T. *Cellulose and cellulose derivatives in the food industry*, Wiley-VCH, 2015.
- (2) Tajeddin, B. Cellulose-Based Polymers for Packaging Applications. In *Lignocellulosic Polymer Composites*, Thakur, V. K., Ed.; John Wiley & Sons, Inc, 2014; pp 477–498. DOI: 10.1002/9781118773949.ch21.
- (3) Jedvert, K.; Heinze, T. Cellulose modification and shaping – a review. *Journal of Polymer Engineering* **2017**, *37* (9), 845–860. DOI: 10.1515/polyeng-2016-0272.
- (4) Song, J.; Chen, C.; Zhu, S.; Zhu, M.; Dai, J.; Ray, U.; Li, Y.; Kuang, Y.; Li, Y.; Quispe, N.; Yao, Y.; Gong, A.; Leiste, U. H.; Bruck, H. A.; Zhu, J. Y.; Vellore, A.; Li, H.; Minus, M. L.; Jia, Z.; Martini, A.; Li, T.; Hu, L. Processing bulk natural wood into a high-performance structural material. *Nature* **2018**, *554* (7691), 224–228. DOI: 10.1038/nature25476.

- (5) Helanto, K. E.; Matikainen, L.; Talja, R.; Rojas, O. J. Bio-based polymers for sustainable packaging and biobarriers: A critical review. *BioResources* **2019**, *14* (2), 4902–4951.
- (6) Hickey, R. J.; Pelling, A. E. Cellulose Biomaterials for Tissue Engineering. *Frontiers in bioengineering and biotechnology* **2019**, *7*, 45. DOI: 10.3389/fbioe.2019.00045.
- (7) Hansen, F.; Brun, V.; Keller, E.; Wegner, T.; Meador, M.; Friedersdorf, L.; others. Cellulose nanomaterials—a path towards commercialization workshop report **2014**.
- (8) Eichhorn, S. J.; Rahatekar, S. S.; Vignolini, S.; Windle, A. H. New horizons for cellulose nanotechnology. *Philosophical transactions. Series A, Mathematical, physical, and engineering sciences* **2018**, *376* (2112). DOI: 10.1098/rsta.2017.0200.
- (9) Zhu, H.; Luo, W.; Ciesielski, P. N.; Fang, Z.; Zhu, J. Y.; Henriksson, G.; Himmel, M. E.; Hu, L. Wood-Derived Materials for Green Electronics, Biological Devices, and Energy Applications. *Chemical reviews* **2016**, *116* (16), 9305–9374. DOI: 10.1021/acs.chemrev.6b00225.
- (10) Sannino, A.; Demitri, C.; Madaghiele, M. Biodegradable Cellulose-based Hydrogels: Design and Applications. *Materials* **2009**, *2* (2), 353–373. DOI: 10.3390/ma2020353.
- (11) Majewicz, T. G.; Erazo-Majewicz, P. E.; Podlas, T. J. Cellulose Ethers. In *Encyclopedia of Polymer Science and Technology*, Fourth edition; Matyjaszewski, K., Ed.; Wiley-Interscience, 2014]-. DOI: 10.1002/0471440264.pst044.
- (12) Moon, R. J.; Martini, A.; Nairn, J.; Simonsen, J.; Youngblood, J. Cellulose nanomaterials review: structure, properties and nanocomposites. *Chemical Society reviews* **2011**, *40* (7), 3941–3994. DOI: 10.1039/c0cs00108b.
- (13) Kabir, S. M. F.; Sikdar, P. P.; Haque, B.; Bhuiyan, M. A. R.; Ali, A.; Islam, M. N. Cellulose-based hydrogel materials: chemistry, properties and their prospective applications. *Progress in biomaterials* **2018**, *7* (3), 153–174. DOI: 10.1007/s40204-018-0095-0.
- (14) Long, L.-Y.; Weng, Y.-X.; Wang, Y.-Z. Cellulose Aerogels: Synthesis, Applications, and Prospects. *Polymers* **2018**, *10* (6). DOI: 10.3390/polym10060623.
- (15) Heredia-Guerrero, J. A.; Williams, C. A.; Guidetti, G.; Cataldi, P.; Ceseracciu, L.; Debellis, D.; Athanassiou, A.; Guzman-Puyol, S.; Hamad, W. Y.; Vignolini, S. Plant-Inspired Polyaleuritate–Nanocellulose Composite Photonic Films. *ACS Appl. Polym. Mater.* **2020**, *2* (4), 1528–1534. DOI: 10.1021/acsapm.9b01205.

- (16) Almeida, A. P. C.; Canejo, J. P.; Fernandes, S. N.; Echeverria, C.; Almeida, P. L.; Godinho, M. H. Cellulose-Based Biomimetics and Their Applications. *Adv. Mater.* **2018**, *30* (19), e1703655. DOI: 10.1002/adma.201703655.
- (17) Guidetti, G. Cellulose photonics: designing functionality and optical appearance of natural materials, Apollo - University of Cambridge Repository, 2018.
- (18) Ashland. *Klucel™ hydroxypropylcellulose*. <https://www.ashland.com/industries/pharmaceutical/oral-solid-dose/klucel-hydroxypropylcellulose>.
- (19) Ashland. *The Use of Klucel™ Pharm Hydroxypropylcellulose to Increase the Utility of Hydroxypropyl Methylcellulose in aqueous film coatings*. https://www.ashland.com/file_source/Ashland/links/PTR_049-1_IRFC_Klucel_HPC_Pharm_Increasing_the_Utility_of_HPMC.pdf.
- (20) Borges, J. P.; Godinho, M. H.; Martins, A. F.; Stamatialis, D. F.; Pinho, M. N. de; Belgacem, M. N. Tensile properties of cellulose fiber reinforced hydroxypropylcellulose films. *Polym Compos* **2004**, *25* (1), 102–110. DOI: 10.1002/pc.20008.
- (21) Wach, R. A.; Mitomo, H.; Yoshii, F.; Kume, T. Hydrogel of Radiation-Induced Cross-Linked Hydroxypropylcellulose. *Macromol. Mater. Eng.* **2002**, *287* (4), 285. DOI: 10.1002/1439-2054(20020401)287:4<285:AID-MAME285>3.0.CO;2-3.
- (22) Liu, X.; Zhou, Y.; Nie, W.; Song, L.; Chen, P. Fabrication of hydrogel of hydroxypropyl cellulose (HPC) composited with graphene oxide and its application for methylene blue removal. *J Mater Sci* **2015**, *50* (18), 6113–6123. DOI: 10.1007/s10853-015-9166-y.
- (23) Ogawa, A.; Nakayama, S.; Uehara, M.; Mori, Y.; Takahashi, M.; Aiba, T.; Kurosaki, Y. Pharmaceutical properties of a low-substituted hydroxypropyl cellulose (L-HPC) hydrogel as a novel external dressing. *International Journal of Pharmaceutics* **2014**, *477* (1-2), 546–552. DOI: 10.1016/j.ijpharm.2014.10.043.
- (24) van Vlierberghe, S.; Dubruel, P.; Schacht, E. Biopolymer-based hydrogels as scaffolds for tissue engineering applications: a review. *Biomacromolecules* **2011**, *12* (5), 1387–1408. DOI: 10.1021/bm200083n.
- (25) Qi, A.; Hoo, S. P.; Friend, J.; Yeo, L.; Yue, Z.; Chan, P. P. Y. Hydroxypropyl cellulose methacrylate as a photo-patternable and biodegradable hybrid paper substrate for cell culture and other bioapplications. *Advanced healthcare materials* **2014**, *3* (4), 543–554. DOI: 10.1002/adhm.201300155.

- (26) Kamita, G.; Frka-Petesic, B.; Allard, A.; Dargaud, M.; King, K.; Dumanli, A. G.; Vignolini, S. Biocompatible and Sustainable Optical Strain Sensors for Large-Area Applications. *Adv. Optical Mater.* **2016**, *4* (12), 1950–1954. DOI: 10.1002/adom.201600451.
- (27) Liang, H.-L.; Bay, M. M.; Vadrucci, R.; Barty-King, C. H.; Peng, J.; Baumberg, J. J.; Volder, M. F. L. de; Vignolini, S. Roll-to-roll fabrication of touch-responsive cellulose photonic laminates. *Nature communications* **2018**, *9* (1), 4632. DOI: 10.1038/s41467-018-07048-6.
- (28) Omenetto, F. G.; Kaplan, D. L. A new route for silk. *Nature Photon* **2008**, *2* (11), 641–643. DOI: 10.1038/nphoton.2008.207.
- (29) Caligiuri, V.; Tedeschi, G.; Palei, M.; Miscuglio, M.; Martin-Garcia, B.; Guzman-Puyol, S.; Hedayati, M. K.; Kristensen, A.; Athanassiou, A.; Cingolani, R.; Sorger, V. J.; Salerno, M.; Bonaccorso, F.; Krahne, R.; Heredia-Guerrero, J. A. Biodegradable and Insoluble Cellulose Photonic Crystals and Metasurfaces. *ACS Nano* **2020**, *14* (8), 9502–9511. DOI: 10.1021/acsnano.0c03224.

CHAPTER 3

Lithographic techniques

State of the art

The fabrication techniques that have emerged as a response to the continuous miniaturization of electronic components have nowadays reached the capability to form structures with extremely high resolution, achieving transistors as small as 5 nm, already commercialized by Samsung¹ and TSMC² companies. Lithography is a fabrication process fundamental for the manufacture of the integrated circuit (IC) chips that operate everyday optical and electronic devices. Multiple-step sequences of lithography and chemical processing steps (etching, oxidation, diffusion and deposition) are necessary in order to create the complex network of materials and relief geometries that gives the IC their specific functionality.

However, the lithographic methods that are currently employed in large scale semiconductor manufacturing are facing some severe limitation summarized in the following points.

- **Low versatility**

Most lithographic techniques are only suitable for very specific processes, being optimized for silicon-based manufacturing, that typically involves light sensitive, corrosive materials and flat, rigid substrates. This strongly limits their application in research areas that employs unconventional materials, like the fast-growing fields of biotechnology and flexible electronics. Those technologies indeed employ soft and frequently require devices with curved or rough surfaces.

- **High cost**

Reaching resolutions below 50 nm over large areas patterns is challenging. It often involves low throughput processes and expensive equipment which further hinders the implementation of traditional photolithographic methods for the large-scale manufacturing of emerging nano-devices.

- **Environmental impact**

Traditional lithographic techniques make use of highly toxic and corrosive solvents. The development of a cleaner nanofabrication process that employs non-toxic materials would be beneficial from an environmental point of view, for the worker health protection, and would decrease the costs of disposal of chemical residues.

Huge progresses have been made in the last few decades, developing many different approaches and variants of standard lithographic techniques that are compatible with a wider range of materials and allow for large-scale fabrication of exotic architectures. In this frame, ancient forms of lithography like embossing, molding, stamping and printing have recently gained increased attention in different fields of nanofabrication for their nanometric resolution, lower cost, high throughput and versatility.

This chapter introduces the state of art of lithographic techniques, explaining their working principle and illustrating some of their most advanced developments in the light of the above discussion. I will present first, the more conventional radiation-based approaches, and second the non-conventional approaches of nanoimprinting and soft lithography. A more technical discussion of the techniques used in this thesis for the fabrication of periodic plasmonic and photonic crystals is reported in chapter 4. The last section of this chapter complements the discussion addressing some environmental and economical consideration and comparing pros and cons of the different technique presented.

3.1 Radiation based lithography

This class of lithographic methods is definitively the most widely used in industry. It is based on the use of an electromagnetic radiation (from x-rays to UV light) or a charged particle beam (electrons, or ions) to modify a resist. Resist materials need to be susceptible to the specific beam radiation and change their chemical status - breaking or formation of chemical bounds - upon irradiation. The radiation source that is employed determines the final theoretical resolution achievable before the occurring of diffractive phenomena. Some of these techniques are based on the use of a shadow mask to define the irradiated area, while some other techniques are mask-less. In the case of charged particles, the beam direction can be controlled by electromagnetic lenses which scan it directly on the target region of the substrate surface (therefore also called "direct-write" techniques). Figure 3.1 Wavelength of typical radiation source and charged particle beams employed in lithography. The blue box specifies whether the technique employ

shadow mask, is mask lees or is a direct write technique. Figure 3.1 illustrates the wavelength of typical radiation source and charged particle beams employed in lithography.

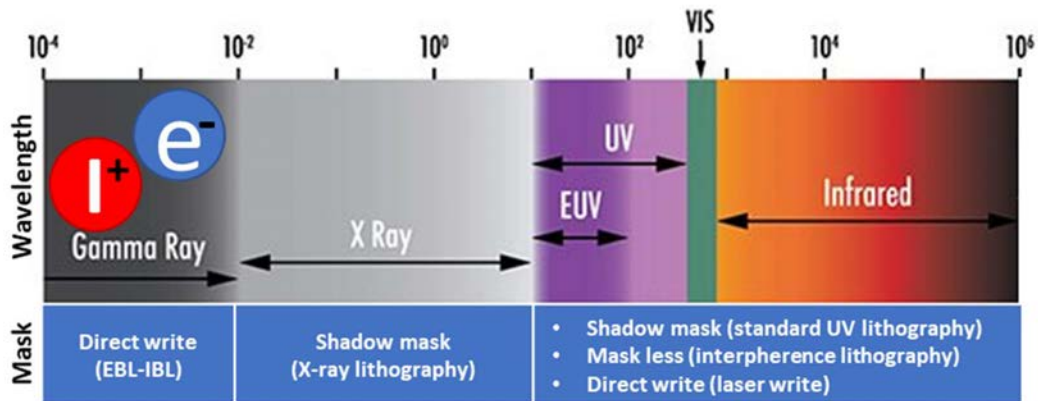


Figure 3.1 Wavelength of typical radiation source and charged particle beams employed in lithography. The blue box specifies whether the technique employ shadow mask, is mask lees or is a direct write technique.

In the next paragraphs, I will analyze more in detail the working principle of the most employed lithographic techniques that are based on radiation sources.

3.1.1 Photolithograhly

Photolithography is a patterning process that uses light in order to project a geometric feature from an optical mask to a light-sensitive film deposited on a substrate. Light exposure selectively changes the solubility of the resist material, allowing to reproduce the mask geometric patterns on the resist film by solvent dissolution of either the exposed (positive resist) or the unexposed (negative resist) area, as illustrated in Figure 3.2a.

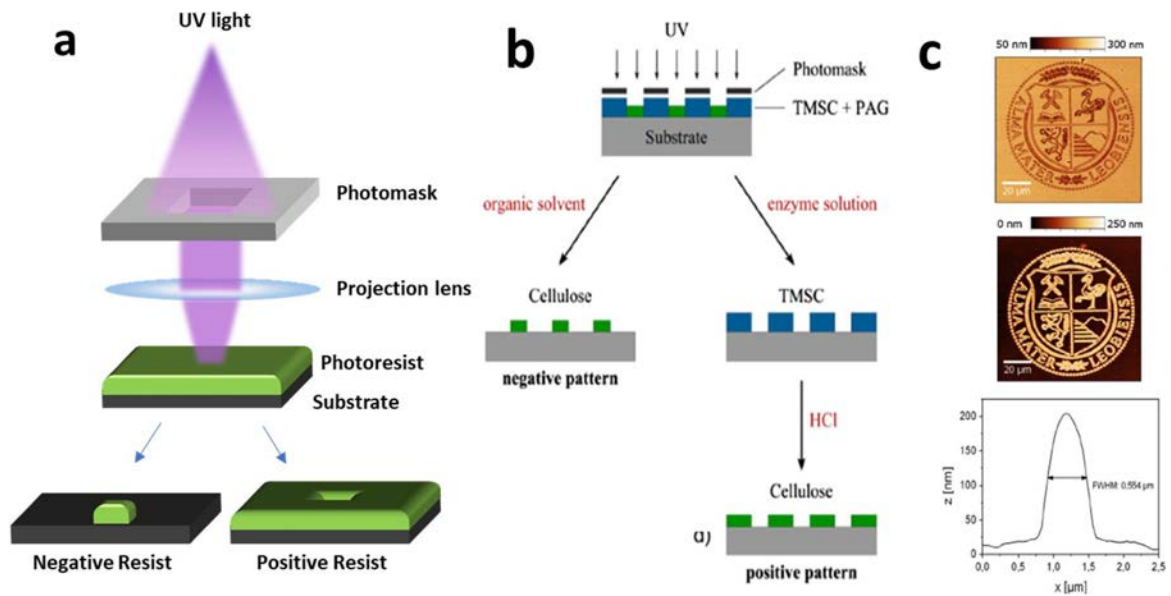


Figure 3.2 Principle of operation of photolithographic techniques. **b)** Schematic of the employment of trimethylsilyl cellulose (TMSC) as positive and negative bio resist and **(c)** cellulose micropattern fabricated.³

Once patterned the photoresist relief geometry is transferred to the substrate material by direct etching of the exposed areas or by new material deposition and resist lift off (see Chapter5, section 5.3). Photolithography is a fundamental process in circuit board (PCB) and microprocessor manufacturing, however, its resolution is limited by the wavelength of the light that is used, following the formula (3.1):

$$CD = k \frac{\lambda}{N.A.} \quad (3.1)$$

Where CD is the critical minimum dimension, λ is the wavelength of the employed radiation, N.A. is the numerical aperture of the projection lenses and k is a coefficient that depends on process related factors. Current state-of-the-art photolithography tools use deep ultraviolet light with wavelengths of 248 and 193 nm, which, together with a finely tuned system of lenses achieve minimum feature sizes down to 50 nm. Smaller resolution can be achieved using extreme ultraviolet radiation ($\lambda = 13.5$ nm) or by liquid immersion which enables to obtain numerical apertures higher than 1.0. However, a modern CMOS wafer requires multiple patterning steps to reach feature size below 10 nm, and usually undergoes up to 50 photolithographic cycles during its fabrication process.

Photolithographic patterning of bio-resists

Various attempts to photopatterned biomaterials like cellulose,⁴⁻⁶ silk,^{7,8} or polyethylene glycol⁹⁻¹¹ could be found in the literature. They follow three main approaches to provide photochemical crosslinking of biomaterials:

- Functionalization with light sensitive groups (e.g. Alkyl moieties)
- Blending with photosensitive resins (e.g. SU8 photoresist)
- Chemical amplification (e.g. addition of photo acid generator)

Figure 3.2b-c shows an example of a lithographic patterning process employed to obtain positive and negative type cellulose patterns, with lateral resolution of 550 nm.³ In that work the cellulose resist consists in trimethylsilyl cellulose, an ethanol soluble derivatives, that has been amplified with a photo acid generator.

3.1.2 Interference lithography

Interference lithography is a variation of photolithography that exploits the diffraction patterns generated by two (or more) coherent light beams to fabricate regular periodic arrays. Figure 3.3a shows a schematic of an interference lithography set-up, while Figure 3.3b shows a large area (1 cm²) square array of holes fabricated using this technique and used in in this thesis in nanoimprint master pattern (see section 3.2).

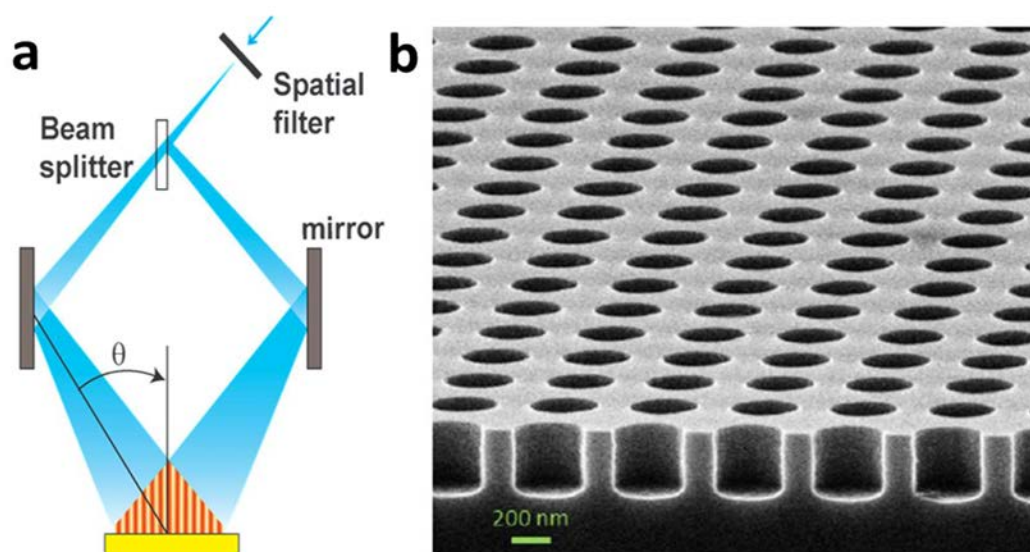


Figure 3.3. a) schematic of an interference lithography set up. b) A large area (1 cm²) square array of holes with diameter of 300 nm and lattice parameter of 500 nm fabricated by CEMITEC (Navarra, Spain) and used in this thesis as master for replication.

Complex interference patterns can be achieved interfering more than 2 beams. For instance, if 3 beams are employed, arrays with hexagonal symmetry will be generated, while employing 4 beams, rectangular symmetry arrays or 3D photonic crystals will be generated. Interference lithography does not require a photomask or complex lens system like in standard photolithography and can produce large area patterns, but its resolution is still limited by light wavelength and only periodic structures are accessible.¹²

3.1.3 Electron beam lithography (EBL)

Electron beam lithography (EBL) employs high energy electrons to change the solubility of the resist material, which usually consists in specially formulated resins that undergo chemical reactions under certain doses of electron exposition. Electron-beam lithography is a direct writing technique, which means it can create custom patterns without requiring a photomask. In EBL the electron beam is focused into a nanometer size spot and scanned directly on the resist surface designing the desired geometry. In negative resists the electron beam initiates intermolecular bonding, cross-linking smaller precursors into larger and insoluble polymeric chains. In a positive resist, such as Poly(methyl methacrylate) (PMMA) the solubility changes instead due to scissions of the polymeric chains upon electron irradiation. This technique has extremely high resolution (sub 10 nm), since it is not limited by light diffraction, but it has very low

throughput, restraining its usage to the typically low volumes of production for research and development applications.

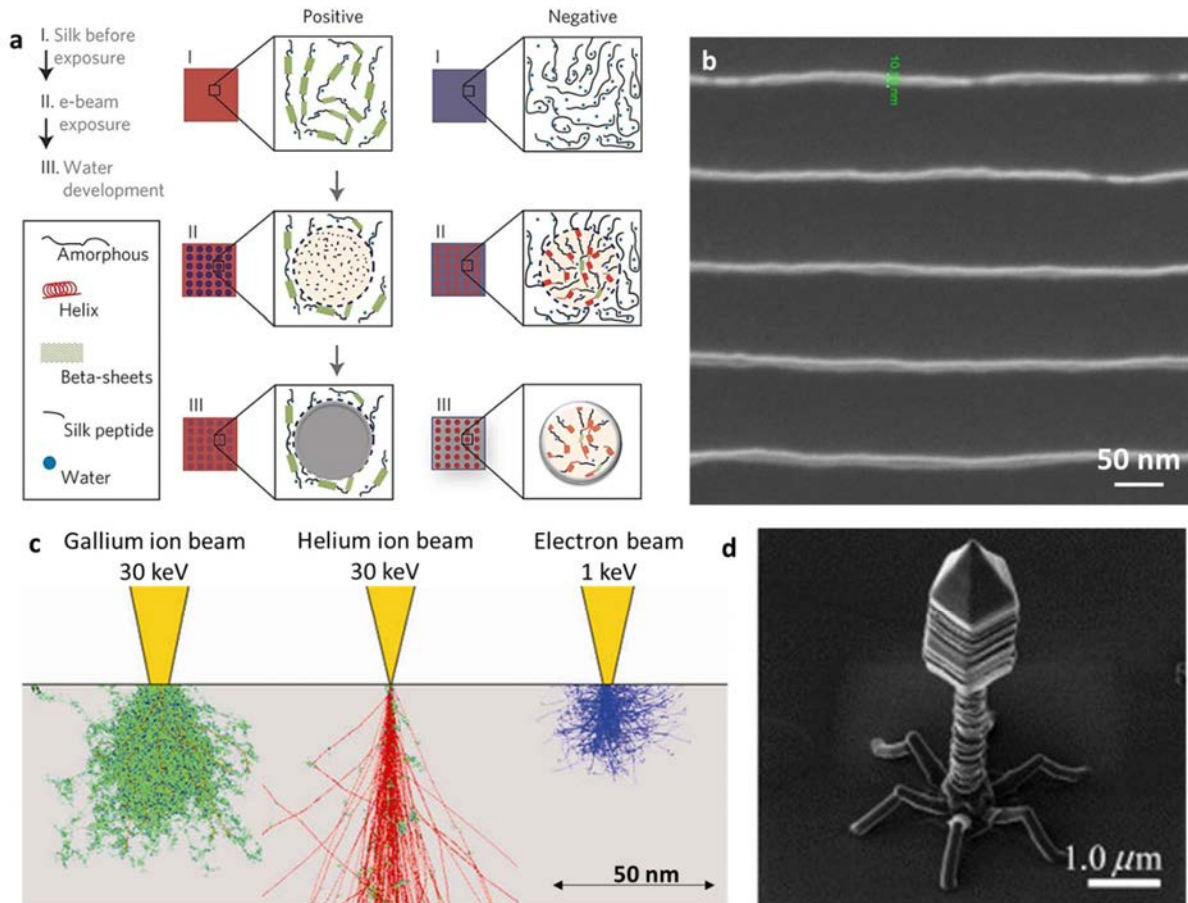


Figure 3.4 Charged particles lithography. **a)** Silk fibroin supramolecular structure modifications induced by electron irradiation.¹³ **b)** 10 nm lines arrays fabricated in hydroxypropyl cellulose via EBL. **c)** Monte-Carlo modeling results of particles volume interactions for representative beams into silicon.¹⁴ **d)** A 3D model of bacteriophage grown by FIB-CVD using gasified phenanthrene ($C_{14}H_{10}$) as a carbon source for the deposition of diamond like carbon.¹⁵

E-beam patterning of bio-resists

Many biomaterials have demonstrated to change their physico-chemical status in response to electron irradiation. The main approaches to obtain patterns in biomaterial using EBL are the following:

- Solvent solubility change due to material crosslinking or degradation
- Solubility change due supramolecular conformational change
- Biodegradability (e.g. enzymatic digestion) change due to chemical modification

E-beam lithography has been widely employed for patterning of bio-based resists,¹⁶ among which proteins films like silk¹³ or egg albumen¹⁷ chemically modified PEG¹⁸ and various cellulose derivatives.¹⁹⁻²¹ For instance, Omenetto et al demonstrated¹³ that the water solubility of silk can be controlled by electron irradiation. This allowed this material to be used both as positive and negative e-beam resist (Figure 3.4a). In this thesis the performance of hydroxypropyl cellulose as positive water developable resist have been tested, featuring resolutions down to 100 nm as illustrated in Figure 3.4b (see Chapter5, section 5.3).

3.1.4 Ion beam lithography (IBL)

Ion beam lithography (IBL) is another direct write and high-resolution nanofabrication technique, which allows to pattern resists, to locally mill atoms, deposit materials or to locally implant ions directly on the substrate surface. IBL uses a narrow beam of charged particles, typically gallium ions, which are accelerated toward the target surface, forcing out material (milling) or modifying its chemical properties (resist patterning). Beam-induced deposition technologies such as focused ion beam chemical vapor deposition (FIB-CVD) and electron-beam-induced deposition (EBID) can also create free standing 3D nanostructures with high spatial accuracy into a nearby substrate by decomposition of gaseous molecules into non-volatile fragments as illustrated in Figure 3.4d.¹⁵

IBL based on gallium ions can reach resolutions below 20 nm and recently, sub-10 nm geometries have been also demonstrated using helium beams as lithographic source, which can produce focused beams that reach sub-nm spot sizes. Compared with EBL, IBL requires only about 1-10% of the particle dose (i.e. the intensity of the particles flux impinging on the target surface) to expose a resist and it benefits from a reduced interaction volume compared to that of an electron beam of similar energy, reducing the long-range scattering (proximity effect), as illustrated in Figure 3.4c.¹⁴

Ion-beam patterning of bio-resists

High energy ions can be used to modify biomaterials. This technique can be implemented to etch off the biopolymer in specific regions (so called “nano-sculpturing”) with increasing depth as the irradiation dosage increases, or similarly to e-beam lithography, the ions that penetrate into the film can crosslink induce chemical modification such crosslinking or degradation.¹⁶

3.2 Nanoimprint lithography

Nanoimprint lithography (NIL) is a straightforward mechanical nanofabrication technique involving a prepatterned stamp, called “master” mattern, which is pressed against a deformable resist in order to retrace the stamp features. NIL presents numerous advantages over standard lithographic techniques like photolithography or e-beam lithography, namely:

- **Low cost and high throughput**

Its sheer simplicity lead to much lower operational costs since there is no need of complex equipment or optical set-up and master molds can be reused several times or directly implemented in high throughput roll-to-roll set-ups (Fig 2.4b), which can dramatically speed up the manufacturing time.

- **High resolution**

In NIL the pattern is transferred not by electron, ion or other beams, which makes possible to reach resolution beyond the limit set by diffraction (down to few nanometers²²⁻²⁴), without requiring complex protocols or high-energy radiation sources.

- **Versatility**

NIL is an intrinsically more versatile technique, allowing for wider range of material that can be patterned, since there is no need of finely tailored light or electron sensitive resists. This characteristic also makes NIL particularly appealing for the rapid and simple patterning of unconventional materials.

Since the initial idea of this technique was developed, numerous variations of the nanoimprint lithography have been suggested. The most common variations of NIL are tNIL and UV-NIL, and they differentiate by the way the resist is hardened i.e. by temperature change or by UV induced crosslinking.

3.2.1 Thermal nanoimprint lithography (tNIL)

When Chou and coworkers first invented this technique in 1995 they simply used a rigid silicon stamp to mechanically deform a thermally softened PMMA film, achieving in a few minutes large area patterns with an extraordinary resolution of 10 nm (Fig. 2.4a),²⁴ far beyond the diffractions limits. tNIL has been the

earliest type of nanoimprinting technique developed, and since its discovery, nanoimprint technology has been continuously expanded, giving rise to a whole set of techniques based on the principle of mechanical deformation of thermo responsive materials, reaching a minimum feature size down to 1 nm.²²

The steps involved in a standard t-NIL process, also called “hot embossing”, are illustrated in Figure 3.5a. Briefly, a thin layer of thermoplastic resist is spin-coated on a substrate and a pre-patterned mold is pressed against the resist-coated substrate while heating above glass transition temperature (T_g) of the resist. The mechanical properties of thermoplastic materials can be reversibly changed from solid to viscous by simply varying the temperature, as illustrated in Figure 3.5b.

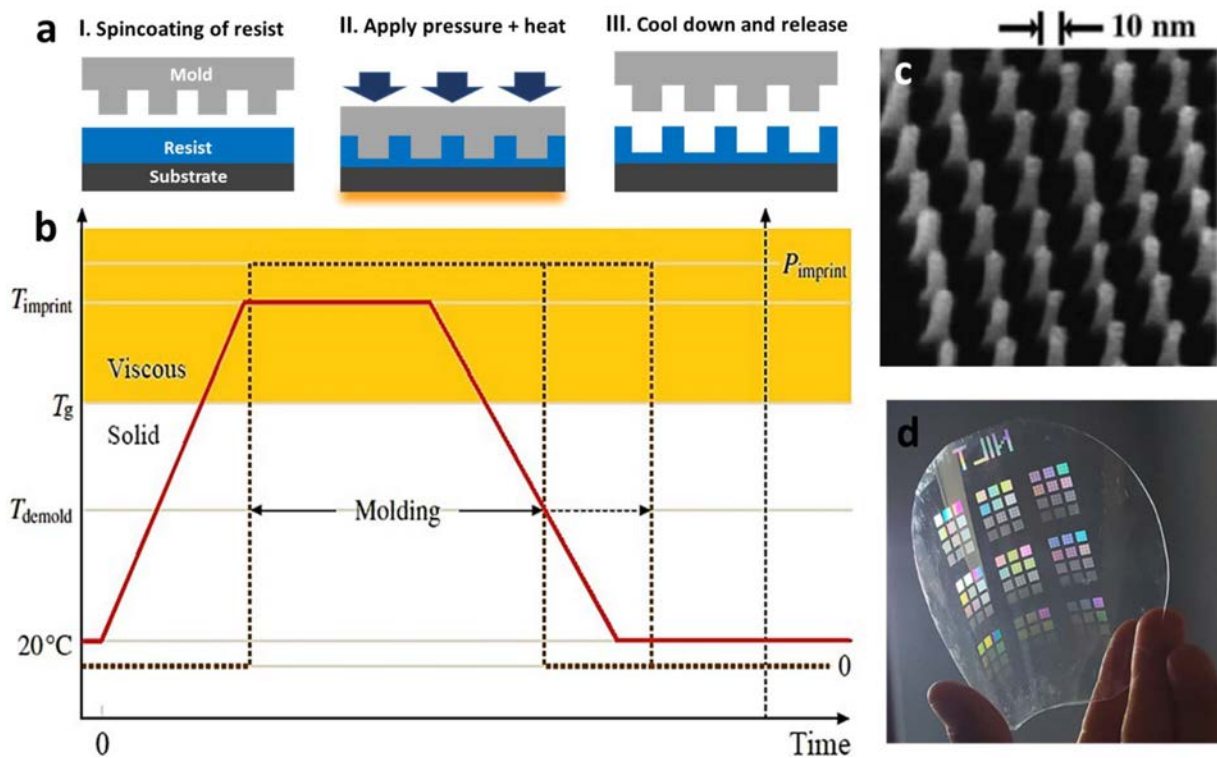


Figure 3.5 Illustration of thermal nanoimprinting process and examples of pattern formation via tNIL process. a) Process steps and elements involved. b) Schematic of pressure and temperature settings during a tNIL process. c) high resolution 10 nm pillars array in PMMA²⁴ d) Wafer scale micrometric patterning in TOPAS flexible membrane, fabricated by the author using the NIL tool available in our group (see paragraph 4.3.1).

Once the system is cooled down, the resist hardens retaining a negative image of the pattern, and the stamp is demolded. Optionally, irreversible curing of the resist can be performed before or after demolding (by UV exposure or by chemical or thermal treatment) in order to cross-link polymeric chains and make patterns more durable in time, obtaining the best mechanical properties and chemical resistance. As previously mentioned, tNIL is a versatile technique that allows the patterning of unconventional material

over large areas. Figure 3.5d shows instead a wafer size micro-pattern fabricated by the author with in TOPAS plastic film using hard a silicon template and a NILT tool (see section 4.3.1 for further details).

Nanoimprinting of bio-resists

Considering that tNIL is based on the mechanical deformation of thermoplastic material, which means that any material that present a softening temperature can be (to some extent) patterned with this technique. This has allowed to use tNIL for nanoscale patterning of various ecofriendly biopolymers, such as Silk,²⁵ polyvinyl alcohol (PVA),²⁶ PEG or Chitosan,²⁷ cellulose derivatives,^{28,29} but also biological media like DNA.³⁰ Figure 3.6a shows as an example the work developed by of Mäkelä. et al, who demonstrated submicrometric patterning of cellulose acetate using a roll to roll set-up with patterning speeds up to 20 m/min. A common variation of tNIL that is often employed for patterning temperature sensitive materials is the solvent assisted method, in which the resist softening is obtained by solvent dissolution (or moisture absorption) and subsequent drying. Figure 3.6b and c show Silk patterning with features resolution down to 200 nm achieved using both solvent assisted and thermal NIL.²⁵

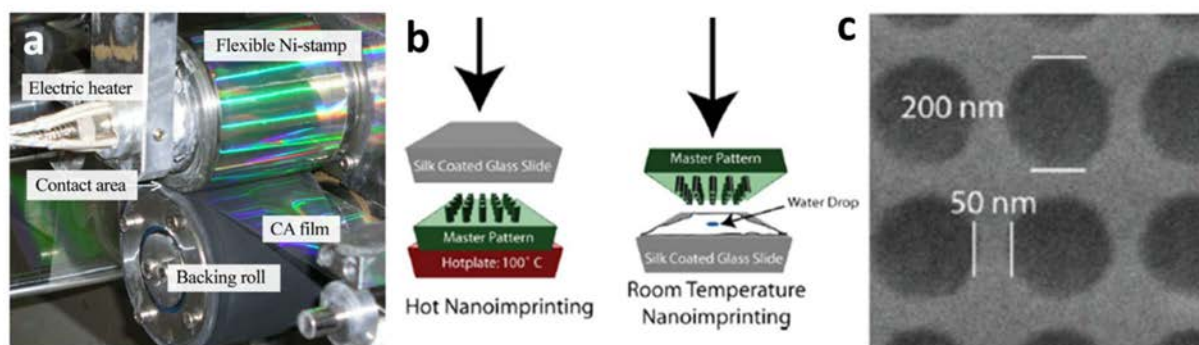


Figure 3.6 Roll-to-roll set up for high-throughput submicrometric patterning of cellulose acetate films using tNIL method.²⁹ b) schematic of tNIL (hot nanoimprinting) and solvent assisted NIL (room temperature Nanoimprinting) employed to pattern Silk biofilm. c) Silk biofilm patterned using NIL methods described in (b).²⁵

3.2.2 UV nanoimprint lithography (UV-NIL).

In UV-NIL, the process steps are very similar to the ones described for tNIL, but in this case, the resist is a photosensitive material and it is hardened by UV-light exposure which cross-links the polymeric chains, as depicted in Figure 3.7a. For this reason, in UV-NIL the imprinting mold is usually a transparent template (quartz, glass or soft silicone stamps). UV-NIL is limited to light sensitive materials, however this technique presents some advantages. While tNIL is based on temperature softening of thermoformable resists, and

pressure is the driving force to displace the viscous flow of material, in UV-NIL extremely low pressure are sufficient to fill the mold features, since the resist material is in the liquid state (or very low viscosity) and the surface energy drives the spreading of the resist material into the features, filled simply by capillary forces. Furthermore, the lower resist viscosity allows filling of the mold cavity in a shorter time maintaining high resolution³¹ (Figure 3.7b). Another advantage of UV-NIL over tNIL is the room temperature processing, which eliminates residual mechanical stresses due to different thermal expansion coefficients of the materials involved (mold, template and substrate), and is compatible with temperature sensitive substrates.

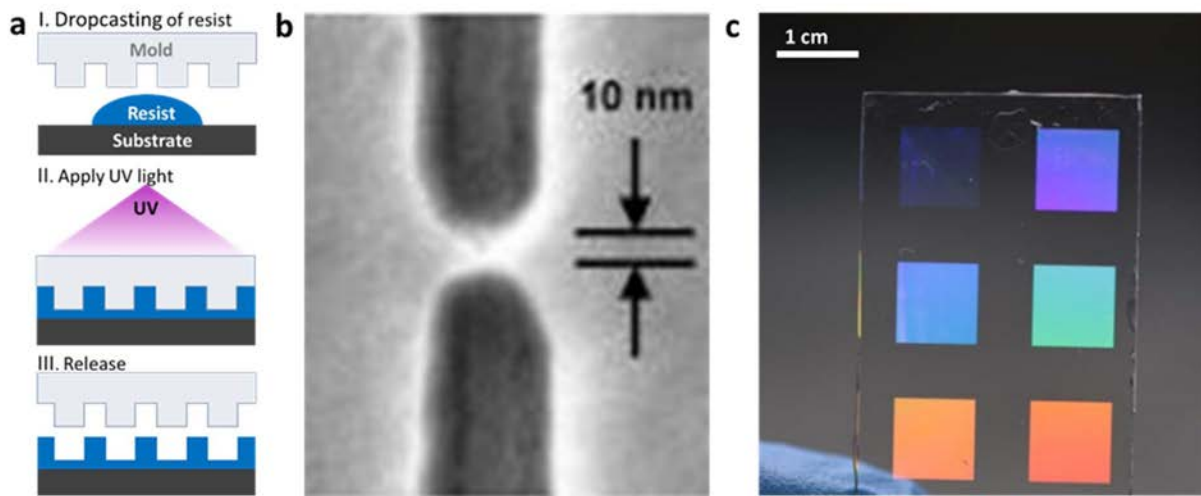


Figure 3.7 Illustration of UV-NIL process and examples of patterns obtained using this technique. **a)** Process steps and elements involved. **b)** 10 nm resolution features.³¹ **c)** Glass slide with nanometric patterns fabricated in Ormostamp by the author using UV-NIL technique.

In this thesis, UV-NIL has been used to fabricate negative image of purchased silicon master in a fast and reliable way using Ormostamp (Microresist technology) resist. This material is a photocurable polydimethylsiloxane with high young modulus (650MPa), suitable to replicate fine structures with high aspect ratio and excellent mechanical stability (see chapter 3.1). The fabrication protocol employed can be described as an inverted UV-NIL, where the silicon template is placed at the bottom and the UV light is shined through a transparent glass substrate that will support the patterned Ormostamp film. Figure 3.7c shows square and hexagonal photonic crystals with features size down do 200 nm and aspect ratio greater than one fabricated in Ormostamp resist.

3.3 Soft lithography

Despite its high potentiality, nanoimprint method presents some problems that are associated with the inherent hardness of the mold. In order to achieve conformal contact between the hard mold and the resist film, and to evacuate the air bubble that might be trapped at the interface, high imprinting pressures are usually required. Under these conditions, the presence of submicron-size impurities at the mold-resist interface can cause serious damage to the mold, limiting its operational lifetime in further imprint processes. Furthermore, the low flexibility of hard molds forbids a smooth separation of the stamp-resist interface (where typically high friction forces are present), which can lead to sudden breakage of the mold or substrate, left resist on the mold pattern, or require specific tools for the demolding step. Those limitations can be detrimental for the cost effectiveness of NIL and its implementation in large scale industrial processes, since hard mold fabrication can be very expensive.

To address those issues, soft and flexible replicas of the hard mold based on polymeric materials can be made. The earliest soft-lithographic method, called μ CP, was developed by the group of Whitesides,³² who used an elastomeric stamp to selectively deposit a molecular ink on a target substrate. This approach immediately raised high interest, thanks to its ability to form submicrometric structures using inexpensive laboratory apparatus and without requiring complex protocols. The invention of μ CP launched indeed a huge number of related techniques, which explore the use of soft molds not only as stamps for microcontact printing, but also as imprinting tools, allowing to pattern curved and irregular surfaces.

The most commonly used material for the mold fabrication is (polydimethylsiloxane) PDMS, however, other polymers such as Poly(methyl methacrylate) (PMMA), PVA or polyurethane (PU) can be used (see chapter 4, for further details about mold fabrication). In this thesis, soft lithographic techniques have been by far the most employed nanofabrication process, particularly in combination with cellulose derivatives biopolymers, as discussed more in details in the articles compilation. Different variation of the soft lithographic method has been explored, allowing the fabrication of challenging functional architectures with feature resolution down to 100 nm.

3.3.1 Soft nanoimprinting lithography

The use of flexible molds solved most of the problem related to hard mold-based nanoimprint processes, resulting in many advantageous properties, while maintaining the high-resolution of standard hot

embossing. The process flow is the same as in standard tNIL and UV-NIL, but instead of hard templates soft and flexible molds are used. Figure 3.8 shows some of the most advanced demonstrations of this technique. Resolution down to 2 nanometers can be achieved using soft nanoimprint, as demonstrated by Rogers and co-workers who successfully replicated the surface topography of single walled carbon nanotubes (Figure 3.8a) into UV sensitive resists.²³ Curved surfaces can be also easily patterned thanks to the flexibility of the mold, as illustrated in Figure 3.8b,³³ where a polybenzylmethacrylate thermal resist has been deposited on top of a glass lens and patterned using a nanocomposite PDMS mold. Furthermore, PDMS presents a certain permeability to solvents, allowing for easy pattern for instance sol-gel materials via the previously explained solvent assisted method. This technique takes advantage of solvent evaporation through the mold to harden the sol gel solution that will retain the mold shape. Figure 3.8c shows a photonic crystal fabricated from a TiO₂ paste containing 20 nm TiO₂ nanoparticles in an organic binder. The TiO₂ paste is diluted in ethanol, spincoated on a glass substrate and imprinted with a soft PDMS mold at RT for 30 minutes, to allow solvent evaporation and dry hardening of the titania NPs porous network. The organic phase is burnt out at 500° C for 1 hour, leaving the inorganic structure behind.³⁴

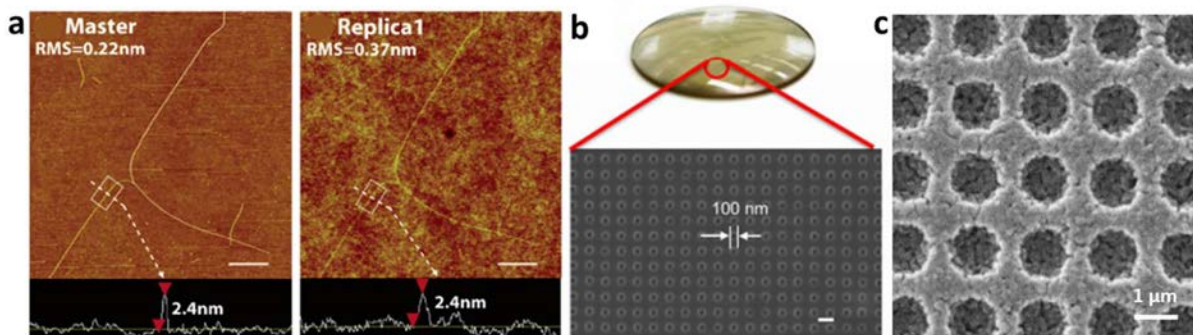


Figure 3.8 Examples of soft lithographic fabrication. a) replica of 2 nm wide single walled carbon nanotube obtained using UV curable resist and soft mold.²³ b) Nanopattern fabricate on the curved surface of a glass lens.³³ c) 1 μm diameter holes array fabricated in sol-gel titania nanoparticles using PDMS soft elastomeric molds.³⁴

3.3.2 Micro-contact printing (μ-CP)

In μCP, a patterned elastomeric stamp is used to transfer an 'inked' material to a target surface. The stamp's protrusions are typically loaded with the ink by immersion in a liquid suspension or by direct evaporation, and then the transfer is made by gently pressing against the receiver substrate. If the interaction between ink-receiver is stronger than the ink-stamp, the ink will be successfully printed on the

receiver substrate. Microcontact printing has undergone a rapid evolution since its first demonstration, reaching 100 nm resolution for self-assembled monolayer patterning, and many books and review articles have been written about the widespread application of this technique.³⁵⁻³⁹ Usually, the patterns of molecular films fabricated via μ CP can be then use as inhibitor or nucleation site for the selective deposition of other materials, as illustrated in Figure 3.9a-d⁴⁰. This strategy is also widely used in biological applications since microcontact printing is particularly suitable for patterning proteins or enzymes films that can serve as precursor for selective attachment of other biological media like DNA⁴¹ or antibodies or for cells growth, as illustrated in Figure 3.9e⁴². Among the diverse development lines of μ CP that are nowadays investigated, ink materials are not limited to molecules and macromolecules, but also to inorganic elements such as nanoparticles. For example, conductive micro structured electrodes can be fabricated using colloidal nanoparticles as ink, as illustrated in Figure 3.9f.⁴³

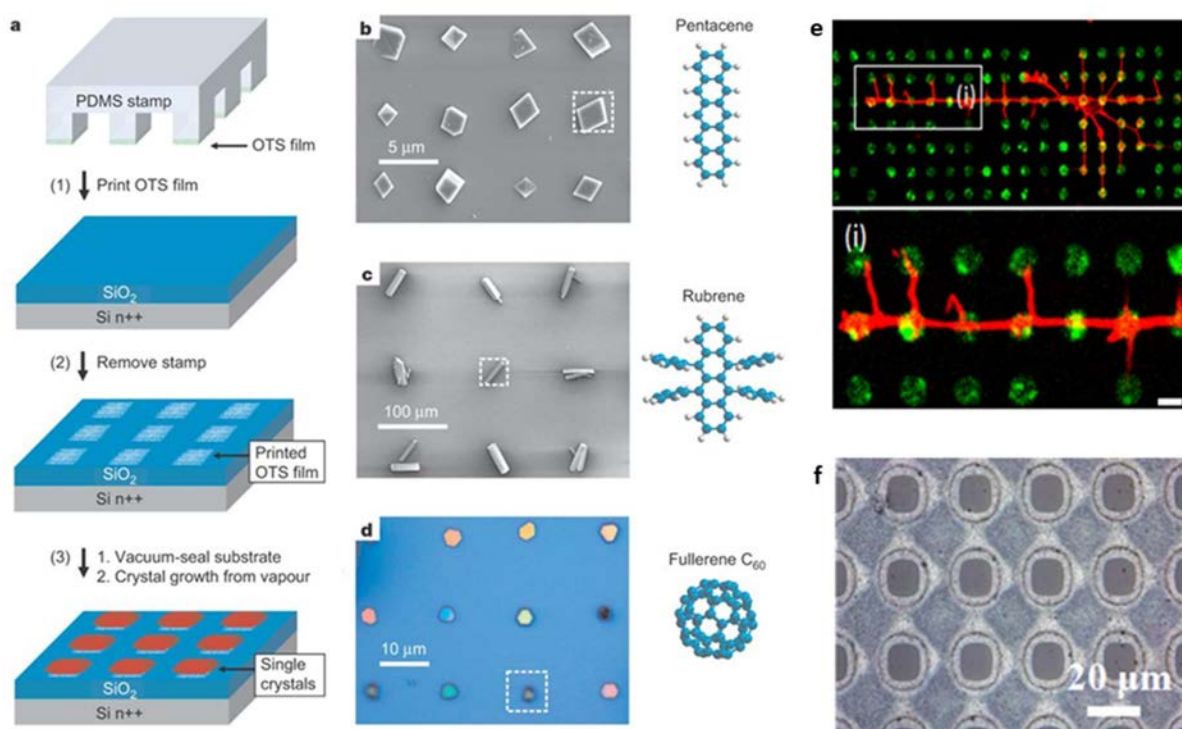


Figure 3.9 Schematic of μ -contact printing process and examples of applications of this technique. a) Process steps for self-assembled monolayer pattern deposition b-d) Selective growth of aromatic hydrocarbons on octadecyltrichlorosilane films patterned via microcontact printing.⁴⁰ e) Influence on mouse hippocampal neuronal growth of poly-L-lysine micro dot arrays deposited via μ -contact printing.⁴² f) Silver colloidal nanoparticles arrays fabricated via μ -contact printing.⁴³

3.3.3 Transfer printing

Transfer printing or nanotransfer printing (nTP) is a recently developed printing technique for micro and nanofabrication, which, differently from μ CP, makes use of interfacial adhesion forces, glues and sacrificial release layers in order to assemble solid materials into functional layouts on a receiver substrate. Different variations of nTP have been developed. The most common approach, illustrated in Figure 3.10a, takes advantage of the speed-dependent adhesion force of PDMS silicone to pick and/or place material from donor to receiver substrates,⁴⁴ allowing to assemble independently processed materials and the generation of exotic structures. For instance, a 3D multiple layers patterns made of overlapped metallic channels fabricate by the group of J.A. Rogers is illustrated in Figure 3.10b.⁴⁵

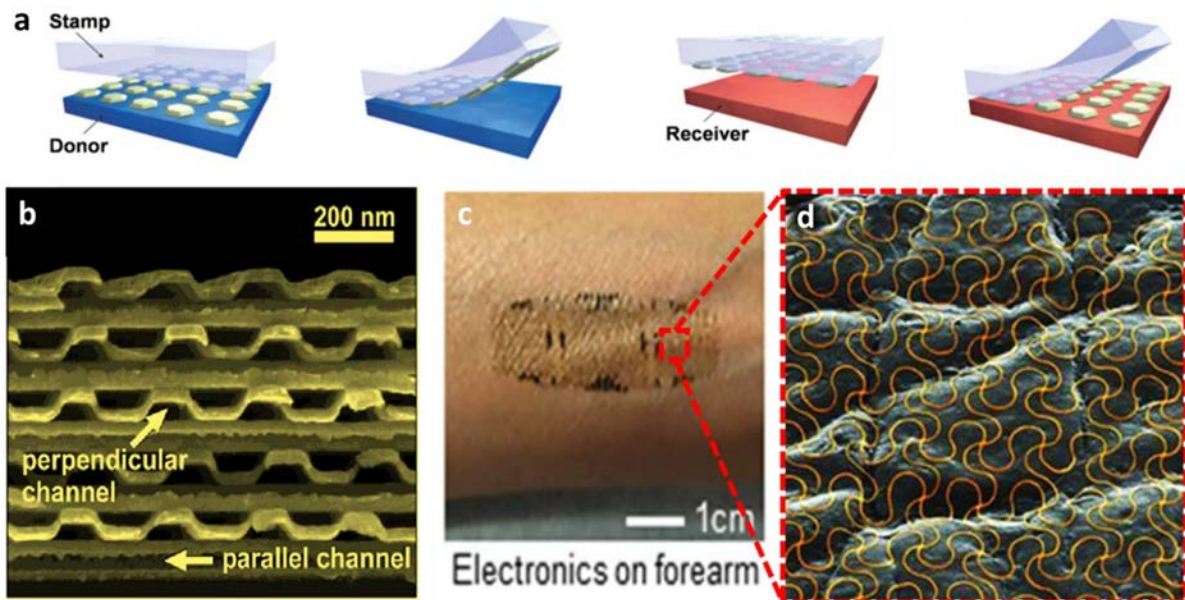


Figure 3.10 Transfer printing process and examples of applications of this technique. a) Process steps schematics. b)⁴⁵ multilayer metallic channel structure fabricated using PDMS kinetic adhesion control transfer printing. c-d) Metal electrode printed directly into human skin.⁴⁶

Transfer printing with bio-based materials

Many variations of nTP have been proposed,^{38,47} and recently, solvent or thermal releasable transfer tapes have emerged as an alternative to silicone molds for printing, creating new engineering opportunities in the field of flexible and biocompatible electronics, where heterogeneous components are required to be transfer-printed onto unconventional substrates materials. nTP tapes show a higher reliability thanks to the stronger adhesion achievable between tape and ink, furthermore tapes can be easily fabricated in a

wide range of materials, allowing their direct implementation also in biocompatible and biodegradable devices.⁴⁸ Figure 3.10c-d show a strain sensor applied to human skin using the tape transfer printing method.⁴⁶

Among the biomaterial employed as transfer tape, direct transfer of metal and fabrication of flexible electronic circuits have been demonstrated using silk^{49,50}. In this thesis, electrical and optically functional architectures of metals and CNTs have been transferred to water-soluble HPC tapes, and deposited at will onto arbitrary substrates (chapter 5, section 5.2).

3.3.4 Template induced assembly

Self-assembly is a bottom-up fabrication technique which takes advantage of the spontaneous aggregation of molecules and nanoparticles, leading to the formation of ordered architectures from randomly allocated single building blocks. The aggregates formed by bottom-up self-assembly possess well defined order at small scales, however uniform patterns over large scales are difficult to achieve due to the formation of multiple domains with different orientations. Top-down fabrication techniques like NIL can provide a straightforward approach to establish regular arrays of well-defined colloidal clusters over large areas.

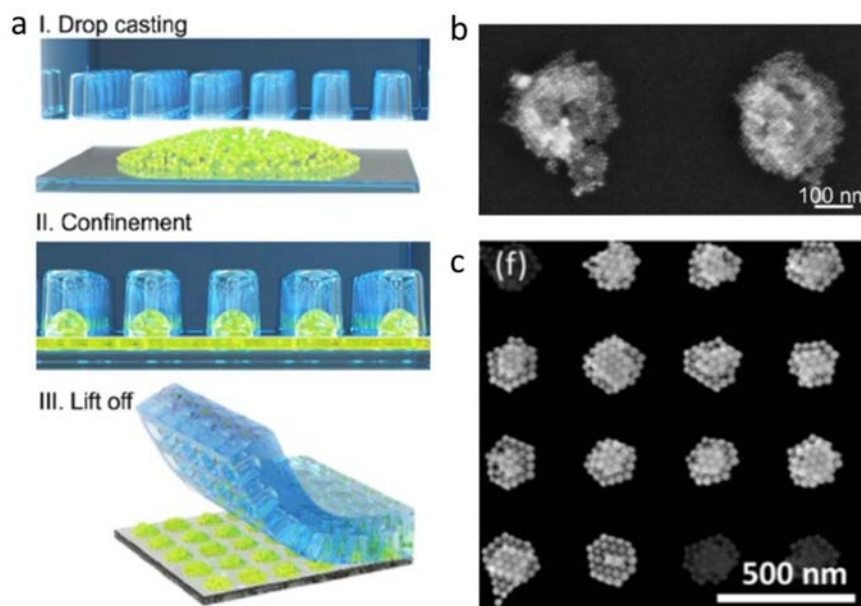


Figure 3.11 Template induced assembly. a) Schematic of the process employ to assembly colloidal CsPbBr₃ nanocrystals. b) SEM image of the clusters assembled as described in (a).⁵¹ c) Gold nanoparticles assembly.⁵²

The use of patterned PDMS molds to assembly of gold colloids into 2D arrays has been reported by the group of L. Marzan and A. Mihi,^{53,54} who developed a template-assisted strategy to assembly gold nanoparticles and nanorods into micrometer and nanometer structures, leading to highly regular plasmonic super crystals (Figure 3.11c) with improved SERS response.⁵² Successful assembly of active materials such as colloidal CsPbBr₃ nanocrystals (NC) has also been demonstrated in our group (Figure 3.11a-b), showing amplified spontaneous emission under lower optical excitation of the superlattice arrangement in contrast to equivalent flat NC films.⁵¹

3.4 Environmental and economic impact of lithography

The substitution of oil-based materials with ecofriendly alternatives has paved the way to the green electronic field, exponentially powering the biomaterial research. Nevertheless, the intensive use and release of hazardous chemicals generated during electronic manufacturing often remains a hidden detail when addressing the environmental impact of electronic devices fabrication. This problem mostly affects Southeast Asia countries (where most manufacturing plants are located) and represents one the largest sources of pollution in the production of electronic devices, with serious consequences for the surrounding environment. To give an example Figure 3.12 shows the estimated greenhouse gas emissions in a

smartphone lifecycle, where it can be seen that the largest contribution is by far due to its fabrication.⁵⁵ Defining new ecofriendly fabrication processes that employs non-toxic material would be extremely beneficial to reduce the environmental impact of electronic mass production. Specifically, in order to fabricate a single, 2 milligram chip it, it is necessary to use 35 kg of water 1,6 kg fossil fuels and 78 g of chemicals.⁵⁶ If we consider the huge amount of electronic components that are manufactured every day, it can be estimated that an electronic manufacturing plant uses anywhere between 2 to 4 million gallons of ultra-pure water per day, which is roughly equivalent to the water usage of a city of 40 000 people.⁵⁷ As suggested by a study on the fabrication of dynamic random access memory (DRAM) between 12% and 25% of the environmental impact (depending on the impact assessment method) of microchips fabrication could be attributed to photolithography.⁵⁸ In particular, during the chip fabrication, 30% of the total chemical consumption is due the lithographic process - this impact is easy to understand if we consider the huge number of photolithographic cycles that are required to fabricate the sub 10 nm features that are currently employed in modern transistors. Highly toxic and corrosive solvents are typically necessary to process standard light or electron sensitive resist materials. Figure 3.12b shows the standard system for the identification of the hazards of materials for emergency response (from the national fire protection association, USA) of some of the commonly employed solvents and resist in our group at ICMAB. The development of a cleaner nanofabrication process that employs non-toxic materials would be beneficial from an environmental point of view, for the worker health protection, and would decrease the costs of disposal of chemical residues.

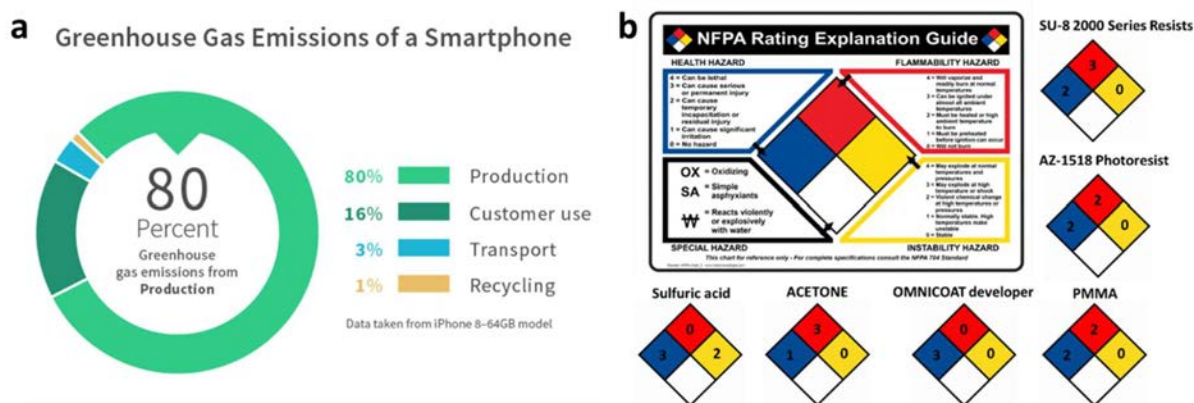


Figure 3.12 a) Green gas emission in a smartphone lifecycle.⁵⁵ b) NFPA hazard chart of some of the solvents and resist employed in our group at ICMAB.

From an economical point of view, current lithographic techniques present several limitations that compromise the downscaling of transistor size. The price for processed wafers has experienced a peak

increase with transistor size dropping below 32 nm,⁵⁹ as can be seen from the chart in Figure 3.13a. This is mostly due to the higher complexity of lithographic processes required to obtain smaller features (Figure 3.13b).⁶⁰

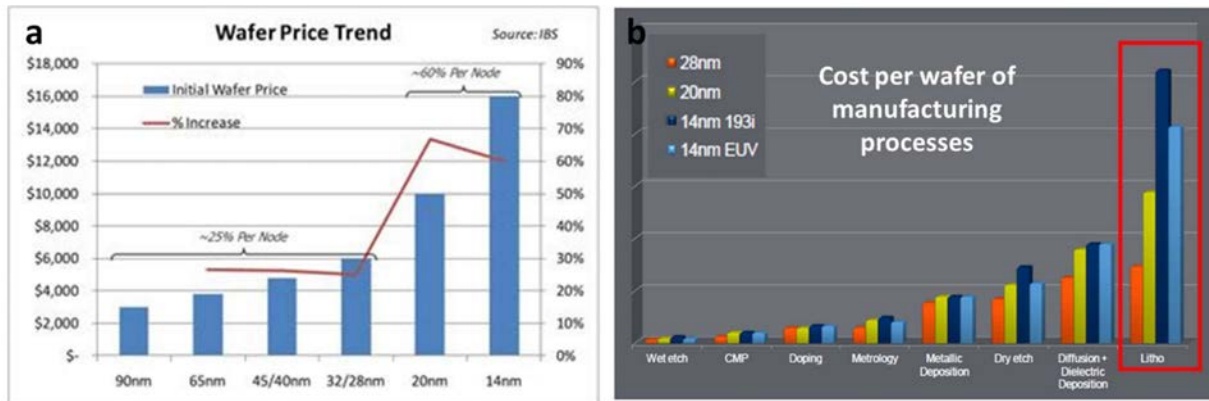


Figure 3.13 a) IC wafer price increase vs technology nodes.⁵⁹ b) Impact of lithography on the wafer cost.⁶⁰

Overall, nanoimprint lithography represents a valid alternative to standard lithographic technique not only because it is not light diffraction limited and suitable for large scale processing, but also because it allows the low cost patterning a wider range of more eco-friendly and less hazardous materials. Those characteristics makes NIL and soft lithographic techniques excellent candidates to pursue a bifold purpose.

- Providing novel functionalities to biomaterials for their implementation in next generation eco-friendly and biocompatible devices.
- Enable the employment of non-toxic material and solvents (e.g. water) as tool for eco-friendly fabrication process in electronic manufacturing.

Table 2 summarize the main advantages and disadvantages of the different lithographic techniques illustrated in this chapter, enhancing their applicability conditions for the patterning of bio-based materials.

Table 2. Advantages and drawbacks of current lithographic techniques

TECHNIQUE	RESOLUTION (nm)	ADAVNTAGES	DRAWBACKS	BIO RESIST COMPATIBILITY
Photolithography	200-10 (Extreme ultraviolet)	High throughput Widely employed	Low resolution or high cost Requires photomasks	Requires photosensitive or chemical amplified resists
Interference lithography	200-10 (Extreme ultraviolet)	Mask less Medium resolution	Limited to periodic patterns	Requires photosensitive or chemically amplified resists
E-beam	5-10	High resolution Direct write	Low throughput High cost	Requires electron sensitive resists
Ion beam	5	High resolution Direct write Milling	Low throughput High cost	Requires electron sensitive resists
Thermal Nanoimprinting	1-10	High resolution High throughput Low cost	Hard master degradation, and complex demolding	Suitable for photosensitive, thermoformable or soluble material.
Soft nanoimprinting	1-10	High resolution High throughput Low cost Curved surfaces	Soft Mold susceptibility to deformation	Suitable for photosensitive, thermoformable or soluble material.
Microcontact printing	50-100	Low cost Curved surfaces Chemical patterning	Lower resolution compared to NIL Non-topographic patterning	Suitable for liquid inks or chemical pick-up
Transfer printing	<10	Low cost Curved surfaces High-throughput Assembly of material with process incompatibility	Requires materials with switchable adhesion, or sacrificial tapes.	Integration of functional materials into arbitrary substrates. Possibility to directly integrate components into biomaterials
Template assembly		Hierarchical order Low cost	Low throughput	Mostly employed for nanoparticles assembly

3.5 References

- (1) Samsung Foundry. *Samsung Successfully Completes 5nm EUV Development to Allow Greater Area Scaling and Ultra-low Power Benefits*. **16/04/2019**. https://www.samsungfoundry.com/foundry/homepage/anonymous/homPressView.do?_mainLayout=homepageLayout&menuIndex=0501&pressId=327.
- (2) Bogdan Solca. *TSMC already sampling Apple's 5 nm A14 Bionic SoCs for 2020 iPhones*. **10/22/2019**. <https://www.notebookcheck.net/TSMC-already-sampling-Apple-s-5-nm-A14-Bionic-SoCs-for-2020-iPhones.440058.0.html>.
- (3) Wolfberger, A.; Petritz, A.; Fian, A.; Herka, J.; Schmidt, V.; Stadlober, B.; Kargl, R.; Spirk, S.; Griesser, T. Photolithographic patterning of cellulose: a versatile dual-tone photoresist for advanced applications. *Cellulose* **2015**, *22* (1), 717–727. DOI: 10.1007/s10570-014-0471-4.

- (4) Zhou, Y.; Li, Y.; Dunder, F.; Carter, K. R.; Watkins, J. J. Fabrication of patterned cellulose film via solvent-assisted soft nanoimprint lithography at a submicron scale. *Cellulose* **2018**, *25* (9), 5185–5194. DOI: 10.1007/s10570-018-1920-2.
- (5) Qi, A.; Hoo, S. P.; Friend, J.; Yeo, L.; Yue, Z.; Chan, P. P. Y. Hydroxypropyl cellulose methacrylate as a photo-patternable and biodegradable hybrid paper substrate for cell culture and other bioapplications. *Advanced healthcare materials* **2014**, *3* (4), 543–554. DOI: 10.1002/adhm.201300155.
- (6) Ji, S.; Hyun, B. G.; Kim, K.; Lee, S. Y.; Kim, S.-H.; Kim, J.-Y.; Song, M. H.; Park, J.-U. Photo-patternable and transparent films using cellulose nanofibers for stretchable origami electronics. *NPG Asia Mater* **2016**, *8* (8), e299-e299. DOI: 10.1038/am.2016.113.
- (7) Kurland, N. E.; Dey, T.; Kundu, S. C.; Yadavalli, V. K. Precise patterning of silk microstructures using photolithography. *Adv. Mater.* **2013**, *25* (43), 6207–6212. DOI: 10.1002/adma.201302823.
- (8) Park, J.; Lee, S.-G.; Marelli, B.; Lee, M.; Kim, T.; Oh, H.-K.; Jeon, H.; Omenetto, F. G.; Kim, S. Eco-friendly photolithography using water-developable pure silk fibroin. *RSC Adv* **2016**, *6* (45), 39330–39334. DOI: 10.1039/C6RA04516B.
- (9) Revzin, A.; Tompkins, R. G.; Toner, M. Surface Engineering with Poly(ethylene glycol) Photolithography to Create High-Density Cell Arrays on Glass. *Langmuir* **2003**, *19* (23), 9855–9862. DOI: 10.1021/la035129b.
- (10) Hahn, M. S.; Taite, L. J.; Moon, J. J.; Rowland, M. C.; Ruffino, K. A.; West, J. L. Photolithographic patterning of polyethylene glycol hydrogels. *Biomaterials* **2006**, *27* (12), 2519–2524. DOI: 10.1016/j.biomaterials.2005.11.045.
- (11) Yan, J.; Pedrosa, V. A.; Simonian, A. L.; Revzin, A. Immobilizing enzymes onto electrode arrays by hydrogel photolithography to fabricate multi-analyte electrochemical biosensors. *ACS applied materials & interfaces* **2010**, *2* (3), 748–755. DOI: 10.1021/am9007819.
- (12) del Barrio, J.; Sánchez - Somolinos, C. Light to Shape the Future: From Photolithography to 4D Printing. *Adv. Optical Mater.* **2019**, *7* (16), 1900598. DOI: 10.1002/adom.201900598.
- (13) Kim, S.; Marelli, B.; Brenckle, M. A.; Mitropoulos, A. N.; Gil, E.-S.; Tsioris, K.; Tao, H.; Kaplan, D. L.; Omenetto, F. G. All-water-based electron-beam lithography using silk as a resist. *Nature nanotechnology* **2014**, *9* (4), 306–310. DOI: 10.1038/nnano.2014.47.

- (14) Hlawacek, G.; Veligura, V.; van Gastel, R.; Poelsema, B. Helium ion microscopy. *Journal of Vacuum Science & Technology B, Nanotechnology and Microelectronics: Materials, Processing, Measurement, and Phenomena* **2014**, *32* (2), 20801. DOI: 10.1116/1.4863676.
- (15) Kometani, R.; Ishihara, S. Nanoelectromechanical device fabrications by 3-D nanotechnology using focused-ion beams. *Science and Technology of Advanced Materials* **2009**, *10* (3), 34501.
- (16) Jianjuan Jiang; Nan Qin; Tiger H Tao. Nanomanufacturing of biopolymers using electron and ion beams. *Journal of Micromechanics and Microengineering* **2020**, *30* (3), 33001.
- (17) Jiang, B.; Yang, J.; Li, C.; Zhang, L.; Zhang, X.; Yang, P. Water-Based Photo- and Electron-Beam Lithography Using Egg White as a Resist. *Adv. Mater. Interfaces* **2017**, *4* (7), 1601223. DOI: 10.1002/admi.201601223.
- (18) Christman, K. L.; Schopf, E.; Broyer, R. M.; Li, R. C.; Chen, Y.; Maynard, H. D. Positioning multiple proteins at the nanoscale with electron beam cross-linked functional polymers. *Journal of the American Chemical Society* **2009**, *131* (2), 521–527. DOI: 10.1021/ja804767j.
- (19) Takei, S.; Maki, H.; Sugahara, K.; Ito, K.; Hanabata, M. Inedible cellulose-based biomass resist material amenable to water-based processing for use in electron beam lithography. *AIP Advances* **2015**, *5* (7), 77141. DOI: 10.1063/1.4927210.
- (20) Henniges, U.; Hasani, M.; Potthast, A.; Westman, G.; Rosenau, T. Electron Beam Irradiation of Cellulosic Materials-Opportunities and Limitations. *Materials (Basel, Switzerland)* **2013**, *6* (5), 1584–1598. DOI: 10.3390/ma6051584.
- (21) Ganner, T.; Sattelkow, J.; Rumpf, B.; Eibinger, M.; Reishofer, D.; Winkler, R.; Nidetzky, B.; Spirk, S.; Plank, H. Direct-Write Fabrication of Cellulose Nano-Structures via Focused Electron Beam Induced Nanosynthesis. *Scientific reports* **2016**, *6*, 32451. DOI: 10.1038/srep32451.
- (22) Rawlings, C. D.; Kulmala, T. S.; Spieser, M.; Holzner, F.; Glinsner, T.; Schleunitz, A.; Bullerjahn, F. Single-nanometer accurate 3D nanoimprint lithography with master templates fabricated by NanoFrazor lithography. In *Novel Patterning Technologies 2018:26 February-1 March 2018, San Jose, California, United States / Eric M. Panning, Martha I. Sanchez, editors*; Panning, E. M., Sanchez, M. I., Eds.; SPIE: Bellingham, Washington, USA, 2018; p 37. DOI: 10.1117/12.2305905.
- (23) Hua, F.; Sun, Y.; Gaur, A.; Meitl, M. A.; Bilhaut, L.; Rotkina, L.; Wang, J.; Geil, P.; Shim, M.; Rogers, J. A.; Shim, A. Polymer Imprint Lithography with Molecular-Scale Resolution. *Nano Lett.* **2004**, *4* (12), 2467–2471. DOI: 10.1021/nl048355u.

- (24) Chou, S. Y. Nanoimprint lithography. *J. Vac. Sci. Technol. B* **1996**, *14* (6), 4129. DOI: 10.1116/1.588605.
- (25) Amsden, J. J.; Domachuk, P.; Gopinath, A.; White, R. D.; Negro, L. D.; Kaplan, D. L.; Omenetto, F. G. Rapid nanoimprinting of silk fibroin films for biophotonic applications. *Adv. Mater.* **2010**, *22* (15), 1746–1749. DOI: 10.1002/adma.200903166.
- (26) Ken-ichiro Nakamatsu; Katsuhiko Tone; Shinji Matsui. Nanoimprint and Lift-Off Process Using Poly(vinyl alcohol). *Japanese Journal of Applied Physics* **2005**, *44* (11), 8186–8188.
- (27) Park, I.; Cheng, J.; Pisano, A. P.; Lee, E.-S.; Jeong, J.-H. Low temperature, low pressure nanoimprinting of chitosan as a biomaterial for bionanotechnology applications. *Appl. Phys. Lett.* **2007**, *90* (9), 93902. DOI: 10.1063/1.2709914.
- (28) Mäkelä, T.; Kainlauri, M.; Willberg-Keyriläinen, P.; Tammelin, T.; Forsström, U. Fabrication of micropillars on nanocellulose films using a roll-to-roll nanoimprinting method. *Microelectronic Engineering* **2016**, *163*, 1–6. DOI: 10.1016/j.mee.2016.05.023.
- (29) Mäkelä, T.; Haatainen, T.; Ahopelto, J. Roll-to-roll printed gratings in cellulose acetate web using novel nanoimprinting device. *Microelectronic Engineering* **2011**, *88* (8), 2045–2047. DOI: 10.1016/j.mee.2011.02.016.
- (30) Fehrman Cory, E. M.; Aga, R. S.; Lombardi, J. P.; Bartsch, C. M.; Sarangan, A.; Heckman, E. M. Nanoimprint lithography of deoxyribonucleic acid biopolymer films. *J. Micro/Nanolith. MEMS MOEMS* **2013**, *12* (4), 40501. DOI: 10.1117/1.JMM.12.4.040501.
- (31) Austin, M. D.; Ge, H.; Wu, W.; Li, M.; Yu, Z.; Wasserman, D.; Lyon, S. A.; Chou, S. Y. Fabrication of 5nm linewidth and 14nm pitch features by nanoimprint lithography. *Appl. Phys. Lett.* **2004**, *84* (26), 5299–5301. DOI: 10.1063/1.1766071.
- (32) Xia, Y.; Whitesides, G. M. SOFT LITHOGRAPHY. *Annual Review of Materials Science* **1998**, *28* (1), 153–184. DOI: 10.1146/annurev.matsci.28.1.153.
- (33) Bhingardive, V.; Menahem, L.; Schwartzman, M. Soft thermal nanoimprint lithography using a nanocomposite mold. *Nano Res.* **2018**, *11* (5), 2705–2714. DOI: 10.1007/s12274-017-1900-0.
- (34) Molet, P.; Gil-Herrera, L. K.; Garcia-Pomar, J. L.; Caselli, N.; Blanco, Á.; López, C.; Mihi, A. Large area metasurfaces made with spherical silicon resonators. *Nanophotonics* **2020**, *9* (4), 943–951. DOI: 10.1515/nanoph-2020-0035.

- (35) Alom Ruiz, S.; Chen, C. S. Microcontact printing: A tool to pattern. *Soft matter* **2007**, *3* (2), 168–177. DOI: 10.1039/b613349e.
- (36) Bhushan, B., Ed. *Springer handbook of nanotechnology*, 2nd rev. & extended ed.; Springer, 2007. DOI: 10.1007/978-3-540-29857-1.
- (37) Kaufmann, T.; Ravoo, B. J. Stamps, inks and substrates: polymers in microcontact printing. *Polym. Chem.* **2010**, *1* (4), 371. DOI: 10.1039/b9py00281b.
- (38) Menard, E.; Rogers, J. Stamping Techniques for Micro- and Nanofabrication. In *Springer handbook of nanotechnology*, 2nd rev. & extended ed.; Bhushan, B., Ed.; Springer, 2007; pp 279–298. DOI: 10.1007/978-3-540-29857-1_9.
- (39) Quist, A. P.; Pavlovic, E.; Oscarsson, S. Recent advances in microcontact printing. *Analytical and bioanalytical chemistry* **2005**, *381* (3), 591–600. DOI: 10.1007/s00216-004-2847-z.
- (40) Briseno, A. L.; Mannsfeld, S. C. B.; Ling, M. M.; Liu, S.; Tseng, R. J.; Reese, C.; Roberts, M. E.; Yang, Y.; Wudl, F.; Bao, Z. Patterning organic single-crystal transistor arrays. *Nature* **2006**, *444* (7121), 913–917. DOI: 10.1038/nature05427.
- (41) Offenhäusser, A.; Böcker-Meffert, S.; Decker, T.; Helpenstein, R.; Gasteier, P.; Groll, J.; Möller, M.; Reska, A.; Schäfer, S.; Schulte, P.; Vogt-Eisele, A. Microcontact printing of proteins for neuronal cell guidance. *Soft matter* **2007**, *3* (3), 290–298. DOI: 10.1039/b607615g.
- (42) Jang, M. J.; Kim, W. R.; Joo, S.; Ryu, J. R.; Lee, E.; Nam, Y.; Sun, W. Cell-Type Dependent Effect of Surface-Patterned Microdot Arrays on Neuronal Growth. *Frontiers in neuroscience* **2016**, *10*, 217. DOI: 10.3389/fnins.2016.00217.
- (43) Zhiqing Xin; Yu Liu; Xiu Li; Shili Liu; Yi Fang; Yongqiang Deng; Chao Bao; Luhai Li. Conductive grid patterns prepared by microcontact printing silver nanoparticles ink. *Materials Research Express* **2017**, *4* (1), 15021.
- (44) Meitl, M. A.; Zhu, Z.-T.; Kumar, V.; Lee, K. J.; Feng, X.; Huang, Y. Y.; Adesida, I.; Nuzzo, R. G.; Rogers, J. A. Transfer printing by kinetic control of adhesion to an elastomeric stamp. *Nature Mater* **2006**, *5* (1), 33–38. DOI: 10.1038/nmat1532.
- (45) Zaumseil, J.; Meitl, M. A.; Hsu, J. W. P.; Acharya, B. R.; Baldwin, K. W.; Loo, Y.-L.; Rogers, J. A. Three-Dimensional and Multilayer Nanostructures Formed by Nanotransfer Printing. *Nano Lett.* **2003**, *3* (9), 1223–1227. DOI: 10.1021/nl0344007.

- (46) Yeo, W.-H.; Kim, Y.-S.; Lee, J.; Ameen, A.; Shi, L.; Li, M.; Wang, S.; Ma, R.; Jin, S. H.; Kang, Z.; Huang, Y.; Rogers, J. A. Multifunctional epidermal electronics printed directly onto the skin. *Adv. Mater.* **2013**, *25* (20), 2773–2778. DOI: 10.1002/adma.201204426.
- (47) Linghu, C.; Zhang, S.; Wang, C.; Song, J. Transfer printing techniques for flexible and stretchable inorganic electronics. *npj Flex Electron* **2018**, *2* (1). DOI: 10.1038/s41528-018-0037-x.
- (48) Kim, K.; Kim, B.; Lee, C. H. Printing Flexible and Hybrid Electronics for Human Skin and Eye-Interfaced Health Monitoring Systems. *Adv. Mater.* **2020**, *32* (15), e1902051. DOI: 10.1002/adma.201902051.
- (49) Lin, D.; Tao, H.; Trevino, J.; Mondia, J. P.; Kaplan, D. L.; Omenetto, F. G.; Dal Negro, L. Direct transfer of subwavelength plasmonic nanostructures on bioactive silk films. *Adv. Mater.* **2012**, *24* (45), 6088–6093. DOI: 10.1002/adma.201201888.
- (50) Kim, D.-H.; Kim, Y.-S.; Amsden, J.; Panilaitis, B.; Kaplan, D. L.; Omenetto, F. G.; Zakin, M. R.; Rogers, J. A. Silicon electronics on silk as a path to bioresorbable, implantable devices. *Appl. Phys. Lett.* **2009**, *95* (13), 133701. DOI: 10.1063/1.3238552.
- (51) Vila-Liarte, D.; Feil, M. W.; Manzi, A.; Garcia-Pomar, J. L.; Huang, H.; Döblinger, M.; Liz-Marzán, L. M.; Feldmann, J.; Polavarapu, L.; Mihi, A. Templated-Assembly of CsPbBr₃ Perovskite Nanocrystals into 2D Photonic Supercrystals with Amplified Spontaneous Emission. *Angewandte Chemie (International ed. in English)* **2020**. DOI: 10.1002/anie.202006152.
- (52) Matricardi, C.; Hanske, C.; Garcia-Pomar, J. L.; Langer, J.; Mihi, A.; Liz-Marzán, L. M. Gold Nanoparticle Plasmonic Superlattices as Surface-Enhanced Raman Spectroscopy Substrates. *ACS Nano* **2018**, *12* (8), 8531–8539. DOI: 10.1021/acsnano.8b04073.
- (53) Charconnet, M.; Kuttner, C.; Matricardi, C.; Mihi, A.; Liz-Marzán, L. M.; Seifert, A. Tunable Plasmonics by Self-Assembled Stretchable Superlattices on Macroscopic Scale. In *OMN 2019:2019 International Conference on Optical MEMS and Nanophotonics : proceedings : July 28-August 1, 2019, KAIST, Daejeon, Korea*, IEEE: [Piscataway, New Jersey], 2019; pp 14–15. DOI: 10.1109/OMN.2019.8925038.
- (54) García-Lojo, D.; Núñez-Sánchez, S.; Gómez-Graña, S.; Grzelczak, M.; Pastoriza-Santos, I.; Pérez-Juste, J.; Liz-Marzán, L. M. Plasmonic Supercrystals. *Accounts of chemical research* **2019**, *52* (7), 1855–1864. DOI: 10.1021/acs.accounts.9b00213.
- (55) Gary Cook and Elizabeth Jardim. *Guide to Greener Electronics 2017*. **2017**. <https://www.greenpeace.org/usa/reports/greener-electronics-2017/#hidden-costs>.

(56) Williams, E. D.; Ayres, R. U.; Heller, M. The 1.7 kilogram microchip: energy and material use in the production of semiconductor devices. *Environmental science & technology* **2002**, *36* (24), 5504–5510.

DOI: 10.1021/es025643o.

(57) Ting Sun. *Semiconductor Manufacturing Plants can use as much water as a small city - IEEE spectrum*. IEEE spectrum - Engineers of the New Millennium: The Global Water Challenge Special Report, 2009. <https://spectrum.ieee.org/podcast/semiconductors/design/semiconductor-manufacturing-plants-can-use-as-much-water-as-a-small-city>.

(58) Liu, C. H.; Lin, S. J.; Lewis, C. Life cycle assessment of DRAM in Taiwan's semiconductor industry. *Journal of Cleaner Production* **2010**, *18* (5), 419–425. DOI: 10.1016/j.jclepro.2009.10.004.

(59) Flamm, K. Measuring Moore's law: evidence from price, cost, and quality indexes. In *Measuring and Accounting for Innovation in the 21st Century*; University of Chicago Press, 2019.

(60) Subi Kengeri. *Assessing the Threats to Semiconductor Growth: Technology Limitations versus Economic Realities*. **2012**. https://sst.semiconductor-digest.com/chipworks_real_chips_blog/author/insights-from-leading-edge/.

CHAPTER 4

Soft nanoimprinting optimization

Design, rules, materials and tools

The soft lithography process can be split into two steps:

- The fabrication of an elastomeric stamp with engineered relief structures,
- Its implementation in order to transfer those geometries to a target material.

In this chapter, the experimental details of these two main process steps are presented. Common issues and optimization strategies developed throughout this thesis are discussed, elucidating the key concepts necessary for the accurate designing of imprinting molds and for their correct employment in hot embossing of thermoformable polymers.

4.1 Replica molding process

Replica molding (RM) is a nanofabrication process in which, a raw material in the liquid or pliable state (precursor) is shaped by casting it into a solid “master” template. After filling of the master’s features, the liquid precursors, are solidified by chemical crosslinking, by solvent evaporation or hardened by cooling down the temperature and, once separated from the rigid template, they will retain the negative shape of the original pattern. The advantages of replica molding are that starting from a single master, many replicas can be rapidly generated and that the replicas can be made of different materials, allowing to obtain inexpensive copies of the original master template. The process schematics is illustrated in Figure 4.1.



Figure 4.1: Schematics of the replica molding process. a) casting of the liquid precursor onto the master template. b) Solidification of the liquid precursor. c) Release of the replicated soft mold.

Depending on the master and mold material it might be necessary to first coat the master surface with an antisticking layer, to avoid chemical bonding at the interface and reduce the friction upon demolding. In the case of silicon templates, they are typically functionalized with a self-assembled monolayer of a passivating molecules, such as 1H,1H,2H,2Hperfluorooctyl-trichlorosilane (PFOTS).

In this thesis replica molding process has been used to fabricate PDMS molds (see section 4.2.3) employed in soft lithographic processes and patterned HPC membrane, as illustrated in chapter 5, section 5.1.

4.2 Molds fabrication

Master templates employed for mold fabrication are usually rigid (silicon, glass or metallic) stamps which have been patterned by high resolution lithographic techniques, typically e-beam or interference lithography. The most notably used material for the fabrication of soft mold is by far Polydimethylsiloxane (PDMS), a silicon elastomer which is relatively low-cost, optically transparent, has a low interfacial free energy, is chemically inert, has good gas permeability and good thermal stability. The surface properties of PDMS are also relatively easy to modify, and PDMS molds can be used multiple times, in fast and straightforward soft lithographic process as explained in section 3.3.

This section addresses some of the common issues encountered in the replica molding of nanostructured templates with high resolution and high aspect ratio features and discusses the strategies that can be employed to overcome these limitations. The following experimental data, are based on molds fabricated with two types of PDMS with different ranges of stiffness:

- Soft PDMS (sPDMS, Young modulus $E=0.1-5$ MPa), commercialized by Dow Corning as Sylgard184.
- Hard PDMS (hPDMS, Young modulus $E=9-11$ MPa), commercialized by Alfa Aesar.

With the exception of the high aspect ratio (HAR) patterns shown in Figure 4.6 where I used SU8 photoresist (manufactured by Microchem, young modulus 1.5 GPa). To define the patterns geometries, I will use the abbreviation illustrated in Figure 4.2.

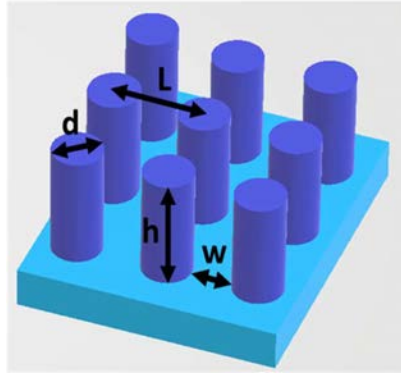


Figure 4.2. List of abbreviation used in this chapter to define the patterns geometry. w = pillar spacing, L = lattice parameter, d = pillar diameter, h = pillar height

4.2.1 Pattern resolution

The resolution of replica molding depends on the ability of the mold liquid precursor to faithfully retrace the geometry of the master pattern, being capable to completely fill all the cavities present in the pattern and to maintain the relief once solidified. There are two main issue that can limit the resolution of the replica:

- Prepolymer viscosity and wetting capability of the master material
- Surface tension of the mold material once solidified.

Precursor viscosity

It is well known that PDMS prepolymer has relatively high viscosity (3900 mPa·s for Sylgard 184), however this issue can be easily addressed by diluting PDMS liquid precursor in chloroform or toluene, as it has been described by Hyewon Kang et al.¹ Figure 4.3 shows the effect of 60% PDMS prepolymer dilution in toluene on the replication of two pillar arrays with pillars spacing w of 200 and 100 nm. In the case of non-diluted PDMS successful replica can be obtained for the $w=200$ nm sample ($L=500$ nm, Figure 4.3b). When the spacing between pillar decreases to 100 nm ($L=400$, Figure 4.3c) the viscosity of the PDMS prepolymer is too high to allow complete filling of the template cavities. As a result, the mold presents a distorted pattern where the PDMS only percolated in the space corresponding to the lattice diagonals. The results obtained using the same master pattern but after 60% toluene dilution are illustrated in Figure 4.3d, showing a perfectly replicated array of holes.

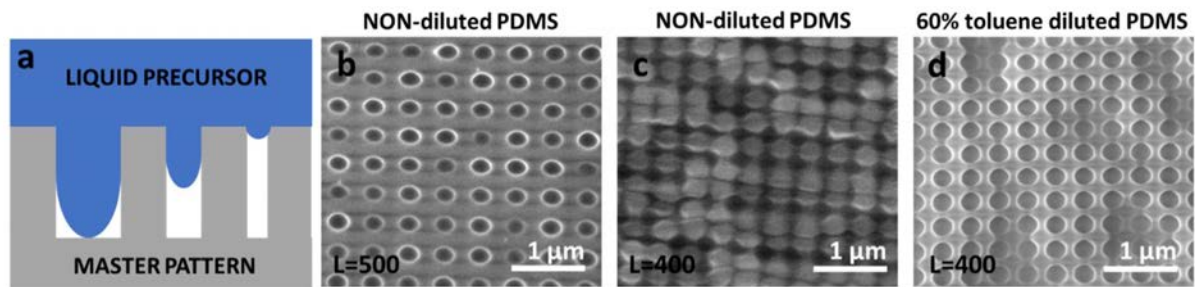


Figure 4.3. a) Schematic representation of Influence of PDMS prepolymer viscosity on the replica molding resolution of pillar arrays with varying lattice parameter. b) SEM image of non-diluted PDMS replica of a in which $w=200$ nm ($L=500$, $d=300$). c) Non-diluted PDMS replica of a pattern with $w=100$ nm ($L=400$, $d=300$). d) Same replica of the geometry used in c obtained with a 60% dilution of the PDMS prepolymer in toluene.

Surface tension of soft materials

Surface tension can intensively affect the pattern resolution, depending on the mold material stiffness. The low stiffness materials which are required in soft lithographic process are inevitably characterized by a high susceptibility to deformation. As previously discussed, this characteristic is a great advantage for many applications, however, it can also represent a limiting factor, since the intrinsic softness of the mold material can lead to undesired distortion of the replicated features. In the case of soft PDMS, for instance, even if surface energy is quite low (22 mN/m), its effective surface tension can compromise the definition of sub micrometer patterns.¹⁻³ This is particularly true for features presenting sharp or pointing edges, where surface tension tends to minimize the area of interfaces resulting in smoothed and rounded features. Figure 4.4 shows the different resolutions obtained using higher (hPDMS) or lower (sPDMS) stiffness modulus PDMS for the replication of an antireflection coating consisting in a hexagonal array of cones with base diameter of 300 nm and cone height of 370 nm. sPDMS molds ($E=1.5$ MPa) led to low resolution replica, with cones height of only 235 nm. The same replica fabricated using a hPDMS ($E=9$ MPa) resulted instead in cones height of 375 nm, equal to the original master geometry.

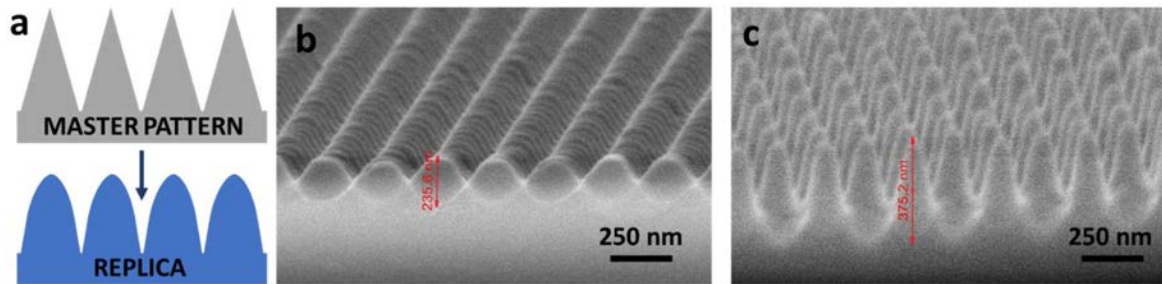


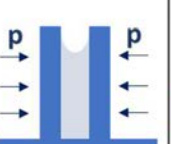
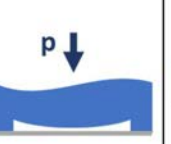
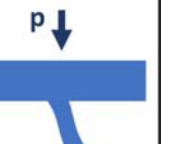


Figure 4.4 a) Schematic of the effect of silicone mold stiffness on the replica resolution of sharp features (hexagonal array of cones) b) soft PDMS replica - young modulus 1 MPa. c) hard PDMS replica - young modulus 10 MPa.

4.2.2 Pattern mechanical instabilities

In addition to the fidelity of the replicas respect to the master features, another fundamental issue that is strongly influenced by the mold material stiffness is the mechanical stability of the pattern. Mold materials must be appropriately chosen to provide not only stamp flexibility but also enough stiffness to the pattern relief features that will have to withstand both internal and external stresses. Surface adhesion forces, capillary forces due to the presence of liquid phases and external forces involved in the printing process, are indeed common causes of different types of mechanical instabilities that often affect the patterns of soft lithographic molds. These types of instabilities are likely to occur with features consisting in high aspect ratio protrusions (rather the cavities) and they can cause severe deformation of the pattern (pattern collapse). In order to understand the way these instabilities arise, I analyze in this section the common failure mechanism of high aspect ratio pillars arrays, discussing the conditions that lead to mechanical instabilities, the different way they affect the patterns, and providing useful design criteria to fabricate mechanically stable, high aspect ratio arrays. The different mechanisms of pattern collapse can be divided in: surface adhesion, capillary force, and imprinting pressure driven instabilities, and their typical effects are illustrated in Table 3.

Table 3. Schematic summary of typical pattern mechanical failure mechanisms in soft mold.

CAUSE	Surface adhesion forces		Imprinting pressure		
EFFECT	Ground collapse	Lateral collapse		Roof collapse	Buckling
SCHEMATIC					
	i	ii	iii	iv	v

Surface adhesion driven instabilities

As the feature dimension decreases, the ratio between surface areas to volumes increases, and surface adhesive forces become significant. For certain pillar geometries, if the mold material is too soft, the adhesion force between a pillar and substrate can become dominating over the pillar elastic energy, causing the pillar to “**ground collapse**” (GC), which means that the pillar bends toward the substrate (see Table 3. Schematic summary of typical pattern mechanical failure mechanisms in soft mold. Table 3, i). The condition to avoid the ground collapse has been estimated by Roca-Cusachs⁴ and co-workers by balancing the elastic energy of the pillar when bended toward the substrate with the energy of adhesion to the substrate, obtaining the critical aspect ratio $(h/d)_{cGC}$ reported in Equation 4.1.

$$\left(\frac{h}{d}\right)_{cGC} = \frac{\pi^{5/3}}{2^{11/2} 3^{1/2}} (1 - \nu^2)^{-1/6} \left(\frac{E}{2\gamma_s}\right)^{2/3} \quad (4.1)$$

In which, ν Poisson’s ratio and γ_s is surface energy of the material, E is the stiffness modulus (or Young modulus).

Besides collapsing to the ground, another common deformation occurring especially in dense arrays of pillars is the so-called “**lateral collapse**”, in which two or more adjacent pillars bend laterally and adhere to the each other (see Table 3. Schematic summary of typical pattern mechanical failure mechanisms in soft

Table 3, ii). To prevent lateral collapse, a stability condition has been obtained by Glassmaker and co-workers⁵ by balancing the elastic energy of bending, the energy of deformation required for pillars to adhere over a finite area and the energy of adhesion, obtaining the critical aspect ratio $(h/d)_{cLC}$ reported in Equation 4.2.

$$\left(\frac{h}{d}\right)_{cLC} = \left(\frac{3^{3/4}\pi E w^{3/2}}{2^{1/4} \cdot 32\gamma_s(1-\nu^2)^{1/4}d^{1/2}}\right)^{1/3} \quad (4.2)$$

In which w is the distance between the pillars and ν , γ_s , E , the previously defined magnitudes.

As can be inferred by Eq. 4.1 the stability condition to avoid the ground collapse only depends on the materials properties (surface energy γ_s and stiffness E) and on the pillar diameter d . Given a certain material, the smaller the diameter, the smaller the lower the pillar aspect ratio achievable. On the other hand, the stability condition to avoid the lateral collapse depends also on the inter-pillar distance w . In order to have stable patterns of pillars, both conditions should be satisfied. Figure 4.5 shows how these two instability mechanisms affect the deformation of soft PDMS ($E=1.5$ MPa, $\gamma_s=0.22$ N/m) pillars arrays. To do so, I compare the stability conditions predicted from equations 1 and 2 with the experimental results obtained replicating three different pillar arrays with the following geometries:

Sample	L [nm]	D [nm]	h [nm]
A	400	300	400
B	500	300	400
C	600	330	400

- **Sample A**

For pillar array with $L= 400$ nm (Figure 4.5a,d) the pattern geometry presents the smallest pillar spacing $w =L-d = 100$ nm and the dominant mechanism of instability is the lateral collapse. This can be clearly seen by the SEM image in which the pillars appear laterally adhered to each other forming domains that range from groups of four pillar to some tens.

- **Sample B**

For the pillar array with $L=500$ ($w=200$) in Figure 4.5b,e it is possible to observe instead a mixed collapsing behavior. This pillar geometry falls between lateral collapse regime and ground collapse regime, and the SEM image shows indeed some area in which the pillars are individually laying on the substrate (ground collapsed), and some areas in which the pillars are laterally collapsed on each other, but in smaller groups compared to the L400 sample.

- **Sample C**

Finally, for the pillar array with $L=600$ ($w=270$) the main mechanism of instability is the ground collapse. Here, since the pillar geometry falls slightly inside the stability condition (Figure 4.5c), besides the collapsed areas, it is possible to observe also some domains in which the pillars are stable, as shown by the SEM analysis in Figure 4.5f.

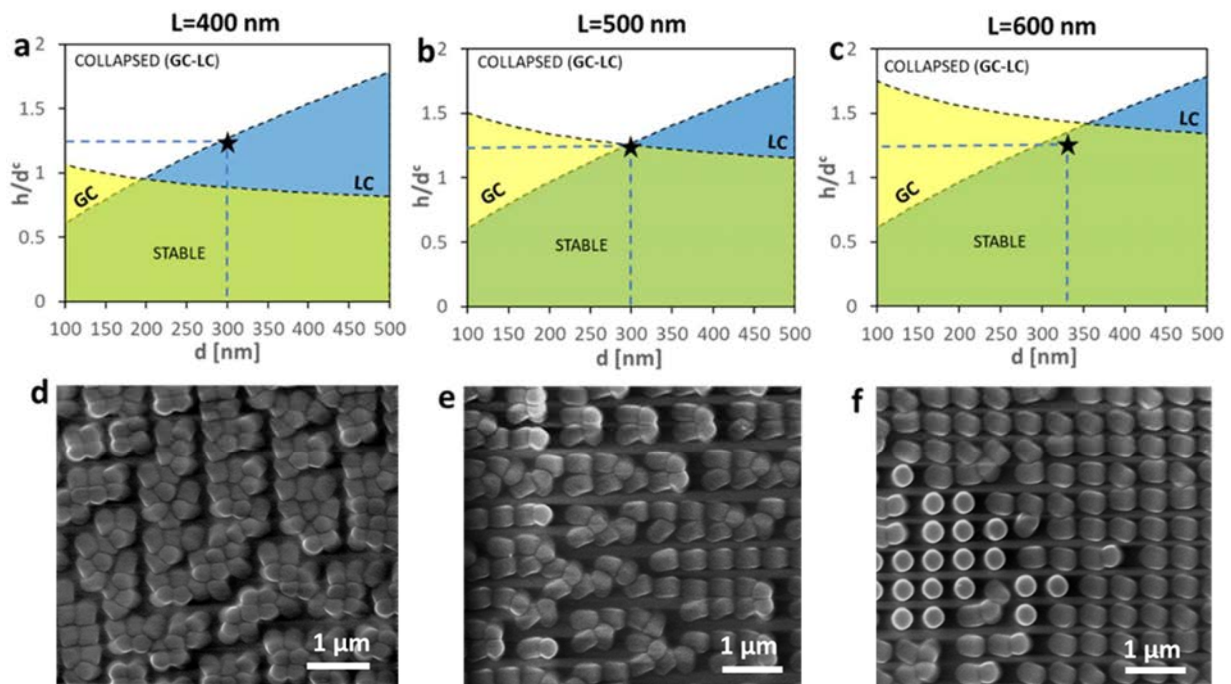


Figure 4.5. Mechanical instabilities generated by surface adhesion forces in soft PDMS pillars array with $(h/d) > 1$. a,b,c) Calculated critical aspect ratios h/d^c vs pillar diameter d . Ground collapse conditions are represented by the yellow areas, lateral collapse conditions by the blue areas. In the white areas the pillars are unstable towards both collapsing modes, while the green area represents the mechanical stability conditions. The black stars identify the aspect ratio h/d and diameter d of the geometries fabricated and (d,e,f) their corresponding SEM images.

Capillary force driven instabilities

Many lithographic methods rely on the use of liquid solvents. For example, in photolithography the pattern is obtained by changing with light the solubility of the resist in specific regions and washing away with

solvent the soluble areas. Also nanoimprinting stamps often require the use of solvents: to rinse the mold after use, to functionalize its surfaces, to pattern resist in liquid solution, or to dissolve the template used for their fabrication. This latter method is particularly employed for the replication of sub 100 nm HAR arrays, such as those obtained by the anodic oxidation of alumina. The extremely high friction generated by the high surface to volume ratio of this kind of patterns, prevents from standard demolding, requiring the employment of sacrificial (destroyable) master templates.^{6,7}

Whenever a solid surface is placed in contact with a liquid phase, capillarity forces generate as a natural tendency of the system to minimize the sum of the liquid-vapor-solid interfacial energies, which can promote mechanical instabilities in the mold features. Capillary forces are typically proportional to the energy of the liquid-vapor interface, but their precise expression and intensity depends on system geometry and on different concurring phenomena such as negative Laplace pressure of capillary bridges, surface tension and interaction of capillary menisci. Detailed analysis and quantification of capillarity forces in pillars arrays goes beyond the scope of this thesis and can be find elsewhere,⁸ however for completeness in this section it is briefly reported the effect of capillarity forces on the lateral collapse of high aspect ratio pillar replicated from porous AAO templates, using a high stiffness, UV curable, SU8 epoxy resin ($E=1.5$ GPa).

In order to replicate AAO porous templates, after casting and hardening of the SU8 resin, to demold the stamp, the AAO template is dissolved in aqueous solution of NaOH to release the stamp. Figure 4.6 shows three different SU8 pillar arrays obtained via replica molding of AAO templates, in which the pores diameter is 90 nm, the lattice parameter L is 125 nm and pores depth are 450 (a), 300 (b) and 150 (c) nm.

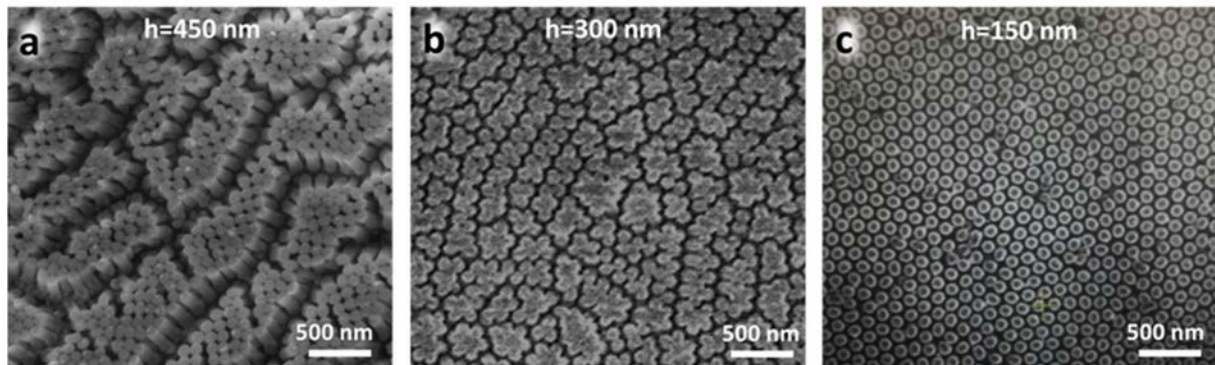


Figure 4.6. SEM pictures of lateral collapse induced by capillarity forces in high aspect ratio SU8 pillars with height of 450 nm (a), 300 nm (b) and 150 nm, obtained by replica molding of anodic alumina oxide templates.

Considering the stability condition for the lateral collapse expressed in equation 2, the maximum aspect ratio theoretically achievable using SU8 ($E=1.5$ GPa, $\gamma_s=0.4$ N/m) should be ≈ 5 (corresponding to $h=450$ nm and $d=90$ nm). However, as can be seen from the SEM analysis, lateral collapse is observed for aspect ratios as low as 2, and pillar clustering in larger and smaller domains is observed for both aspect ratios of 5 and of 3.3 ($h=300$ nm). This behavior has been previously observed in literature,⁸ the lateral collapse can be attributed to capillarity forces generated by the high surface tension of water used for the dissolution of the AAO templates.⁹

Instabilities due to imprinting pressure

Besides the failure mechanisms that can arise from intrinsic stresses (e.g. surface adhesion force), during its operational lifetime, the mold will have to withstand external stresses, particularly, the load pressure applied during the imprinting process. As pointed out by Hui et al¹⁰ high aspect ratio features can collapse when loaded with excessive pressure, resulting in a buckling of the protrusions. On the other hand, applying excessive pressure on molds with sparse, low aspect ratio features can lead to unwanted bending of the mold roof,¹¹ as schematized in table 1. In this thesis we used low pressures (between 0.5 and 2 bars), seldomly causing the arise of those kinds of failures, which have been therefore not further investigated. For illustrative purposes Figure 4.7 reports a cross-sectional view of an array of pillars imprinted in a thin layer of SU8 at an exaggerated pressure of 3 bars, in which the occurrence of pillars buckling is clearly visible.

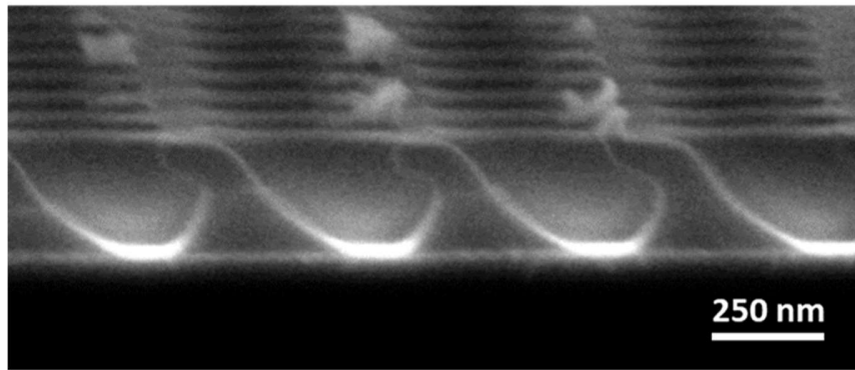


Figure 4.7 SEM picture illustrating the effect of pillars buckling on an imprinted pattern in SU8. Patter geometry is $d = 200$ nm, $L = 500$ nm and $h = 350$ nm.

In this thesis, we used composite molds in which the pattern is made of a thin film of hard PDMS ($E = 9$ MPa), supported by a thicker and flexible soft PDMS ($E = 1.5$ MPa) backbone, obtaining high resolution, mechanically stable and large area patterns. The most challenging features fabricated using this type of mold have been a square array of pillars with holes diameter 120 nm, holes depth 400 nm and lattice parameter of 400 nm, illustrated in chapter 5, section 5.3. Further details about composite mold and reprographic materials are detailed in the next paragraph.

4.2.3 Materials for stamp fabrication

Feature resolution and large area patterning are two main point of interest in any patterning technique. Considering the stability criteria explained in the previous paragraph, the smallest feature size that can be obtained in a mold is largely determined by the stiffness (i.e. the Young modulus) of the mold material. Surface chemistry also plays an important role, since low surface energy pattern are desirable to allow easy demolding and to prevent adhesion collapse. The ability to pattern large areas instead is mostly dependent on the mold flexibility, which must provide conformal contact with the substrate. Considering that any rigid material can become flexible when sufficiently thin, a key strategy in mold fabrication is to design engineered multilayer stamps made of a thin layer of a more rigid material to provide stability to the nanoscale relief features, supported by a thicker, flexible backbone of a softer material to ensure conformal contact.

PMDS is one of the most used materials in the fabrication of lithographic molds. Soft PDMS is commercially available as a 2-component mixture (Sylgard 184), a prepolymer and a curing agent, and it is sufficiently hard ($E = 1-5$ MPa) to transfer most micro-sized features. Furthermore, its mechanical properties can be

easily tuned by changing the components ratio, the curing time and temperature, as illustrated in Figure 4.8a. However, the replication of nanostructures with high aspect ratio requires the employment of harder materials to provide enough mechanical stability to the pattern, as it clearly appears from Figure 4.5. For this reason, PDMS is often employed as soft backbone while tailored formulation of harder silicones with better reprographic properties have been expressively developed for nanofabrication purpose, such as hard PDMS.

The recipe to obtain hard PDMS (young modulus of 9-12 MPa) was established by IBM in 2000,¹² optimizing the chain length and the number of reactive groups in each precursor, in order to obtain the highest crosslinking degree via a platinum catalyzed addition reaction. PDMS variants with even higher modulus up to 80 MPa have been also demonstrated by Verschuuren et al.¹³ who added to the linear molecular chains of standard PDMS precursor a more rigid quaternary branched siloxane precursor.

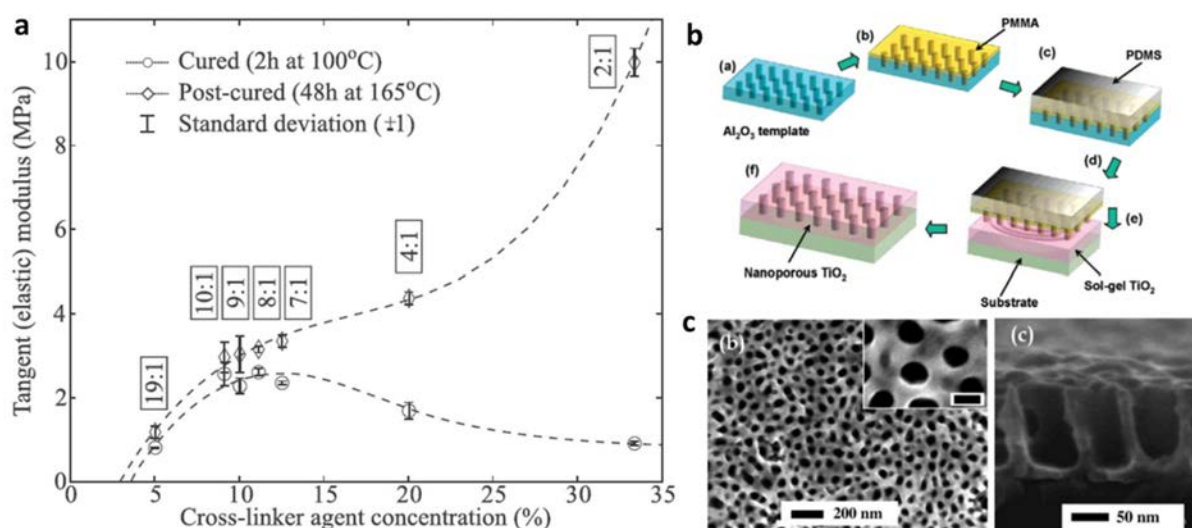


Figure 4.8a) Stiffness of Sylgard 184 PDMS as a function of prepolymer to curing agent mixing ratio and curing process (time and temperature). b-c) Schematic (b) and results obtained nanoimprinting titania sol-gel NPs by with sacrificial PMMA molds made from anodic alumina templates.

Besides PDMS silicones, a wider range of materials have been nowadays implemented for the fabrication of lithographic molds finding applications in different fields. The pattern material indeed can be selected and engineered to comply its reprographic task (high resolution and mechanical stability of the features) but also to provide additional functionalities to the mold. Sacrificial materials like PVA or PMMA present higher stiffness than PDMS and they can be used to fabricate patterns with dense, high aspect ratio arrays that can be later simply dissolved in water or acetone after imprinting, avoiding a complex demolding step, as illustrated in Figure 4.8b-c. Also, UV-curable polymers like Ormstamp, perfluoropolyether (PFPE) or

polyurethane-acrylate (PUA) are frequently employed for high resolution pattern replication, often in combination with polyethylene terephthalate (PET) substrates.¹⁴ This class of materials presents interesting properties such as precursor with very low viscosity¹⁵ high Young modulus^{9,16} (PU, Ormostamp) and a low surface energy (PFPE).¹⁷

In this thesis we fabricated mechanically stable, high resolution and highly flexible composite molds made employing toluene diluted hPDMS and standard sPDMS as backbone. Ormostamp has been extensively used with UV-imprinting technique, obtaining high quality hard templates on glass substrates, as explained in section 3.2.2. Soft composite molds made of Ormostamp and soft PDMS backbones have also been fabricated, however, compared to hPDMS-sPDMS molds, they presented several problems such as cracking of the Ormostamp film during imprinting and bending of the mold of upon curing due to different crosslinking and thermal shrinkage.¹⁸ Finally, I developed HPC water-soluble sacrificial templates supported by a soft PDMS backbones that I implemented for μ -contact printing of carbon nanotubes films, as illustrated in chapter 5, section 5.2.

Table 2 Table 4 summarizes the most used materials in the fabrication of lithographic molds, providing relevant information for their application as reprographic materials.

Table 4. Mechanical and chemical properties of different materials employed for the fabrication of soft lithographic molds.

	Stiffness modulus	Surface energy	Solubility	UV-curable
SU8	1-2 GPa	40 mN/m	low	yes
PFPE	1-10 MPa	12 mN/m	low	yes
PUA	100-400 MPa	23 mN/m	low	yes
sPDMS	0.1-5 MPa	22 mN/m	low	no
hPDMS	9 MPa	22 mN/m	low	no
XPDSM	80 MPa	22 mN/m	low	no
ORMOSTAMP	650 MPa	n.a.	low	yes
PMMA	2-3 GPa	30-40 mN/m	Organic solvents	no
PVA	1.5-5 GPa	30-40 mN/m	water	no
HPC	20- 110 MPa	43 mN/m	water	no

4.3 Hot embossing process

High temperatures induce a decrease in polymer viscosity due to the increased mobility of the chains, as a result of their reduced entanglements and van der Waals interactions.

Thermoplastic polymers are characterized by the presence of a temperature window, called glass transition temperature (T_g), above which there is enough thermal energy to allow changes in the molecules conformation. Differently from the melting temperature in crystalline materials, the glass transition is a non-sharp change in the macroscopic mechanical properties of the polymer, which slowly pass from a pure elastic to a mixed viscoelastic behavior. As illustrated in Figure 4.9, for molding of thermoplastic materials the flow temperature T_f is more suitable value than T_g , since it characterizes the drop of viscosity to useful values needed for fast and lower pressure imprints, and strongly depends on the material intrinsic characteristic (i.e. molecular weight, crosslinking, crystallinity etc.).

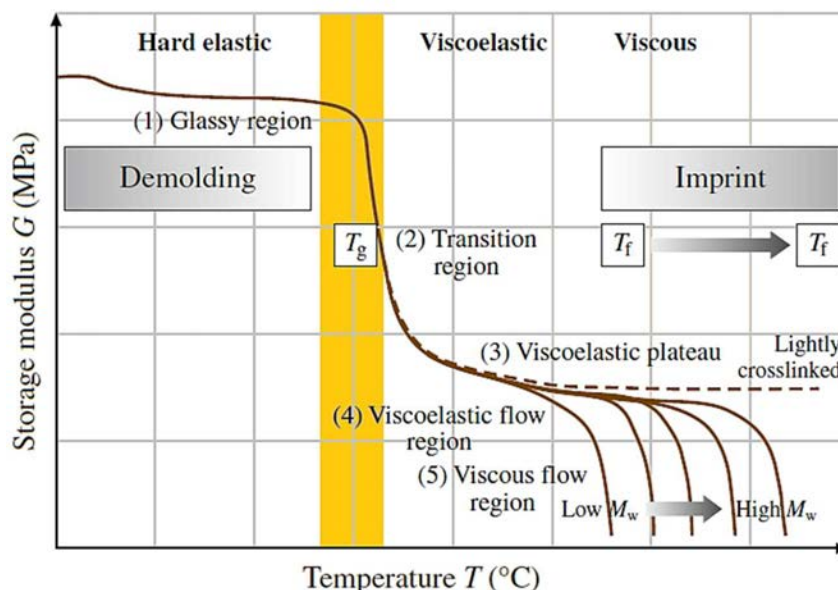


Figure 4.9 a) Schematics of the mechanical properties of thermoplastic polymers dependence on temperature and molecular weight. The graph illustrates the large drops of stiffness modulus around T_g and T_f and the three correspondent behaviors: hard elastic, viscoelastic and viscous.

The main differences between hot embossing and traditional photolithographic techniques based on exposure and development, is that after demolding, there is an excess of material left below the imprinted features, that is the so called “residual layer”. During the embossing step, indeed sinking of the stamp is accomplished by a complex squeeze flow of the viscous material in the lateral directions. The thickness

evolution of the residual layer $h(t)$, can be calculated considering the squeezed flow of a thermoplastic polymer underneath a cylindrical stamp protrusion described by the Stefan equation (4.3).

$$\frac{1}{h^2(t)} = \frac{1}{h_0^2} + \frac{4F}{3\pi\eta_0 r^4} t \quad (4.3)$$

Where h_0 is the initial thickness of the layer, η_0 is the viscosity of the polymer, r is the radius of the protrusion and F is the applied pressure.

Due to the strong dependence of $h(t)$ on the pressing area, two observation can be made:

- 1) Smaller protrusions will penetrate at a much faster rate into the viscous medium.
- 2) Once the filling of the stamp features is completed, the polymer flow drastically decreases and the thickness h_f of the residual layer left below the imprinted features does not change significantly with the time (Figure 4.10).

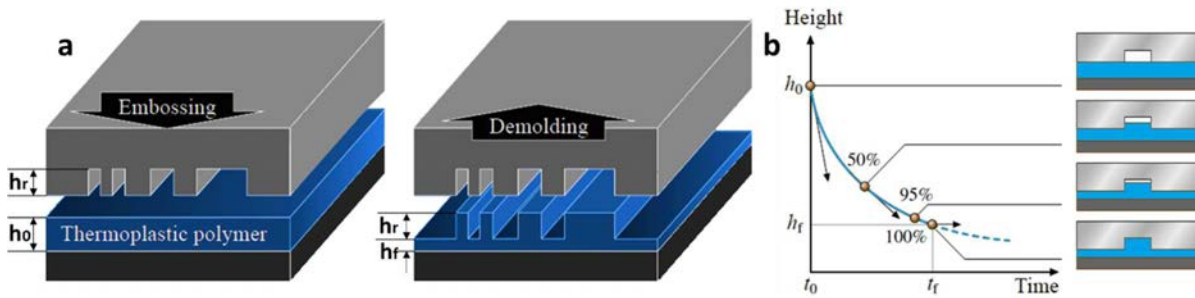


Figure 4.10 Viscous flow of a polymeric film with initial thickness h_0 pressed under stamp protrusions with height h_r . Once the stamp is fully insert, the flow practically stops leaving under the imprinted features a residual layer with a thickness h_f .

For most applications it is important to determine and control the thickness h_f of this residual layer before proceeding to the next processing step. Particularly when the pattern must be transferred to the substrate after the embossing step (e.g. deposition or etching), or when the residual layer thickness influences the final properties of the sample (e.g. optical properties). Furthermore, it is also important to avoid thickness variation of the residual layer to ensure structural homogeneity over the patterned area. For example, when the pattern must be transferred from the resist material to the underlying substrate, depending on the degree of anisotropy of the etching technique used for the pattern transfer, a more or less intense broadening of the imprinted features can occur. Minimizing the thickness of the residual layer can dramatically improve the quality of the final pattern, minimizing the lateral erosion during the etching

process. Since an excessively prolonged embossing time might be not convenient in terms of throughput for industrial applications, other parameters can be tuned to minimize the final thickness of the residual layer:

- i) increasing the temperature of embossing (i.e. decreasing the viscosity of the polymer)
- ii) higher pressure can be applied on the mold.
- iii) the initial resist layer thickness can be decreased.

However, high pressures for embossing as well as excessive temperature increase can causes the breakage of the substrate or local deformations and bending of the mold, with detrimental effects on the residual layer homogeneity and on the quality of the transferred pattern.

More conveniently, assuming that after filling of the mold feature the polymer flow practically stops, the residual layer thickness can be calculated considering a volume conserving model. A directly proportional relation between residual layer thickness and the initial film thickness, which depends on the geometry of the pattern, can thus be obtained, as explained in the supporting information of chapter 5, section 5.3. The difference in the rate of deformation arising from the viscoelastic flow of polymer has been instead exploited in this thesis to perform selective pick up of carbon nanotubes, as explained in chapter 5, section 5.1 **Error! Reference source not found.**

4.3.1 Nanoimprinting tool (NILT CNI)

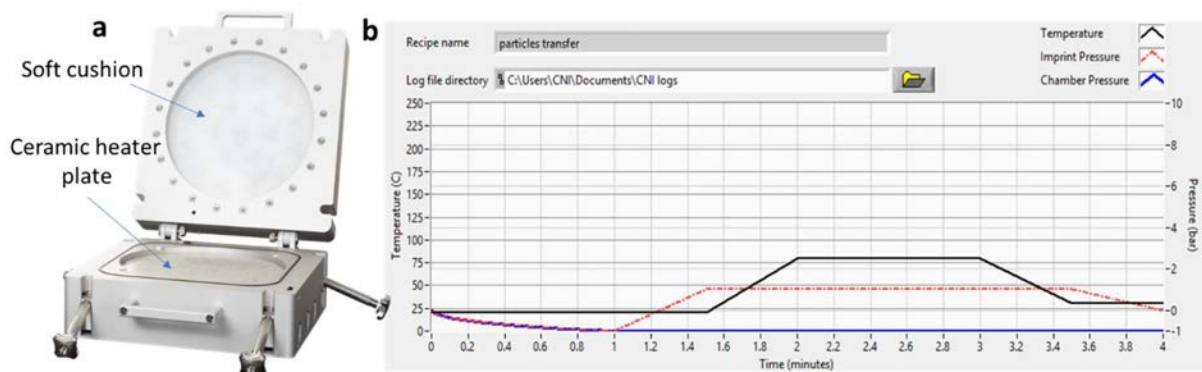


Figure 4.11 NILT CNI nanoimprint lithography tool. **a)** picture of the device **b)** graphical illustration of imprint pressures and temperatures set points.

Fine control over the imprinting parameters is crucial in order to have homogeneous and reproducible patterning in tNIL. The CNI tool illustrated in Figure 4.1 1 a is a desktop imprinting system that can perform both thermal and UV replication of nanoscale patterns fast and cost-efficiently supporting masters and

substrates of up to 120 mm in diameter. The CNI tool allows for accurate control of imprint pressure, gas pressure and temperature in the imprint chamber.

- The force pressure, p_1 is controlled using a soft cushion that inflates with compressed air generating an isostatic distribution on the chamber with pressure ranging from 1 to 11 bars. Furthermore, the elastic membrane is transparent to the UV, allowing for simultaneously embossing and UV crosslinking.
- The chamber is connected to a vacuum pump to control the pressure inside the chamber from 0 to 1 Bar, allowing drying of resist in solvent assisted imprints.
- The temperature is provided through the ceramic plate (ceramic stamp carrier), which is placed at the bottom of the chamber. The CNI stamp carrier is an integrated hotplate and temperature sensor with very small thermal mass, ensuring uniform fast heating and cooling of stamp carrier.

In a typical imprinting process, the resist material is spin-coated on a substrate, which is then placed on top of the ceramic plate. The prepatterned stamp is placed above the substrate, sandwiching the resist film between substrate and patterned surfaces. The NILT tool is then closed and the desired chamber pressure, temperature and processing times are set using the control software. The software controls everything in the imprint process (pressures, temperatures, UV exposure, timing) and allows to design multiple steps. Graphical illustration of imprint pressures and temperature set points used for transfer printing of metallic films into hydroxypropyl cellulose membranes are shown in Figure 4.11b. Real-time values are also provided by the software during replication process.

4.4 References

- (1) Hyewon Kang; Jiyeon Lee; Joonhyung Park; Hong H Lee. An improved method of preparing composite poly(dimethylsiloxane) moulds. *Nanotechnology* **2005**, *17*(1), 197–200.
- (2) Jagota, A.; Paretkar, D.; Ghatak, A. Surface-tension-induced flattening of a nearly plane elastic solid. *Physical review. E, Statistical, nonlinear, and soft matter physics* **2012**, *85* (5 Pt 1), 51602. DOI: 10.1103/PhysRevE.85.051602.
- (3) Delamarche, E.; Schmid, H.; Michel, B.; Biebuyck, H. Stability of molded polydimethylsiloxane microstructures. *Adv. Mater.* **1997**, *9*(9), 741–746. DOI: 10.1002/adma.19970090914.

- (4) Roca-Cusachs, P.; Rico, F.; Martínez, E.; Toset, J.; Farré, R.; Navajas, D. Stability of Microfabricated High Aspect Ratio Structures in Poly(dimethylsiloxane). *Langmuir* **2005**, *21* (12), 5542–5548. DOI: 10.1021/la046931w.
- (5) Glassmaker, N. J.; Jagota, A.; Hui, C.-Y.; Kim, J. Design of biomimetic fibrillar interfaces: 1. Making contact. *J. R. Soc. Interface*. **2004**, *1* (1), 23–33. DOI: 10.1098/rsif.2004.0004.
- (6) Goh, C.; Coakley, K. M.; McGehee, M. D. Nanostructuring titania by embossing with polymer molds made from anodic alumina templates. *Nano Lett.* **2005**, *5* (8), 1545–1549. DOI: 10.1021/nl050704c.
- (7) Fang, J.; Song, Y.; Chen, Z. D. Nanoimprinted SU-8 Nanopillars and Hierarchically Branched Nanowires by Anodic Aluminum Oxide Templates and Their Optical Properties. *ECS Trans.* **2010**, *33* (9), 67–73. DOI: 10.1149/1.3493684.
- (8) Chandra, D.; Yang, S. Stability of high-aspect-ratio micropillar arrays against adhesive and capillary forces. *Accounts of chemical research* **2010**, *43* (8), 1080–1091. DOI: 10.1021/ar100001a.
- (9) Zhang, Y.; Lo, C.-W.; Taylor, J. A.; Yang, S. Replica molding of high-aspect-ratio polymeric nanopillar arrays with high fidelity. *Langmuir* **2006**, *22* (20), 8595–8601. DOI: 10.1021/la061372.
- (10) Hui, C. Y.; Jagota, A.; Lin, Y. Y.; Kramer, E. J. Constraints on Microcontact Printing Imposed by Stamp Deformation. *Langmuir* **2002**, *18* (4), 1394–1407. DOI: 10.1021/la0113567.
- (11) Sharp, K. G.; Blackman, G. S.; Glassmaker, N. J.; Jagota, A.; Hui, C.-Y. Effect of stamp deformation on the quality of microcontact printing: theory and experiment. *Langmuir* **2004**, *20* (15), 6430–6438. DOI: 10.1021/la036332.
- (12) Schmid, H.; Michel, B. Siloxane Polymers for High-Resolution, High-Accuracy Soft Lithography. *Macromolecules* **2000**, *33* (8), 3042–3049. DOI: 10.1021/ma982034l.
- (13) Verschuuren, M. Substrate conformal imprint lithography for nanophotonics **2010**.
- (14) Kwon, B.; Kim, J. H. Importance of Molds for Nanoimprint Lithography: Hard, Soft, and Hybrid Molds. *Journal of Nanoscience* **2016**, *2016*, 1–12. DOI: 10.1155/2016/6571297.
- (15) Lan, H.; Liu, H. UV-nanoimprint lithography: structure, materials and fabrication of flexible molds. *Journal of nanoscience and nanotechnology* **2013**, *13* (5), 3145–3172. DOI: 10.1166/jnn.2013.7437.
- (16) Mühlberger, M.; Bergmair, I.; Klukowska, A.; Kolander, A.; Leichtfried, H.; Platzgummer, E.; Loeschner, H.; Ebm, C.; Grützner, G.; Schöftner, R. UV-NIL with working stamps made from Ormostamp. *Microelectronic Engineering*, *86*(4-6), 691-693. *Microelectronic Engineering* **2009**, *86* (4-6), 691–693. DOI: 10.1016/J.MEE.2008.11.020.

(17) Masciullo, C.; Sonato, A.; Romanato, F.; Cecchini, M. Perfluoropolyether (PFPE) Intermediate Molds for High-Resolution Thermal Nanoimprint Lithography. *Nanomaterials (Basel, Switzerland)* **2018**, *8* (8).

DOI: 10.3390/nano8080609.

(18) Papenheim, M.; Steinberg, C.; Dhima, K.; Wang, S.; Scheer, H.-C. Flexible composite stamp for thermal nanoimprint lithography based on OrmoStamp. *Journal of Vacuum Science & Technology B, Nanotechnology and Microelectronics: Materials, Processing, Measurement, and Phenomena* **2015**, *33*

(6), 06F601. DOI: 10.1116/1.4929885.

CHAPTER 5

Compilation of articles

5.1 Hydroxypropyl cellulose photonic architectures by soft nanoimprinting lithography

Espinha, A., Dore C., Matricardi, C., Alonso, M. I., Goñi A. R. & Mihi, A. Hydroxypropyl cellulose photonic architectures by soft nanoimprinting lithography. *Nature Photonics* 12, 343–348 (2018).
link: <https://www.nature.com/articles/s41566-018-0152-1>

5.2 Adhesives for Transfer Printing of Carbon Nanotubes and Metallic Nanostructures

Dore, C., Dörling, B., Garcia-Pomar, J. L., Campoy-Quiles, M. & Mihi, A. Hydroxypropyl Cellulose Adhesives for Transfer Printing of Carbon Nanotubes and Metallic Nanostructures. *Small* 2004795 (2020). doi:10.1002/sml.202004795
link: <https://onlinelibrary.wiley.com/doi/full/10.1002/sml.202004795>

5.3 A water-processable cellulose-based resist for advanced nanofabrication

Dore, C., Osmond, J. & Mihi, A. A water-processable cellulose-based resist for advanced nanofabrication. *Nanoscale* 10, 17884–17892 (2018).
link: <https://pubs.rsc.org/ko/content/articlehtml/2018/nr/c8nr04851g>

Hydroxypropyl cellulose photonic architectures by soft nanoimprinting lithography

André Espinha¹, Camilla Dore¹, Cristiano Matricardi¹, Maria Isabel Alonso¹, Alejandro R. Goñi^{1,2} and Agustín Mihi^{1*}

As contamination and environmental degradation increase, there is a huge demand for new eco-friendly materials. Despite its use for thousands of years, cellulose and its derivatives have gained renewed interest as favourable alternatives to conventional plastics, due to their abundance and lower environmental impact. Here, we report the fabrication of photonic and plasmonic structures by moulding hydroxypropyl cellulose into submicrometric periodic lattices, using soft lithography. This is an alternative way to achieve structural colour in this material, which is usually obtained by exploiting its chiral nematic phase. Cellulose-based photonic crystals are biocompatible and can be dissolved in water or not depending on the derivative employed. Patterned cellulose membranes exhibit tunable colours and may be used to boost the photoluminescence of a host organic dye. Furthermore, we show how metal coating these cellulose photonic architectures leads to plasmonic crystals with excellent optical properties acting as disposable surface-enhanced Raman spectroscopy substrates.

Sustainability is one of the fundamental challenges of modern society and in this regard, materials science has been evolving towards the preferential substitution of highly contaminating materials by others with lower environmental impact. Polymeric materials are not an exception. It is estimated that the production of plastics worldwide is around 320 million tons each year and increasing¹, and only about 10% of that amount is recycled, implying an enormous generation of waste with its dramatic effects on ecosystems at the global scale. In this context, biopolymers offer an excellent alternative to common plastics due to characteristics such as large availability, low cost and biodegradability. They entail advantages in three parts of product life cycle: material harvesting, processing and fabrication, and disposal. An added value of these materials is their possible biocompatibility, which enables their use in new applications within areas such as medical or food processing. Cellulose is probably the most interesting of these biopolymers because it is the most abundant on Earth and for centuries has had a wide technological impact in areas such as textiles, packaging and knowledge storage. Cellulose is a polysaccharide that results from the repetition of glucose units (Supplementary Fig. 1). It is typically extracted from vegetal sources and consists of fibres with dimensions of 2 to 4 mm in length and diameters in the range of 2 to 200 μm (ref. ²). Importantly, these fibres are organized in a hierarchical structure. By further processing them by appropriate means such as mechanical, chemical or enzymatic treatments, it is possible to obtain cellulose nanoparticles (nanofibrils or nanocrystals). This nanocellulose is being actively investigated for many electronics, energy and biological applications^{3,4}. Cellulose and particularly nanocellulose have also enabled new avenues in the fabrication of photonic components used, for example, in chiral reflectors^{5,6}, photonic electrodes⁷, anti-reflection coatings in solar cells⁸, multifunctional thermal⁹ or humidity¹⁰ responsive optical materials, flexible substrates for plasmonic sensing¹¹ and surface-enhanced Raman scattering spectroscopy¹².

The typical arrangement of cellulose microfibrils scatters light diffusively, providing the well-known white colour of paper. Nanocellulose instead can form compact and transparent films² or

colourful optically active ones⁵, depending on the amorphous or crystalline arrangement of the particles. In suspension, it is known that cellulose and some of its derivatives may present liquid crystalline phases with bright colours¹³. In particular, the observation of a mesophase in hydroxypropyl cellulose (HPC) was first reported by Werbowyj and co-workers¹⁴. HPC has a structure similar to cellulose but some of the hydroxyl groups of the glucose building blocks are hydroxypropylated (Supplementary Fig. 1). Concentrated solutions of HPC present iridescent colours and chiral behaviour due to the molecular arrangement of the linear chains in a helicoidal structure. This mesophase in HPC may be very attractive for the development of responsive systems, such as recently reported strain sensors¹⁵. Here, we propose an alternative route to easily provide cellulose derivatives with an optical functionality. We fabricate cellulose-based two-dimensional photonic structures with submicrometre features and demonstrate their potential in a variety of photonic applications.

Results and discussion

Nanoimprinting HPC. In the search for more versatile methods for achieving structural colour in cellulose derivatives, current soft lithography techniques¹⁶ are especially suited, as they have already been demonstrated to be useful for the fabrication of nanostructures in biopolymers¹⁷. Compared with traditional optical lithography, soft lithography techniques present advantages such as a low cost, large patterned areas, good quality and reproducibility, non-diffraction-limited and compatible with roll-to-roll processing. Furthermore, while the achievement of structural colour in HPC by self-assembly is time consuming due to the requirement of molecular ordering, which may last for days or weeks, soft lithography allows for a much faster processing. For example, it has been shown that it is possible to hot emboss liquid wood¹⁸ or to use imprinting methods compatible with roll-to-roll^{19,20} to structure cellulose-based polymers in a rapid way.

Concentrated HPC dilutions (above 35 wt%) may form anisotropic phases²¹; however, in this work, we used diluted solutions

¹Institut de Ciència de Materials de Barcelona, Consejo Superior de Investigaciones Científicas, Barcelona, Spain. ²Institució Catalana de Recerca i Estudis Avançats, Barcelona, Spain. *e-mail: amihi@icmab.es

(<20 wt%) which, additionally, were quickly dehydrated so that the self-assembly was hindered. Therefore, unpatterned regions of the samples are homogeneous, isotropic and transparent. For nanoimprinting of the HPC membranes with submicrometric features, the two soft lithography protocols illustrated in Fig. 1a were used. The first approach consisted of a hot embossing technique where a composite²² hard polydimethylsiloxane (h-PDMS) stamp was slightly pressed against a heated HPC membrane. In the second case—replica moulding procedure—the HPC solution was poured directly on top of the h-PDMS stamp, then dried and finally peeled off. Both methodologies produced equivalent structures on the cellulose derivative, only differing in the higher feature depth of the hot embossing approach (Supplementary Figs. 2 and 3). The replica moulding is more adequate for producing thick, flexible membranes while the hot embossing is preferred when highest optical quality is intended throughout the entire area of the crystal. Different kinds of lattices, such as square, hexagonal or simple grooves, with different lattice parameters (L) in the submicrometre region may be obtained in this way, depending only on the mould used (Supplementary Figs. 4–7).

HPC photonic crystals. Free-standing patterned membranes were achieved after peeling-off the samples fabricated with replica moulding (Fig. 1b). Patterns with areas of $1 \times 1 \text{ cm}^2$, with good reproducibility through the entire sample, were easily produced. Moreover, the patterned films performed as photonic crystals, presenting the characteristic iridescent colour. Another attractive feature is their flexibility (Fig. 1c) and therefore the potential transfer to other surfaces in a conformal way. The possibility of retaining a rigid or flexible substrate underneath, accomplished with hot embossing, is also useful for enhancing mechanical stability and ease of inspection of the optical properties on a flat surface. One major advantage of these photonic crystals is their biodegradability inherited from the HPC material. In fact, they can be washed away just by immersing them in water (Fig. 1d).

Although fast solubility in water is an attractive feature for environmental purposes, some strategies may be adopted for obtaining cellulose-based insoluble photonic films. Figure 1d–f compares the behaviour of three different cellulose-based membranes in water. Bare HPC-based films completely dissolved after being immersed in water for approximately 30 s (Fig. 1d). A step towards enhanced stability was the use of crosslinked HPC membranes (Fig. 1e). The crosslinking was achieved by adding divinyl sulfone to the HPC solution in water and increasing its pH with sodium hydroxide, before carrying out the soft lithographic step. The result is a patterned hydrogel²³ that becomes white on water immersion due to the increased light scattering coming from the nanopores swelling in the film. Incidentally, this system is a fast and visual humidity sensor as it undergoes a dramatic transition from colourful to white aspect. Finally, full mechanical stability under water could be achieved by imprinting a non-soluble cellulose derivative—acetyl cellulose (Supplementary Fig. 1). In this case, it is possible to obtain a non-degradable photonic film that retains its iridescence after immersion in water for 60 s (Fig. 1f).

Nanoimprinting is a versatile strategy that allows the fabrication of HPC photonic crystal films operating at spectral ranges determined by their geometry. The different colours exhibited by the films depend on the structure, topology or lattice parameter imprinted. To exemplify the structural colour functionality and characterize the optical properties of the HPC photonic crystal membranes, a set of samples with square lattice and varying L was tested. Photographs of the samples under normal incidence to the films (Fig. 2a) clearly showed the change from blue to green to red, as L was increased from 400 to 500 to 600 nm, in agreement with the colour observed with an optical microscope (Fig. 2b). The scanning electron microscopy (SEM) analysis confirmed the good replication of the square array of holes, 300 nm in diameter and 220 nm in depth, for the three lattice parameters studied (Fig. 2c)—larger-area images may be found in Supplementary Fig. 4. Characterization

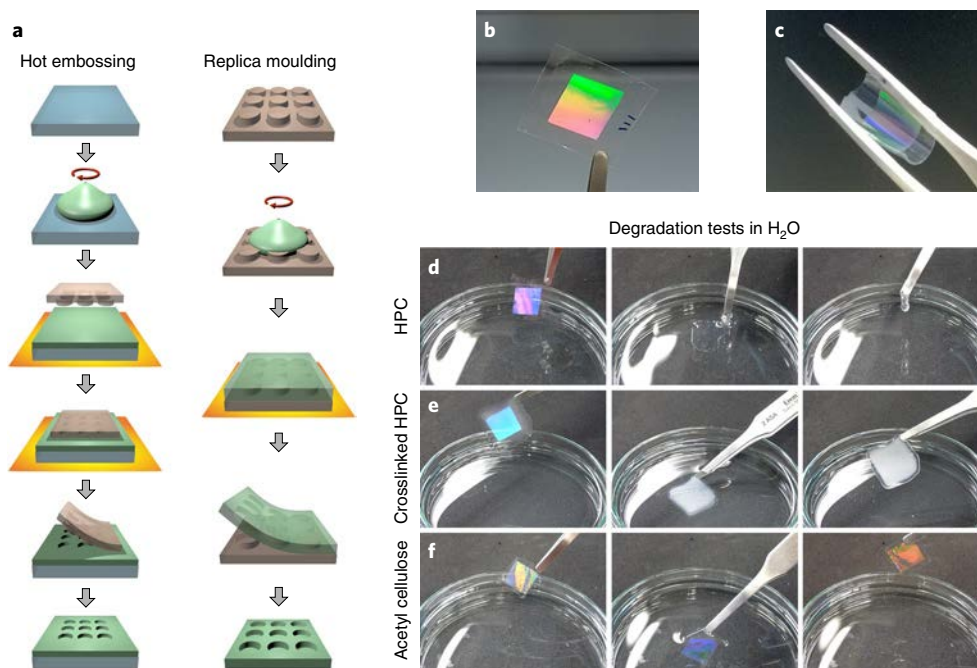


Fig. 1 | Fabrication procedures and water solubility tests of cellulose photonic crystal films. **a**, Scheme illustrating the hot embossing and replica moulding procedures used for the fabrication of cellulose-based photonic thin films and membranes. Glass substrate, blue; HPC, green; PDMS mould, brown. See main text for detailed fabrication details. **b**, Example image of a free-standing HPC photonic crystal. Lateral size of the imprinted area is 1 cm. **c**, Example image of the flexibility exhibited by a self-standing HPC photonic film. **d**, Sequence of photos illustrating the facile solubility of HPC photonic membranes in water. **e**, Sequence of photos showing the pattern loss of crosslinked HPC in water. **f**, Sequence of photos exemplifying the stability of patterned acetyl cellulose films in water.

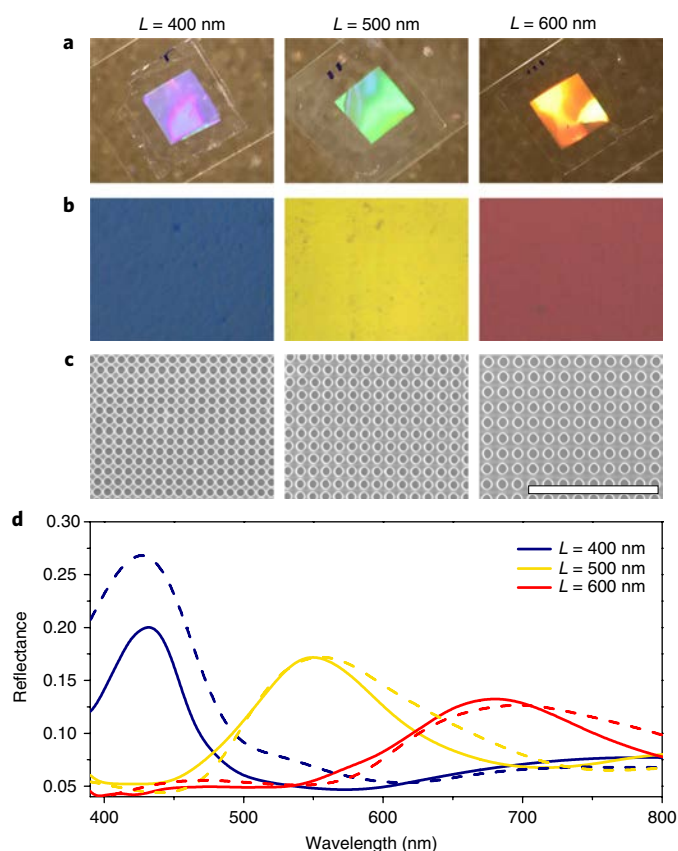


Fig. 2 | HPC photonic crystals. **a**, Photographs of the HPC photonic films (square lattice of imprinted cylindrical holes), for lattice parameters of 400, 500 and 600 nm. Square lateral size is 1 cm. **b**, Images of the HPC photonic films acquired with an optical microscope (4 \times objective, NA 0.1). **c**, SEM micrographs of the HPC photonic films (top view). Scale bar, 5 μ m. **d**, Specular reflectance characterization of the samples (solid curves), along with theoretical modelling of the structures by FDTD calculations (dashed curves).

of the reflectance by Fourier-transform infrared spectroscopy (Fig. 2d) revealed a peak centred at 430, 550 or 680 nm for each sample, respectively, in good agreement with simulations performed by finite-difference time-domain (FDTD) calculations, also shown Fig. 2d. It is important to highlight that the colours observed in these solid crystals arise from the two-dimensional patterned surface, in contrast to the colour achieved by the presence of anisotropic phases in concentrated HPC dispersions in water.

HPC plasmonic crystals. Enhanced optical properties and further functionality can be achieved by metal coating the cellulose-based photonic membranes. Such plasmonic crystals were produced by thermal evaporation of 50 nm of silver on top of HPC gratings. In doing so, the optical properties of these samples result from the combination of photonic and plasmonic modes. In plasmonic crystals, light fulfilling the condition of Bragg diffraction imposed by the lattice launches surface plasmon polaritons (SPPs), where strong electric fields at the surface of the metal can be used to enhance any light–matter interaction. Previous studies have reported that plasmonic crystals have been used to enhance light emission,²⁴ amplify light absorption in photodetectors²⁵ and produce structural colour in metallic surfaces^{26,27}.

Owing to the negative dielectric permittivity of the metal, the overall refractive index contrast of the system is enhanced, giving origin to much more vivid colours in the cellulose-based plasmonic

crystals than in their dielectric counterparts (Fig. 3a). Moreover, the samples keep the original flexibility (Fig. 3b). Optical characterization of plasmonic crystals consisting of a hexagonal lattice of imprinted nanoholes (Fig. 3c), revealed extinction peaks with up to 80% derived from the presence of the nanopatterns. These peaks correspond to the excitation of Bragg SPPs and as L is increased, the resonances redshift accordingly. Both the position and the intensity of the Bragg SPPs agreed significantly well with theoretical simulations performed by FDTD calculations (dashed curves in Fig. 3c).

As pointed out before, a major advantage of the fabrication methods used in this study is the possibility of imprinting HPC on top of different substrates. For providing additional functionality to the photonic and plasmonic crystals, we tested the fabrication of our plasmonic architectures using regular paper as substrate. HPC was coated on top of a piece of paper and then nanoimprinted, followed by metal evaporation. As illustrated by the SEM images (Fig. 3d,e), the patterns were transferred with extremely good quality also in this case. This particular example demonstrates the potential of the proposed system for functioning as a colourful photonic ink²⁸ in applications such as anti-counterfeiting technology, packaging or decorative paper. In fact, intense colours were easily achieved without the use of any expensive or toxic chemical pigment and in all cases, the photonic crystal presented a good adhesion to the paper substrate as the HPC infiltrated the porous cellulose fibres of the paper sheet (Supplementary Fig. 8). This method could be adapted to other kinds of paper or cardboard with notable industrial impact.

HPC plasmonic crystals for photoluminescence enhancement.

Plasmonic architectures have been sought as a way to modify and enhance the emission of light sources²⁶. The performance of HPC-based plasmonic crystals was further tested by doping HPC with an organic dye—rhodamine B (RhB). This dye is attractive due to its high quantum yield and has already been used for doping biopolymers such as silk²⁹ or polydiolcitrate³⁰. The samples as viewed from the HPC side exhibited the characteristic magenta colour of RhB, whereas inside the patterned areas, strong iridescence was observed, as in bare plasmonic crystals (Fig. 3f). Photoluminescence measurements were done on these crystals (see Supplementary Section 5), according to scheme in Fig. 3g, comparing the emission from nanopatterned regions and flat regions. An example is presented for a hexagonal plasmonic crystal of $L = 800$ nm (Fig. 3h). The detected photoluminescence for regions inside the patterned area was approximately tenfold the signal detected in the reference flat area. RhB has a high quantum yield (close to 70%) and in the proposed system, the plasmonic structure provided a more efficient way to extract light from the membrane.

HPC plasmonic crystals for SERS sensing. Once the optical properties of the HPC plasmonic crystal membranes had been characterized, we investigated the use of these architectures as disposable substrates for the detection of surface-enhanced Raman scattering (SERS). Raman sensing is one of the fields where plasmonics has had the greatest impact. The use of plasmonic resonances greatly amplifies the Raman scattering from the analyte, leading to its identification, even in scarce amounts. Patterned HPC membranes with hexagonal lattice and pillar morphology ($L = 700$ nm) were fabricated using the replica moulding technique previously explained. Afterwards, they were silver coated by thermal evaporation (100 nm). A representative extinction spectrum of the samples is shown in Fig. 4a. The optical characterization of these architectures revealed an extinction peak attributed to the excitation of a plasmonic resonance sustained by the architecture. To assess the SERS performance of these substrates, the samples were functionalized with thiophenol via the vapour phase and analysed (Supplementary Fig. 10). Thiophenol (Fig. 4b, inset) is a well-known Raman probe that easily binds to metal surfaces. Its characteristic vibrational

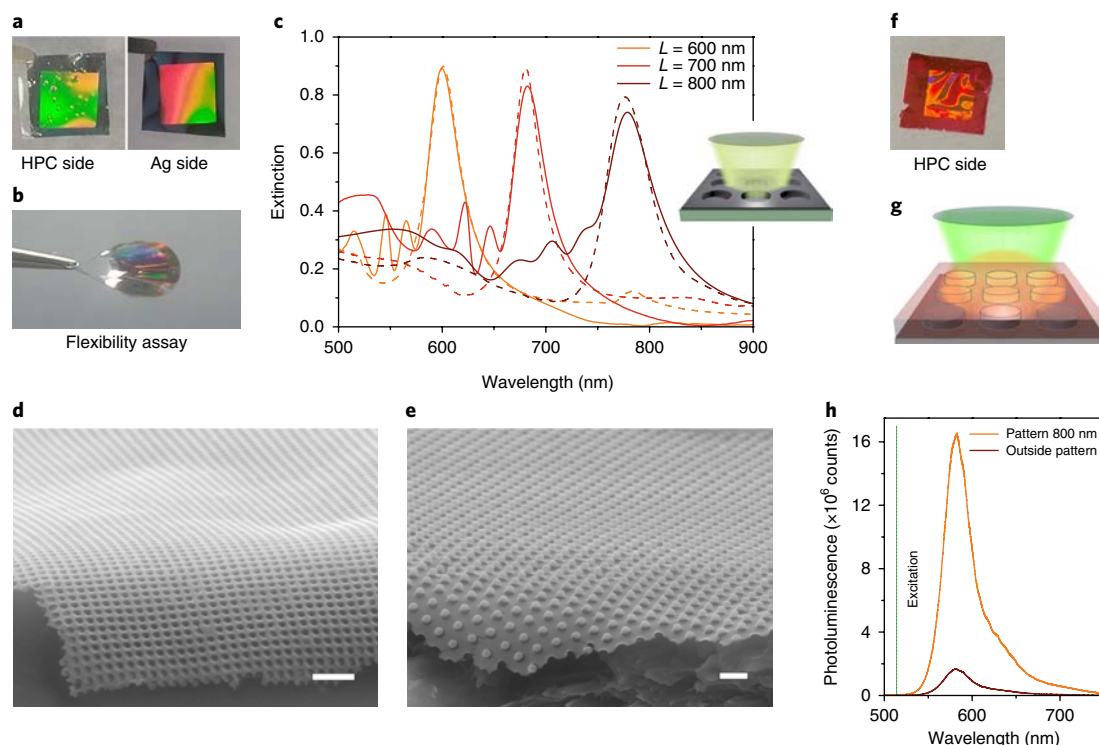


Fig. 3 | HPC plasmonic crystals. **a**, Picture of both sides of a plasmonic crystal made of silver (50 nm) deposited on a HPC patterned membrane. **b**, Example of the flexibility of plasmonic crystals. **c**, Experimental (solid curves) and simulated (dashed curves) optical extinction spectra of HPC-based plasmonic crystals (hexagonal array of holes, $L = 600$, 700 and 800 nm). Inset: measurement scheme (sample studied from the metal side). **d**, SEM lateral view of a HPC plasmonic crystal on a paper substrate (square lattice of imprinted holes). Scale bar, $1\ \mu\text{m}$. **e**, Similar view of a hexagonal lattice of imprinted pillars. Scale bar, $1\ \mu\text{m}$. **f**, Image of a plasmonic crystal fabricated with RhB-doped HPC. **g**, Scheme of photoluminescence measurements showing light impinging the HPC face. **h**, Comparison between photoluminescence spectrum of RhB in a patterned area (hexagonal plasmonic crystal; $L = 800$ nm) and a planar reference.

modes are positioned at $1,001$, $1,026$, $1,094$ and $1,586\ \text{cm}^{-1}$ (ref. ³¹). These modes could be clearly identified in the spectra taken from the probe adsorbed to the surface of our plasmonic crystals (Fig. 4b). Interestingly, the geometry employed in our plasmonic crystals was suitable for the excitation of plasmonic resonances, which in turn facilitated the use of these membranes as SERS substrates, active at different excitation wavelengths ($\lambda = 532$ and $633\ \text{nm}$). When comparing spectra collected from the flat regions of the substrate (grey curves in Fig. 4b) with the spectra collected inside the patterns, a clear enhancement of the signal was observed.

SERS is a phenomenon characterized by the presence of hotspots at the dielectric/metal interface. These are spatial regions with extremely intense electric field³¹. The Raman signal measured originates from the effect of these hotspots on the molecules placed therein. There is great interest in the imaging of the above mentioned hotspots, to identify the active sensing regions of the SERS substrate. Here we demonstrate how the excellent quality of our HPC plasmonic crystal membranes enables the identification of the hotspots for the two laser frequencies employed. First, electron microscopy images (Fig. 4c) and optical microscopy images (Fig. 4d) were used to illustrate the hexagonal array of Ag-coated pillars forming the plasmonic substrate. Second, Raman spectroscopy maps were performed by scanning the signal throughout the surface and monitoring the Raman peak of thiophenol at $1,578\ \text{cm}^{-1}$ (Fig. 4e), for both laser frequencies. The Raman signal map for the $532\ \text{nm}$ laser excitation revealed that the majority of the signal came from the regions located between the metallic pillars. In contrast, when the sample was illuminated with the $633\ \text{nm}$ laser, coinciding with the extinction peak, the Raman signal originated at the pillars themselves. This observation was further corroborated with numerical

simulations, in which the position of the extinction peak was fitted and the spatial distribution of the electric field intensity at both laser frequencies reproduced (Fig. 4f and Supplementary Fig. 12). Whereas at $\lambda = 532\ \text{nm}$ the electric field distribution revealed the presence of an extended mode, $\lambda = 633\ \text{nm}$ corresponded to a hybrid mode where the electric field was concentrated mostly at the top of the pillars. The good agreement between simulations and Raman measurement maps demonstrated that we were capable of imaging the spatial distribution of hotspots in our plasmonic structures for two different resonant optical modes. Moreover, they demonstrate the importance of the imprinted nanostructure for enhancing the Raman signal.

Conclusions

We have shown how to produce photonic and plasmonic crystal thin films out of HPC. The resulting structures incorporate the biocompatibility and biodegradability aspects inherited from the cellulose derivative used. Following the recent tendency to explore materials for transient electronics^{32,33}, our system opens a wide range of potential applications in transient photonics. Two routes were presented to integrate these photonic architectures in applications: to produce free-standing flexible samples that may be transferred to other surfaces; and to directly nanoimprint a HPC coating on the desired substrate. HPC nanoimprinted crystals are a convenient platform for the realization of plasmonic systems by simply metal coating the HPC photonic membranes. Different morphologies and topologies were produced with this method, both free-standing and on top of functional substrates. These samples offer a convenient opportunity for the production of colour in packaging systems and in photonic papers³⁰ and they could accomplish the function of washable and edible³⁴ detectors or labels in food industry. In fact, HPC is an excellent candidate for such

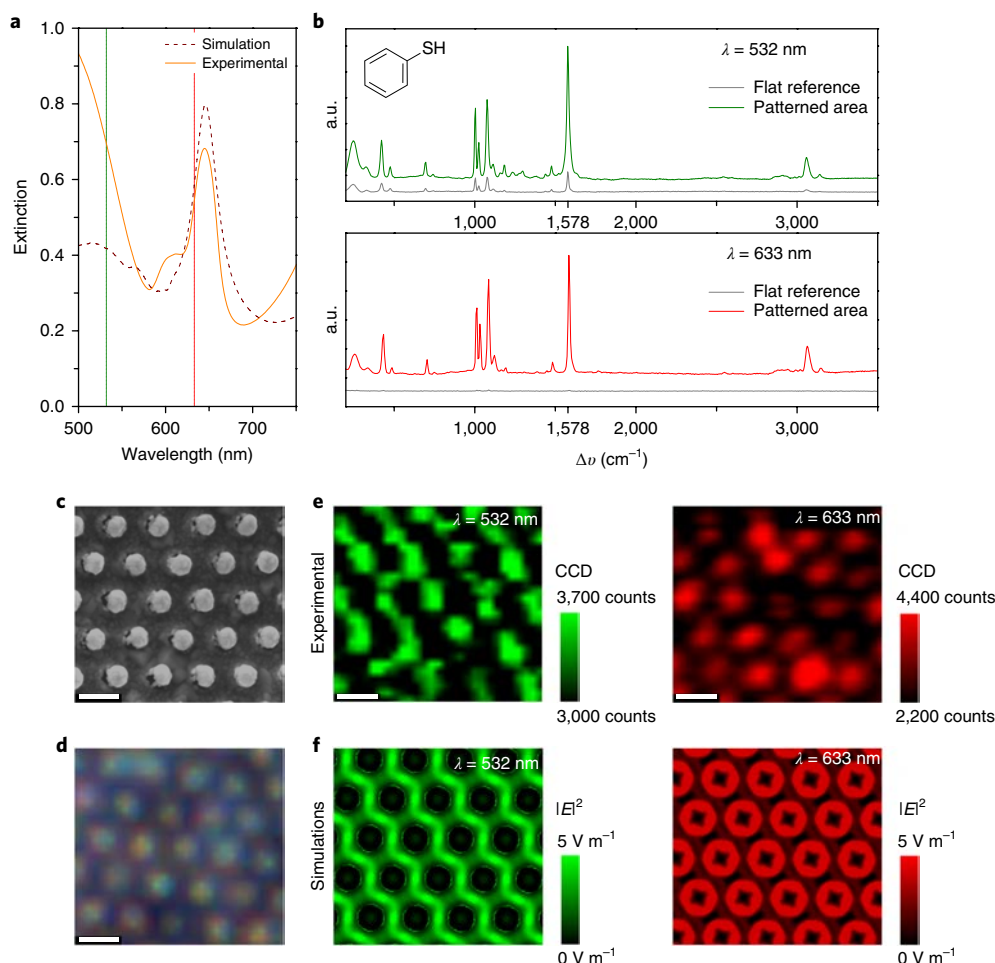


Fig. 4 | HPC plasmonic crystal membranes as SERS substrates. **a**, Representative extinction spectrum of a silver-coated HPC hexagonal lattice of pillars ($L=700$ nm)—experimental results (solid curve) and FDTD simulation (dashed curve). **b**, Raman spectra of thiophenol (inset) collected in reference flat areas (grey curves) and in HPC/Ag patterned substrates, for excitation wavelengths of 532 and 633 nm; curves are vertically displaced for clarity. **c**, Representative SEM image of the sample. Scale bar, 600 nm. **d**, Representative optical microscopy image of the sample observed with a 100 \times magnification objective used to measure Raman maps. Scale bar, 600 nm. **e**, Raman maps of the surface, monitoring the intensity of the peak at 1,578 cm^{-1} , for excitation wavelengths of 532 nm (left) and 633 nm (right). Scale bars, 600 nm. **f**, FDTD theoretical simulations of the electric field (E) spatial distributions for the corresponding wavelengths.

matters due to its already established applicability as drug excipient or ophthalmic lubricant³⁵. Moreover, we explored the possibility of doping HPC with an organic dye to achieve a luminescent system. It was made evident that the plasmonic crystal improved the out-coupling of light, enhancing the photoluminescence signal by tenfold with respect to a flat reference. Finally, HPC-based plasmonic crystals in the context of SERS were tested. An enhancement of Raman signal due to the presence of the nanostructure determined by the HPC surface underneath was demonstrated.

Methods

Methods, including statements of data availability and any associated accession codes and references, are available at <https://doi.org/10.1038/s41566-018-0152-1>.

Received: 3 October 2017; Accepted: 12 March 2018;

Published online: 09 April 2018

References

1. *Plastics—the Facts 2016* <https://www.plasticseurope.org/application/files/4315/1310/4805/plastic-the-fact-2016.pdf> (PlasticsEurope, 2016).
2. Hoeng, F., Denneulin, A. & Bras, J. Use of nanocellulose in printed electronics: a review. *Nanoscale* **8**, 13131–13154 (2016).
3. Lagerwall, J. et al. Cellulose nanocrystal-based materials: from liquid crystal self-assembly and glass formation to multifunctional thin films. *NPG Asia Mater.* **6**, e80 (2014).
4. Zhu, H. et al. Wood-derived materials for green electronics, biological devices, and energy applications. *Chem. Rev.* **116**, 9305–9374 (2016).
5. Dumanli, A. et al. Controlled, bio-inspired self-assembly of cellulose-based chiral refl ctors. *Adv. Opt. Mater.* **2**, 646–650 (2014).
6. Fernandes, S. et al. Mind the microgap in iridescent cellulose nanocrystal films. *Adv. Mater.* **29**, 1603560 (2017).
7. Águas, H. et al. Thin film silicon photovoltaic cells on paper for flex ble indoor applications. *Adv. Funct. Mater.* **25**, 3592–3598 (2015).
8. Ha, D., Fang, Z., Hu, L. & Munday, J. Paper-based anti-refl ction coatings for photovoltaics. *Adv. Energy Mater.* **4**, 1301804 (2014).
9. Espinha, A. et al. Shape memory cellulose-based photonic refl ctors. *ACS Appl. Mater. Inter.* **8**, 31935–31940 (2016).
10. Wu, T. et al. A bio-inspired cellulose nanocrystal-based nanocomposite photonic film with hyper-refl ction and humidity-responsive actuator properties. *J. Mater. Chem. C* **4**, 9687–9696 (2016).
11. Polavarapu, L. & Liz-Marzán, L. Towards low-cost flex ble substrates for nanoplasmonic sensing. *Phys. Chem. Chem. Phys.* **15**, 5288–5300 (2013).
12. Tian, L. et al. Bacterial nanocellulose-based flex ble surface enhanced Raman scattering substrate. *Adv. Mater. Interfaces* **3**, 1600214 (2016).
13. Gilbert, R. & Patton, P. Liquid crystal formation in cellulose and cellulose derivatives. *Prog. Polym. Sci.* **9**, 115–131 (1983).
14. Werbowyj, R. & Gray, D. Liquid crystalline structure in aqueous hydroxypropyl cellulose solutions. *Mol. Cryst. Liq. Cryst.* **34**, 97–103 (1976).

15. Kamita, G. et al. Biocompatible and sustainable optical strain sensors for large-area applications. *Adv. Opt. Mater.* **4**, 1950–1954 (2016).
16. Xia, Y. & Whitesides, G. Soft lithography. *Angew. Chem. Int. Ed.* **37**, 550–575 (1998).
17. Espinha, A., Serrano, M., Blanco, A. & López, C. Thermoresponsive shape-memory photonic nanostructures. *Adv. Opt. Mater.* **2**, 516–521 (2014).
18. Worgull, M. et al. Hot embossing and thermoforming of biodegradable three-dimensional wood structures. *RSC Adv.* **3**, 20060–20064 (2013).
19. Mäkelä, T., Kainlahti, M., Willberg-Keyriläinen, P., Tammelin, T. & Forsström, U. Fabrication of micropillars on nanocellulose films using a roll-to-roll nanoimprinting method. *Microelectron. Eng.* **163**, 1–6 (2016).
20. Mäkelä, T., Haatainen, T. & Ahopelto, J. Roll-to-roll printed gratings in cellulose acetate web using novel nanoimprinting device. *Microelectron. Eng.* **88**, 2045–2047 (2011).
21. Werbowyj, R. & Gray, D. Optical properties of hydroxypropyl cellulose liquid crystals. I. Cholesteric pitch and polymer concentration. *Macromolecules* **17**, 1512–1520 (1984).
22. Odom, T., Love, J., Wolfe, D., Paul, K. & Whitesides, G. Improved pattern transfer in soft lithography using composite stamps. *Langmuir* **18**, 5314–5320 (2002).
23. Kabra, B., Gehrke, S. & Spontak, R. Microporous, responsive hydroxypropyl cellulose gels. I. Synthesis and microstructure. *Macromolecules* **31**, 2166–2173 (1998).
24. Yang, A. et al. Unidirectional lasing from template-stripped two-dimensional plasmonic crystals. *ACS Nano* **9**, 11582–11588 (2015).
25. de Arquer, F., Mihi, A. & Konstantatos, G. Large-area plasmonic-crystal-hot-electron-based photodetectors. *ACS Photon.* **2**, 950–957 (2015).
26. James, T., Mulvaney, P. & Roberts, A. The plasmonic pixel: large area, wide gamut color reproduction using aluminum nanostructures. *Nano Lett.* **16**, 3817–3823 (2016).
27. Cheng, F., Gao, J., Luk, T. & Yang, X. Structural color printing based on plasmonic metasurfaces of perfect light absorption. *Sci. Rep.* **5**, 11045 (2015).
28. Fudouzi, H. & Xia, Y. Photonic papers and inks: color writing with colorless materials. *Adv. Mater.* **15**, 892–896 (2003).
29. Min, K., Kim, S., Kim, C. & Kim, S. Colored and fluorescent nanofibrous silk as a physically transient chemosensor and vitamin deliverer. *Sci. Rep.* **7**, 5448 (2017).
30. Espinha, A., Serrano, M., Blanco, A. & López, C. Random lasing in novel dye-doped white paints with shape memory. *Adv. Opt. Mater.* **3**, 1080–1087 (2015).
31. Macias, G., Alba, M., Marsal, L. & Mihi, A. Surface roughness boosts the SERS performance of imprinted plasmonic architectures. *J. Mater. Chem. C.* **4**, 3970–3975 (2016).
32. Bae, H. et al. Physically transient memory on a rapidly dissolvable paper for security application. *Sci. Rep.* **6**, 38324 (2016).
33. Hwang, S. et al. A physically transient form of silicon electronics. *Science* **337**, 1640–1644 (2012).
34. Tao, H. et al. Silk-based conformal, adhesive, edible food sensors. *Adv. Mater.* **24**, 1067–1072 (2012).
35. Luchs, J., Nelinson, D. & Macy, J. Efficacy of hydroxypropyl cellulose ophthalmic inserts (LACRISERT) in subsets of patients with dry eye syndrome: findings from a patient registry. *Cornea* **29**, 1417–1427 (2010).

Acknowledgements

The authors acknowledge M. Simón and A. Gómez for AFM measurements. The Spanish Ministerio de Economía, Industria y Competitividad (MINECO) is gratefully acknowledged for its support through grant no. SEV-2015-0496 in the framework of the Spanish Severo Ochoa Centre of Excellence programme and also for its support through grant MAT2016-79053-P. A.M. was funded by a Ramón y Cajal fellowship (RYC-2014-16444). This project has received funding from the European Research Council under the European Union's Horizon 2020 research and innovation programme (grant agreement no. 637116, ENLIGHTMENT).

Author contributions

A.E. and C.D. developed the concept, fabricated and characterized the samples. C.M. provided patterned PDMS moulds. A.R.G. and M.I.A. carried out photoluminescence and Raman measurements. A.E. and A.M. wrote the manuscript. All authors contributed to fruitful discussions and corrected the manuscript. A.M. supervised the research.

Competing interests

The authors declare no competing interests.

Additional information

Supplementary information is available for this paper at <https://doi.org/10.1038/s41566-018-0152-1>.

Reprints and permissions information is available at www.nature.com/reprints.

Correspondence and requests for materials should be addressed to A.M.

Publisher's note: Springer Nature remains neutral with regard to jurisdictional claims in published maps and institutional affiliations.

Methods

Chemicals. A h-PDMS kit was acquired from Gelest and a soft poly-PDMS Sylgard 184 kit was acquired from Dow Corning. 1H,1H,2H,2H-perfluorooctyltrichlorosilane, 97% was purchased from Alfa Aesar. Acetone, divinyl sulfone, acetyl cellulose with average molecular weight $M_w = 30$ kDa and HPC with average $M_w = 100$ kDa were acquired from Sigma-Aldrich. All chemicals were used as received.

Stamps preparation. Composite bilayer stamps comprising a thin h-PDMS layer to ensure good pattern replica and mechanical stability, and a thick soft PDMS (s-PDMS) layer to allow their manipulation were prepared according to previously reported methods²².

Nanoimprinting of cellulose derivatives. A HPC solution in water was prepared by adding 23 ml of deionized water to 5 g of HPC powder. The solution was intensively stirred and reserved for use in a sealed vial. Regarding the replica moulding procedure, the HPC solution was poured on top of a h-PDMS mould and spin coated at 500 r.p.m. with an initial acceleration of 100 r.p.m. min⁻¹. Once finished, the membranes were peeled off to obtain free-standing samples. For hot embossed samples, a dilution of the original HPC at a new concentration of 41 mg ml⁻¹ was initially prepared. Then thin films were prepared by spin coating (parameters: acceleration ramp of 1,000 r.p.m. s⁻¹, duration of 60 s at 3,500 r.p.m.) on top of glass slides or silicon wafers as substrate. The samples were heated at 140 °C and imprinted with the h-PDMS mould by applying a light pressure for approximately 30 s. Finally, the h-PDMS was demoulded. In the case of samples produced with the crosslinker, a solution of NaOH in water was first prepared at a concentration of 1 mg ml⁻¹. A HPC mass of 0.16 g was added to a volume of 1.808 ml of the NaOH solution and magnetically stirred overnight. A divinyl sulfone mass of 0.032 g were added to the mixture and stirred for a few more minutes. The replica moulding process was repeated. Insoluble photonic membranes were prepared by mixing 0.16 g of acetyl cellulose in 1.832 ml of acetone, magnetically stirring overnight and repeating the replica moulding procedure. Silver films were deposited on top of HPC membranes using a MBRAUN thermal evaporator. The chamber pressure was 4×10^{-7} bar and an evaporation rate of 10 nm min⁻¹ was used.

Photoluminescence measurements. The photoluminescence was excited using either the 405 nm line of a continuous-wave laser diode or the 514 nm line of an Ar⁺-ion gas laser. The photoluminescence signal was collected using an Olympus microscope with a 20× objective (numerical aperture (NA) = 0.35) in

backscattering geometry. The microscope was coupled to a high-throughput and high-resolution LabRam HR800 spectrometer using a grating of 600 lines mm⁻¹ and equipped with a liquid nitrogen cooled charge-coupled device (CCD) detector. A scheme of the experimental setup is provided in Supplementary Fig. 9. All measurements were performed at room temperature.

Raman spectroscopy measurements. The initially free-standing membranes were transferred to a flat PDMS block so that their surface was free from wrinkles or curving. Raman images were obtained at ambient conditions and in backscattering geometry using the WITec Alpha300 R confocal setup. For excitation, either a frequency-doubled neodymium-doped yttrium aluminium garnet (Nd:YAG) laser emitting at 532 nm or a He-Ne gas laser (633 nm) was coupled into a Zeiss microscope through a wavelength-specific single-mode fibre and collimated by an achromatic lens. The beam was focused onto the sample, with power 0.25 mW, using a Zeiss EC Epiplan-Neofluar (100×, 0.9 NA) objective, giving an estimated spot size of 0.35 μm (green) or 0.43 μm (red). The pixel size for the images was $0.1 \times 0.1 \mu\text{m}^2$, given by the scanning movement of a piezo-motor-driven sample stage. The collected light was focused into a multimode optical fibre, which served as the entrance slit for the spectrometer. The 3.5-μm-diameter single-mode input fibre and the 50-μm-diameter multimode output fibre provided the optical apertures for the confocal arrangement. A Si back-illuminated 1,024 × 127 pixel CCD cooled at -60 °C was used for detection. Using gratings of 600 grooves mm⁻¹ with blaze at 500 nm (green) and of 300 grooves mm⁻¹ with blaze at 750 nm (red), complete Raman spectra in the interesting spectral range (from about 200 to 3,500 cm⁻¹) were acquired at each image pixel using integration times of 0.1 s with submicrometre spatial resolution (Supplementary Fig. 10). Images were analysed using WITec Project FOUR software.

Theoretical modelling. A commercial-grade simulator based on the FDTD method was used to perform the calculations (Lumerical Solutions, <https://www.lumerical.com/tcad-products/fDTD>). For simulating the thick free-standing HPC membranes, 120 reflectance spectra for different thicknesses were calculated and averaged so that oscillations due to Fabry–Perot interference were averaged. A mesh refinement of 5 nm was used in all structures. Transmittance (T) and reflectance (R) were calculated and extinction as $1 - R - T$. The simulations were performed for both polarizations and averaged to reproduce unpolarized light (Supplementary Fig. 12).

Data availability. The data that support the plots within this paper and other findings of this study are available from the corresponding author upon reasonable request

In the format provided by the authors and unedited.

Hydroxypropyl cellulose photonic architectures by soft nanoimprinting lithography

André Espinha ¹, Camilla Dore¹, Cristiano Matricardi¹, Maria Isabel Alonso ¹, Alejandro R. Goñi^{1,2}
and Agustín Mihi ^{1*}

¹Institut de Ciència de Materials de Barcelona, Consejo Superior de Investigaciones Científicas, Barcelona, Spain. ²Institució Catalana de Recerca i Estudis Avançats, Barcelona, Spain. *e-mail: amihi@icmab.es

Supporting Information

Hydroxypropyl cellulose photonic architectures by soft nanoimprinting lithography

André Espinha¹, Camilla Dore¹, Cristiano Matricardi¹, Maria Isabel Alonso¹, Alejandro R. Goñi^{1,2}, Agustín Mihi^{1,*}

¹Institut de Ciència de Materials de Barcelona, Consejo Superior de Investigaciones Científicas, Carrer dels Til·lers S/N, Campus de la UAB, 08193 Bellaterra, Barcelona, Spain. ²Institució Catalana de Recerca i Estudis Avançats, Passeig Lluís Companys 23, 08010 Barcelona, Spain.
*e-mail: amihi@icmab.es

Contents:

Section 1. Cellulose and cellulose derivatives

Section 2. Comparison of replica molding and hot embossing fabrication methods

Section 3. Additional scanning electron microscopy photos

Section 4. Additional photos of samples imprinted on top of common paper.

Section 5. Photoluminescence (PL) experiments

Section 6. Micro-Raman experiments

Section 7. Electric fields simulations.

1. Cellulose and cellulose derivatives

Cellulose is a polysaccharide composed of linear chains of glucose units, as represented in Figure S1. Furthermore, these molecular chains organize in a hierarchical structure. The two cellulose derivatives used in this work were hydroxypropyl cellulose and acetylcellulose. In the first case, some of the hydroxyl groups are substituted by hydroxypropyl groups while in acetylcellulose, the substituting group is the acetyl. Further information and molar substitution rates can be found here [<https://www.sigmaaldrich.com/catalog/papers/22961411>].

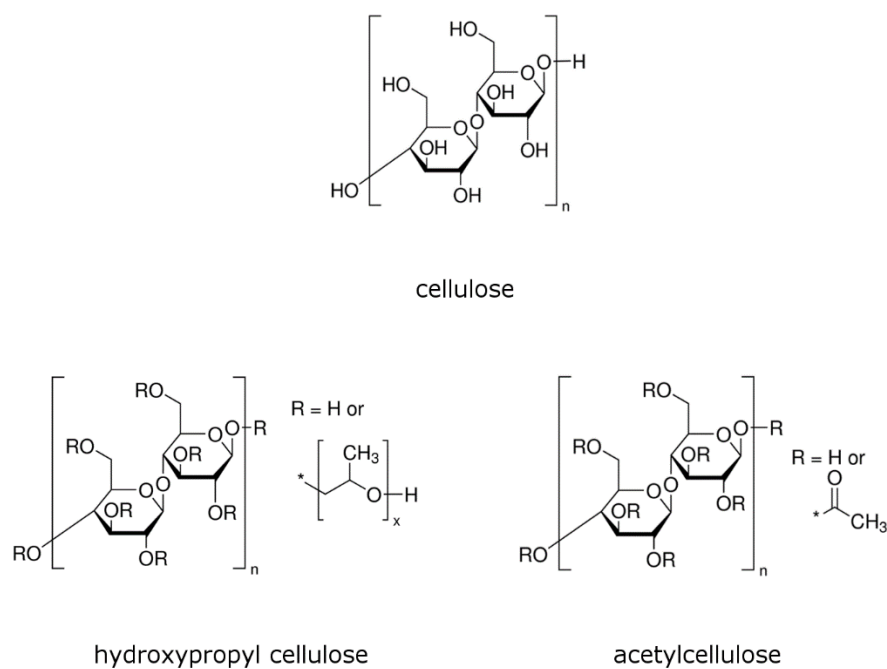


Figure S1. Chemical formulas. Chemical formulas of the cellulose and of its derivatives hydroxypropyl cellulose and acetylcellulose resulting from the substitution of the hydroxyl groups in the original glucose unit.

2. Comparison of replica molding and hot embossing fabrication methods

As stated in the main manuscript, two experimental proceedings were used for fabricating hydroxypropyl cellulose photonic membranes namely, replica molding and hot embossing. The first one is more convenient for producing thicker samples ($> 20 \mu\text{m}$) which are easy to peel-off in order to obtain free standing and flexible membranes (Figure S2a). A very precise alignment of the sample is required to characterize optical properties, due to frequent curving or bending of the membrane. The hot embossing procedure is preferable whenever very reproducible optical properties are required throughout the entire area of the sample and in this case, a rigid substrate is typically kept underneath the imprinted HPC thin film (Figure S2b).

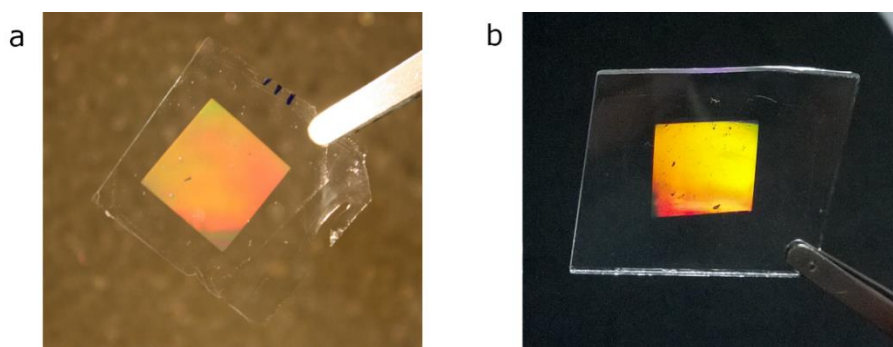


Figure S2. Photos of samples produced by replica molding or hot embossing procedures.

Exemplar photo of a free standing HPC photonic membrane fabricated by replica molding (a). Exemplar image of a HPC photonic membrane fabricated by hot embossing, whereas a rigid substrate is kept below (b).

For further comparing the two processes, atomic force microscopy analysis was performed in representative HPC crystals of imprinted holes, square lattice and lattice parameter of 500 nm. Results are exhibited in Figure S3. The photonic structure was clearly observed in both cases although two aspects highlight from the results. The first one concerns the depth of the cylinders that resulted in approximately $220 \pm 30 \text{ nm}$ in the replica molding case while it was

approximately 270 ± 10 nm in the case of the hot embossed crystal. Different factors may contribute to this difference such as the different processing temperatures and the different cellulose concentration. In fact, it is possible that shrinking effect occurs during the replica molding drying step, which does not occur in hot embossing since the sample is already dried.

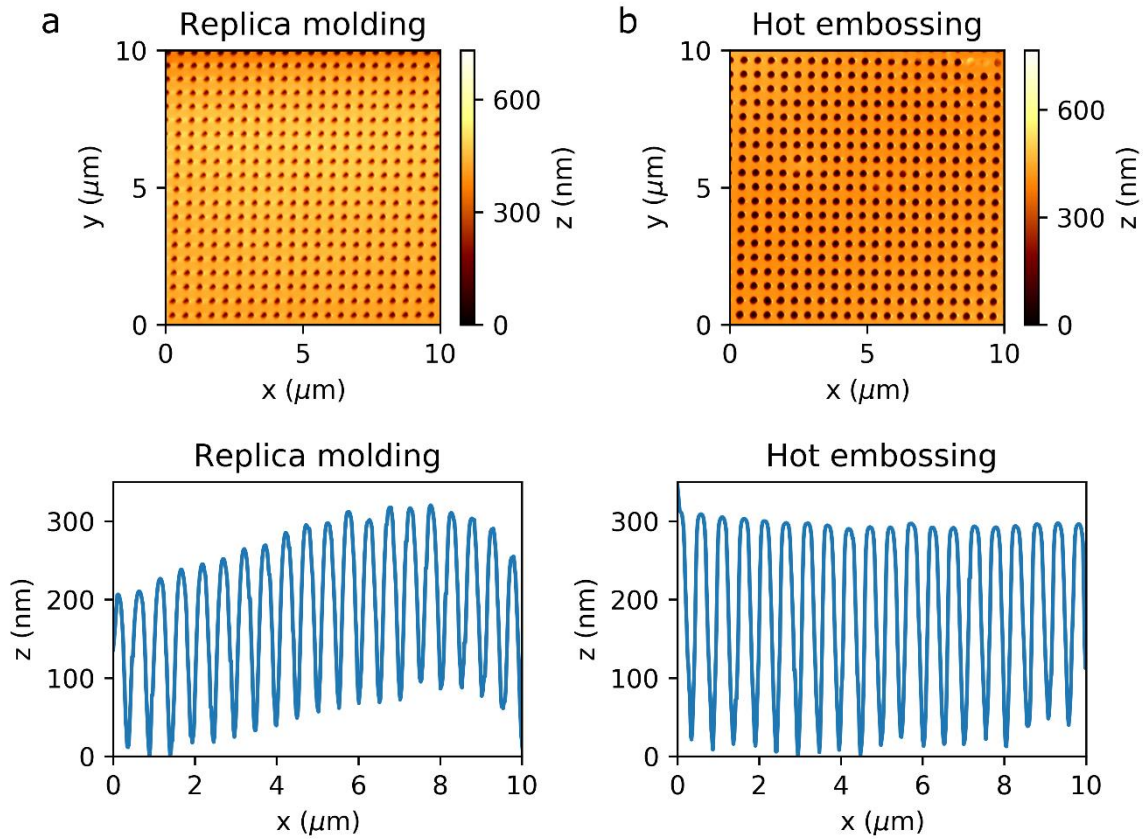


Figure S3. Replica molding vs hot embossing procedures. **a**, Atomic force microscopy image and a representative profile of a free standing HPC photonic membrane fabricated by replica molding and **b**, one fabricated by hot embossing, whereas a rigid glass substrate is kept underneath.

The second point regards the overall profile on the two samples. While the nanostructure is superposed to a curved profile with maximum around 7 μm in the case of the replica molding sample, the global profile of the hot embossed sample is much more planar. This result points out the difference of having the sample freestanding and free to curve or constrained with the rigid substrate.

3. Additional scanning electron microscopy photos

Additional scanning electron microscopy images of photonic membranes, of different morphologies and topologies are presented in this section. As may be appreciated, hydroxypropyl cellulose was suitable for imprinting large areas of holes or pillars arrays, with different lattice parameters and square, linear or hexagonal lattice morphologies.

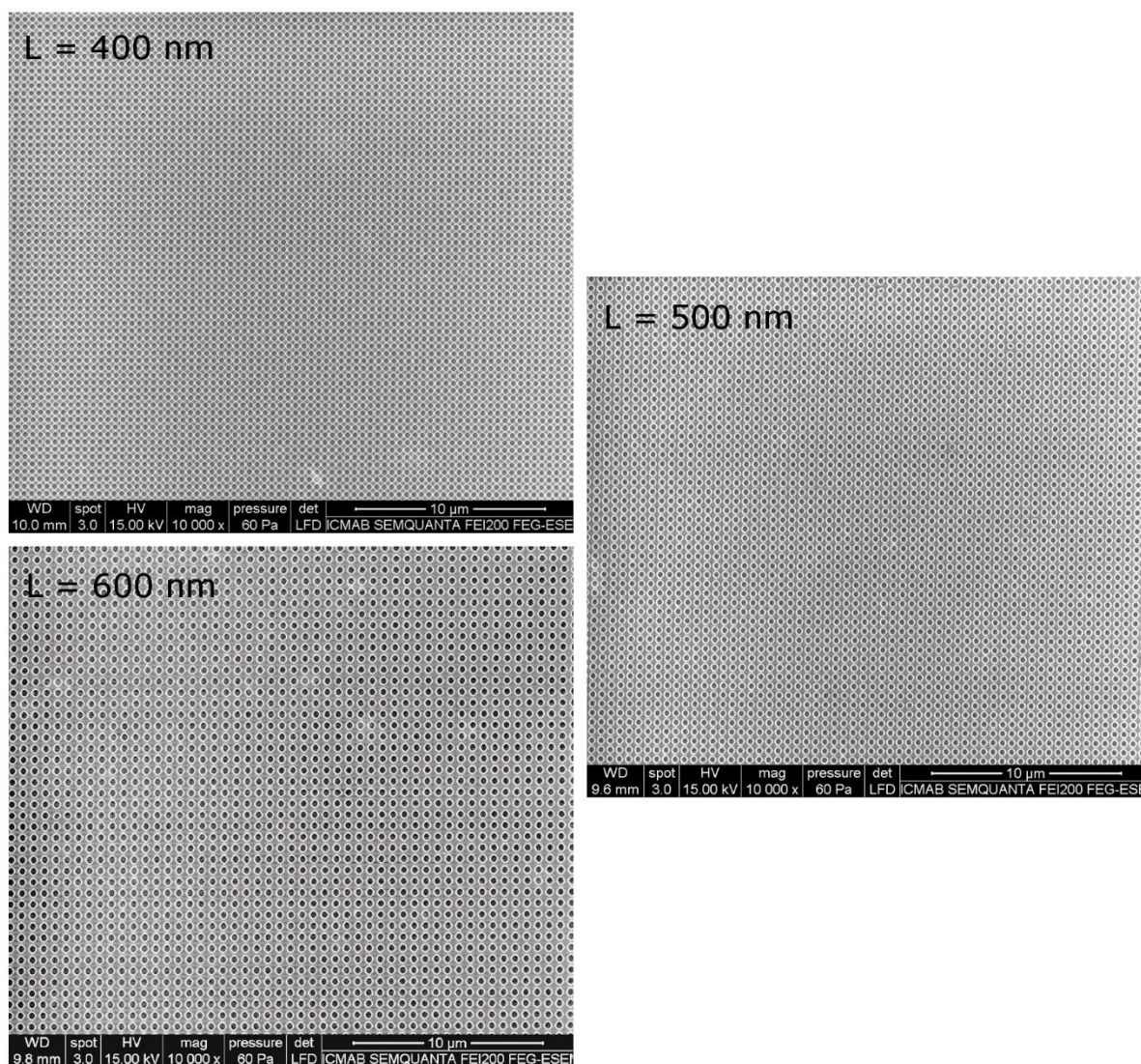


Figure S4. Additional SEM images. Scanning electron microscopy images of hydroxypropyl cellulose photonic membranes with a square lattice of imprinted holes and lattice parameters of 400, 500 and 600 nm.

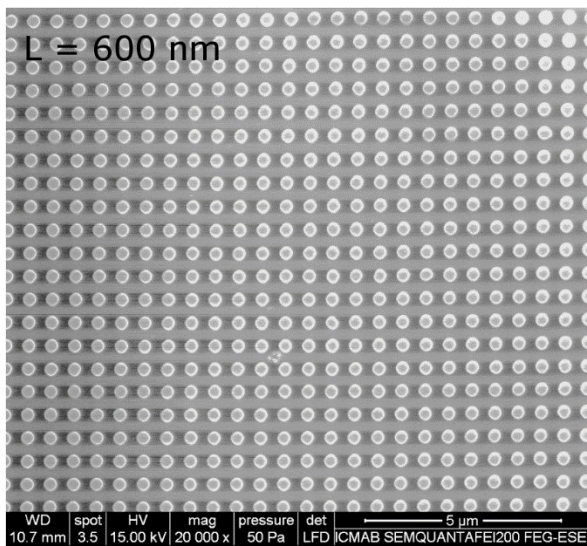
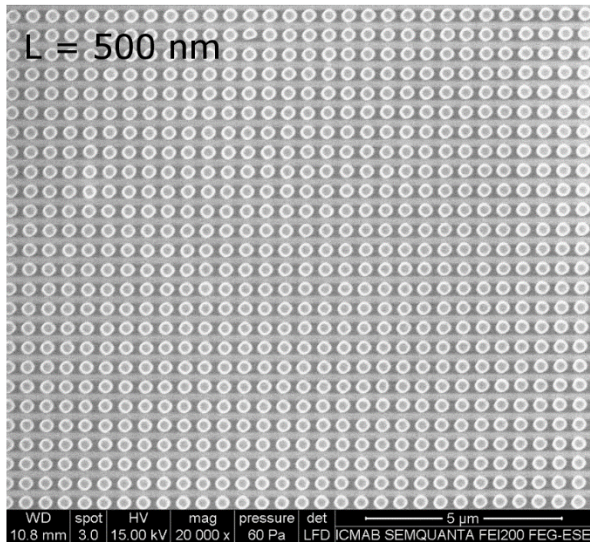
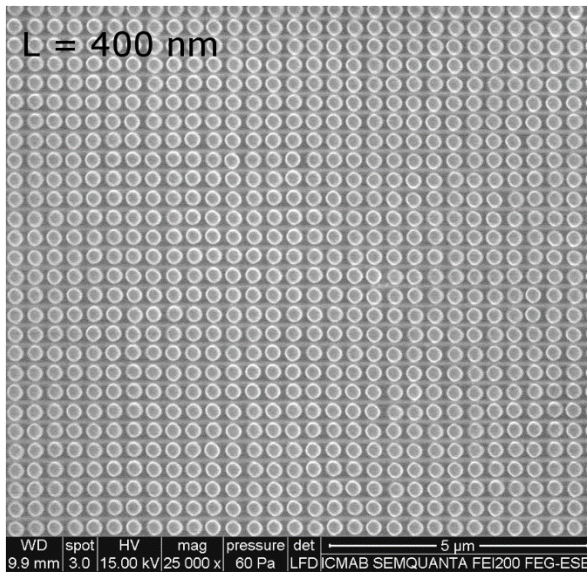


Figure S5. Additional SEM images. Scanning electron microscopy images of hydroxypropyl cellulose photonic membranes with a square lattice of imprinted pillars and lattice parameters of 400, 500 and 600 nm.

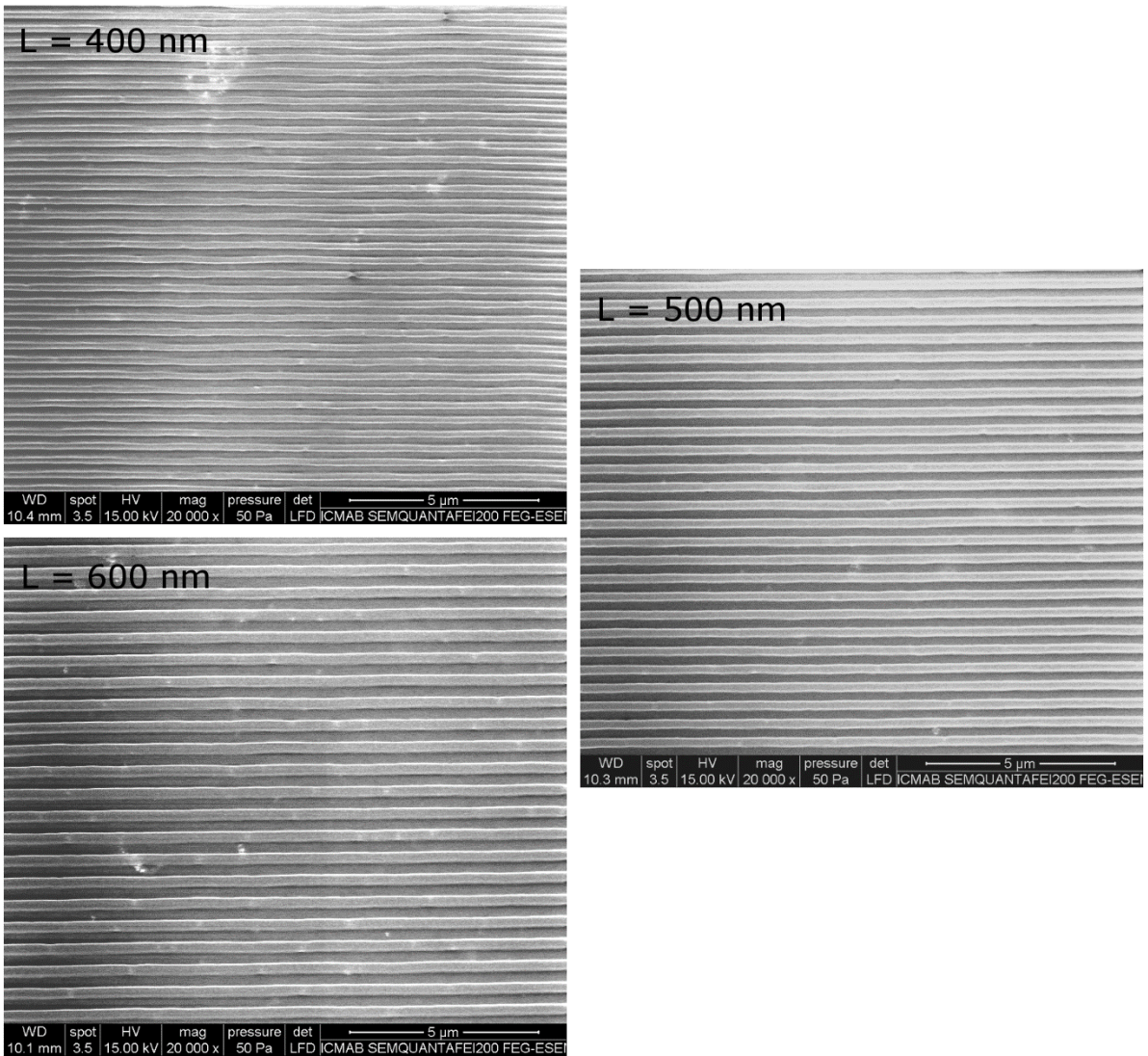


Figure S6. Additional SEM images. Scanning electron microscopy images of linear grooves imprinted in hydroxypropyl cellulose with lattice parameters of 400, 500 and 600 nm.

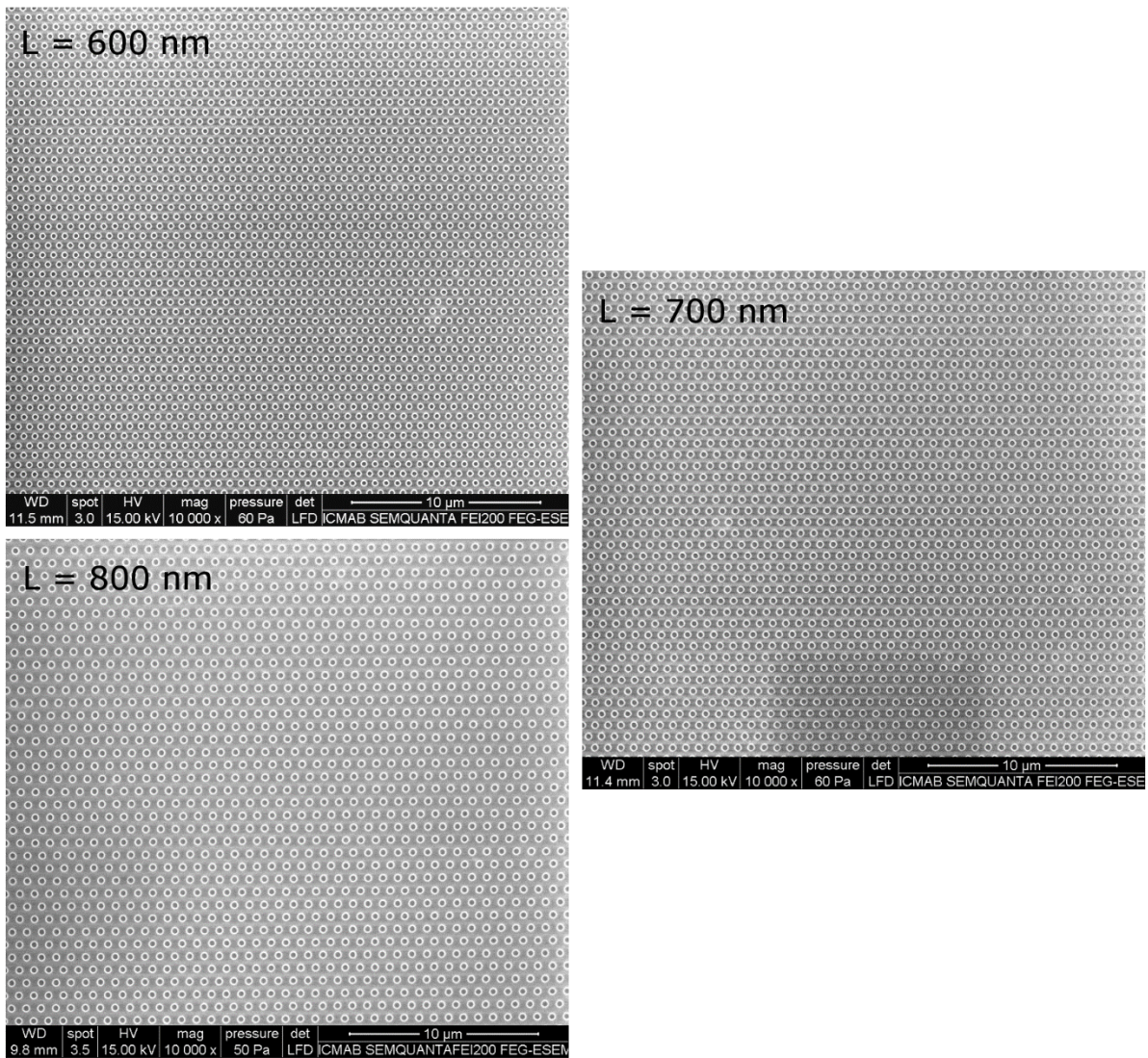


Figure S7. Additional SEM images. Scanning electron microscopy images of hydroxypropyl cellulose photonic membranes with a hexagonal lattice of imprinted holes and lattice parameters of 600, 700 and 800 nm.

4. Additional photos of samples imprinted on top of common paper.

Photonic papers or photonic inks, based on structural color have been suggested for the production of colorful systems without the use of toxic, expensive or rare pigments that generate color due to selective light absorption. In contrast, structural color is achieved by nano-structuring non-absorbent materials like HPC, suggested in this communication. In recent years also plasmonic crystals are being actively explored for photonic papers or inks applications. Nanoimprinting HPC on top of common paper and then coating it with a silver film is therefore a very convenient and straightforward way of achieving plasmonic color.

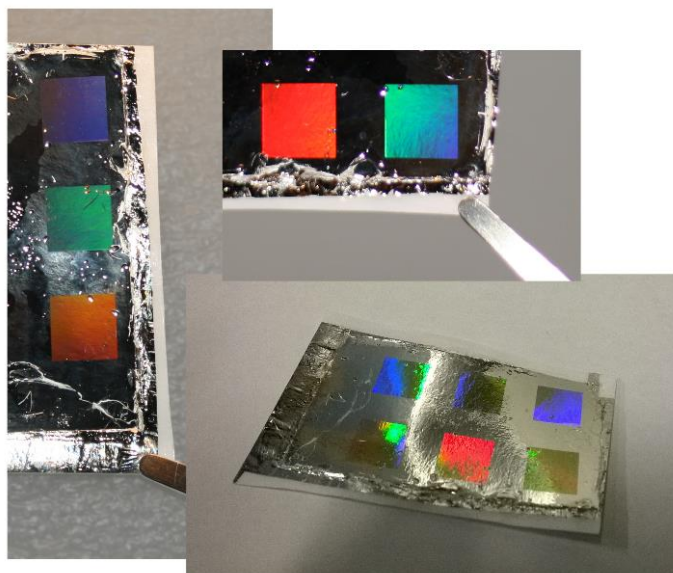


Figure S8. Photos of plasmonic crystals imprinted on paper. Photographs of plasmonic crystals imprinted on HPC and coated with silver, using regular paper as substrate. Each square corresponds to a different morphology or lattice parameter. Imprinted areas are $1 \times 1 \text{ cm}^2$.

Figure S8 shows some examples of plasmonic crystals fabricated on paper in our laboratory. Very intense colors exhibited by these crystals can be observed in the photos, demonstrating the potential of the method.

5. Photoluminescence (PL) experiments

For PL measurements, radiation from a diode laser (405 nm) or from a Ar⁺-ion gas laser (514 nm) was used as excitation source. The selection of the beam is done by changing the configuration of the entrance mirrors and holographic filters. The complete setup is depicted in Figure S9.

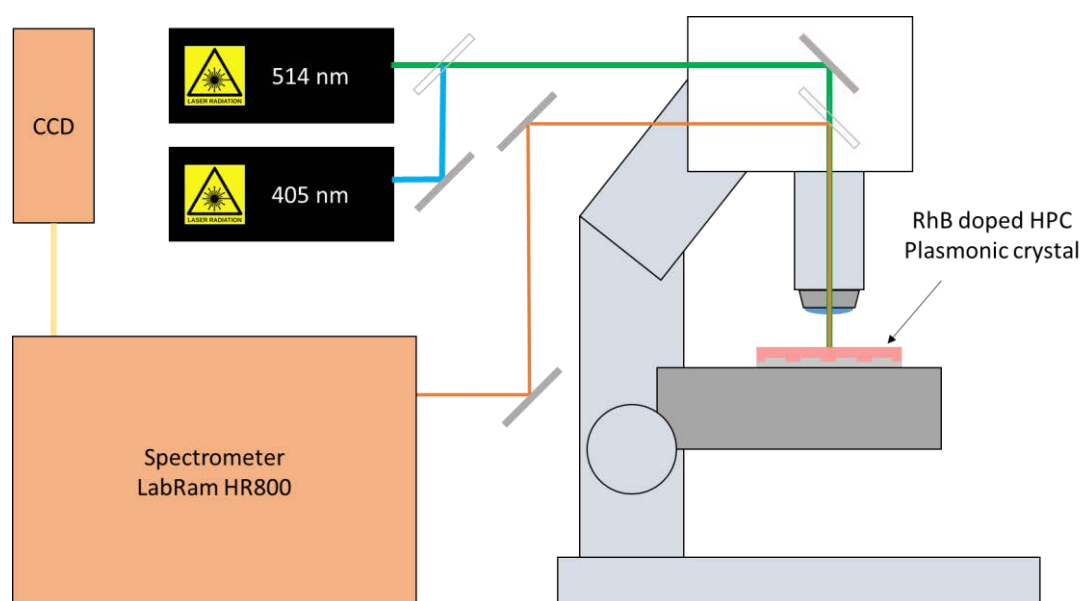


Figure S9. Experimental setup used for PL measurements. Scheme illustrating the setup used for measurements of photoluminescence.

The input laser excites the sample through an Olympus microscope equipped with a 20 × objective (NA = 0.35). Luminescence from the RhB doped HPC plasmonic crystals was collected in backscattering geometry and analyzed with a LabRam HR800 spectrometer coupled to a liquid nitrogen refrigerated CCD.

6. Micro-Raman experiments

SERS signal of thiophenol functionalized HPC plasmonic crystals was analyzed in backscattering configuration with the confocal setup WITec Alpha300 R. A simplified scheme is presented in Figure S10. Two lasers (a frequency-doubled NdYAG - $\lambda = 532$ nm or a He-Ne - $\lambda = 633$ nm) were used as excitation sources.

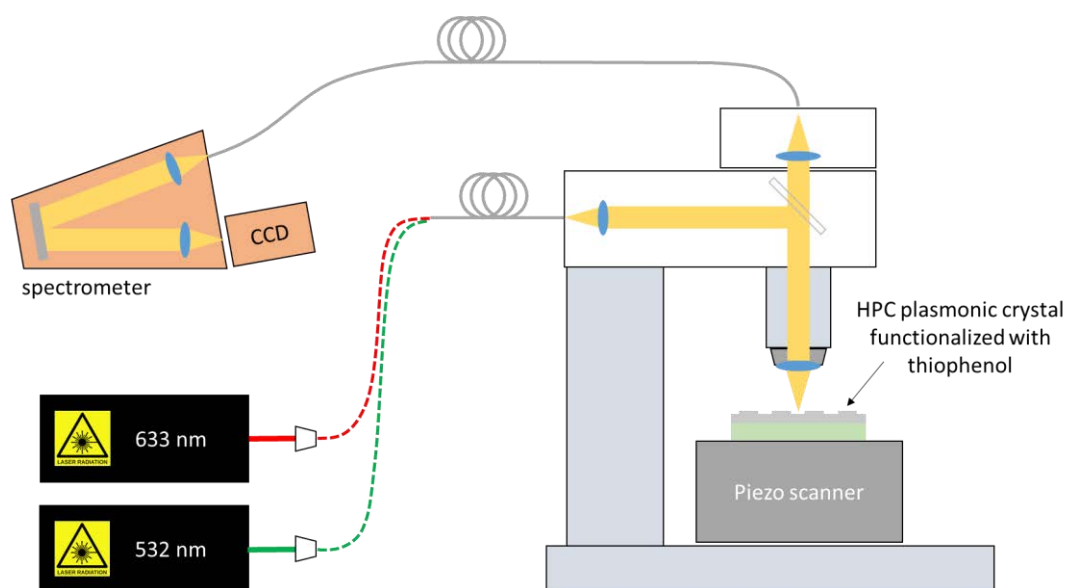


Figure S10. Experimental setup used for micro-Raman measurements. Simplified scheme illustrating the WITec Alpha300 R setup used for measurements of Raman signal.

7. Electric fields simulations.

A scheme of the cell used in FDTD calculations, in cross section, is shown in Figure S11. It extends throughout 2500 nm in the z direction. The red line marks the position of the z plane where the projection of the electric field was done. The original plots of the electric field distribution calculated using FDTD simulations along two different projections, corresponding to the samples prepared for the Raman spectroscopy experiment may be seen in Figure S12.

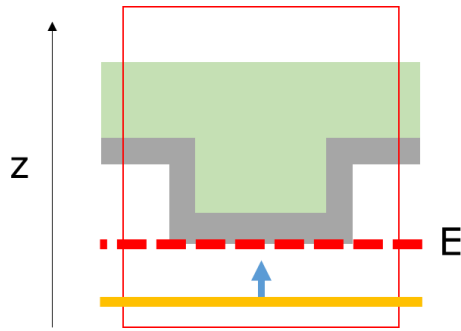


Figure S11. Cross section of FDTD cell. Scheme illustrating the cross sectional view of the cell used in FDTD calculations of HPC based plasmonic crystals. The light source is displayed in yellow and propagates upwards along the z axis. HPC crystal is illustrated in green and silver coating in gray.

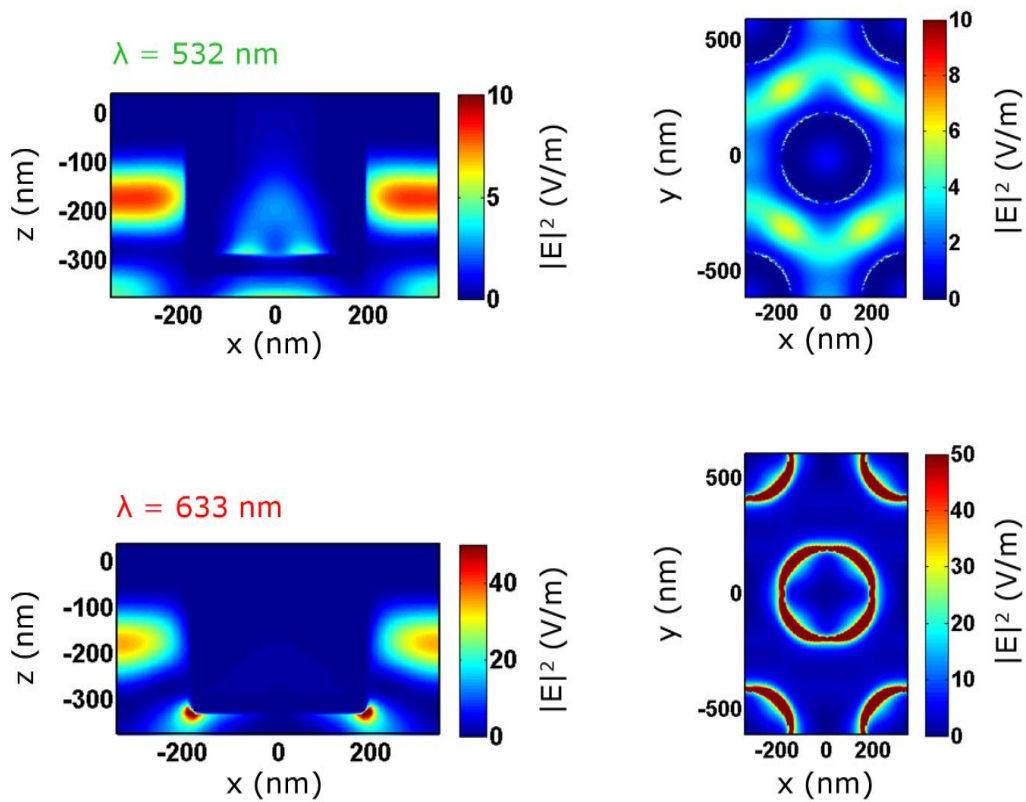


Figure S12. Electric field spatial distribution in HPC plasmonic crystals. xz and xy projections of the electric field distribution for the wavelength of 532 nm (top) and 633 nm (bottom).

Hydroxypropyl Cellulose Adhesives for Transfer Printing of Carbon Nanotubes and Metallic Nanostructures

Camilla Dore, Bernhard Döring, Juan Luis Garcia-Pomar, Mariano Campoy-Quiles, and Agustín Mihi*

Transfer printing is one of the key nanofabrication techniques for the large-scale manufacturing of complex device architectures. It provides a cost-effective and high-throughput route for the integration of independently processed materials into spatially tailored architectures. Furthermore, this method enables the fabrication of flexible and curvilinear devices, paving the way for the fabrication of a new generation of technologies for optics, electronics, and biomedicine. In this work, hydroxypropyl cellulose (HPC) membranes are used as water soluble adhesives for transfer printing processes with improved performance and versatility compared to conventional silicone alternatives. The high-water solubility and excellent mechanical properties of HPC facilitate transfer printing with high yield for both metal and carbon nanotubes (CNTs) inks. In the case of metal inks, crack-free stripping of silver films and the simple fabrication of Moiré Plasmonic architectures of different geometries are demonstrated. Furthermore, HPC membranes are used to transfer print carbon nanotube films with different thicknesses and up to 77% transparency in the visible and near infrared region with potential applications as transparent conductive substrates. Finally, the use of prepatterned HPC membranes enables nanoscale patterning of CNT with feature resolution down to 1 μm .

of conductive and semiconducting materials in organic substrates overcoming fabrication incompatibilities such as different processing temperatures, chemical resistance or solubility. Furthermore, transfer printing allows nanofabrication on nonplanar substrates, a useful trait in the production of a wide range of flexible and innovative devices, such as flexible quantum dot displays^[1] multifunctional epidermal and intracorporeal electrodes,^[2–4] 3D metamaterials,^[5,6] graphene wearable transparent electrodes,^[7,8] smart textile materials,^[9] and curvilinear optoelectronic lenses.^[10] In general, these fabrication methods employ flexible adhesive stamps to transfer certain components (called inks) from a donor substrate to a secondary receiver substrate. This usually requires two steps, namely picking up the ink from the donor substrate and its release onto the receiver substrate. The ability of the stamp to switch between strong and weak adhesion, for retrieval and printing, is a critical parameter for

the reliability and yield of transfer printing processes.


Transfer printing techniques are classified according to the methodology used to modulate the adhesion at the stamp/ink interface.^[11–13] The most common technique exploits the speed rate dependent adhesion of polydimethylsiloxane (PDMS) stamps to enable peeling or releasing the ink material by kinetic control.^[14] However, issues such as low transfer yields, and low adhesion switchability limit the versatility and reliability of this technique, hindering further implementation in high throughput processes.^[11] Furthermore, because of the intrinsic softness of PDMS, the inks are likely to be damaged by cracks or deformations. This issue is particularly relevant for transfer printing of metallic films, since it directly deteriorates the electrical properties of the transferred electrode.^[15]

A more straightforward technique is tape transfer printing, where solvent or thermal releasable adhesive tapes are implemented instead of the elastomeric stamps. This approach shows a higher reliability thanks to the stronger adhesion achievable between tape and inks, and the improved mechanical properties of tape materials, which prevents inks from cracking. Moreover, transfer printing tapes not only function as sacrificial tools for ink transfer,^[9,16] but can also act as the final receiving substrate,^[17,18] allowing to perform only the pick-up step

1. Introduction

Among the most recently developed nanofabrication techniques, transfer printing is an ideal candidate for bringing the next generation of optoelectronic devices closer to large scale manufacturing. This method is low cost and roll-to-roll compatible and allows for processing of materials and substrates separately only to be assembled in a later step. This characteristic has significantly facilitated the implementation

C. Dore, Dr. B. Döring, Dr. J. L. Garcia-Pomar, Dr. M. Campoy-Quiles, Dr. A. Mihi
Institut de Ciència de Materials de Barcelona (ICMAB-CSIC)
Campus de la UAB, Bellaterra 08193, Spain
E-mail: amih@icmab.es

 The ORCID identification number(s) for the author(s) of this article can be found under <https://doi.org/10.1002/sml.202004795>.

© 2020 The Authors. Small published by Wiley-VCH GmbH. This is an open access article under the terms of the Creative Commons Attribution-NonCommercial-NoDerivs License, which permits use and distribution in any medium, provided the original work is properly cited, the use is non-commercial and no modifications or adaptations are made.

DOI: 10.1002/sml.202004795

without requiring further processing. Solvent soluble transient tapes can be easily fabricated in a wide range of materials and offer the highest transfer yields. Among them, water soluble tapes such as hyaluronic acid or polyvinyl alcohol adhesives, have the additional appeal of allowing their implementation in biocompatible and biodegradable flexible devices.^[9,16] These technologies have recently produced extraordinary feats: from the easier substitution of traditional substrates by inexpensive alternatives with a smaller environmental footprint,^[19,20] to innovative medical electronic devices.^[21–23]

In this work we propose the use of cellulose derivatives as water soluble tapes, demonstrating improved performance compared to traditional silicone transfer and higher versatility and lower complexity compared to transfer processes employing other soluble tapes (see Section S8, Supporting Information). Cellulose is the most abundant polymer on Earth, has been widely investigated and a huge variety of cellulose derivatives are currently commercialized and implemented as substrate in a new generation of flexible and biocompatible electronic devices^[24,25] and in low cost paper-based technologies such as transient or edible labels for food industry,^[26,27] biosensors and biomedical devices,^[28] photovoltaic cells,^[29] and paper displays.^[30] Among cellulose derivatives, hydroxypropyl cellulose (HPC) is a commercially available, low cost, and biocompatible material that can form flexible and transparent membranes with excellent mechanical properties.^[20] HPC is a cellulose ether in which the hydroxyl groups on the cellulose backbone have been hydroxypropylated. HPC is fully soluble in water at temperatures below the cloud-point, which is around 45 °C) and in most of the organic solvents (ethanol, isopropyl alcohol, and acetone), hot or cold.^[31]

In this work, we employ HPC as versatile adhesives for straightforward transfer printing of nanostructured materials. In particular, we fabricate HPC adhesive membranes that can act both as sacrificial water-soluble transfer tapes and as the final substrate for applications in transient optoelectronics. In the first section of this work, we describe the use of the cellulose membranes as water soluble transfer tapes, demonstrating their high performance in transfer printing of nanopatterned metallic films. HPC mediated transfer printing, provides a crack-free process, while keeping large area (cm²) and high throughput production. Besides the use of HPC as sacrificial layer, the capability to rapidly integrate nanostructures directly into the HPC paves the way for novel functional transient metallic or carbon nanotubes (CNTs) based electrodes, as shown in the second part of the paper. Finally, we implement prepatterned HPC membranes for μ contact printing of CNTs, achieving in a single step large area patterning and transfer of CNTs arrays with feature sizes down to 1 μ m.

2. Results and Discussion

Cellulose-based materials meet most of the requirements of a good adhesive, due to their semicrystalline structure and complex network of interactions, both hydrophilic (such as hydrogen bonding) and hydrophobic.^[32] HPC solutions in water and alcohol, for instance, are currently implemented as ecofriendly glues for leather binding and paper restoration

(e.g., KlucelG). Bioadhesive properties of HPC films to human skin have also been already demonstrated both in liquid crystalline solutions^[33] and in hot-melt extruded films.^[34]

A key parameter for a good adhesive is to provide enough deformation to conformally contact the substrate, maximizing the total adhesion force. Thus, adhesive tapes should ideally provide low hardness surfaces, but at the same time, they should guarantee high cohesive strength and mechanical stability to withstand stresses during pick-up and to avoid damage during handling. Interestingly, dry films of HPC show thermo-plastic behavior with a dual glass transition temperature: a beta transition in the side chains at around 0 °C, which provides increased plasticity and flexibility at lower temperatures, and a second one at 150 °C.^[31] This means that HPC softens and deforms plastically and at relatively low temperatures, passing smoothly from a viscoelastic behavior to a viscous one for temperatures closer to its second T_g . Furthermore, the Young modulus of HPC is 110 MPa at room temperature,^[35] about 100 times higher than PDMS. This characteristic is of great advantage for transfer printing, particularly during the pick-up and handling steps, since it reduces the mechanical stress induced to the ink during bending and stretching, preventing it from cracking.^[16] Another advantage of HPC comes from its mixed hydrophilic–hydrophobic behavior (see Section S1, Supporting Information) meaning it can be rapidly dissolved both in water and in most organic solvents at room temperature. Since the membrane can be simply dissolved after transfer, successful deposition of the material on the receiver substrate does not depend on the interface interaction between the transferred material and receiver substrate. With HPC, no complex chemical treatments are required and it is possible to transfer a wider range of materials on a wider range of substrates in an easier and straightforward way.

Our transfer printing process is carried out using a flat HPC membrane supported by a PDMS slab as illustrated in **Figure 1a**. Here we chose to transfer a continuous 50 nm thick Ag membrane patterned with a square array of nanoholes (diameter $\phi = 300$ nm, lattice parameter $l = 500$ nm) obtained evaporating the metal on top of a silicon template. Metallic nanohole arrays have attracted great interest in the literature for exhibiting extraordinary optical transmission among other plasmonic properties, finding application as transparent conductive electrodes and metamaterials.^[36–38]

Figure 1a shows a schematic of the template-assisted transfer printing technique used to pick and place the nanopatterned silver films from their donor silicon templates onto the new surfaces (flat or curved glass substrates). The HPC membrane/PDMS slab is pressed against the metal ink for 2 min at 80 °C (i). This temperature has been found optimal to ensure pick-up of only the top silver layer, providing at the same time enough plastic deformation to conformally contact the metal while maintaining sufficiently high viscosity to avoid percolation of HPC into the silicon template features. After cooling down, the HPC/PDMS stack is simply lifted off from the donor substrate with the nanostructured metal attached to the HPC membrane (ii). It is worth emphasizing that we can easily pick up 1 cm \times 1 cm areas of patterned silver films without requiring any chemical modification of the silicon surface. The as obtained HPC/metal stack is then pressed against the recipient substrate

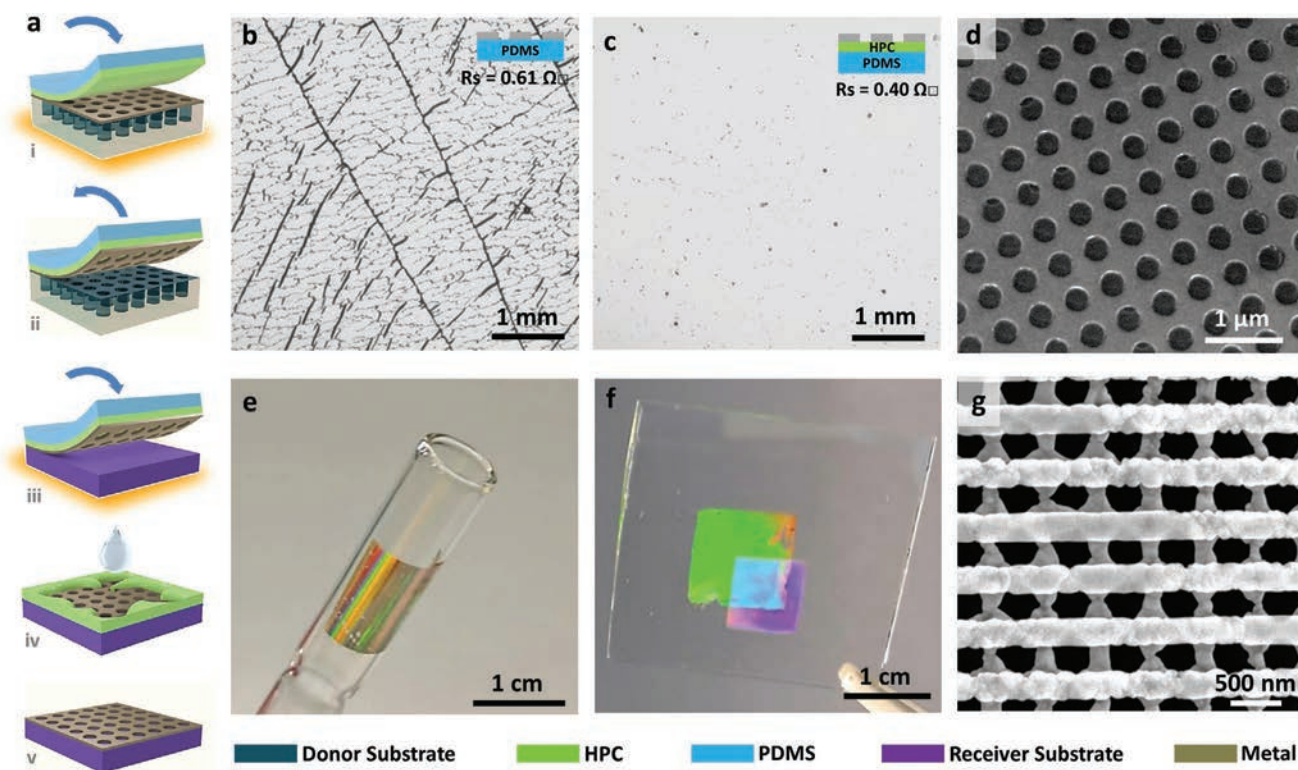


Figure 1. a) Schematic of the transfer printing technique used to pick and place nanopatterned silver films. b,c) $2\times$ optical microscope images and sheet resistance values (R_s) of 50 nm thick silver films transferred using HPC/PDMS and bare PDMS, respectively. d) SEM picture of the sample in (c). e) Photo of nanopatterned silver film transferred to a curved surface. f) Multilayer silver nanostructures on glass obtained by HPC double transfer. Silver films thickness is 50 nm. Iridescent colors arise from: holes arrays (green), lines array (purple) and patterns overlapping area (blue). g) SEM image of the overlapping area in (f).

(iii). During this step pressure and temperature are applied to soften the HPC adhesive, ensuring complete evacuation of the air at the interface and conformal contact with the receiver substrate. After cool down, the HPC/metal stack becomes attached to the receiver substrate and the PDMS support can be easily released. The as obtained sample is then rinsed with water to dissolve the HPC layer (iv), leaving the target material physically attached to the receiver substrate (v).

As can be seen in Figure 1b–d, the reduced strains occurring in the HPC film, prevent the transferred metal layer from cracking, unlike what is observed in the case of bare PDMS mediated transfer printing. This characteristic is of great advantage when the goal is to transfer metal contacts. We measured the sheet resistance of the 50 nm silver on glass obtained respectively by the HPC/PDMS mediated transfer developed in this work (Figure 1c) and by the standard PDMS transfer (Figure 1b). We measured a value of $0.6 \Omega \text{ sq}^{-1}$ for the PDMS transferred film, while in the case of HPC/PDMS the sheet resistance is as low as $0.4 \Omega \text{ sq}^{-1}$ (see Section S2 of the Supporting Information for further details). Despite the larger Young modulus of the HPC, the thin membranes employed in this work maintained a high flexibility, which allows to easily place the Ag plasmonic ink onto curved surfaces as shown in Figure 1e. By simply iterating the transfer printing method illustrated in Figure 1a, complex metal multilayer architectures can be easily achieved. To illustrate the potential of HPC adhesives for multilayer nanofabrication, we built 3D metamaterials

by subsequently stacking nanopatterned silver films with different geometries. Figure 1f shows an array of silver lines transferred on top of the 2D silver array of holes on a glass slide. The two patterned films (Figure 1f) are shifted with respect to each other to better identify each component and the overlapping area, which is further detailed in the SEM (Figure 1g). In this work aligning of the patterns has been done by eye, obtaining a precision of $\pm 1^\circ$ (calculated measuring the twisting angles a posteriori). Using this technique, we stacked Ag lines with varying lattice parameters (from 400 until 600 nm) on top of 500 nm holes arrays (Figure 2c,d) and measured their optical properties. The extinction of the 3D metamaterials (Figure 2e,f) was obtained from reflectance and transmittance measurements (Figure S3, Supporting Information). These values were compared with their corresponding theoretical values calculated via finite-difference time-domain (FDTD) method. The good agreement between both sets of data is depicted in Figure 2e,f, highlighting the high quality of the plasmonic stack. The versatility of this approach allows for crack free fabrication of countless exotic structures with tailored functionality and in a scalable manner. Further examples can be found in Figures S3–S7 of the Supporting Information, and further investigation of the optical properties and their dependence on the twisting angle are detailed in Section S4 of the Supporting Information.

As inferred from the SEM images in Figure 2, this technique is uniquely suited to fabricate Moiré metamaterials. Moiré photonic lattices have received increasing attention lately since they allow

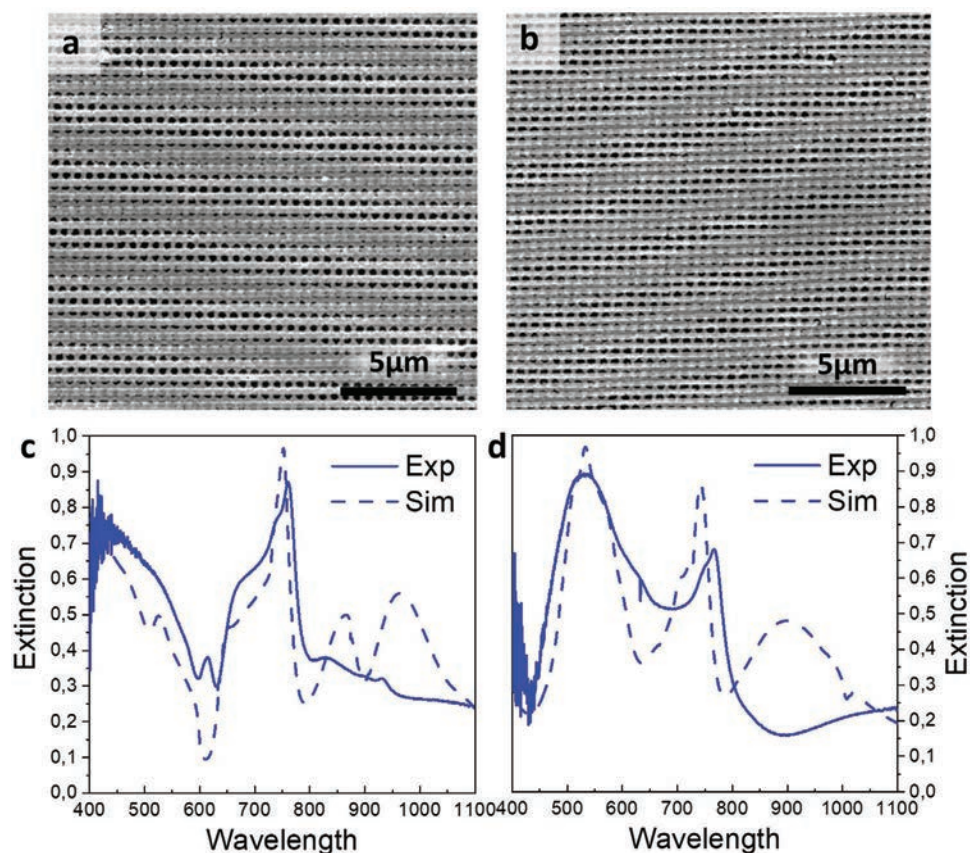


Figure 2. Stacked silver nanostructures on glass obtained by HPC double transfer SEM images from a) lines (600 nm pitch) on top of hole array (500 nm pitch) and b) lines (400 nm pitch) on top of hole array (500 nm pitch). c,d) Simulated (dashed line) and experimental (continuous line) extinction from samples a) and b) respectively.

the exploration of transitions between structures with fundamentally different geometries (periodic, general aperiodic, and quasicrystalline).^[39] However achieving these kind of architectures scalably and with high optical quality remains a daunting challenge.^[37,40] Here we use our HPC adhesives to produce Moiré patterns by stacking square arrays of discrete silver nanoparticles (NPs). The two Ag NP arrays are twisted with respect to each other and separated by an HPC layer whose thickness can be precisely adjusted to provide an additional functionality and tunability of the optical properties. For instance, the HPC film can host an organic dye as it has been shown elsewhere.^[20]

The fabrication process of the Moiré metamaterials (Figure 3a) begins with the thermal evaporation of 50 nm on top of a PDMS mold prepatterned with an array of pillars. The Ag coated PDMS is pressed against an HPC film previously spin-coated on a glass slide. This process takes place for 5 min using a nanoimprinting tool (NILT) at 0.5 bar and 80 °C, after which the system is allowed to cool down to room temperature and the mold released. As a result, the array of Ag NPs is transferred from the PDMS mold to the HPC film. Next, we deposit an HPC thin film as a spacer on top of the already transferred Ag array. To do so, we spin cast HPC on a PDMS flat mold to form a thin film and then, we transfer it onto the Ag nanostructure using the same NILT settings. HPC films with thicknesses ranging from 200 to 1000 nm can be fabricated via direct spin-coating on the PDMS slab as described in the Experimental Section. Finally, simply repeating

the first step, a second layer of NPs is placed on top of the spacer introducing a desired twisting angle.

The large area patterns used in this work (1 cm²) greatly facilitate the handling and orientation of the membranes in this last process. SEM images (Figure 3b–d) clearly show the twisting angle-dependent patterns that arise when two NP arrays are stacked on top of each other. For a twisting angle of 10°, the formation of a square Moiré superlattice with a new superperiod of 6 μm is clearly visible and responsible for the diffraction pattern shown in the inset of Figure 3e. Smaller twisting angles lead to larger periodicities (see Figure S6, Supporting Information) while increasing the angle leads to a more complex pattern (Figure 3b corresponds to a 45° twist bilayer). The differences in the superlattice formation are also observed in the diffraction pattern from both 10° and 45° twisted metasurfaces when illuminated with a 532 nm laser.

To illustrate the influence of the thickness of the HPC interlayer on the optical properties, the transmittance spectra from different spacer thickness are shown in Figure 3f. The fixed NP bilayer indeed act like a cavity sustaining Fabry–Perot modes as can be seen from the thickness dependent features in the mid infrared range in the transmission. Cavity-coupled plasmonic systems with tunable resonances and Moiré interferences are particularly promising for application in information encoding^[41] and in anticounterfeiting.^[42,43] To the best of our knowledge this is the first demonstration of the integration

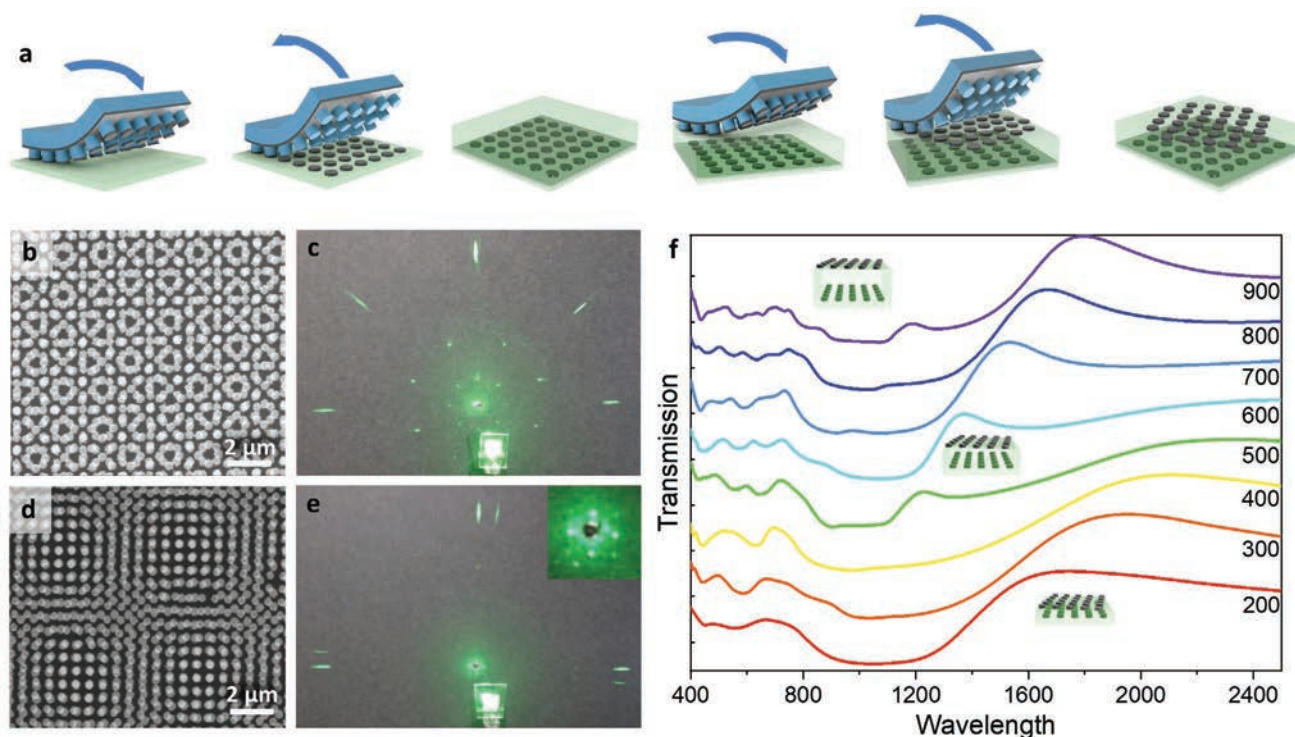


Figure 3. Multilayer silver nanoparticles arrays embedded in HPC. a) Schematic of the procedure used to transfer print plasmonic arrays from a PDMS mold to an HPC film. b–d) SEM back scattered electron image of double particle arrays in HPC. The thickness of the particles is 50 nm, the diameter is 330 nm, and lattice period is 600 nm. The rotation angles between 1st and 2nd layer are respectively 45° and 10°. c–e) Diffraction patterns from samples (b) and (d), respectively. f) Transmission spectra of double layer with HPC interlayer thickness ranging from 200 to 900 nm. Particle diameter is 300 nm, with lattice period of 500 nm and rotation angle of 40°.

of those structures in a cellulose-based material, using a cost effective and scalable fabrication technique. Most of the integration of functional materials in paper-based substrates, indeed, relies on the spraying of functional inks, which limits material performance by restricting the minimum feature size achievable to the order of tenths of micrometers, or requires complex fabrication protocols that are not compatible with large scale manufacturing.^[11,44,45]

Our technique can be applied to a wide variety of inks while simultaneously providing means for high-resolution nanopatterning. In this next section, we apply the HPC adhesives to transfer printing of CNTs. CNTs are a particularly promising material for flexible electronics and for implementation as transparent electrodes, due to their high conductivity, carrier mobility, and superior mechanical properties.^[46,47]

Here, the same fabrication process illustrated in Figure 1a, is used to transfer 50 to 100 nm thick films of CNTs (CoMoCAT, Sigma-Aldrich) from filter paper to the HPC adhesive. By pressing a flat HPC membrane for 3 min at 0.5 bars and 100 °C against the CNT film, we obtained a flexible stack in which the dense pattern of CNTs was completely transferred to the HPC (Figure 4a,b). Macrodesigns of the CNT area can be easily achieved by cutting the filter paper in the desired shape before transferring, as illustrated in Figure 4a. Interestingly, the thickness of the CNT film transferred to the HPC can be tuned by changing the temperature applied before the pick-up step, allowing obtaining HPC–CNTs flexible stacks with tailored transparency. The key to transfer CNT films with different

thickness resides in the different percolation depth of the HPC in the CNT network at different temperatures as schematized in Figure S8 of the Supporting Information. For pick-up temperatures below 80 °C indeed, the decreased viscosity of the HPC membrane hinder the percolation of the polymer into the CNT film, which, in this way, is only partially transferred to the HPC membrane. Figure 4c shows the transmission spectra of HPC membranes with CNTs with decreasing thickness, in comparison with the most commonly used transparent conductive substrates in optoelectronics; indium-doped tin oxide (ITO) and fluor-doped tin oxide (FTO). Here, pick-up temperatures have been set to 70, 60, and 50 °C obtaining respectively 30, 20, and 15 ± 5 nm CNT film thicknesses. In this preliminary work we measured the sheet resistance of the CNT electrodes to be as low as 305 Ω sq⁻¹ with a 77% averaged transparency in the 450–1100 nm wavelength range. Detailed electrical characterization of CNT semitransparent electrodes transfer printed using HPC membranes is reported in Section S6 of the Supporting Information.

The definition of active areas in most devices relies on the fabrication of electrodes with specific sizes and shapes, often achieved by evaporation of metals through shadow masks. Following the same rational, in order to fully exploit the potential of CNTs networks as functional electrodes, it is therefore crucial to find high throughput processes that allow to pattern them with high-lateral resolution, over large areas, and to deposit them on arbitrary substrates. To address this issue, we used prepatterned HPC membranes as transient molds for μ-contact

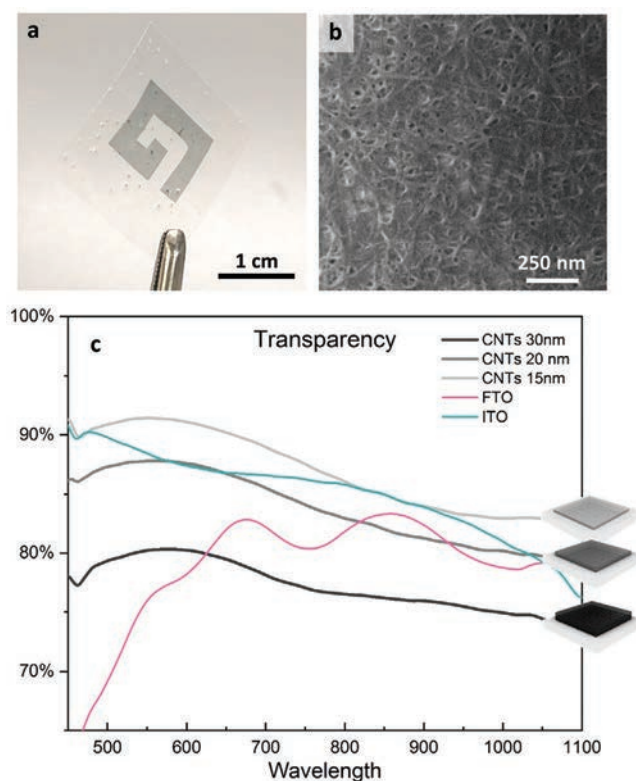


Figure 4. CNTs integrated in HPC membranes. a) HPC membrane after CNTs pick up at 100 °C from a G shaped paper filter. b) SEM of the CNTs film. c) Transmission spectra of CNT films with decreasing thickness of 30 nm (black), 20 nm (dark gray), and 15 nm (light gray) compared with commercial substrates ITO (Ossila) and FTO (Xop Glass).

printing of carbon nanotubes, testing the performances of the process in terms of lateral features resolution. Compared to the previously described template assisted process, in which we use flat HPC stamp to pick up metallic films from patterned templates, here CNTs patterning is obtained by stamp selective pick-up (so-called “stamp inking”) from a continuous film of CNTs. HPC membranes indeed can be easily molded with feature size down to 100 nm as already described in our prior work.^[19] The process is illustrated in Figure 4a: the prepatterned HPC adhesive is pressed against a continuous film of CNTs, selectively picking up the material. The CNT-inked HPC stamp can be now placed on the receiver substrate and dissolved in water, leaving CNT micropatterns attached to the target surface.

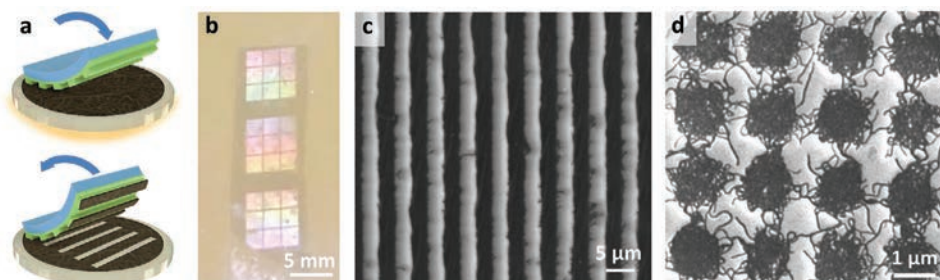


Figure 5. CNTs microstructures arrays fabricated via μ -contact printing technique. a) Schematic of selective CNTs pick-up technique using patterned HPC membrane. b) Iridescent colors arising from 3 μ m wide CNTs lines array transferred to glass. c) SEM picture of lines array in (b). d) SEM image of 1 μ m CNTs dot arrays transferred to glass. Lattice parameter is 1.7 μ m.

Using patterned HPC membranes, large area homogenous micropatterns of conductive CNTs showing iridescence under white light have been fabricated (Figure 5b,c). The best resolution obtained in this preliminary research corresponds to the 1 μ m dot array, illustrated in Figure 5d. The correct setting of temperature, pressure, and time during the pick-up step is the key for obtaining pattern resolution down to the μ m scale. Considering a viscoelastic flow of the polymer, plastic deformations at the nanometer scale (i.e., at the CNT–HPC interface) will occur at faster rates than the ones at micrometer scale (i.e., the HPC stamp features).^[48] It is therefore necessary to find a tradeoff which allows for percolation of the stamp protrusion in the CNTs film, but that at the same time avoids excessive deformation of the micropattern in the HPC mold. The patterns shown in Figure 5 have been obtained setting the temperature to 100 °C and the pressure to 0.5 bar for 20 s. Longer times led to deformation of the HPC mold hence a loss of resolution. On the other hand, lower time or temperatures provide only partial percolation of the protrusions in the CNTs, with consequent only partial pick up of the film and loss of optical contrast.

3. Conclusions

HPC membranes are promising platforms for the rapid integration of a wide range of functional materials into flexible and biocompatible and water soluble substrates. Here, we have demonstrated the use of HPC membranes as adhesives for improved transfer printing of metallic and CNT nanostructures. Our approach stands out for its higher simplicity and versatility compared to other water soluble tables (see Section S8, Supporting Information). In sum, both continuous and discrete metallic films are successfully stripped from silicon and PDMS templates without requiring any additional surface treatment. The inks can be transferred to the receiving substrate in a completely crack free manner and the HPC simply dissolved in water. Thanks to its mechanical properties and high solubility in water at room temperature, HPC enables fast and reliable transfer printing process. Furthermore, HPC tapes are versatile platforms, which enable advanced nanofabrication routes: multiple ink layers can be easily stacked, offering a rapid method to obtain Moiré architectures with tunable optical properties. Finally, we also demonstrate the validity of the HPC adhesives for the simultaneous transfer and nanostructuring of CNTs conductive layers, obtaining tunable thicknesses and lateral feature sizes down to 1 μ m.

4. Experimental Section

Materials: Silicon templates, PDMS molds, and HPC membranes were fabricated as described in the previous works.^[19,20] Hard PDMS silicone elastomer kit was purchased from Gelest (Morrisville, PA 19067, USA) and soft PDMS Sylgard184 silicone elastomer kit from Dow Corning Corporation (Auburn, MI 48611, USA). HPC, with average Mw ≈ 100 000, powder, 20 mesh particle size (99% through), and degree of substitution DS = 3, was purchased from Sigma-Aldrich.

CNTs Films: CoMoCAT CNTs (SG65i) were obtained from Sigma-Aldrich and used as received. 0.2 mg mL⁻¹ of CNTs were dispersed in water, using 2 mg mL⁻¹ of sodium dodecylbenzenesulfonate as surfactant. After 15 min of tip-sonication the dispersion was centrifuged and the supernatant was used to prepare samples via vacuum filtration. To this end, several milliliters of dispersion were filtered with PVP-coated polycarbonate filters with a pore size of 0.1 μm. The films were washed with copious amounts of water to remove the surfactant, and then dried at room temperature.

Simulations: Numerical calculations were performed using Lumerical FDTD solutions (www.lumerical.com). A polarized plane wave source, with electric field transversal to the lines, impinging at normal incidence to different samples was modeled in a Moiré unit cell with periodic boundaries. Finally, only the normal diffraction order was considered to achieve similar conditions to the experimental setup. The complex refractive index of silver was obtained.^[49] The glass substrate was set with a refractive index of $n_{\text{glass}} = 1.46$.

Flat PDMS Slabs: PDMS slabs were fabricated by pouring a Sylgard184 with curing agent to prepolymer ration equal to 1:10 on top of a silicon wafer and curing for 4 h at 60 °C. An aluminum frame was used to obtain 1 cm thick slabs.

HPC Spacer Layers: 27 mg mL⁻¹ HPC solution in water was poured on the flat PDMS slab and spin-coated at 4000 rpm, obtaining films of 100 nm thickness. Film thickness was measured by transferring the film to silicon substrates and numerical fitting of the Fabry–Perot oscillations from the experimental reflection spectra using the transfer matrix formalism. Thicker spacers ranging from 200 to 900 nm were obtained by subsequent stacking of the 100 nm thick layers.

Samples Characterization: The reflectivity and transmission of the samples were measured using a Fourier transform infrared spectrometer (Bruker Vertex 70) attached to a microscope with a 4× objective. Optical properties of lines-holes bilayer arrays were measured with light polarized transversally to the line direction. SEM QUANTA FEI 200 FEG-ESEM was used to characterize the morphology of the transferred patterns. CNT film thickness and HPC spacers with variable thickness were measured using an Alpha-Step D-500 Profilometer from KLA Tencor. Sheet resistance was measured on ≈15 × 15 mm² samples using the van der Pauw method.

Supporting Information

Supporting Information is available from the Wiley Online Library or from the author.

Acknowledgements

This project received funding from the European Research Council (ERC) under the European Union's Horizon 2020 research and innovation program (Grant Agreement No. 637116, ENLIGHTMENT and No. 648901) and the Generalitat de Catalunya program AGAUR 2017-SGR-00488. The Spanish Ministerio de Ciencia e Innovación is gratefully acknowledged for its support through Grant Nos. PGC2018-095411-B-I00, PID2019-106860GB-I00, and SEV-2015-0496, in the framework of the Spanish Severo Ochoa Centre of Excellence program. This work was done in the framework of the doctorate in Materials Science of the Autonomous University of Barcelona.

Conflict of Interest

The authors declare no conflict of interest.

Keywords

carbon nanotubes, hydroxypropyl cellulose, large scale, Moiré metamaterials, scalable, transfer printing, water soluble

Received: August 6, 2020

Revised: September 18, 2020

Published online:

- [1] T.-H. Kim, K.-S. Cho, E. K. Lee, S. J. Lee, J. Chae, J. W. Kim, D. H. Kim, J.-Y. Kwon, G. Amaratunga, S. Y. Lee, B. L. Choi, Y. Kuk, J. M. Kim, K. Kim, *Nat. Photonics* **2011**, *5*, 176.
- [2] Y. Chen, Y. Zhang, Z. Liang, Y. Cao, Z. Han, X. Feng, *npj Flex Electron.* **2020**, *4*, 2.
- [3] T. Someya, Z. Bao, G. G. Malliaras, *Nature* **2016**, *540*, 379.
- [4] W.-H. Yeo, Y.-S. Kim, J. Lee, A. Ameen, L. Shi, M. Li, S. Wang, R. Ma, S. H. Jin, Z. Kang, Y. Huang, J. A. Rogers, *Adv. Mater.* **2013**, *25*, 2773.
- [5] D. Chanda, K. Shigeta, S. Gupta, T. Cain, A. Carlson, A. Mihi, A. J. Baca, G. R. Bogart, P. Braun, J. A. Rogers, *Nat. Nanotechnol.* **2011**, *6*, 402.
- [6] S. Lee, B. Kang, H. Keum, N. Ahmed, J. A. Rogers, P. M. Ferreira, S. Kim, B. Min, *Sci. Rep.* **2016**, *6*, 27621.
- [7] M. K. Choi, I. Park, D. C. Kim, E. Joh, O. K. Park, J. Kim, M. Kim, C. Choi, J. Yang, K. W. Cho, J.-H. Hwang, J.-M. Nam, T. Hyeon, J. H. Kim, D.-H. Kim, *Adv. Funct. Mater.* **2015**, *25*, 7109.
- [8] D. Song, A. Mahajan, E. B. Secor, M. C. Hersam, L. F. Francis, C. D. Frisbie, *ACS Nano* **2017**, *11*, 7431.
- [9] J. Ko, Z.-J. Zhao, S. H. Hwang, H.-J. Kang, J. Ahn, S. Jeon, M. Bok, Y. Jeong, K. Kang, I. Cho, J.-H. Jeong, I. Park, *ACS Nano* **2020**, *14*, 2191.
- [10] H. C. Ko, M. P. Stoykovich, J. Song, V. Malyarchuk, W. M. Choi, C.-J. Yu, J. B. Geddes, J. Xiao, S. Wang, Y. Huang, J. A. Rogers, *Nature* **2008**, *454*, 748.
- [11] C. Linghu, S. Zhang, C. Wang, J. Song, *npj Flex Electron.* **2018**, *2*, 26.
- [12] A. Carlson, A. M. Bowen, Y. Huang, R. G. Nuzzo, J. A. Rogers, *Adv. Mater.* **2012**, *24*, 5284.
- [13] H. Zhou, W. Qin, Q. Yu, H. Cheng, X. Yu, H. Wu, *Nanomaterials* **2019**, *9*, 283.
- [14] M. A. Meitl, Z.-T. Zhu, V. Kumar, K. J. Lee, X. Feng, Y. Y. Huang, I. Adesida, R. G. Nuzzo, J. A. Rogers, *Nat. Mater.* **2006**, *5*, 33.
- [15] M. J. Lee, J. Kim, J. S. Lee, Y. S. Kim, *J. Mater. Chem.* **2010**, *20*, 2746.
- [16] R. F. Tiefenauer, K. Tybrandt, M. Aramesh, J. Vörös, *ACS Nano* **2018**, *12*, 2514.
- [17] C. Zheng, Y. Shen, M. Liu, W. Liu, S. Wu, C. Jin, *ACS Nano* **2019**, *13*, 5583.
- [18] Q. Wang, W. Han, Y. Wang, M. Lu, L. Dong, *Microsyst. Nanoeng.* **2018**, *4*, 31.
- [19] C. Dore, J. Osmond, A. Mihi, *Nanoscale* **2018**, *10*, 17884.
- [20] A. Espinha, C. Dore, C. Matricardi, M. I. Alonso, A. R. Goñi, A. Mihi, *Nat. Photonics* **2018**, *12*, 343.
- [21] S.-W. Hwang, H. Tao, D.-H. Kim, H. Cheng, J.-K. Song, E. Rill, M. A. Brenckle, B. Panilaitis, S. M. Won, Y.-S. Kim, Y. M. Song, K. J. Yu, A. Ameen, R. Li, Y. Su, M. Yang, D. L. Kaplan, M. R. Zakin, M. J. Slepian, Y. Huang, F. G. Omenetto, J. A. Rogers, *Science* **2012**, *337*, 1640.
- [22] D.-H. Kim, N. Lu, R. Ma, Y.-S. Kim, R.-H. Kim, S. Wang, J. Wu, S. M. Won, H. Tao, A. Islam, K. J. Yu, T.-i. Kim, R. Chowdhury, M. Ying, L. Xu, M. Li, H.-J. Chung, H. Keum, M. McCormick, P. Liu, Y.-W. Zhang, F. G. Omenetto, Y. Huang, T. Coleman, J. A. Rogers, *Science* **2011**, *333*, 838.

- [23] S. Wang, J. Xu, W. Wang, G.-J. N. Wang, R. Rastak, F. Molina-Lopez, J. W. Chung, S. Niu, V. R. Feig, J. Lopez, T. Lei, S.-K. Kwon, Y. Kim, A. M. Foudeh, A. Ehrlich, A. Gasperini, Y. Yun, B. Murmann, J. B.-H. Tok, Z. Bao, *Nature* **2018**, 555, 83.
- [24] Y. Zhang, L. Zhang, K. Cui, S. Ge, X. Cheng, M. Yan, J. Yu, H. Liu, *Adv. Mater.* **2018**, 30, 1801588.
- [25] Y. H. Jung, T.-H. Chang, H. Zhang, C. Yao, Q. Zheng, V. W. Yang, H. Mi, M. Kim, S. J. Cho, D.-W. Park, H. Jiang, J. Lee, Y. Qiu, W. Zhou, Z. Cai, S. Gong, Z. Ma, *Nat. Commun.* **2015**, 6, 7170.
- [26] G. Grau, R. Kitsomboonloha, S. L. Swisher, H. Kang, V. Subramanian, *Adv. Funct. Mater.* **2014**, 24, 5067.
- [27] G. E. Bonacchini, C. Bossio, F. Greco, V. Mattoli, Y.-H. Kim, G. Lanzani, M. Caironi, *Adv. Mater.* **2018**, 30, 1706091.
- [28] J.-H. Kim, S. Mun, H.-U. Ko, G.-Y. Yun, J. Kim, *Nanotechnology* **2014**, 25, 092001.
- [29] A. Hübler, B. Trnovec, T. Zillger, M. Ali, N. Wetzold, M. Mingeback, A. Wagenpfahl, C. Deibel, V. Dyakonov, *Adv. Energy Mater.* **2011**, 1, 1018.
- [30] L. Wang, G.-S. Liu, Y.-C. Wang, J. Su, X.-D. Wang, X. Zeng, Z.-S. Zhang, S.-Z. Deng, H.-P. D. Shieh, B.-R. Yang, *Int. Soc. Inf. Disp.* **2017**, 25, 384.
- [31] Ashland Inc., *Klucel hydroxypropylcellulose – Physical and chemical properties*, https://www.ashland.com/file_source/Ashland/Product/Documents/Pharmaceutical/PC_11229_Klucel_HPC.pdf (accessed: June 2020).
- [32] S. Magalhães, L. Alves, B. Medronho, A. C. Fonseca, A. Romano, J. F. J. Coelho, M. Norgren, *Polymers* **2019**, 11, 1685.
- [33] T. Borodulina, E. Bermesheva, N. Smirnova, S. Ilyin, T. Brantseva, S. Antonov, *J. Adhes. Sci. Technol.* **2014**, 28, 1629.
- [34] M. A. Repka, J. W. McGinity, *J. Controlled Release* **2001**, 70, 341.
- [35] J. P. Borges, M. H. Godinho, A. F. Martins, D. F. Stamatialis, M. N. de Pinho, M. N. Belgacem, *Polym. Compos.* **2004**, 25, 102.
- [36] P. B. Catrysse, S. Fan, *Nano Lett.* **2010**, 10, 2944.
- [37] H.-H. Hsiao, C. H. Chu, D. P. Tsai, *Small Methods* **2017**, 1, 1600064.
- [38] Z. Wu, Y. Zheng, *Adv. Opt. Mater.* **2017**, 5, 1700034.
- [39] P. Wang, Y. Zheng, X. Chen, C. Huang, Y. V. Kartashov, L. Torner, V. V. Konotop, F. Ye, *Nature* **2020**, 577, 42.
- [40] Z. Wu, Y. Liu, E. H. Hill, Y. Zheng, *Nanoscale* **2018**, 10, 18096.
- [41] D. Franklin, S. Modak, A. Vázquez-Guardado, A. Safaei, D. Chanda, *Light: Sci. Appl.* **2018**, 7, 93.
- [42] V. J. Cadarso, S. Chosson, K. Sidler, R. D. Hersch, J. Brugger, *Light: Sci. Appl.* **2013**, 2, 86.
- [43] I. Amidror, S. Chosson, R. D. Hersch, *J. Phys.: Conf. Ser.* **2007**, 77, 12001.
- [44] S. Thomas, *IPC APEX EXPO Conf. Proc.*, Steve Thomas Conductive Inkjet Technology, Cambridge, UK **2009**.
- [45] K. Fukuda, T. Someya, *Adv. Mater.* **2017**, 29, 1602736.
- [46] S. Park, M. Vosguerichian, Z. Bao, *Nanoscale* **2013**, 5, 1727.
- [47] D. Abol-Fotouh, B. Döring, O. Zapata-Arteaga, X. Rodríguez-Martínez, A. Gómez, J. S. Reparaz, A. Laromaine, A. Roig, M. Campoy-Quiles, *Energy Environ. Sci.* **2019**, 12, 716.
- [48] H. Schiff, A. Kristensen, in *Springer Handbook of Nanotechnology* (Ed: B. Bhushan), Springer, Berlin **2010**, p. 271.
- [49] H.-J. Hagemann, W. Gudat, C. Kunz, *J. Opt. Soc. Am.* **1975**, 65, 742.



Supporting Information

for *Small*, DOI: 10.1002/sml.202004795

Hydroxypropyl Cellulose Adhesives for Transfer Printing of
Carbon Nanotubes and Metallic Nanostructures

*Camilla Dore, Bernhard Dörling, Juan Luis Garcia-Pomar,
Mariano Campoy-Quiles, and Agustín Mihi**

Supporting Information

Hydroxypropyl cellulose adhesives for transfer printing of carbon nanotubes and metallic nanostructures.

Camilla Dore¹, Bernhard Dörfling¹, Juan Luis Garcia¹, Mariano Campoy¹, Agustin Mihi^{1,}*

¹Institut de Ciència de Materials de Barcelona (ICMAB-CSIC), Campus de la UAB, 08193 Bellaterra, Spain.

(*corresponding authors: amihi@icmab.es)

Contents:

Section 1. Hydroxypropyl cellulose specifications

Section 2. Continuous metal film transfer

Section 3. Experimental and simulated extinction spectra of multilayer nanopattern stacks.

Section 4. Influence of twisting angle on the optical properties of Moiré metamaterials.

Section 5. Additional Moiré metamaterials fabricated

Section 6. Additional characterization of CNT transparent films.

Section 7. Additional images of patterned CNT arrays

Section 8. Benchmarking with other soluble tapes

Section 9. Roughness analysis of transfer printed silver films

Section 1. Hydroxypropyl cellulose specifications

Hydroxypropyl cellulose (HPC) is an ether of cellulose in which some of the -OH groups in the backbone glucose chain (Figure S1b) have been substituted with an OCH₂CH(OH)CH₃ groups. HPC presents a combination of both hydrophobic and hydrophilic groups, for this reason it has a lower critical solution temperature (LCST) and it is soluble in water at temperatures below 45°C. Given the high crystallinity of cellulose, HPC must have an MS (average number of substituted hydroxyl groups per glucose unit) about 4 to obtain water solubility. It is commonly used as passive excipient in pharmaceutical drugs, and as eye protectant and lubricant (artificial tears). The chemical formula of HPC is illustrated if Figure S1.

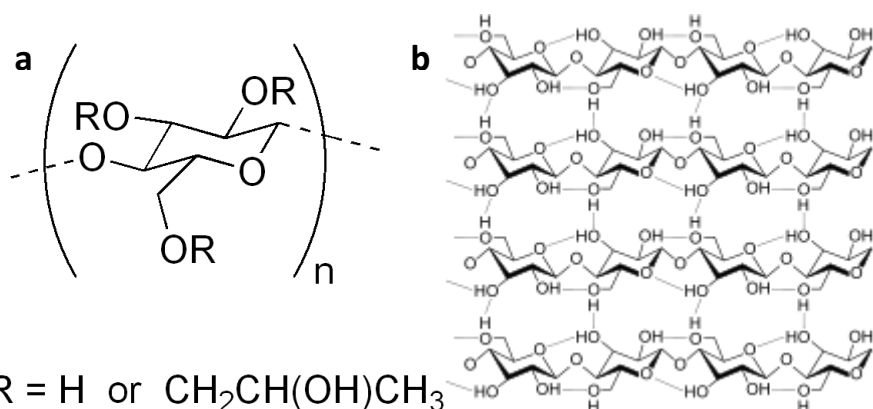


Figure S1. a) Chemical structure of HPC b) Chemical structure of cellulose showing hydrogen bonding in crystalline configuration.

Section 2. Continuous metal film transfer

A 50 nm thick silver layer has been thermally evaporated on a silicon wafer at a rate of 20 Å/s. The silver layer then was transferred using HPC as described in the main manuscript. PDMS mediated transfer of the silver film has been done by pressing and retrieving a flat slab of PDMS at room temperature. In order to transfer the as-obtained film (Figure S2,b) we spin-coated HPC solution in water (0,27g/mL) on top of the PDMS/Ag stack and let it dry for 2 hours at room temperature. After drying, we peeled off the HCP membrane from the PDMS, retrieving the silver film from the PDMS surface. The as obtained HPC/Ag stack was transferred to glass as described in the main text.

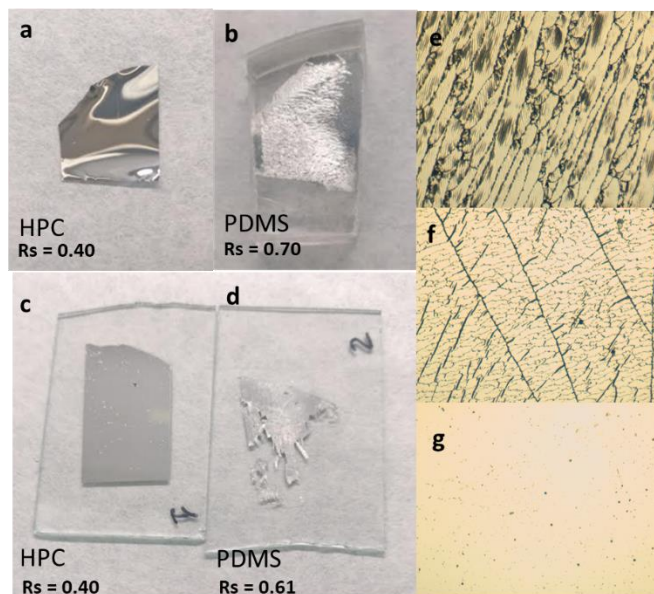


Figure S2. Sheet resistance values (R_s), photos and optical microscope images of transfer printing of 50 nm silver with HPC compared to PDMS. a) silver on HPC after being stripped from silicon. b) silver on PDMS after strip from silicon. c) silver on glass after transfer from a. d) silver on glass after transfer from b. e) optical microscope of b. f) optical microscope of d. g) optical microscope of a-c.

Section 3. Experimental and simulated extinction spectra of multilayer nanopattern stacks

Additional SEM images and Transmittance and Reflectance (theory and experimental) data from stacked silver nanostructures (line array on top of a hole square array). Here in order to reproduce the condition of the experimental measurements, the order zero of diffraction in normal direction for the simulated values of T0 and R0 are considered. Disagreements between experimental and simulated values for wavelengths above 850 nm are attributed to exceeding the operational range of the light polarizer used for those experiments.

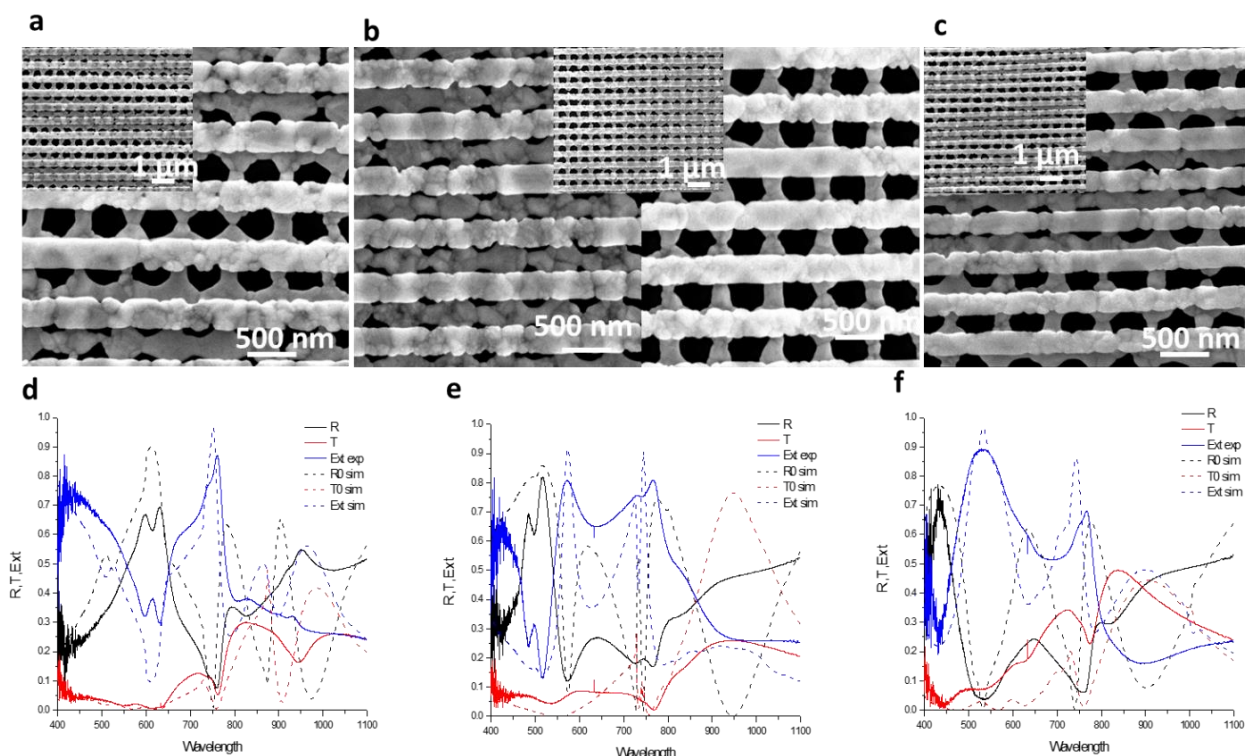


Figure S3. Additional SEM images with simulated (dashed lines) and measured reflection/transmission spectra for holes-lines double layer arrays with varying lattice period. a-d) Hole period 500 nm, line period 600 nm. b-e) Hole period 500 nm, line period 500 nm. c-f) Hole period 500 nm, line period 400 nm. Extinction is calculated as $1-R-T$.

Section 4. Influence of twisting angle on the optical properties of Moiré metamaterials.

The optical properties of double layer structures in the visible range are mostly independent on the twisting angle between the patterned arrays for the lattice parameters considered herein, since the associated Moiré features appear at longer wavelengths. To verify this argument, we measured transmission and reflection for both holes-lines array stacks and Moiré nanoparticle stacks varying the twisting angle. Figure S4 shows the results obtained for combination of hole arrays with 500 nm lattice period and line arrays with 600 nm (left panel) and 500 nm (right panel) lattice period. We tested 4 different twist angles for each combination and measured different points to ensure reproducibility, without finding any significant changes in the optical properties. Figure S5 shows the calculated absorption of the Moiré double layer presented in Figure 2 of the main text. Also, in this case we did not find any difference in the spectra for 10° and 45° rotation angles. For completeness we compare those plots with the ones of the bare bottom (black line) and top (green line) Ag nanoparticle layers.

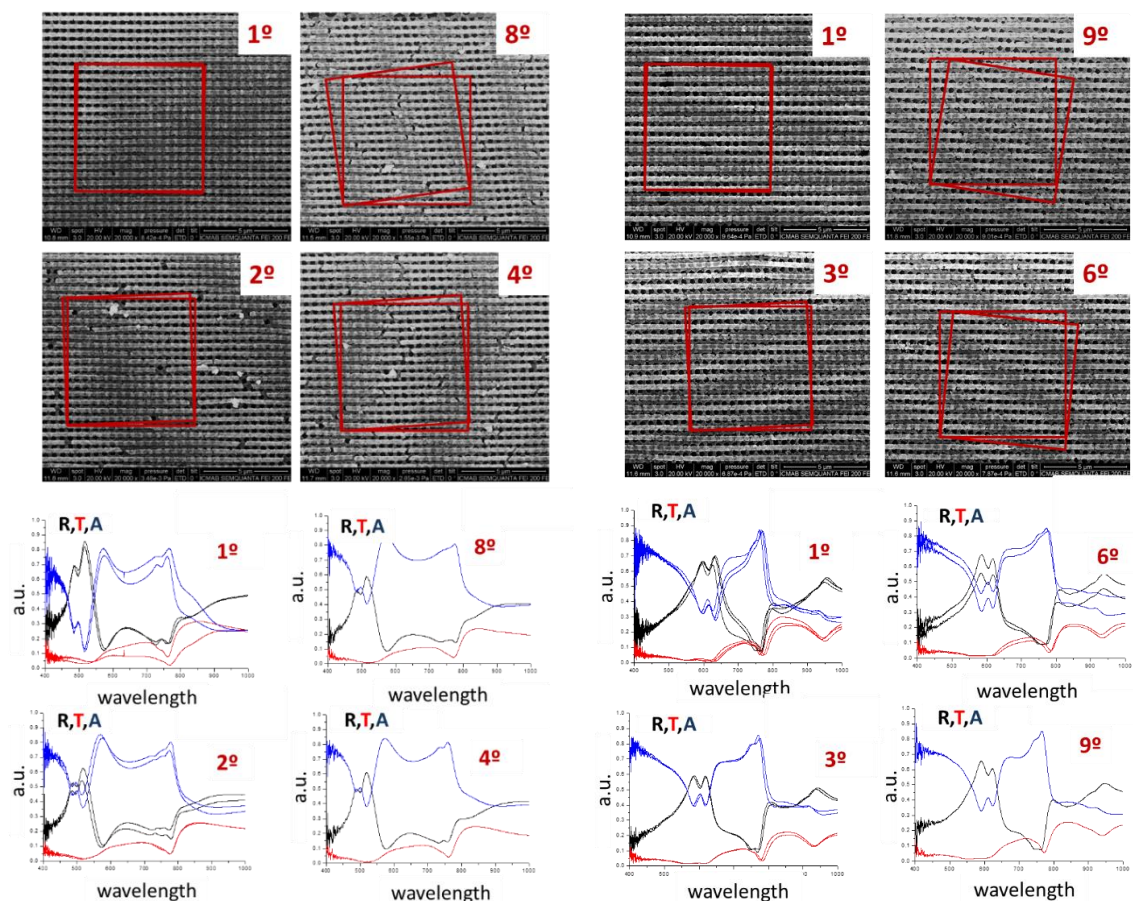


Figure S4. Additional SEM pictures with measured reflection, transmission and absorption spectra of silver holes-lines double arrays with varying twisting angles. Left panel: hole period 500 nm, line period 600 nm. Right panel: hole period 500 nm, line period 500 nm. Extinctions are calculated as $1-R-T$.

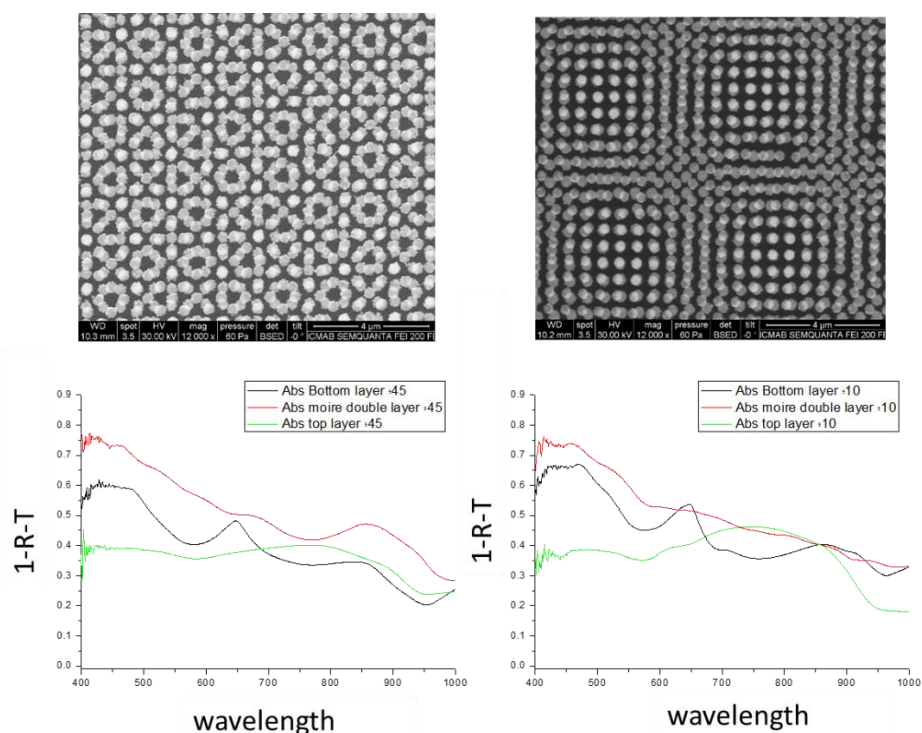


Figure S5. Additional SEM pictures with absorption spectra calculated as 1-R-T of silver nanoparticle Moiré stacks with varying twisting angle.

Section 5. Additional Moiré metamaterials fabricated

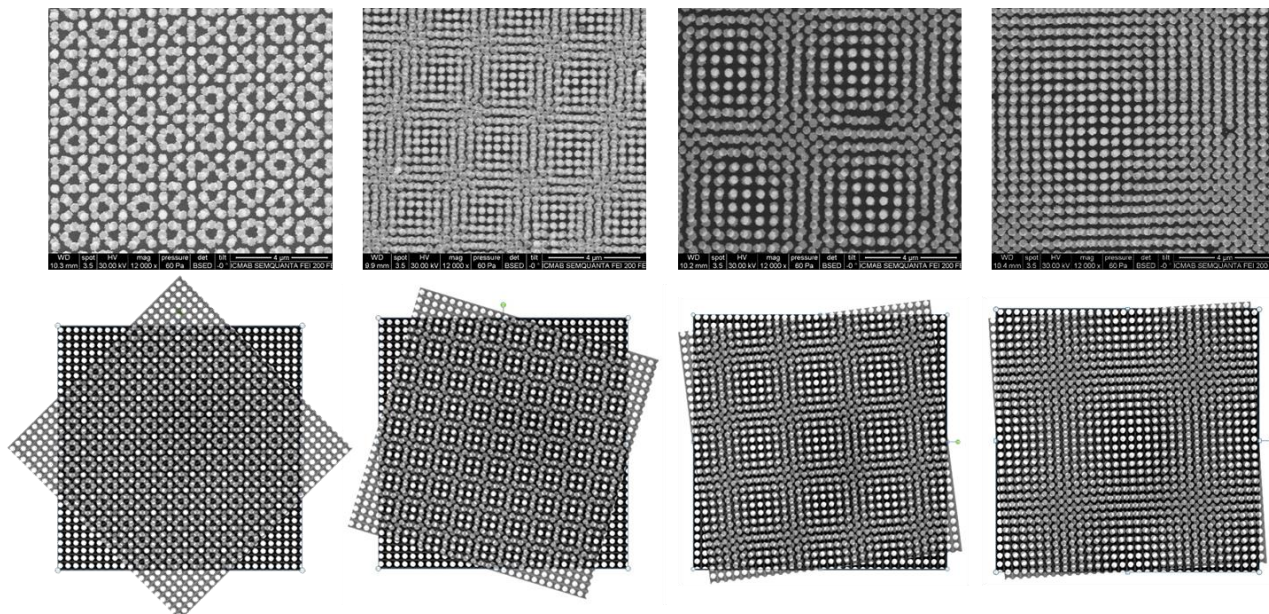


Figure S6. Additional SEM pictures of Moiré patterns obtained by twisted stacking of silver nanoparticles square array with schematic of the angle dependence of the interference pattern.

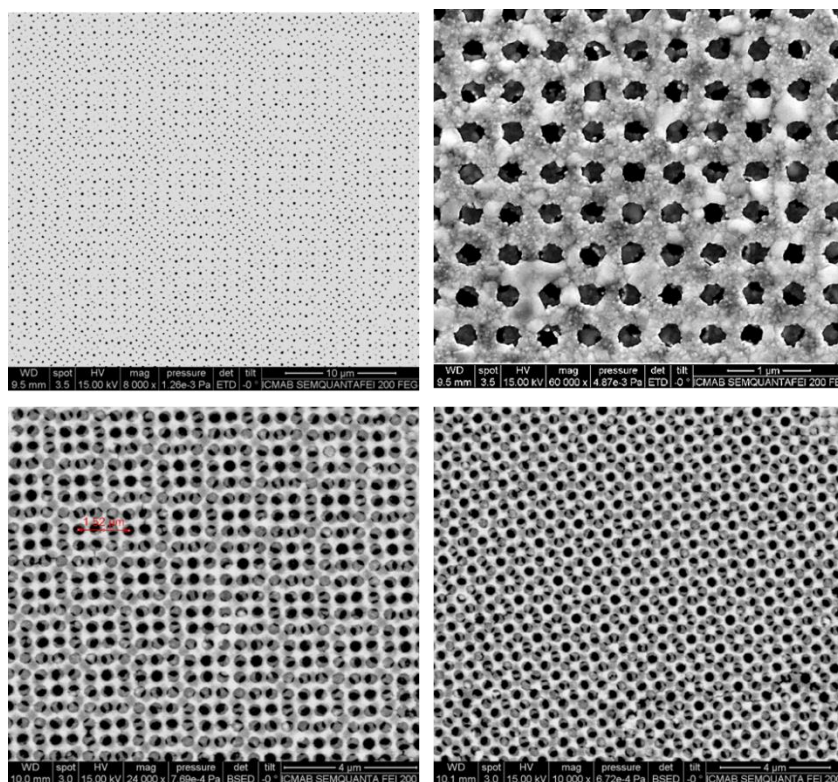


Figure S7. Additional SEM pictures of multilayer stacks consisting of double stacks of holes array in silver with lattice period 500 nm and varying twisting angle.

Section 6. Additional characterization of CNT transparent films.

The key to transfer CNT films with different thickness resides in the different percolation depth of the HPC in the CNT network at different temperatures rather than a change in adhesive strength of the cellulose. The temperature and pressure are applied when the HPC and the CNT film are in contact. Under these conditions, the percolation depth of the HPC into the CNTs network can be tuned with the temperature and the duration of this step, as we illustrate in the scheme **Figure S8e**.

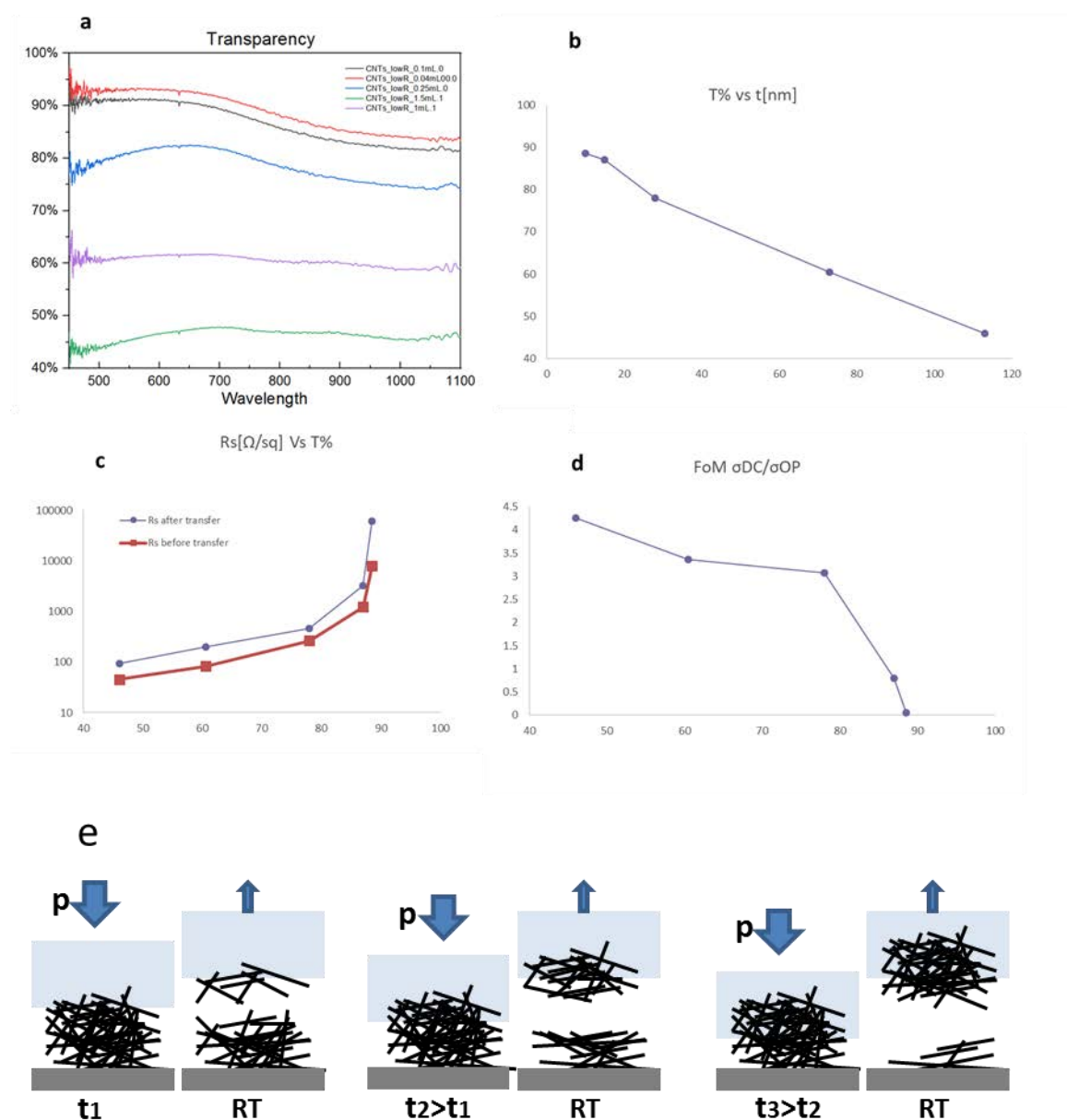


Figure S8. eDIPS CNTs transferred film characterization a) Measured transparency for films of varying thickness transferred to glass. b) average transparency percentage vs measured thickness. c) Sheet resistance before and after transfer vs average percentage transparency. d) Figure of merit for CNT films of different thickness. e) Scheme illustrating the different percolation of HPC within the CNT network with increasing temperature.

In this section we analyze the electrical performance of a different set of CNTs; eDIPS SWCNTs, transferred to glass using the HPC mediated transfer print developed in this work.

Due to their longer length compared to CoMoCAT CNTs, the partial film transfer described in figure S8e by tuning the pick-up temperature was not successful when using eDIPS CNTs. Instead, we transferred entire films of different initial thickness and compared their sheet resistances before and after transfer.

Films with different thickness were fabricated by vacuum filtration of diluted solution the same way as described for the CoMoCAT CNTs in the Materials and Methods section in the main manuscript. As seen in Figure S8, for films of about 100 nm thickness, we observed that the sheet resistance increased by a factor of 2 after transfer. For 10 nm thin films, the effect of transfer was more pronounced, and the sheet resistance instead increased by a factor of 9. This effect can be attributed to the partial disruption of CNT-CNT interfaces, due to CNTs moving during the dissolution step of HPC in water. To evaluate these transparent conductive films, we calculated the figure of merit according to the following formula:

$$FOM = \frac{188.5}{Rs(\sqrt{T} - 1)}$$

Section 7. Additional images of patterned CNT arrays

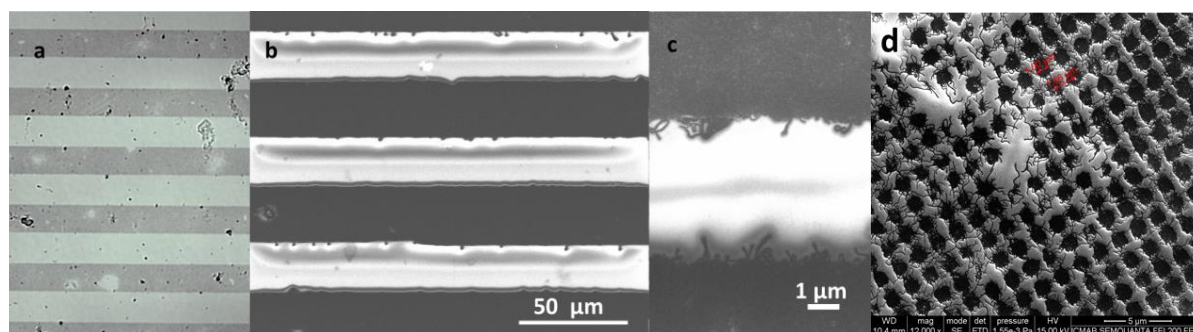


Figure S9. a-b) Optical transmission image and SEM pictures 25 μm wide CNT line pattern. c) SEM close view of 5 μm wide gap between two CNTs lines. d) low magnification SEM picture of the 1 μm features CNT pattern.

Section 8. Benchmarking with other soluble tapes

Table 1. Comparison of soluble tapes based transfer processes

Tape material	Ink material	Method	Ink release	Selective pick-up	Advantages	Limitations
PMMA ¹	Au, Ag	Template assisted	ND	ND	Low complexity	Low versatility
PVA ²	Au/CNT/FET	Template assisted	Water vapor 95°C for 90 min	ND	Working FET device demonstrated	Complex, slow release.
PDMS ³	Au, Pd	From PS/P4VP soluble template	Toluene swollen PDMS gel pads	ND	Versatile (various target substrates and inks)	Complex method (many process steps). Requires specific (soluble) materials for donor template.
Scotch tape ⁴	Au, TiO ₂ , SiO ₂	Template assisted	Soaking in chloroform and fishing	ND	Low complexity, quite versatile	Complex release.
PVA ⁵	Au	Template assisted	Water dissolution	ND	Low complexity, many receiver substrate	Slow dissolution rate of PVA @RT.
HA ⁶	Au, Ag, Pd, Al, SiO ₂	Direct evaporation on HA template	Water dissolution	ND	Low complexity an application to textile	Ink material must be processed on HA
AST ⁷	silicon	Pick up si inks	Acetone dissolution	ND	Faster than PDMS	Requires O ₂ cleaning.
HPC (this work)	Metal, CNT	Template assisted & μ-transfer print	Water dissolution + soluble in organic solvents	Yes, 1 μm resolution	Versatility and low complexity	Suitable for processing of non-soluble materials

Section 9. Roughness analysis of transfer printed silver films

The pressure applied during the transfer process facilitates the conformal contact between the Ag and the receiver substrate. We include here an AFM analysis to illustrate the effect of the applied pressure on the transferred metal film and its surface roughness. From these analysis, we conclude that this pressure range does not seem to deform the Ag layer and that only a slight increase of roughness is observed comparing the as deposited film (3,4 nm) versus the 1 bar transferred film (4,2 nm).

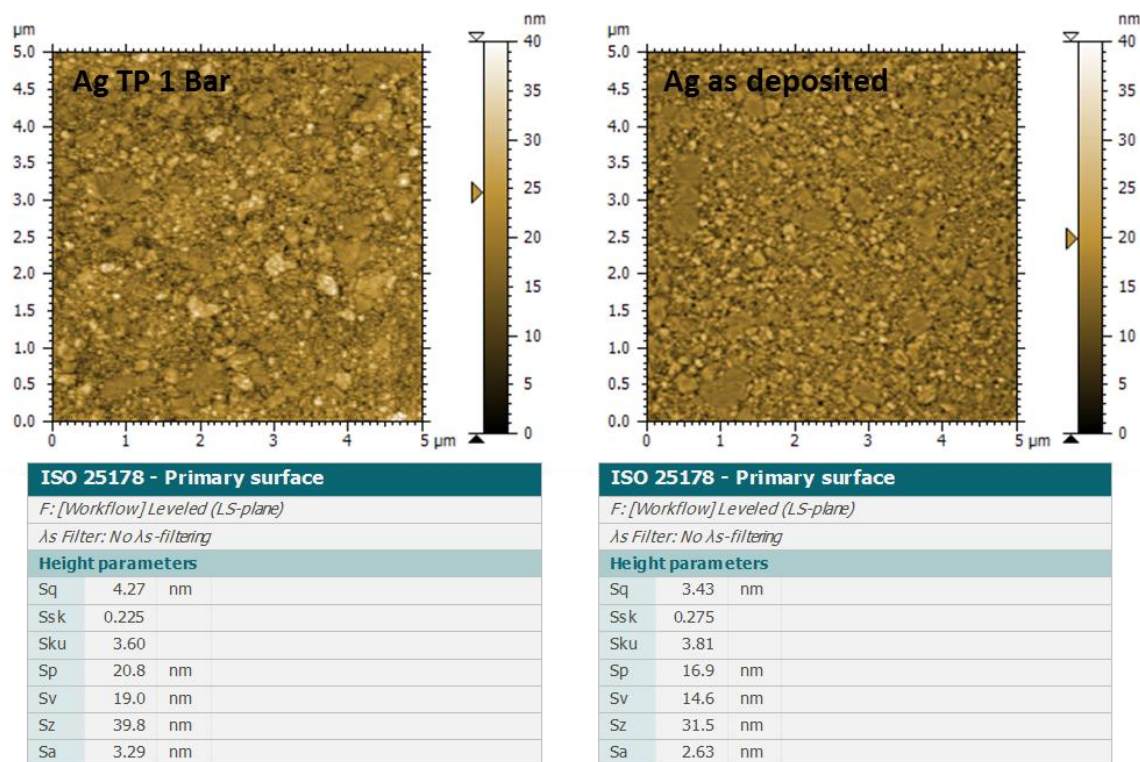


Figure S10. AFM analysis and surface roughness values of silver films transfer printed (TP) using pressures of 0.5 an 1 Bar, compared with the as deposited silver film.

References

- (1) Zhang, J.; Wu, Y.; Li, Z.; Zhang, Y.; Peng, Y.; Chen, D.; Zhu, W.; Xu, S.; Zhang, C.; Hao, Y. High-performance Acetone Soluble Tape Transfer Printing Method for Heterogeneous Integration. *Scientific reports* **2019**, *9*, 15769.
- (2) Ko, J.; Zhao, Z.-J.; Hwang, S. H.; Kang, H.-J.; Ahn, J.; Jeon, S.; Bok, M.; Jeong, Y.; Kang, K.; Cho, I.; *et al.* Nanotransfer Printing on Textile Substrate with Water-Soluble Polymer Nanotemplate. *ACS nano* **2020**, *14*, 2191–2201.
- (3) Tiefenauer, R. F.; Tybrandt, K.; Aramesh, M.; Vörös, J. Fast and Versatile Multiscale Patterning by Combining Template-Stripping with Nanotransfer Printing. *ACS nano* **2018**, *12*, 2514–2520.
- (4) Wang, Q.; Han, W.; Wang, Y.; Lu, M.; Dong, L. Tape nanolithography: a rapid and simple method for fabricating flexible, wearable nanophotonic devices. *Microsystems & nanoengineering* **2018**, *4*, 31.
- (5) Jeong, J. W.; Yang, S. R.; Hur, Y. H.; Kim, S. W.; Baek, K. M.; Yim, S.; Jang, H.-I.; Park, J. H.; Lee, S. Y.; Park, C.-O.; *et al.* High-resolution nanotransfer printing applicable to diverse surfaces via interface-targeted adhesion switching. *Nature communications* **2014**, *5*, 5387.

- (6) Shi, J.; Guo, C. X.; Chan-Park, M. B.; Li, C. M. All-printed carbon nanotube finFETs on plastic substrates for high-performance flexible electronics. *Adv. Mater.* **2012**, *24*, 358–361.
- (7) Zhao, Z.-J.; Hwang, S. H.; Kang, H.-J.; Jeon, S.; Bok, M.; Ahn, S.; Im, D.; Hahn, J.; Kim, H.; Jeong, J.-H. Adhesive-Layer-Free and Double-Faced Nanotransfer Lithography for a Flexible Large-Area MetaSurface Hologram. *ACS applied materials & interfaces* **2020**, *12*, 1737–1745.



Cite this: *Nanoscale*, 2018, **10**, 17884

A water-processable cellulose-based resist for advanced nanofabrication†

Camilla Dore,^a Johann Osmond^b and Agustín Mihi *^a

The ideal nanofabrication technique is one that allows the mass production of high resolution submicrometric features in a cost efficient and environmentally friendly fashion. A great step towards achieving this goal has been the development of nanoimprinting lithography, a procedure with tenths of nanometres resolution while being compatible with roll-to-roll manufacturing. However, an ecofriendly resist that can be efficiently combined with this process is still missing. In this work, we demonstrate the use of hydroxypropyl cellulose (HPC) as a biocompatible, biodegradable, and water processable resist for temperature assisted nanoimprint lithography (tNIL) by fabricating different photonic architectures. The cellulose derivative is easily patterned with submicrometric features with aspect ratios greater than 1 using an elastomeric stamp and a hot plate. Silicon photonic crystals and metal nanoparticle arrays are fabricated combining cellulose with traditional nanofabrication processes such as spincasting, reactive ion etching and metal lift off. Furthermore, advanced nanofabrication possibilities are within reach by combining the HPC with traditional resists. In particular, poly(methyl methacrylate) and HPC stacks are easily produced by liquid phase processing, where one of the two materials can be selectively removed by developing in orthogonal solvents. This capability becomes even more interesting by including nanoimprinted layers in the stack, leading to the encapsulation of arrays of air features in the resist.

Received 14th June 2018,
Accepted 16th August 2018

DOI: 10.1039/c8nr04851g

rsc.li/nanoscale

Introduction

Environmental pollution and worker health protection play nowadays a key role in electronic manufacturing, driving cutting-edge technologies towards an ongoing reduction of toxic and contaminating substances in their production lines. The development of a ‘green’ nanofabrication process is not only beneficial from an environmental point of view, but also reduces the costs associated with the disposal of hazardous chemicals and creates a friendly working environment. Furthermore, avoiding organic solvents and corrosive reagents enables the direct patterning of a wide range of biomaterials that were incompatible with previous processes.

In light of this, the greatest challenge for emerging nanofabrication technologies will be the integration of ecofriendly fabrication approaches with the cost effective and high throughput procedures required in large scale industrial production. To this end, next-generation lithographic methods

should rely on inexpensive, biodegradable and easily accessible materials.^{1–3}

Following the recent developments in the semiconductor and flexible electronics industries, among the emerging high-resolution patterning techniques, nanoimprint lithography (NIL) can be considered the most promising approach for mass production of innovative optic and electronic devices. Features as small as 10 nm can be produced using NIL,⁴ and when compared to electron beam lithography (EBL) and other high-end photolithographic methods, NIL is simultaneously a low cost and more versatile technique; it is compatible with roll-to-roll technology and is suitable for large area patterning. Furthermore, in nanoimprinting lithography, resist molding is attained *via* mechanical deformation, making this technique suitable for patterning a broader range of materials independently of their light or electron sensitivity.

Nanoimprinting lithography is a simple and scalable technique that enables moving from the laboratory to a larger scale; however, a viable water processable ecofriendly resist for this technology is still missing. Indeed, despite the attractive features of NIL techniques, there are only a few examples of biodegradable materials used as resists for NIL, while most of the studies have aimed at developing photolithographic⁵ and EBL ecofriendly resists, as recently demonstrated for silk fibroin and cellulose based materials.^{6,7}

^aInstitut de Ciència de Materials de Barcelona (ICMAB-CSIC), Campus de la UAB, 08193 Bellaterra, Catalonia, Spain. E-mail: amihi@icmab.es

^bICFO-The Institute of Photonic Sciences, Av. Carl Friedrich Gauss, 3, 08860 Castelldefels, Barcelona

†Electronic supplementary information (ESI) available. See DOI: 10.1039/c8nr04851g



NIL is a suitable method for the patterning of biopolymers, finding a wide range of applications, particularly in the production of biophotonic platforms.⁸ Molding of diverse cellulosic materials has previously been reported; for instance, it is possible to hot emboss liquid wood⁹ or to use fast imprinting methods compatible with roll-to-roll to pattern cellulose-based polymers.^{10–12} The feasibility of patterning these eco-friendly materials is the starting point for the development of a viable green resist for nanoimprinting lithography.

In this work, we utilize hydroxypropyl cellulose (HPC) as a thermal aided nanoimprint (tNIL) resist fully processed with water. We aim to provide the first characterization of the HPC as a green resist and demonstrate its potential by fabricating photonic crystals and 2D metal nanoparticle arrays. In doing so, we provide data on the performance of this material in common nanofabrication processes such as spincoating, reactive ion etching and metal lift off. The opportunity to use cellulose-based materials as lithographic resists is particularly appealing, first of all because cellulose is the most abundant polymer on Earth and since centuries it has been extracted from vegetal sources. In particular, hydroxypropyl cellulose is a water soluble derivative of cellulose in which some of the OH groups from the polysaccharide chain have been substituted with an ether group. HPC is cheap, commercially available, biodegradable and biocompatible and it is already widely used in the pharmaceutical industry as a passive drug excipient. Previous patterning attempts of water processable biopolymers such as poly vinyl alcohol (PVA) were mainly achieved in the form of free-standing membranes and by using replica molding techniques (pouring the polymer directly on the PDMS mold). PVA is frequently used only as a lift-off layer since nanoimprinting this material requires the use of hard molds under high pressures (5 MPa), which hinder conformal contact with the substrate.¹³ In contrast, we demonstrate herein the imprinting of HPC with extremely low pressures (*ca.* 0.05 MPa) and flexible PDMS molds.

Furthermore, this cellulose based resist is not only an eco-friendly alternative, but also can be combined with traditional resists insoluble in water, leading to advanced fabrication possibilities. As an example, we fabricated alternating stacks of HPC and PMMA in which each material can be selectively removed with water or toluene, demonstrating its potential as a sacrificial layer. Polymeric multilayers are widely studied systems that find application in many different fields ranging from biotechnology¹⁴ to optics¹⁵ and that are currently employed in advanced lithographic techniques.^{16,17} Moreover, combining this method with tNIL, we have been able to produce ordered arrays of air-holes embedded in PMMA, opening up the path towards a straightforward nanofabrication strategy that can find application in the production of innovative optofluidic devices.¹⁸

The characterization of the cellulose-based resist begins with the fabrication of typical nanostructures by tNIL. The performance of the cellulose derivative in each lithographic step (dry etching, water lift-off and selective development) is subsequently analyzed.

The patterning process of the HPC film on silicon wafers is illustrated in Fig. 1a. Briefly, a spincoated HPC film is heated at 140 °C on a hot plate above the HPC glass transition temperature while gently pressing with a pre-patterned PDMS mold. After being cooled down, the mold is released, leaving the negative pattern on the HPC layer.

Results and discussion

The first requirement for a good nanoimprinting resist is the possibility to obtain smooth and homogeneous films with tunable thicknesses *via* spin coating. The thickness of the film depends on the concentration of the polymer solution (which determines the solution viscosity) and on the spin-coating speed. HPC solutions in water are optically transparent and homogeneous. They are simply prepared by stirring HPC powder in deionized water (see the Experimental section). The cellulose solutions can be readily spincoated on silicon wafers or glass substrates without any pre-treatment of the substrate surface. Smooth and homogeneous films of HPC with different thicknesses are obtained after spincoating. To the best of our knowledge, there is no preexisting data describing thin films of HPC obtained by spincoating from aqueous media. We provide herein a spin rate *vs.* thickness standard curve, recorded for different cellulose concentrations (Fig. 1b). Highly homogeneous layers of HPC on silicon were fabricated by varying the spin speed between 2000 and 5000 rpm. Lower spin rates resulted in inhomogeneous HPC films while at higher spin rates there were not considerable variations in the film thickness.

In order to characterize the surface roughness of the HPC films, a topographic analysis (Fig. 1c) of the HPC layers before and after the imprinting process was performed. We found that the root-mean-square height (*Sq*) of the as prepared film was only 3 nm, which further decreased to 0.8 nm after the hot embossing process using a PDMS mold.

One of the main differences between thermally assisted nanoimprinting or hot embossing and traditional photolithographic techniques is that the patterning process always leaves an excess of material between the imprinted features and the substrate.¹⁹ This residual layer must be removed in order to expose the underlying wafer and use the polymer as a lithographic mask. Good control over the thickness and homogeneity of this residual layer is required for a successful replication of the pattern in the substrate. Minimizing the residual layer thickness dramatically improves the quality of the final pattern,²⁰ minimizing the lateral erosion during the etching process.

During the embossing step of the HPC films, the polymer flows until filling the mold features after which point it stops,²¹ and no decrease in thickness of the residual layer occurs even after prolonged embossing time. A similar behavior was observed by Lee *et al.*²² during hot embossing of PMMA films on silicon using tNIL. Following a volume conserving model, it is possible to calculate a directly proportional



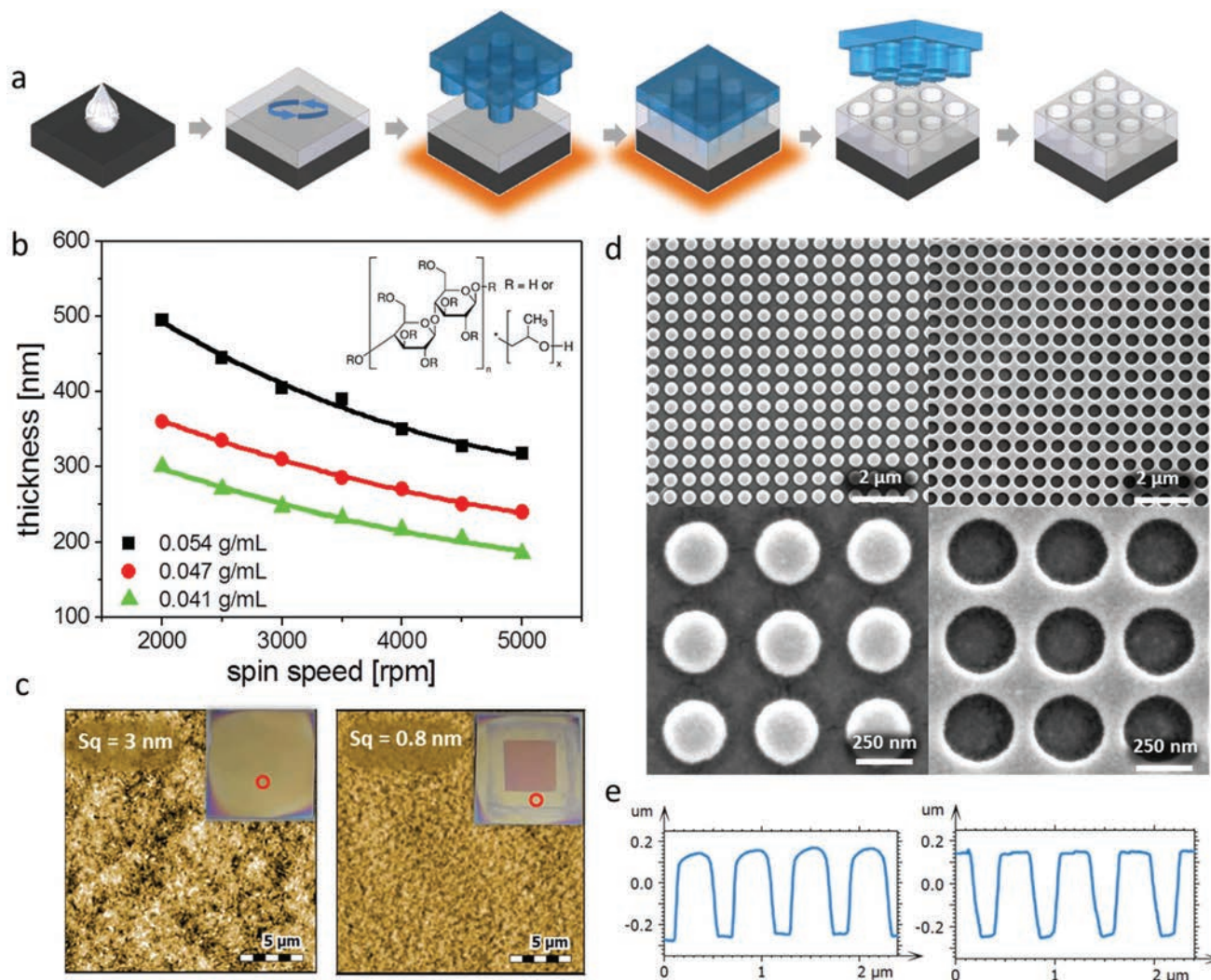


Fig. 1 (a) Schematic representation of the thermal nanoimprinting (tNIL) process employed to pattern the HPC resist on glass and silicon substrates. (b) Spin rates vs. thickness curves for HPC films spincoated from aqueous solutions with concentrations of 0.054 g mL⁻¹ (black), 0.047 g mL⁻¹ (red) and 0.041 g mL⁻¹ (green). (c) Atomic Force Microscopy pictures of flat HPC films as prepared (left) and after imprinting (right), reporting the measured root-mean-square height, Sq. The insets show a photograph of the samples before and after imprinting, in which the red dot highlights the scanned area. (d) Exemplar SEM top view image of the pillars (left) and holes (right) of an imprinted hydroxypropyl cellulose film on silicon at different magnifications (samples have been covered with 10 nm of gold). (e) Atomic Force Microscopy cross sectional profiles of the imprinted features in (d).

relationship between residual layer thickness and the initial film thickness that depends only on the mold pattern geometry.

The excellent mechanical stability of HPC enabled the fabrication of pillar and hole arrays with aspect ratios greater than 1 and with minimum feature size down to 100 nm (Fig. 1d, e and 2f). Alternatively, HPC can also be patterned *via* electron beam lithography (EBL) with analogous submicrometre resolution. Dosage tests and further details of the performance of HPC under electron beam exposure are provided in the ESI.†

Large area patterns of 1 cm² were produced with tNIL in cellulose showing excellent replication of the PDMS pattern. Furthermore, hot embossing of HPC does not require any surface treatment of the PDMS mold and it can be performed

at relatively low temperatures (140 °C) gently pressing the mold against the film for 1 minute.

At this point of the process, a patterned hydroxypropyl cellulose layer is left on top of a silicon wafer. To transfer the pattern from the resist to the underlying substrate, dry etching processes are typically applied. Reactive Ion Etching (RIE) is one of the most advanced techniques suitable for large scale integration in surface micromachining processes. However, the production of high aspect ratio features (deep etching) requires a fine-tuning of the process parameters and an adequate choice of precursor gases to obtain anisotropic etching.

Silicon deep etching processes often rely on chemistries that protect the side walls to ensure minimum lateral erosion and produce vertical side walls and sharp features.²³ Among these techniques, the mixed mode Bosch process (pseudo



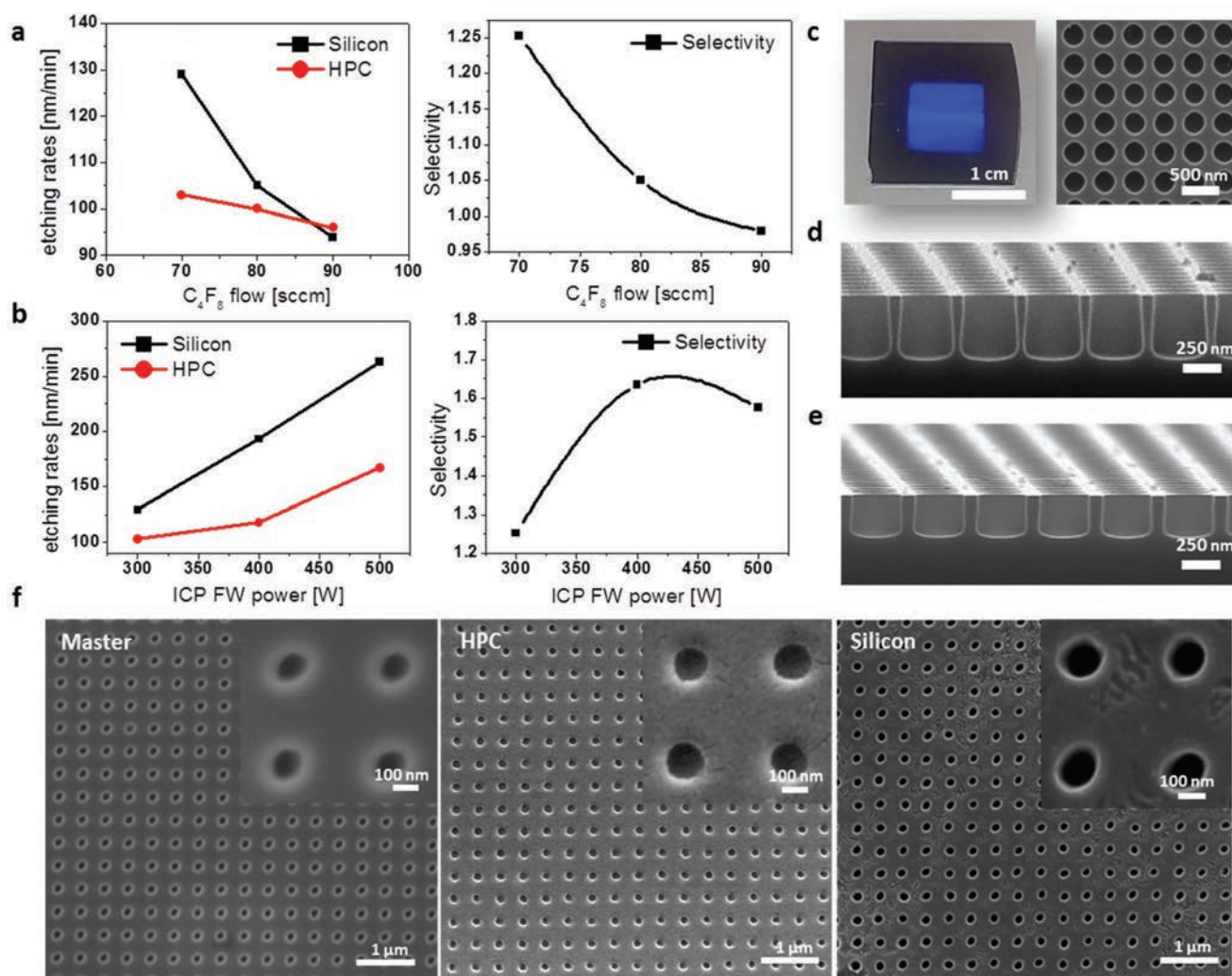


Fig. 2 (a) Etching rates of silicon (black) and HPC (red) and the calculated selectivity of the process for C_4F_8 flows equal to 70, 80 and 90 sccm with a fixed ICP power of 300 W. (b) Etching rates of silicon (black) and HPC (red) and the calculated selectivity of the process for ICP powers equal to 300, 400 and 500 W with a C_4F_8 flow of 70 sccm. (c) Picture and top view SEM image of a patterned silicon substrate after RIE. (d) SEM cross section of a sample etched for 2 min with 70 sccm C_4F_8 flow and 500 W ICP power. Hole depth corresponds to 410 nm. (e) SEM cross section of a sample etched for 3 min with 90 sccm C_4F_8 flow and 300 W ICP power. Holes depth corresponds to 260 nm. (f) 120 nm diameter hole patterns transferred to silicon using HPC as a resist. From left to right: SEM top view images of the original master, imprinted HPC and silicon substrate after RIE.

Bosch) used in this work is particularly suitable for nanoscale etching^{24,25} since it allows us to obtain smooth sidewalls without the need for cryogenic cooling. For the RIE conditions used in this study (see the Experimental section), we investigated the etching rate of HPC and its selectivity *versus* silicon. The ratio between the etching rate of the resist and the wafer substrate determines the maximum possible depth of the etched features that can be transferred to the substrate. Mask erosion can thus be an extremely limiting factor in dry etching processes, particularly when a polymeric resist is employed.

The imprinted HPC films on silicon wafers underwent different RIE steps, which were performed in order to determine the effect of the RIE conditions on the replication of the pattern. Setting the optimal etching parameters usually

requires several sets of experiments and is far beyond the purpose of this paper. Here we report a preliminary study of the etching behavior of hydroxypropyl cellulose in a DRIE process as a general guideline that can be subjected to further optimizations. In general, all the etching conditions studied herein yielded a faithful replication of the pattern into the silicon wafer. Optical and electron microscopic inspections indicated excellent homogeneity along the patterned area and the samples showed the characteristic iridescent color of photonic crystals (Fig. 2c). The minimum feature size tested in this work is 100 nm as illustrated in the ESI† (Fig. S10) and was only limited by the lack of pre-patterned molds with smaller features in our laboratory. We have not observed any increase in roughness or distortion of the features in any of



the patterned HPC films; hence, we believe that smaller features can be achieved in HPC if new composite stamps with nanometric patterns are utilized.²⁶

Fig. 2a and b show the etching rates of silicon and HPC and the corresponding selectivity obtained for three different C_4F_8 flows at a fixed ICP power of 300 W and for three different ICP powers at a fixed C_4F_8 flow of 70 sccm. The maximum selectivity is obtained for an ICP power of 400 W with a C_4F_8 flow of 70 sccm and corresponds to a value of 1.64, which is comparable with the values reported for PMMA (*ca.* 2).^{27–29} Fig. 2d and e show SEM cross sections of two samples etched under different RIE conditions. It is worth noting that increasing the ICP power value with a C_4F_8 flow fixed at 300 sccm deteriorates the degree of anisotropy of the process. To compensate for this effect one possibility is to increase the C_4F_8 flow (Fig. 2e); however, this deteriorates the selectivity of the process.

The poor selectivity of resist masks is well known to the nanofabrication community, which restricts their use to low aspect ratio features. When deep etching is required, photoresist masks are an intermediate step towards the deposition of a more robust material such as metals. In these cases, a metal is evaporated on top of the resist mask, and then the resist is removed from the wafer, leaving the desired metallic pattern behind. The removal of the resist mask that prevented the metal deposition on the silicon wafer, typically called “lift-off”, is a commonly used nanofabrication step that is most necessary to obtain well-defined features. The possibility to employ the lift-off technique using HPC as a sacrificial layer is particularly attractive^{5,6} considering that the whole process can be implemented using only water as a solvent, therefore minimizing the use and generation of hazardous and polluting wastes.

To demonstrate the validity of the cellulose resist in a lift-off process with water, an array of aluminium nanoparticles organized in a square array were fabricated. A schematic of the fabrication process is depicted in Fig. 3c: briefly, HPC was spincoated on glass substrates and thermally imprinted, followed by a short RIE step required to remove the residual layer from the imprinted HPC structures and to expose the glass substrate underneath. Next, 150 nm of aluminium are thermally evaporated above the sample. Finally, the HPC sacrificial layer is removed in water. After this lift-off step, only an array of aluminium nanoparticles remains on the glass surface.

Nanoparticle square arrays with lattice parameters of 400, 500 and 600 nm were fabricated using HPC as a sacrificial layer. A representative SEM picture of the 400 nm lattice parameter nanoparticle array is shown in Fig. 3a. The optical characterization of the samples (Fig. 3b) shows the presence of an intense extinction peak corresponding to the Bragg surface plasmon polariton (Bragg-SPP), which red-shifts with increasing lattice parameter, which evidences the high quality of the plasmonic crystals fabricated. Further tuning of the nanoparticle diameter can be achieved by varying the duration of the etching step that precedes the metal deposition (ESI†).

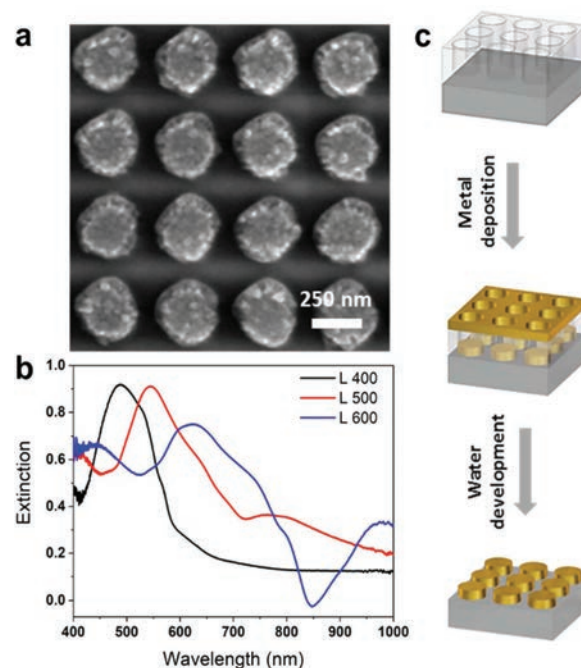


Fig. 3 (a) Top view SEM of the fabricated square array of aluminium pillars with 300 nm diameter, 150 nm height and 400 nm lattice parameter. (b) Extinction spectra of the metal arrays with varying lattice parameters of 400 nm (black), 500 nm (red) and 600 nm (blue). (c) Schematic of the lift-off process employed to fabricate aluminium nanoparticle arrays on glass substrates.

We have demonstrated so far the viability of hydroxypropyl cellulose as an environmentally friendly water processable resist, providing spin rates, etching selectivity values and lift off procedures. It is worth noting that the type of cellulose derivative and its substitution degree might affect the performance of the polymer under chemical etching and water development. Therefore, it might be possible to find derivatives with improved response under the nanofabrication processes.

In the following sections, we will demonstrate that HPC is not only a water processable resist but can also yield new and exciting advanced nanofabrication possibilities. HPC is biocompatible and is completely processed in water; thus it can be used as a means to pattern many biological materials incompatible with previous corrosive reagents. Furthermore, water is orthogonal to most solvents used with traditional resists, meaning that HPC can be combined with them *via* liquid-phase processing and selectively removed. To demonstrate this additional functionality, we fabricated HPC and poly(methyl methacrylate) (PMMA) multilayers by alternate deposition of both polymers. ABAB and BABA stacks were fabricated by alternate spincoating of A (HPC solutions in water) and B (PMMA solutions in Toluene). Considering that HPC is not soluble in toluene and PMMA³⁰ is not soluble in water, it is possible to employ both orthogonal solvents to specifically dissolve a particular polymer in the stack.

Fig. 4 shows cross-sectional SEM images of the ABAB and BABA multilayer stacks prior to and after removal of the A or B



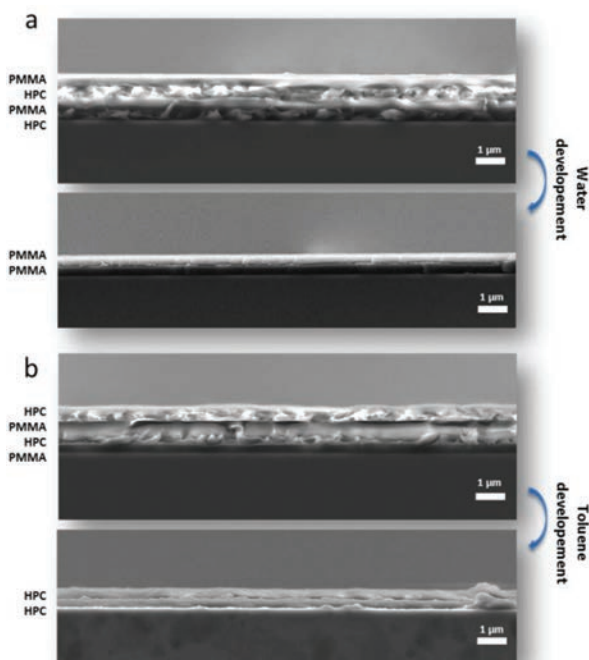


Fig. 4 Cross sectional SEM images of polymeric stacks on silicon substrates. The film thickness is 450 ± 50 nm for both HPC and PMMA layers. (a) HPC-PMMA-HPC-PMMA four layer stacks before and after development in water (HPC layer dissolution). (b) PMMA-HPC-PMMA-HPC four layer stack before and after development in toluene (PMMA layer dissolution).

layers. As can be clearly seen from the picture, depending on the solvent used for the development it is possible to completely dissolve one or the other material, obtaining a monocomponent system consisting of two layers separated by a thin film of air. It is worth noting that if the films are developed carefully it is possible to avoid the lift-off of the upper layer and the remaining undeveloped films adhere to the substrate and collapse onto each other. Since we believe that water diffuses laterally from the edges of the film towards the center, dissolving the HPC can lead to delamination if thick layers of HPC are employed. Using submicrometric HPC films minimized the cracking of the PMMA layers and facilitated stack fabrication.

This can be exploited to fabricate novel architectures with embedded air cavities for instance. To illustrate this advanced nanofabrication possibility, we combined thermal nanoimprint lithography with multilayer stacks of PMMA and HPC to fabricate a 2D air cavity array embedded in PMMA (Fig. 5a).

To fabricate this challenging architecture, a 300 nm layer of PMMA is spin coated on a silicon substrate and thermally imprinted as previously described. Next, HPC and PMMA are sequentially spin coated on the tNIL-PMMA layer: first a thin layer of HPC followed by a second layer of PMMA at the top of the stack. The development of the stack with water dissolves the thin cellulose layer and the top PMMA layer collapses onto the bottom one, encapsulating the nanoimprinted array of holes. Fig. 5 shows cross sectional SEM images of the tNIL-PMMA/HPC/PMMA stack before and after development with water of the HPC. The presence of air cavities in the film of PMMA is further confirmed by changes in the reflectance spectra of the stacks (Fig. 5c) and by optical inspection of the

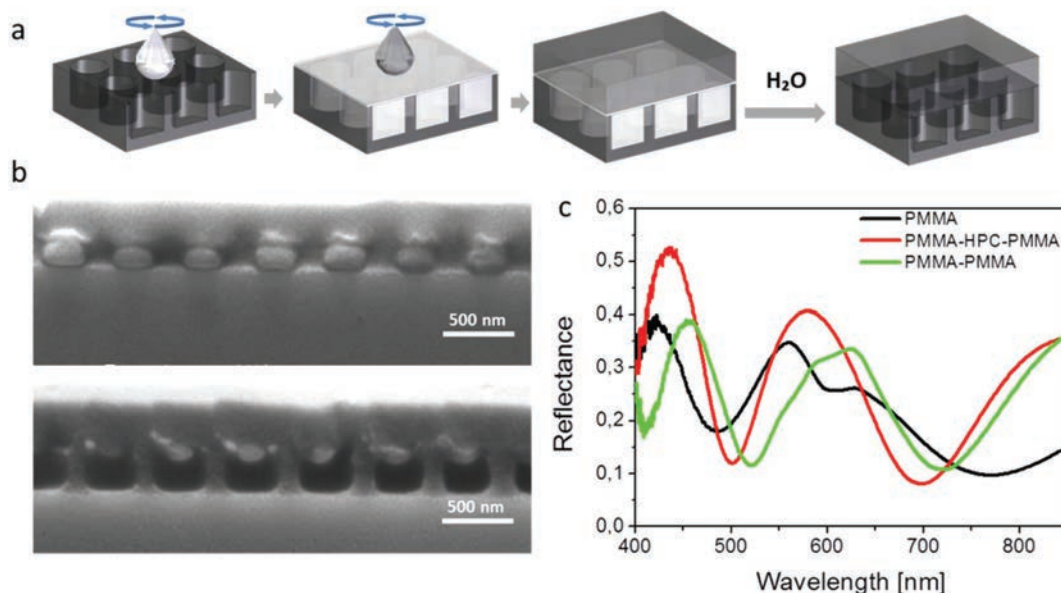


Fig. 5 (a) Schematic process employed to fabricate periodic air cavity arrays embedded in PMMA: briefly, HPC is spincast on thermally imprinted PMMA (tNIL-PMMA), and then a layer of PMMA is spincast on top of the stack. Finally, the HPC is removed with water, leaving a hole-array embedded in PMMA. (b) Cross sectional SEM images of imprinted PMMA-HPC-PMMA stacks on silicon substrates before (top) and after (bottom) development in water. (c) FTIR reflection spectra of imprinted PMMA on silicon (black) and imprinted PMMA-HPC-PMMA stacks on silicon substrates before (red) and after (green) development in water.



films with the naked eye. The tNIL-PMMA film appears iridescent due to the 500 nm lattice parameter 2D grating. The specular reflectance spectrum from tNIL-PMMA (Fig. 5c, black line) presents the characteristic Fabry–Perot oscillations originating from the thin film, together with presenting features in the 550 and 700 nm wavelength ranges, indicating the existence of diffraction.

When the holes in the stack are filled with HPC, the HPC and PMMA layers are index matched (refractive indexes are 1.49 for both materials), the iridescence of the pattern disappears and no distinctive features are present in the reflection spectra (red line). After developing HPC, the presence of periodic air voids imbedded in the PMMA returns the iridescent aspect of the sample and diffraction features appear again in the reflection spectrum in the 550–700 nm range.

Conclusions

We have demonstrated the use of hydroxypropyl cellulose as a water processable resist. Patterned areas of 1 cm² with submicrometric features and aspect ratios higher than 1 were fabricated in silicon using a thermally assisted nanoimprinting technique. We provide key values for spincasting rates, dry etching recipes and selectivity values of the cellulose resist comparable with the data reported in the literature for PMMA. The fabrication of metal nanostructures is also possible by combining metal deposition on the imprinted resist followed by water removal of the cellulose derivative. High quality plasmonic crystals with varying lattice parameter were fabricated and their optical response was characterized by optical spectroscopy. The cellulose based resist has similar characteristics to traditional resists but is biocompatible and is completely processed with water, opening up possibilities for nanostructuring many biological materials. Furthermore, HPC can be used in combination with PMMA, both resists being processed with orthogonal solvents, enabling many advanced nanofabrication possibilities. To illustrate this added functionality, we fabricated multilayer stacks of PMMA and HPC in which one of the two materials can be selectively removed by just developing the stack in water or toluene. In sum, hydroxypropyl cellulose is a green and water processable nanoimprinting resist compatible with mass production processes. HPC is processed orthogonally to most common resists; hence it can be combined with them to yield novel nanostructures with potential application in photonics, microfluidics and advanced lithographic techniques.

Experimental

Materials

Prepatterned silicon masters were purchased from Cemitec (Navarra, Spain) and from EULITHA (Switzerland). A hard polydimethylsiloxane (PDMS) silicone elastomer kit was purchased from Gelest (Morrisville, PA 19067, USA) and a soft PDMS

Sylgard184 silicone elastomer kit from Dow Corning Corporation (Auburn, MI 48611, USA). 1H,1H,2H,2H-Perfluorooctyltrichlorosilane (PFOTS), 97%, was purchased from Alfa Aesar (Thermo Fisher GmbH, Karlsruhe, Germany). Hydroxypropyl cellulose (HPC), with average $M_w \sim 100\,000$, powder, 20 mesh particle size (99% through) and degree of substitution DS = 3, and poly(methylmethacrylate) (PMMA), average $M_w \sim 15\,000$, were purchased from Sigma-Aldrich Quimica SL (Madrid, Spain).

PDMS molds

PDMS molds were fabricated following previously reported methods.³¹ Briefly, silicon masters were functionalized with PFOTS (perfluorooctyltrichlorosilane) as an anti-sticking layer, lowering the surface energy and allowing the easy release of cured PDMS. The molds were fabricated casting on the master first a thin layer of hard-PDMS and a second thick layer of soft PDMS as supports. The choice of using a composite mold is necessary in order to achieve simultaneously mechanical stability of the pattern and conformal contact with the substrate.

The three 1 cm² patterns used in this work consist of square arrays of cylindrical pillars with 300 nm diameter, 350 nm height and lattice parameters of 400, 500 and 600 nm.

HPC films

First, a stock solution of HPC powder in water with a concentration of 217 mg mL⁻¹ was prepared by mixing and intensively stirring the HPC powder in DI water. This stock solution was further diluted in water in order to obtain three different aqueous solutions of 41, 47 and 54 mg mL⁻¹. Each of the aqueous solutions was stirred on a magnetic plate for 3 h. The HPC solutions were directly spin coated on clean silicon and glass surfaces. The spin time was 1 minute and the spin acceleration 1000 rpm s⁻¹ for all the experiments performed. Thin films of HPC with thickness ranging between 2 μm and 50 nm were obtained by changing the HPC solution concentrations and the speed of spin coating.

Thermal nanoimprint lithography

HPC films deposited on silicon were placed on a hot plate at 140 °C (glass transition temperature of HPC is 105 °C³²). Next, a patterned PDMS mold was gently pressed against the substrate for 1 minute. Samples were left to cool down to room temperature and finally demolded.

Sample characterization

Flat HPC film thicknesses were obtained by the numerical fitting of the Fabry–Perot oscillations from the experimental reflection spectra using the transfer matrix formalism. The HPC refractive index value was reported in previous studies.³³ The reflectivity and transmission of the samples were measured using a Fourier Transform Infrared Spectrometer (FTIR, Bruker Vertex 70) attached to a microscope with a 4× objective. The depth of the features in HPC and silicon patterns was measured using a Keysight 5100 scanning probe microscope (AFM tapping mode configuration) and scanning



electron microscopy (SEM QUANTA FEI 200 FEG-ESEM) cross sectional image analysis.

Dry etching conditions

Samples were etched using an Oxford Instruments Plasmalab System 100 ICP. Selectivity values were calculated from five different sets of etching conditions: (i) 300 W ICP Fw power and 70 sccm C₄F₈ flow, (ii) 300 W ICP Fw power and 80 sccm C₄F₈ flow, (iii) 300 W ICP Fw power and 90 sccm C₄F₈ flow, (iv) 400 W ICP Fw power and 70 sccm C₄F₈ flow, and (v) 300 W ICP Fw power and 90 sccm C₄F₈ flow. In all the processes, the pressure has been set to 15 mTorr, the RF generator power to 35 W and the SF₆ gas flow to 45 sccm. Silicon and HPC etching rates were calculated by linear fitting of the etching depth (see ESI†) for 1, 2 and 3 minutes etching time (samples i, ii, and iii) and for etching times 1 and 2 minutes (iv, v).

Metal deposition and lift off

Aluminum was deposited *via* e-beam evaporation (AJA International Inc. ATC-8E Orion). Samples were developed in running DI water for 30 seconds followed by 20 minutes sonication in DI H₂O.

PMMA-HPC multilayer stacks: HPC and PMMA stacks were fabricated by alternate spin coating at 3000 rpm an HPC solution in DI water (0.054 g mL⁻¹) and a solution of PMMA in toluene (10 wt%) followed by drying at 50 °C on a hot plate for 15 min. HPC (PMMA) layers were developed by immersing the samples in water (toluene) for 10 minutes. The samples were dried in air.

Imprinted multilayer stacks: first, a thin layer of PMMA (10 wt%, $w = 3000$ rpm) was hot embossed at 90 °C. Second, a dispersion of HPC in water (0.0165 g mL⁻¹) was spin coated at 3000 rpm on top of the imprinted PMMA. Finally, a layer of PMMA was deposited using the same conditions as for the first PMMA layer. Samples were developed in water for 10 minutes and dried in air.

Conflicts of interest

There are no conflicts to declare.

Acknowledgements

The Spanish Ministerio de Economía, Industria y Competitividad (MINECO) is gratefully acknowledged for its support through Grant No. MAT2016-79053-P and through Grant No. SEV-2015-0496 in the framework of the Spanish Severo Ochoa Centre of Excellence program. AM was funded by a Ramón y Cajal fellowship (RYC-2014-16444). This project has received funding from the European Research Council (ERC) under the European Union's Horizon 2020 research and innovation program (Grant Agreement No. 637116, ENLIGHTMENT). The authors would like to acknowledge M. Simón and A. Gómez for AFM measurements.

References

- 1 A. M. Pandeale, P. Neacsu, A. Cimpean, A. I. Staras, F. Miculescu, A. Iordache, S. I. Voicu, V. K. Thakur and O. D. Toader, *Appl. Surf. Sci.*, 2018, **438**, 2.
- 2 D. Trache, M. H. Hussin, M. K. M. Haafiz and V. K. Thakur, *Nanoscale*, 2017, **9**, 1763.
- 3 S. I. Voicu, R. M. Condruz, V. Mitran, A. Cimpean, F. Miculescu, C. Andronescu, M. Miculescu and V. K. Thakur, *ACS Sustainable Chem. Eng.*, 2015, **4**, 1765.
- 4 S. Y. Chou and P. R. Krauss, Imprint lithography with sub-10 nm feature size and high throughput, *Microelectron. Eng.*, 1997, **35**, 237–240, DOI: 10.1016/S0167-9317(96)00097-4.
- 5 V. Linder, B. D. Gates, D. Ryan, B. A. Parviz and G. M. Whitesides, Water-soluble sacrificial layers for surface micromachining, *Small*, 2005, **1**, 730–736, DOI: 10.1002/sml.200400159.
- 6 S. Kim, B. Marelli, M. A. Brenckle, A. N. Mitropoulos, E.-S. Gil, K. Tsioris, H. Tao, D. L. Kaplan and F. G. Omenetto, All-water-based electron-beam lithography using silk as a resist, *Nat. Nanotechnol.*, 2014, **9**, 306–310, DOI: 10.1038/NNANO.2014.47.
- 7 S. Takei, H. Maki, K. Sugahara, K. Ito and M. Hanabata, Inedible cellulose-based biomass resist material amenable to water-based processing for use in electron beam lithography, *AIP Adv.*, 2015, **5**, 77141, DOI: 10.1063/1.4927210.
- 8 J. J. Amsden, P. Domachuk, A. Gopinath, R. D. White, L. D. Negro, D. L. Kaplan and F. G. Omenetto, Rapid nanoimprinting of silk fibroin films for biophotonic applications, *Adv. Mater.*, 2010, **22**, 1746–1749, DOI: 10.1002/adma.200903166.
- 9 M. Worgull, M. Schneider, M. Röhrig, T. Meier, M. Heilig, A. Kolew, K. Feit, H. Hölscher and J. Leuthold, Hot embossing and thermoforming of biodegradable three-dimensional wood structures, *RSC Adv.*, 2013, **3**, 20060, DOI: 10.1039/C3RA42642D.
- 10 T. Mäkelä, M. Kainlahti, P. Willberg-Keyriläinen, T. Tammelin and U. Forsström, Fabrication of micropillars on nanocellulose films using a roll-to-roll nanoimprinting method, *Microelectron. Eng.*, 2016, **163**, 1–6, DOI: 10.1016/j.mee.2016.05.023.
- 11 T. Mäkelä, T. Haatainen and J. Ahopelto, Roll-to-roll printed gratings in cellulose acetate web using novel nanoimprinting device, *Microelectron. Eng.*, 2011, **88**, 2045–2047, DOI: 10.1016/j.mee.2011.02.016.
- 12 A. Espinha, C. Dore, C. Matricardi, M. I. Alonso, A. R. Goñi and A. Mihi, Hydroxypropyl cellulose photonic architectures by soft nanoimprinting lithography, *Nat. Photonics*, 2018, **8**, 13131, DOI: 10.1038/s41566-018-0152-1.
- 13 K. ichiro Nakamatsu, K. Tone and S. Matsui, Nanoimprint and Lift-Off Process Using Poly(vinyl alcohol), *Jpn. J. Appl. Phys.*, 2005, **44**(11), 8186–8188.
- 14 S. de Koker, R. Hoogenboom and B. G. de Geest, Polymeric multilayer capsules for drug delivery, *Chem. Soc. Rev.*, 2012, **41**, 2867–2884, DOI: 10.1039/C2CS15296G.



- 15 Z. Wang, J. Zhang, J. Xie, Z. Wang, Y. Yin, J. Li, Y. Li, S. Liang, L. Zhang, L. Cui, H. Zhang and B. Yang, Polymer Bragg stack as color tunable photonic paper, *J. Mater. Chem.*, 2012, **22**, 7887, DOI: 10.1039/C2JM15943K.
- 16 C. Wang and S. Y. Chou, Integration of Metallic Nanostructures in Fluidic Channels for Fluorescence and Raman Enhancement by Nanoimprint Lithography and Lift-off on Compositional Resist Stack, *Microelectron. Eng.*, 2012, **98**, 693–697, DOI: 10.1016/j.mee.2012.05.051.
- 17 Y. Chen, Nanofabrication by electron beam lithography and its applications, *Microelectron. Eng.*, 2015, **135**, 57–72, DOI: 10.1016/j.mee.2015.02.042.
- 18 H. Andagana and X. A. Cao, Nanofabrication of photonic crystal slabs with sealed airholes for optofluidic applications, *Microelectron. Eng.*, 2014, **114**, 17–21, DOI: 10.1016/j.mee.2013.09.005.
- 19 J. A. Rogers and H. H. Lee, *Unconventional nanopatterning techniques and applications*, Wiley-Blackwell, Oxford, 2009.
- 20 K.-d. Kim, J.-h. Jeong, Y.-s. Sim and E.-s. Lee, Minimization of residual layer thickness by using the optimized dispensing method in S-FILTM process, *Microelectron. Eng.*, 2006, **83**, 847–850, DOI: 10.1016/j.mee.2006.01.037.
- 21 H. Schiff and A. Kristensen, in *Springer Handbook of Nanotechnology*, ed. B. Bhushan, Springer Berlin Heidelberg, Berlin, Heidelberg, 2010, pp. 271–312.
- 22 H.-J. Lee, H. W. Ro, C. L. Soles, R. L. Jones, E. K. Lin, W.-l. Wu and D. R. Hines, Effect of initial resist thickness on residual layer thickness of nanoimprinted structures, *J. Vac. Sci. Technol., B: Microelectron. Nanometer Struct.–Process., Meas., Phenom.*, 2005, **23**, 3023, DOI: 10.1116/1.2101776.
- 23 H. V. Jansen, M. J. de Boer, S. Unnikrishnan, M. C. Louwerse and M. C. Elwenspoek, Black silicon method, *J. Micromech. Microeng.*, 2009, **19**, 33001, DOI: 10.1088/0960-1317/19/3/033001.
- 24 S. S. Walavalkar, C. E. Hofmann, A. P. Homyk, M. D. Henry, H. A. Atwater and A. Scherer, Tunable visible and near-IR emission from sub-10 nm etched single-crystal Si nanopillars, *Nano Lett.*, 2010, **10**, 4423–4428, DOI: 10.1021/nl102140k.
- 25 M. D. Henry, S. Walavalkar, A. Homyk and A. Scherer, Alumina etch masks for fabrication of high-aspect-ratio silicon micropillars and nanopillars, *Nanotechnology*, 2009, **20**, 255305, DOI: 10.1088/0957-4484/20/25/255305.
- 26 M. A. Verschuuren, M. Megens, Y. Ni, H. van Sprang and A. Polman, Large area nanoimprint by substrate conformal imprint lithography (SCIL), *Adv. Opt. Technol.*, 2017, **6**, 9554, DOI: 10.1515/aot-2017-0022.
- 27 M. D. Henry, S. Walavalkar, A. Homyk, M. D. Henry, A. Scherer and C. D. O. Silicon, *ICP etching of silicon for micro and nanoscale devices*, 2010.
- 28 A. Goodyear, M. Boettcher, I. Stolberg and M. Cooke, in *Direct comparison of the performance of commonly used e-beam resists during nano-scale plasma etching of Si, SiO₂, and Cr*, ed. Q. Lin, S. U. Engelmann and Y. Zhang, SPIE, 2015, p. 94280V.
- 29 J. Kim, D. C. Joy and S.-Y. Lee, Controlling resist thickness and etch depth for fabrication of 3D structures in electron-beam grayscale lithography, *Microelectron. Eng.*, 2007, **84**, 2859–2864, DOI: 10.1016/j.mee.2007.02.015.
- 30 C. B. Walsh and E. I. Franses, Ultrathin PMMA films spin-coated from toluene solutions, *Thin Solid Films*, 2003, **429**, 71–76, DOI: 10.1016/S0040-6090(03)00031-2.
- 31 T. W. Odom, J. C. Love, D. B. Wolfe, K. E. Paul and G. M. Whitesides, Improved Pattern Transfer in Soft Lithography Using Composite Stamps, *Langmuir*, 2002, **18**, 5314–5320, DOI: 10.1021/la020169l.
- 32 A. Gómez-Carracedo, C. Alvarez-Lorenzo, J. L. Gómez-Amoza and A. Concheiro, *J. Therm. Anal. Calorim.*, 2003, **73**, 587–596, DOI: 10.1023/A:1025434314396.
- 33 P. Molet, J. L. Garcia-Pomar, C. Matricardi, M. Garriga, M. I. Alonso and A. Mihi, Ultrathin Semiconductor Superabsorbers from the Visible to the Near-Infrared, *Adv. Mater.*, 2018, **30**(9), 1705876, DOI: 10.1002/adma.201705876.



Water-processable cellulose-based resist for advanced nanofabrication

Camilla Dore¹, Johann Osmond² and Agustín Mihi^{1}*

1 Institut de Ciència de Materials de Barcelona (ICMAB-CSIC), Campus de la UAB, 08193 Bellaterra, Catalonia, Spain

2 ICFO-The Institute of Photonic Sciences, Av. Carl Friedrich Gauss, 3, 08860 Castelldefels – Barcelona

*(corresponding author: *amihi@icmab.es)*

Supporting Information

Contents:

Section 1. Calculation of HPC film thickness

Section 2. Depth of the imprinted features in HPC films

Section 3. Calculation of the Residual layer thickness

Section 4. Calculation of the Reactive Ion Etching rates

Section 5. Additional photos of Al Nanoparticle arrays fabricated with the lift off technique

Section 6. Additional photos of high resolution patterning of Silicon using HPC as resist

Section 7. Patterning of HPC using electron beam lithography (EBL)

Section 1. Calculation of HPC film thickness

Hydroxypropyl cellulose (Mw=100000 KDa) was obtained from Sigma-Aldrich. Further information on the material can be found in the following link:

<https://www.sigmaaldrich.com/catalog/papers/22961411> .

The thickness of flat HPC films on silicon was extracted by fitting the experimental reflectivity with spectra calculated by the transfer matrix method.³⁰ The reflection spectrum from a thin film of the HPC shows characteristic oscillations (Fabry-Perot oscillations) which depend on the films thickness and dielectric constants of the layered materials. **Figure S1** shows both experimental (blue) and calculated (red) reflection spectra in the visible range for two exemplar HPC films with different thicknesses. The averaged refractive indexes used for the fittings are 1.47 for HPC²⁹ and 3.9 for silicon,³¹ and the film thickness are set to 220 nm for the spectrum on the left and to 405 nm for the spectrum on the right. Experimental spectra were acquired using an FTIR spectroscope attached to a microscope with a 4X objective. Different spots of the samples have been probed, showing a high homogeneity of the HPC film.

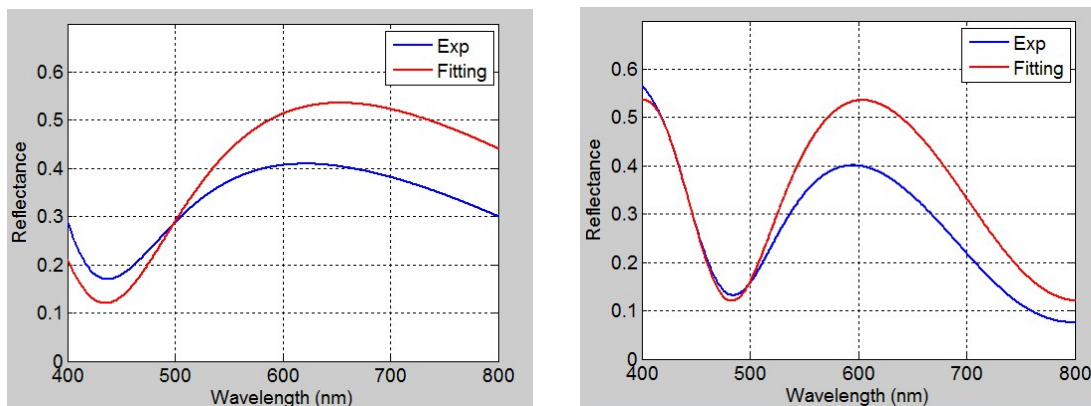
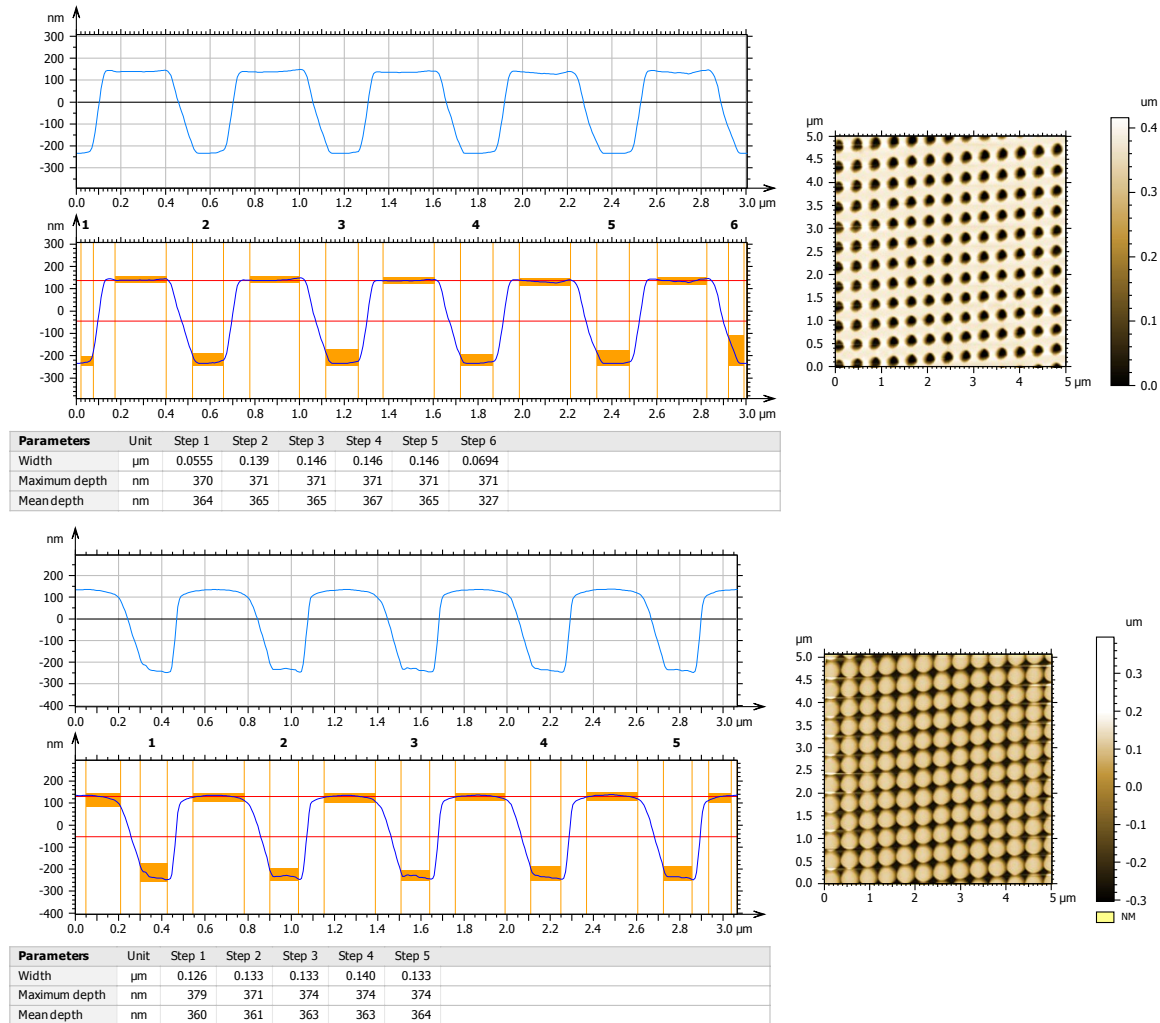


Figure S1: Experimental (blue) and calculated (red) reflection spectra for HPC films on silicon with thicknesses of 220 nm (left) and 405 nm (right).

Section 2. Depth of the imprinted features in HPC films

Atomic force microscopy analysis was performed in representative HPC films imprinted with holes and pillars with lattice parameter of 400 nm in order to measure the depth or height of the

imprinted features. Results are exhibited in **Figure S2**. The holes depth was approximately 365 nm while the pillars height was 362 nm. The estimate AFM error in the Z direction is ± 40 nm.



Figure

re S2: representative HPC imprinted pillar and holes AFM measurements: Atomic force microscopy image and representative profiles with step height calculation for holes and pillars imprinted in HPC.

Section 3. Calculation of the Residual layer thickness

The resist volume equivalence model assumed to calculate the residual layer thickness is schematized in **Figure S3**. Once the PDMS mold features are filled with the HPC, the material flow stops and the initial HPC volume V_1 must be equal to the volume V_2 obtained after the HPC

patterning. The initial thickness h_i required to obtain a residual layer with thickness h_f equal to zero, can thus be calculated knowing the pattern geometry and the features depth h_r .

As an example we apply this model to one of the PDMS molds used in this work and consisting of a 1 cm^2 imprinted area of pillars in a square array with radius $r=150 \text{ nm}$, pillars height $h_r=350 \text{ nm}$ and lattice parameter $L=400$. Using the formulas and schemes depicted in **Figure S4**, the minimum initial layer thickness h_{\min} required to fill the mold feature and ideally leaving no residual layer corresponds to 195 nm . Spin coated layers with thicknesses h_i above the calculated minimum thickness h_{\min} will result in the formation of a residual layer with thickness $h_f = h_i - h_{\min}$.

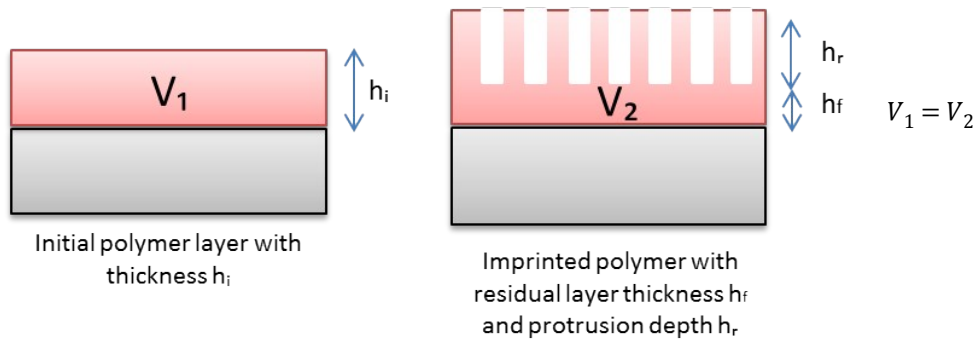


Figure S3: resist volume equivalence model: Schematic of volumes involved during HPC molding.

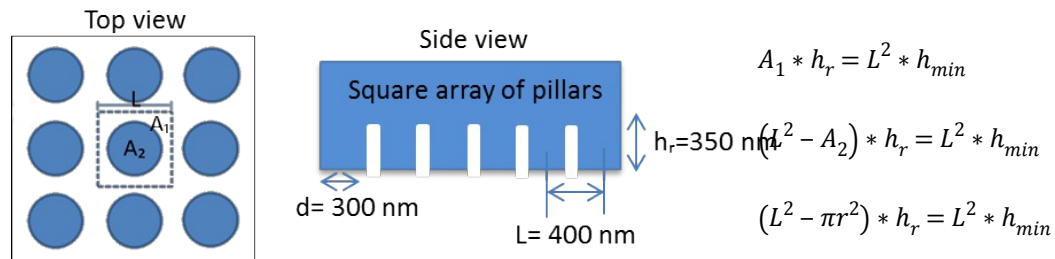


Figure S4: PDMS mold geometry: Top view and side view of the PDMS mold used and related minimum initial layer thickness calculation.

To verify experimentally this calculation we scratched the HPC film inside and outside the patterned area and we measured via atomic force microscopy the steps height. Outside the pattern (Figure S6) we obtained an HPC layer thickness of 223 nm , consistent with previous optical measurements. Inside the pattern (Figure S5) we measured a film thickness of 381 nm . This

thickness represents the distance between the top of the imprinted feature and the underlying substrate. Considering that the holes depth is 350 nm, the residual layer thickness for this sample is 31 nm, which is quite close to the theoretically calculated one (28 nm).

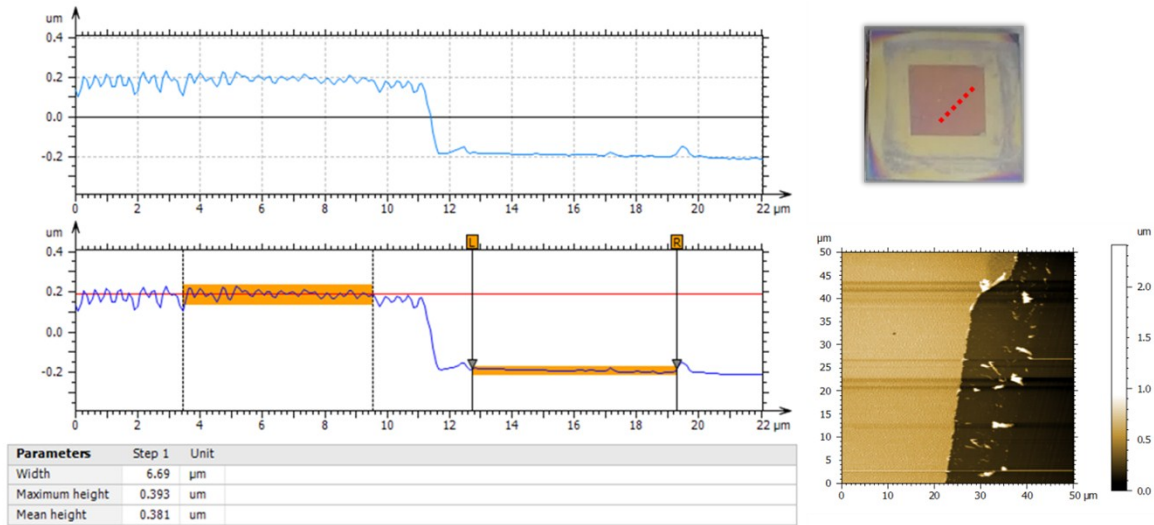


Figure S5: HPC thickness inside pattern: Atomic force microscopy image and representative profiles with step height of a scratched area inside the HPC patterned region (red dashed line in the sample photo).

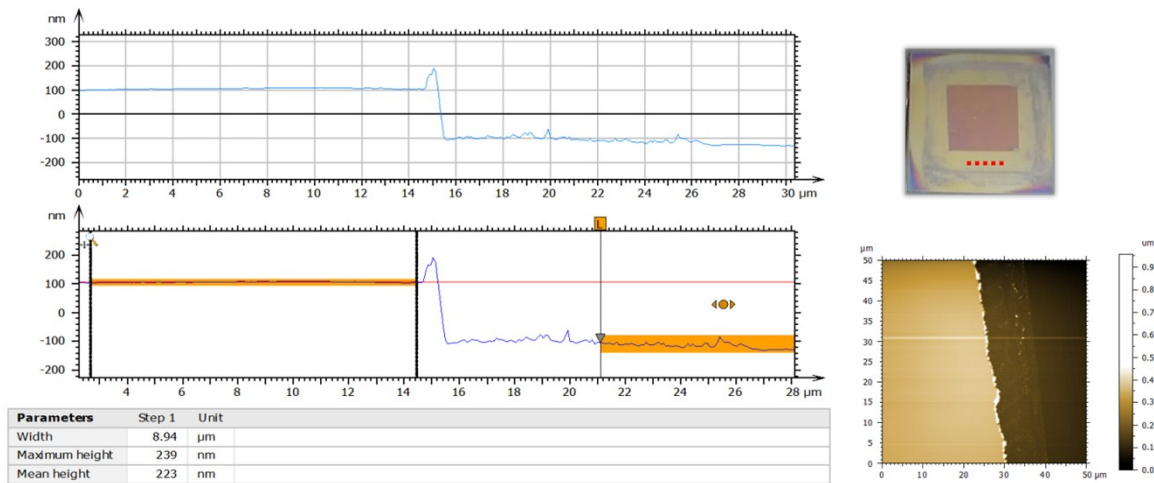


Figure S6: HPC thickness outside pattern: Atomic force microscopy image and representative profiles with step height of a scratched area outside the HPC patterned region (red dashed line in the sample photo).

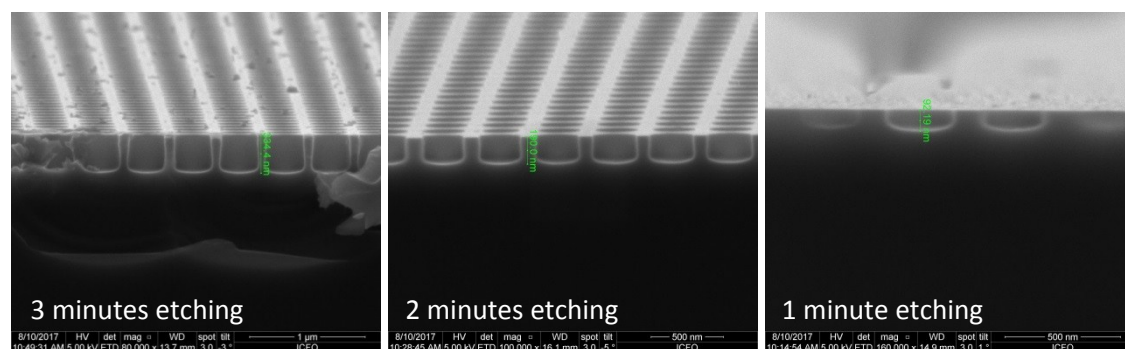
Section 4. Calculation of the Reactive Ion Etching rates

In order to etch the residual layer of cellulose and to transfer the pattern to the silicon wafer, we followed a pseudo Bosch etching process. In a pseudo Bosch etching a mixture of C_4F_8 and SF_6 gases is simultaneously injected in the RIE chamber. The ionization of C_4F_8 leads to the formation of a polymeric chain of CF_2 that settles on the substrate protecting it from erosion while substrate milling is carried out by the accelerated SF_x and F_y ions impinging on the substrate. However, the DC bias accelerates the ions towards the target material and the passivation layer deposited on the horizontal surfaces is removed at a faster rate than the one deposited on the vertical side walls. As a result, with an appropriate tuning of the gas ratio and the ICP power, it is possible to achieve a dynamic equilibrium in which the Silicon vertical sidewalls are protected by the CF_2 polymer while the horizontal surfaces remains exposed to milling ions. Selectivity values (Etching rate Si/etching rate HPC) have been estimated testing five different set of etching parameters: i) 300 W ICP Fw (forward) power and 70 sccm C_4F_8 flow, ii) 300 W ICP Fw power and 80 sccm C_4F_8 flow, iii) 300 W ICP Fw power and 90 sccm C_4F_8 flow, iv) 400 W ICP Fw power and 70 sccm C_4F_8 flow, v) 300 W ICP Fw power and 90 sccm C_4F_8 flow. For all the experiment, pressure has been set to 15 mtorr, RF generator power to 35 W, SF_6 gas flow to 45 sccm.

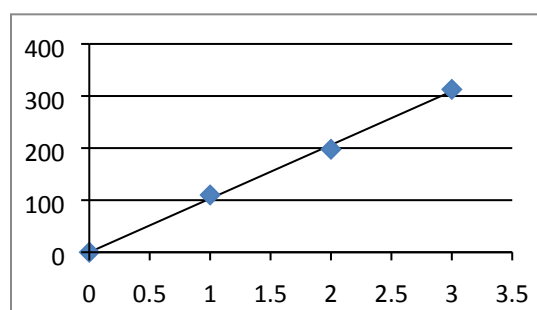
Silicon and HPC etching rates shown in figure S7 have been calculated by the linear fit of etching depth for etching times of 1, 2 and 3 min. (batches i, ii, iii) and for etching times 1 and 2 min. (batches iv, v). HPC thicknesses have been calculated by fitting the Fabry Perot oscillation as previously described. Measurements have been done on flat HPC areas outside the pattern, or using a flat layer of HPC with a known initial thickness as reference. Silicon holes depth has been measured with SEM cross section (figure S7). Data in the graphs were calculated in the following way:

- Etching rates HPC: $[220 - (\text{measured HPC thickness outside pattern})]/\text{etching time}$
- Etching rate Silicon: $(\text{Holes depth})/[(\text{time etching}) - (\text{time to remove residual layer})]$
- Time to remove the residual layer: $[(\text{cellulose etching rate}) * (\text{residual layer thickness})]$ assuming a residual layer thickness of 25 nm.

Batch (i): Fw power: 300 W, C₄F₈ flow: 70 sccm



HPC etching rate



Silicon

etching

rate

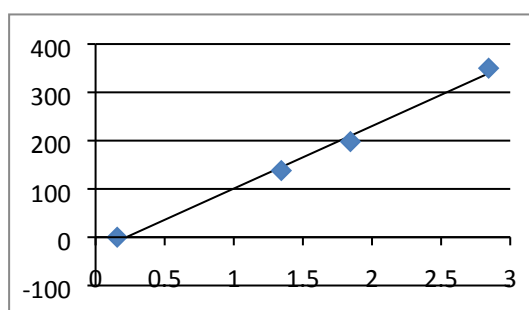


Figure S7: Exemplar calculation of etching rates for silicon and HPC for the Batch (i) (300 W of Fw power and 70 sccm C₄F₈ flow). SEM cross sectional photo shows the depth of the holes transferred in silicon for etching time of 1, 2 and 3 minutes.

Section 5. Additional photos of Al Nanoparticle arrays fabricated with the lift off technique

Aluminum nanoparticles arrays with varying lattice parameter of 400, 500 and 600 nm fabricated with metal deposition and water lift off are shown in **Figure S8**. Prior to depositing the 150 nm Al layer, the samples were etched for 10s using a Reactive Ion Etcher RIE 2000 CE (South Bay Technology Inc.). The etching parameters are 20 sccm of O₂ flow, 5 mTorr pressure and 30 W power and the HPC etching rate is c.a. 160 nm/min. Residual layer thickness of 20 nm was considered for each pattern geometry. Further tuneability of the nanoparticle diameter can be achieved by varying the duration of the etching step that precedes the metal deposition, taking advantage of the lateral erosion that occurs during RIE process (**Figure S9**).

L= 400, etching time 10 s L=500, etching time 10 s L=600 , etching time 10 s

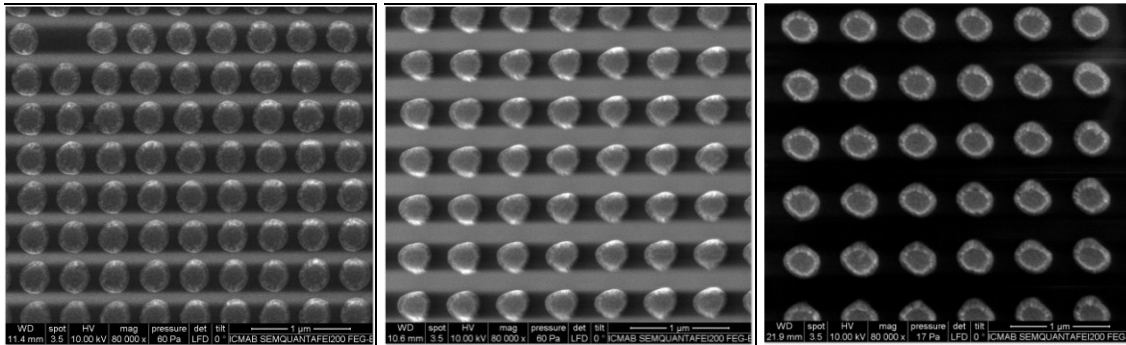


Figure S8: SEM photos of Al nanoparticles arrays with increasing lattice parameter (400, 500 and 600 nm) deposited via metal deposition and lift off.

L= 400, etching time 10 s L=400, etching time 20 s L=400 , etching time 30 s

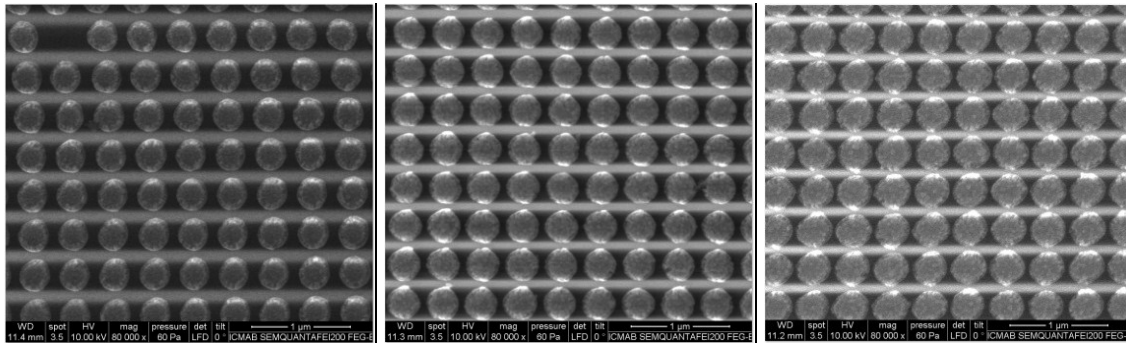


Figure S9: SEM photos of Al nanoparticles arrays with increasing nanoparticles diameter (326, 336 and 356 nm), deposited via metal deposition and lift off.

Section 6. Additional photos of high resolution patterning of Silicon using HPC as resist

Anti reflection patterns (AR) have been successfully transferred to silicon using tNIL and HPC as resist. The AR nanostructures of the master (NIL technology Aps, Denmark) make use of the bio-inspired moth-eye effect, and consist in a hexagonal array of conical shaped pillars (holes), with lattice parameter of 300 nm. Using these structures we could fabricate asymmetrical holes arrays on silicon with minimal dimension of 100 nm (**Figure S10**). The apparent non-conformity of the HPC pattern in the SEM images is essentially an artifact due to the damage of the HPC pillar during electron scanning.

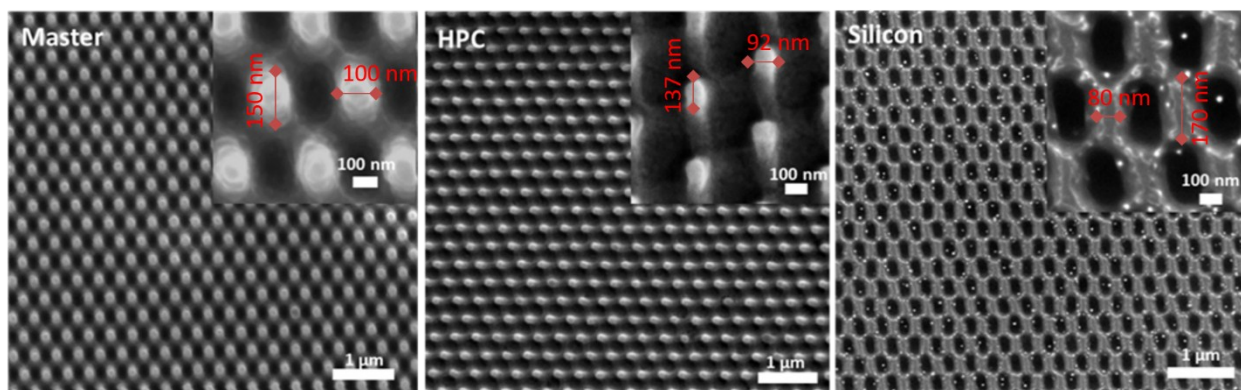


Figure S10: Anti reflection pattern transferred to silicon using HPC as resist. From left to right: SEM top view images of aluminum, imprinted HPC and silicon substrate after RIE.

Section 7. Patterning of HPC using electron beam lithography (EBL)

Hydroxypropyl cellulose was tested under exposure of electron-beam irradiation (SEM FEI InspectF with Raith Elphy add-on) to test its conversion from soluble to insoluble phase. **Fig S11a** shows square patterns after ebeam exposure at different doses and 1 min development in H₂O. The corresponding dose curve extracted from these experiments is summarized in **Fig S12**. The Ideal dose inferred from these results is around 150 $\mu\text{C}/\text{cm}^2$ while lower dose values correspond to an under conversion and higher dose values to an overexposure leading to a thickness decrease. At optimal dose 20% of thickness loss compared to initial cellulose layer thickness is attributed to a swelling of cellulose material.

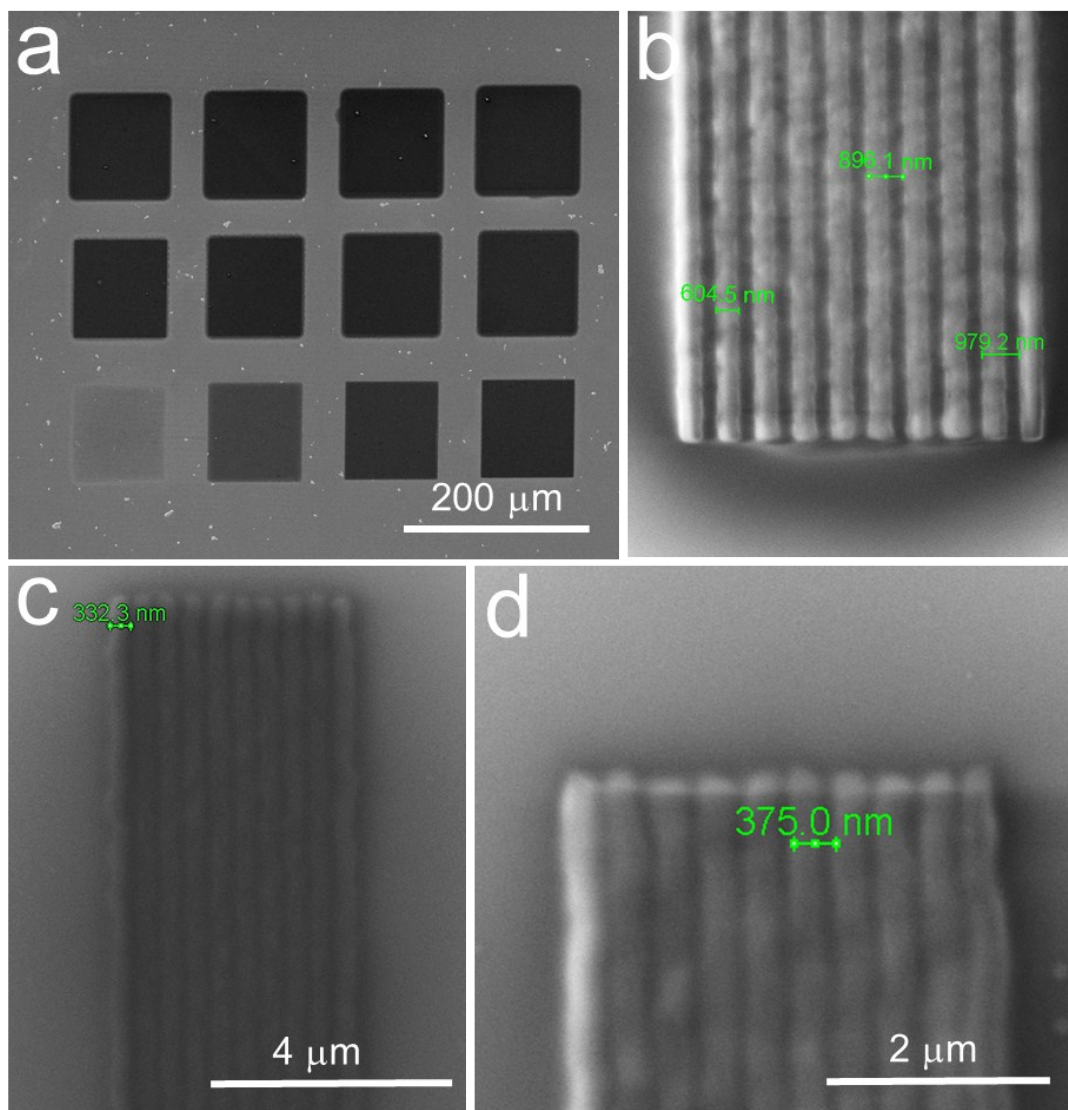


Figure S11 a) Electron beam exposure of cellulose on Si substrate. Dose ranges from 10 to $\mu\text{C}/\text{cm}^2$ to 20500 $\mu\text{C}/\text{cm}^2$, increasing from left to right and from bottom to top. Acceleration voltage of e-beam was 30kV, current 25 pA. b - d) Close up SEM top views of different size e-beam patterned lines in hydroxypropyl cellulose .

Fig S12.b –d depicts several SEM images from different size line arrays written with e-beam on cellulose using the optimal conditions. Resolutions as low as 350 nm could be achieved using bare hydroxypropyl cellulose in this preliminar study.

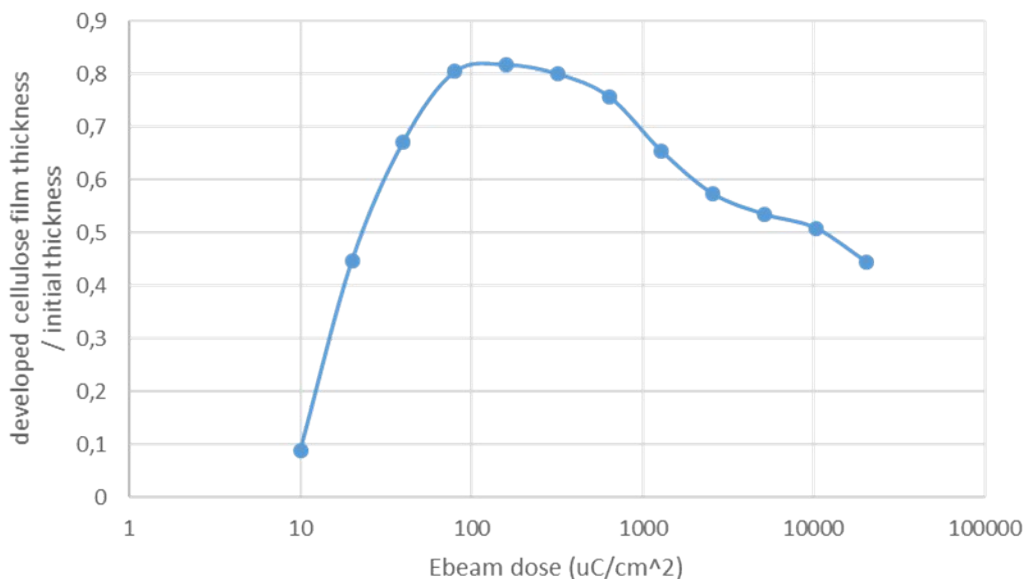


Figure S12: Ratio of the thicknesses of e-beam irradiated structures with initial cellulose layer thickness versus the applied electron beam dose

Comparison of HPC with PVA under EBL patterning

HPC shows much higher sensitivity to electron beam patterning than PVA; the dose required for PVA patterning⁴ is at least one order of magnitude higher than the one required for HPC.

[1] P. D. T. Huibers, D. O. Shah, *Langmuir* **1997**, *13*, 5995.

[2] P. Molet, J. L. Garcia-Pomar, C. Matricardi, M. Garriga, M. I. Alonso, A. Mihi, *Advanced materials (Deerfield Beach, Fla.)* **2018**.

[3] D. E. Aspnes, A. A. Studna, *Phys. Rev. B* **1983**, *27*, 985.

[4] José Marqués-Hueso, Rafael Abargues, Josep Canet-Ferrer, Saïd Agouram, José Luis Valdés and Juan P. Martínez-Pastor, *Langmuir*, **2010**, *26* (4), 2825

Summary of results

In this thesis I adapted and optimized industrially scalable nanofabrication processes based on soft-lithographic techniques, for the realization of tailored photonic architectures into hydroxypropyl cellulose (HPC). The key findings at the basis of this work are:

- HPC free-standing membranes as well as thin films on rigid substrates with thicknesses varying from few millimeters to tens of nanometers can be easily fabricated via spin-coating of HPC water solution. Fine control over thickness of the film can be achieved tuning solution concentration and spinning conditions.
- HPC films are biocompatible non-toxic and edible. Furthermore, free-standing membranes have high flexibility and possess adhesive properties, indeed they can conformally adhere to uneven surfaces and they can retrieve different materials from donor substrates.
- HPC is soluble in water and thermoformable, so two different methods were employed to pattern its surface: replica molding, more suitable for the realization of thick free-standing film, and thermal soft nanoimprinting, employed to pattern thin films deposited on solid substrates. A huge number of patterns geometry have been demonstrated, reaching minimum feature sizes of 100 nm.
- Different cellulose derivatives (acetyl cellulose) or cross-linked HPC can be used to fabricate photonic crystals featuring solubility, hydrogel formation or insolubility under water immersion.

In order to demonstrate the relevance of these findings, I characterized the performance of the fabricated HPC-based structures for several specific applications, benchmarking them with the current state of the art technology. In doing so, I followed two main goals.

1 Provide innovative optical and electrical functionality to hydroxypropyl cellulose.

To the extraordinary properties of cellulose based materials, I added a light management functionality by shaping HPC films into photonic and plasmonic crystal structures via nanoimprinting lithography.

I also demonstrated the easy incorporation into HPC membranes of functional materials like carbon nanotubes or exotic metal nanostructures like Moiré multilayers, using a novel modification of the transfer printing technique. The versatility of these approaches, opens up new venues in the field of cellulose based photonic architectures, offering a smart opportunity for the ecofriendly mass-production of color in photonic papers, transient optoelectronics for wearable and packaging systems, anti-counterfeiting technologies, washable and edible detectors or labels for the food industry. Furthermore, the biocompatibility of HPC architectures enables their use in medical applications where the photonic and plasmonic crystals could enhance the performance of light driven therapies and monitoring systems. Specifically, we obtained the following results:

- The optical properties of cellulose based photonic crystals can be tuned by changing the pattern geometry, so they can display different structural colors. Furthermore, by metal coating of the photonic crystal membranes it is possible to obtain self-standing and highly flexible plasmonic crystals, with even brighter iridescent colors. Furthermore, both cellulose photonic and plasmonic crystals can be easily fabricated on office paper substrates. **(Section5.1)**
- Plasmonic crystals can be used to boost the photoluminescence of light emitting media. By doping the HPC based plasmonic crystals with an organic dye - rhodamine B (RhB) - we measured a photoluminescence enhancement of the dye in the PhC of ten times respect to a flat film. Interestingly, HPC's high solubility in water and most organic solvents makes it an excellent host matrix for a wide range of materials (fluorescent dyes, nanoparticles or any other polymer with same solvent compatibility). **(Section5.1)**
- Plasmonic crystal membranes were further tested as disposable SERS substrates by detecting a thiophenol probe. The extremely high quality of the nanostructured pattern enabled to perfectly match the simulated spatial distribution of the plasmonic field enhancement with the intensity map of the Raman signal arising from thiophenol molecules deposited on the plasmonic crystal. **(Section5.1)**

- Transparent conductive electrodes can be fabricated by embedding thin films of Carbon Nanotubes into HPC using temperature assisted transfer printing technique. Thickness of the film can be tuned by changing transfer temperature, featuring a sheet resistance of 305 Ω /sq with a 77% film transparency. **(Section 5.2)**
- Moiré multilayer stacks with tunable optical properties were fabricated by embedding into HPC multiple nanoparticles arrays using a modify transfer printing technique. **(Section 5.2)**

2 Employing hydroxypropyl cellulose as a tool for green nanofabrication.

I have introduced an exciting new path for HPC as non-toxic and water processable sacrificial material for advanced ecofriendly nanofabrication. I developed HPC water soluble adhesives that can be employed as transient tapes for transfer printing (and optionally, simultaneous patterning) of functional materials into arbitrary substrates, and simply dissolved in water afterward. Furthermore, I demonstrated the viability of HPC as ecofriendly lithographic resist employing it in typical electronic manufacturing processes such as reactive ion etching and metal deposition and lift off, using only water as solvent. Specifically, I obtained the following results:

- HPC transient tape mediated transfer printing enable crack-free stripping of flat and patterned metallic layers, while keeping large area and high throughput production. We compared the transferred films obtained with our method against conventional PDMS (polydimethylsiloxane) transfer and only in our case, we observed the crack-free transfer from silicon to glass of a 50 nm Ag film, with no measurable differences in sheet resistance before and after transfer. Furthermore, HPC transient tapes allowed fabrication of Moiré metamaterials on a target substrate by 3D stacking different nanopatterned silver motifs (simply iterating the transfer process). **(Section5.2)**
- I used pre-patterned HPC membranes for μ -contact printing of Carbon Nanotubes (CNTs) into tailored geometries within a single step, over 1 cm² areas and with unprecedented feature sizes down to 1 μ m (see Figure 1 below). It is worth noting that achieving large area and high throughput patterning of CNTs is of paramount importance in order to take advantage of their excellent physical properties. This innovative approach directly provides patterning of the CNTs and transfer

seamlessly and without additional processing, which greatly facilitates the implementation of this exciting material in many applications. **(Section 5.2)**

- HPC can be used as water-processable and non-toxic NIL resist for ecofriendly nanofabrication. I used only hydroxypropyl cellulose and water to fabricate photonic crystals in silicon and 2D metal nanoparticle arrays with up to 100 nm resolution over 1 cm² areas. In particular, I optimized RIE conditions in Pseudo Bosch processes, and obtained a selectivity of HPC vs silicon of a value of 2, which is comparable with commonly used resist like PMMA **(Section 5.3)**.
- I combined HPC with PMMA, a water insoluble polymer, demonstrating advanced fabrication possibilities. I fabricated alternating stacks of HPC and PMMA in which each material can be selectively removed with the proper solvent. Furthermore, when combined with nanoimprinting, sub-micrometric air cavities are left inside the PMMA, enabling a straightforward nanofabrication strategy for novel optofluidic devices. **(Section 5.3)**

Conclusions and Outlook

This thesis contributes to the current research on cellulose based materials, providing innovative functionalities to HPC and designing novel application for this material in the emerging field of nanophotonics. All the nanofabrication processes implemented are based on cheap, straightforward and industrially scalable techniques. Two main conclusions can be drawn:

- Both nanoimprint lithography (NIL) and nanotransfer printing (nTP) techniques bring additional optical and electrical functionalities to the HPC.
- HPC can be used as water-processable resist, representing a promising tool for green nanofabrication.

Given the novelty of this thesis's findings, several further investigation paths could be followed:

- The patterning resolution can be decreased below the 100 nm minimum feature size presented here. The bottle neck in this case would be the mold fabrication, given the pattern instability issues that typically arise for sub 100 nm features. However, this issue can be addressed for instance by changing the mold material, and the excellent mechanical properties of HPC (Young modulus from 20 to 150 MPa) should definitively permit to imprint it with higher resolutions.
- Sustainable product design and development involves more than one concept, starting from the employment of renewable, nontoxic and biodegradable materials, environmentally sustainable manufacturing, and design for disassembly and recycling. Further investigation should be done in order to address the environmental impact of HPC. In particular, life cycle analysis and biodegradability rate test should be done in order to give a more quantitative data on the pollution that derives from HPC products fabrication and disposal.
- The fabrication processes developed in this thesis are extremely versatile and can lead to countless optically and electrically functional architectures that could be manufactured in a mass-production compatible fashion. This definitively opens the path to further development of HPC based technologies

in different application fields, but at the same time, the fabrication strategies developed in this work could be easily adapted to other (bio)materials.

The relevance of the paths opened up by this work is further corroborated if we contextualize them in the exponentially growing research areas to whom they belong. Figure 7.1 shows the increase number of publications on naturally derived polymers in photonic and cellulose based materials in nanotechnology in the last 20 years.

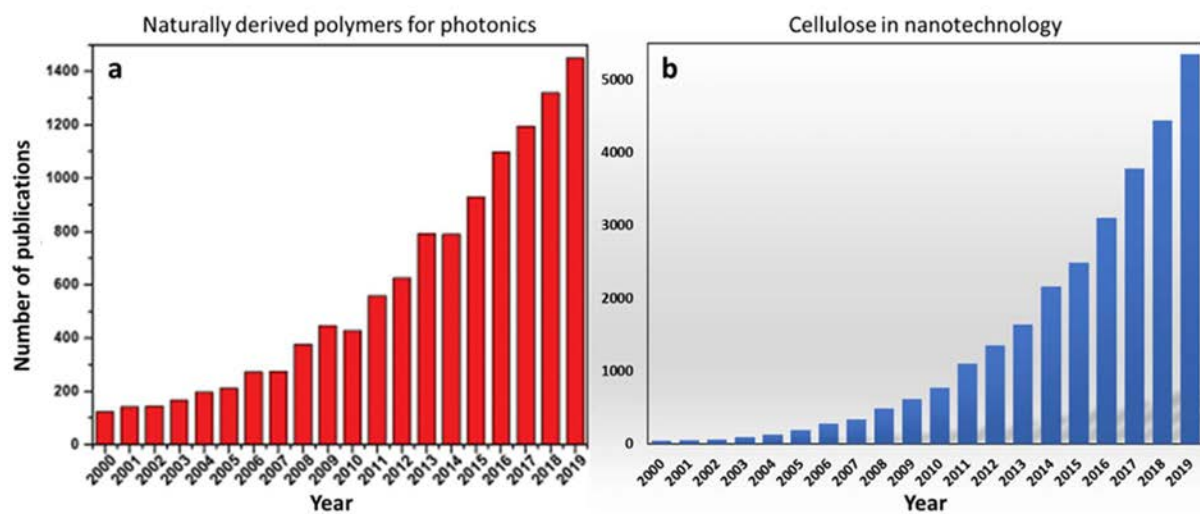


Figure 7.1 Number of publications per year about a) Naturally derived polymers for photonics and b) Cellulose in nanotechnology. Sources: Web of science.

Appendix A

Optimization of metal films deposition

Thermal evaporation condition for high quality optical response

In order to obtain the best optical performances from plasmonic structures it is fundamental to employ metallic films with high structural quality. The amount of electromagnetic losses of a metallic film depends on the specific dielectric function (or relative permittivity) of the material and on the film morphology. The latter greatly depends on the deposition conditions including the deposition rate, the pressure in the deposition chamber, the substrate type and temperature. This paragraph reports the analysis of the optical response of plasmonic film of silver decorated with a square array of holes, produced under different thermal evaporation condition. All the metallic films analyzed have been transfer printed into silicon substrate using HPC membranes (see chapter 5 section 5.2 for further details). Structural quality has been checked via SEM analysis, while in order to address the optical quality, the measured transmission and reflection spectra have been compared with the simulated counterpart. The results of this optimization have been particularly useful for the fabrication of high quality multilayer nanopatterned films via HPC transfer, illustrated in chapter 5 section 5.2.

Influence substrate wettability.

The first evaporation test has been done with the following condition:

- Evaporation substrate: **PDMS**
- Evaporation rate: **1 Å/s**
- Film thickness **60 nm**

As can be seen from the SEM analysis shown in figure A.1. surface salinization negatively affects the final quality of the Ag film, being responsible for film irregularities due to partial dewetting of the deposited metal from the donor substrate.

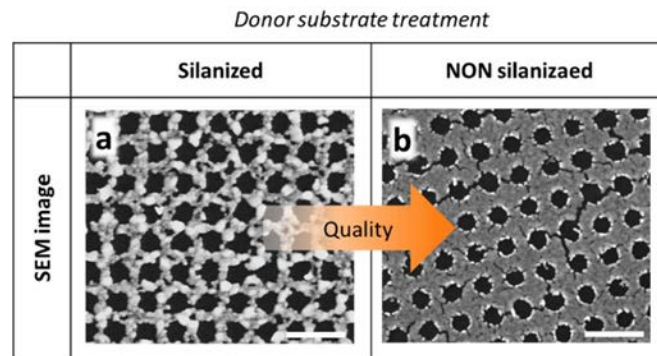


Figure A.8.1: Influence of donor substrate wettability on silver films evaporated on PDMS substrates at an evaporation rate of 1 Å/s. Scale bar is 1 μm.

The following analysis address the influence of the silver evaporation rate on the final film quality, using NON-silanized PDMS molds as donor substrates.

Influence of the evaporation rate.

This second evaporation test has been done fixing the following condition:

- Evaporation substrate: **PDMS (NON-silanized)**
- Ag thickness: **60 nm**

It has been demonstrated in previous works¹ that, fast evaporation rates and lower pressures can induce formation of smaller grains, diminishing the number of nucleation sites and the grain-boundary pinning by residual gases during the metal deposition. This can improve the structural and optical qualities of the film, reducing the scattering and the electrical losses at the grain boundaries. Figure 8.2 illustrate the effect of the evaporation rate on the optical and morphological properties of silver films.

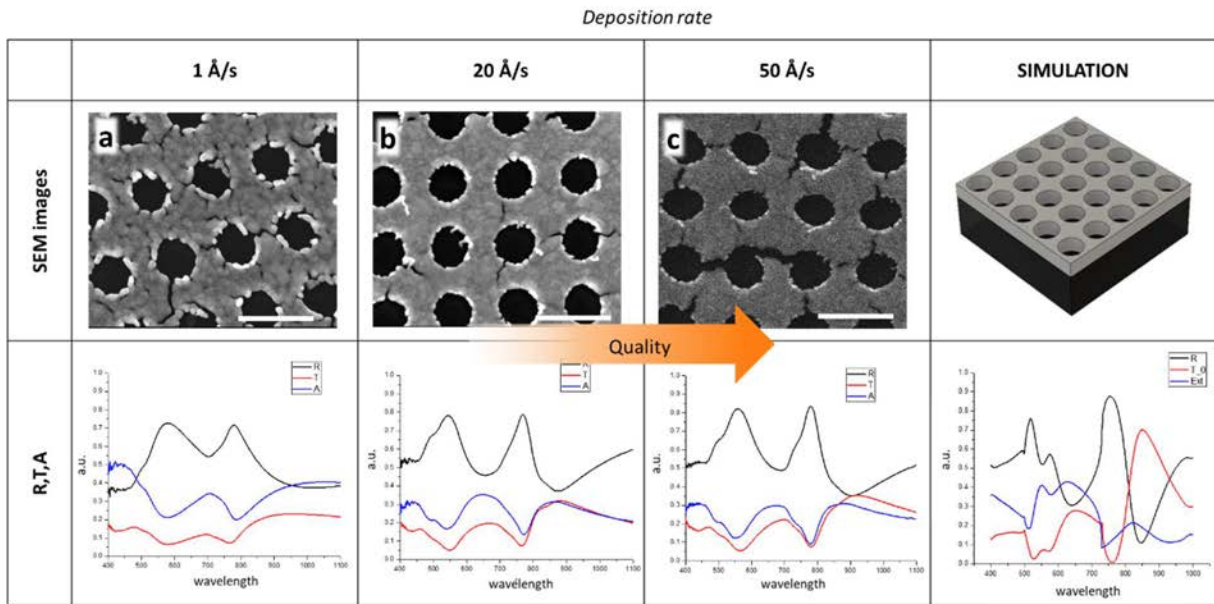


Figure 8.2 Influence of the evaporation rate on 60 nm thick silver films evaporated on PDMS substrates. Scale bar is 500 nm. R stand for reflection, T for transmission and A is the extinction calculated as $A=1-R-T$.

As can be seen from both the SEM inspection and from the comparison of the measured optical properties with the simulated one, the best quality film is obtained for the highest evaporation rate tested. However it is visible from the SEM images, that all films presents some cracks that are due to the mechanical deformation of the underlying soft PDMS. The last test addresses this issue analyzing the influence of the substrate using the optimized condition obtained so far.

Influence of the substrate stiffness

This last evaporation test has been done with the following condition:

- Evaporation rate: 50 Å/s
- Ag thickness: 60 nm

As expected, by changing PDMS with a non-flexible material like the silicon substrate, we obtained the highest quality film. The experimental transmission and reflection spectra (solid lines) almost perfectly match the simulated ones (dashed lines), as can be seen from sample b in Figure 8.3

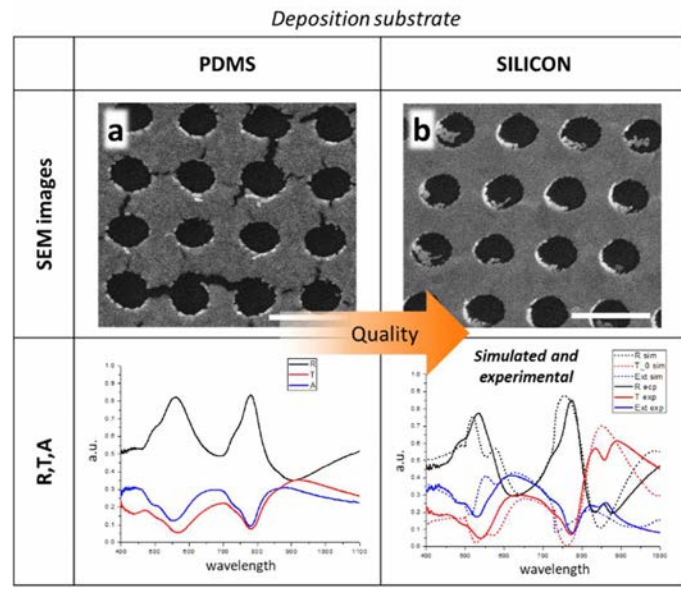


Figure 8.3 Influence of the substrate stiffness on 60 nm thick silver films evaporated at 50 Å/s. Scale bar is 500 nm. R stand for reflection, T for transmission and A is the extinction calculated as $A=1-R-T$.

8.1 References

(1) McPeak, K. M.; Jayanti, S. V.; Kress, S. J. P.; Meyer, S.; Iotti, S.; Rossinelli, A.; Norris, D. J. Plasmonic Films Can Easily Be Better: Rules and Recipes. *ACS photonics* **2015**, *2* (3), 326–333. DOI: 10.1021/ph5004237.

Appendix B

Cellupack: hydroxypropyl cellulose packaging

Ideas generation program

The Ideas Generation Program is organized every year by the Universitat Autònoma de Barcelona (UAB) Research Park and promotes the entrepreneurial spirit and the culture of innovation supporting researchers and PhD students from different academic fields in bringing their research to the market, looking for the best solutions to specific industrial challenges.

The 10th edition of the program was entitled “smart food” and addressed various thematic related to the food industry, such as reducing food waste, eliminating plastics or decreasing the use of antibiotics.

Cellupack, was chosen as the most innovative project of the Generating Ideas Program on Smart Food (figure B.1), proposing and developing an idea of business based on the use of HPC as an alternative to plastic for single use, short-life packaging. The competing projects were evaluated on the bases of the innovativeness of the idea, on the business plan development and on the quality of the project presentation to the jury.



Figure B.1 Photo of the ideas generation program award ceremony: Cellupack project win the first prize. The member of the group, from left to right: Michele Dei (researcher at IMB-CNM), me, Elena Jacas (food technologist).

Hydroxypropyl cellulose presents a set of unique characteristics that makes it a particularly appealing material for packaging proposes:

- It is biodegradable, non-toxic and soluble in water, leaving a minimum ecological footprint at the end of its service life.
- It is edible, tasteless, and odorless, allowing to implement it directly as food coating.
- Differently from PLA or starch it is not food-competing (it is not extracted from alimentary resources).
- It has good final mechanical properties, and act as a discrete oil barrier.
- It has good film formation properties, it is thermoformable and sealable.

In the frame of the project, I developed different packaging prototypes fabricated via thermoforming of HPC dry films and via casting of HPC from liquid water solution. Figure B1 illustrates some of the prototypes realized, from left to right: A single-dose toothpaste encapsulated in HPC, an ice-cream cup and an espresso coffee cup.



Figure B.2. Cellupack prototypes. Soluble packaging example made of HPC. From left to right: A single-dose toothpaste encapsulated in HPC, an ice-cream cup and an espresso coffee cup.

Scientific contributions

Publications derived from this thesis

1. Espinha, A., Dore C., Matricardi, C., Alonso, M. I., Goñi A. R. & Mihi, A. Hydroxypropyl cellulose photonic architectures by soft nanoimprinting lithography. *Nature Photonics* 12, 343–348 (2018).
link: <https://www.nature.com/articles/s41566-018-0152-1>
2. Dore, C., Dörling, B., Garcia-Pomar, J. L., Campoy-Quiles, M. & Mihi, A. Hydroxypropyl Cellulose Adhesives for Transfer Printing of Carbon Nanotubes and Metallic Nanostructures. *Small* 2004795 (2020). doi:10.1002/sml.202004795
link: <https://onlinelibrary.wiley.com/doi/full/10.1002/sml.202004795>
3. Dore, C., Osmond, J. & Mihi, A. A water-processable cellulose-based resist for advanced nanofabrication. *Nanoscale* 10, 17884–17892 (2018).
link: <https://pubs.rsc.org/ko/content/articlehtml/2018/nr/c8nr04851g>
4. Ciancico, C., Schädler, K. G., Pazzagli, S., Colautti, M., Lombardi, P., Osmond, J., Dore, C., Mihi, A., Ovvyan, A. P., Pernice, W. H. P., Berretti, E., Lavacchi, A., Toninelli, C., Koppens, & Reserbat-Plantey, F. H. L., Narrow Line Width Quantum Emitters in an Electron-Beam-Shaped Polymer. *ACS Photonics* (2019), 6, 12, 3120-3125
link: <https://pubs.rsc.org/ko/content/articlehtml/2018/nr/c8nr04851g>
5. Salles, P., Caño, I., Guzman, R., Dore, C., Mihi, A., Zhou, W. & Coll, M., Facile chemical route to prepare water soluble epitaxial Sr₃Al₂O₆ sacrificial layers for free-standing oxides. *Advanced Materials Interfaces* (2020) – SUBMITTED.

6. Chiang, N., Scarabelli, L., Vinnacombe-Willson, G. A., Pérez, L. A., Dore, C., Mihi, A. Jonas, S. J., & Weiss, P. S., Large-Scale Soft-Lithographic Patterning of Plasmonic Nanoparticles, *ACS Materials Letters* (2020) – SUBMITTED.

Conferences presentations

1. C. Dore, Cellulose-based photonic architectures, *Nanophotonics and Micro/Nano Optics International Conference*, Munich (Germany), September **2019**, Talk.
2. J. Osmond, C. Dore, A. Mihi, Environmentally friendly nanofabrication with cellulose and water, *MNE 45th International Conference on Micro & Nano Engineering*, Rhodes (Greece) September **2019**, Talk.
3. P. Molet, C. Dore, Cellulose photonics, *META 2019, the 10th International Conference on Metamaterials, Photonic Crystals and Plasmonics*, Lisbon (Portugal), July **2019**, Poster.
4. C. Dore, Water-processable cellulose-based sacrificial layers for advanced nanofabrication, *4th Scientific Meeting of BCN-c Students, Barcelona (Spain)*, June **2019**, Barcelona (Spain), Talk.
5. C. Dore, Water-processable cellulose-based resist for green nanofabrication *Material Research Society falls meeting*, November **2018**, Boston (USA), Talk.
6. C. Dore, Cellulose photonics, *Nanophotonics and Micro/Nano Optics International Conference*, Rome (Italy), October **2018**, Poster.
7. C. Dore, A. Espinha, C. Matricardi, M. I. Alonso, A. R. Goñi, A. Mihi, Cellulose based photonic architectures, *ImagineNano2018 International Event - 3PM2018 Conference*, March **2018**, Bilbao (Spain), Talk.

8. C. Dore, Multifunctional cellulose based photonic architectures, *3rd Scientific Meeting of BCN-c Students, Barcelona (Spain)*, November **2017**, Barcelona (Spain), Talk.